
**Molecular innovations in bryophyte lineages assisting
adaptations for survival in terrestrial environments**



Dissertation

der Fakultät für Biologie

der Ludwig-Maximilians-Universität München

Erika Csicsely

München, 2024

Diese Dissertation wurde angefertigt unter der Leitung von Prof. Dr. Wolfgang Frank im Bereich Molekulare Zellbiologie der Pflanzen an der Fakultät für Biologie der Ludwig-Maximilians-Universität München.

Erstgutachter: Prof. Dr. Wolfgang Frank

Zweitgutachter: Prof. Dr. Thomas Nägele

Eingereicht am: 14.03.2024

Datum der mündlichen Prüfung: 05.06.2024

Eidesstattliche Erklärung

Ich versichere hiermit an Eides statt, dass meine Dissertation selbständig und ohne unerlaubte Hilfsmittel angefertigt worden ist. Die vorliegende Dissertation wurde weder ganz, noch teilweise bei einer anderen Prüfungskommission vorgelegt. Ich habe noch zu keinem früheren Zeitpunkt versucht, eine Dissertation einzureichen oder an einer Doktorprüfung teilzunehmen.

München, 14.03.2024

Erika Csicsely

Statutory Declaration

I declare that I have authored this thesis independently and that I have not used other than the declared sources and resources. As well, I declare that I have not submitted a dissertation without success and have not passed the oral exam. The present dissertation (neither the entire dissertation nor in parts) has not been presented to another examination board.

Munich, 14.03.2024

Erika Csicsely

Table of contents

Table of contents	I
List of figures	III
List of tables	IV
Summary	V
Zusammenfassung	V
1 Introduction	9
1.1 Plant terrestrialization – an essential step for the evolution of modern life.....	9
1.2 Phytohormone evolution enabled plant terrestrialization.....	10
1.2.1 Role of auxin during the development of bryophytes.....	12
1.2.2 ABA regulates signaling pathways during salt, drought and cold stress.....	13
1.2.3 Phytohormone regulation during pathogen defense and symbiotic infections.....	14
1.3 sRNA biosynthesis and sRNA-dependent gene regulation	16
1.3.1 Evolution of sRNA signaling and DICER-LIKE proteins during plant terrestrialization.....	16
1.3.2 Role of DCL proteins during sRNA biosynthesis	17
1.3.3 Influence of phytohormone signaling on miRNAs expression and vice versa	20
1.3.4 DCL1 feedback regulation in <i>A. thaliana</i> and <i>P. patens</i>	21
1.4 The Band-7 protein family protein FLOTILLIN	22
1.5 Bryophytes – the ideal clade to study plant terrestrialization.....	23
1.5.1 The moss <i>Physcomitrium patens</i>	24
1.5.2 The liverwort <i>Marchantia polymorpha</i>	25
1.6 Research Questions.....	26
1.6.1 Question 1 – How does the loss of DCL genes influence the phytohormone response, salt tolerance, gene expression and the sRNA profile of <i>M. polymorpha</i> ? Does the function of MpDCLs differ from those in <i>P. patens</i> ?	26
1.6.2 Question 2 – Does the Band-7 protein FLOT modulate stress tolerance in <i>P. patens</i> ? How is the expression of <i>PpFLOT</i> regulated? Are there differences in the function of bryophyte and seed plant FLOT?	26
2 Material and Methods	28
2.1 Experiments Question 1 - How does the loss of DCL genes influence the phytohormone response, salt tolerance, gene expression and the sRNA profile of <i>M. polymorpha</i> ? Does the function of MpDCLs differ from those in <i>P. patens</i> ?	28
2.2 Experiments Question 2 - Does the Band-7 protein FLOT modulate stress tolerance in <i>P. patens</i> ? How is the expression of <i>PpFLOT</i> regulated? Are there differences in the function of bryophyte and seed plant FLOT?	33
2.3 Additional Methods	40
3 Results	41
3.1 Results Question 1 - How does the loss of DCL genes influence the phytohormone response, salt tolerance, gene expression and the sRNA profile of <i>M. polymorpha</i> ? Does the function of MpDCLs differ from those in <i>P. patens</i> ?	41
3.2 Results Question 2 - Does the Band-7 protein FLOT modulate stress tolerance in <i>P. patens</i> ? How is the expression of <i>PpFLOT</i> regulated? Are there differences in the function of bryophyte and seed plant FLOT?	64

4	Discussion.....	91
4.1	Discussion Question 1 - How does the loss of DCL genes influence the phytohormone response, salt tolerance, gene expression and the sRNA profile of <i>M. polymorpha</i> ? Does the function of MpDCLs differ from those in <i>P. patens</i> ?	91
4.2	Discussion Question 2 - Does the Band-7 protein FLOT modulate stress tolerance in <i>P. patens</i> ? How is the expression of <i>PpFLOT</i> regulated? Are there differences in the function of bryophyte and seed plant FLOT?	100
4.3	Outlook	108
	References	110
	List of abbreviations.....	121
	Appendix.....	125
	Acknowledgements	147
	Curriculum vitae.....	148

List of figures

Figure 1: Evolution of land plants	11
Figure 2: Phytohormone signaling in land plants	15
Figure 3: sRNA biogenesis in land plants	19
Figure 4: <i>PpDCL1a</i> autoregulatory feedback loop in <i>P. patens</i>	22
Figure 5: Life cycle of <i>P. patens</i> and <i>M. polymorpha</i>	24
Figure 6: Phylogenetic analysis of DCL proteins and their functional domains	43
Figure 7: Generation of <i>Mpdc1^{9e}</i> mutant lines	46
Figure 8: Phenotypic analysis of <i>Mpdc1^{9e}</i> mutant lines	47
Figure 9: Growth of WT and <i>Mpdc1^{9e}</i> mutant lines on high salt concentration	49
Figure 10: Phytohormone treatment of mutant <i>Mpdc1^{9e}</i> lines	52
Figure 11: Expression analysis of miRNAs and sRNAs in mutant <i>Mpdc1^{9e}</i> lines grown under standard and salt stress conditions	54
Figure 12: Expression of protein-coding transcripts in the <i>Mpdc1^{9e}</i> mutant lines when grown under standard and salt stress conditions	58
Figure 13: Localization of <i>PpFLOT::citrine</i> and comparison of its peptide sequence to homologs in other plant species	65
Figure 14: Generation of $\Delta PpFLOT$ and <i>PpFLOT</i> -OEX lines	67
Figure 15: Growth phenotype of $\Delta PpFLOT$ and <i>PpFLOT</i> -OEX lines	69
Figure 16: Phenotypic analysis of $\Delta PpFLOT-1$ and all <i>PpFLOT</i> -OEX lines	71
Figure 17: <i>PpFLOT</i> expression is regulated by daytime, light, ABA and salt	73
Figure 18: Changes in H ₂ O ₂ levels and gene expression corresponding to changes in <i>PpFLOT</i> expression	76
Figure 19: Effects of changes in <i>PpFLOT</i> expression on chlorophyll content and photosynthetic activity	80
Figure 20: Pigment composition of all <i>PpFLOT</i> mutant lines	82
Figure 21: Proteomics and GO term analysis of all <i>PpFLOT</i> -OEX lines compared to <i>P. patens</i> WT	83
Figure 22: Identification of differentially expressed protein groups in all <i>PpFLOT</i> -OEX lines	86
Figure 23: Analysis of changes in the lipid profile of <i>PpFLOT</i> mutant lines	88
Figure 24: Altered <i>PpFLOT</i> expression leads to changes in the chloroplast thylakoid structure	90
Figure 25: Effect of <i>PpFLOT</i> overexpression in protonema cells	106
 Supplementary Figure 1: Overview of all generated <i>Mpdc1^{9e}</i> mutant lines	 125
Supplementary Figure 2: Growth of gametophores from <i>PpFLOT</i> -OEX lines submerged in liquid medium	126
Supplementary Figure 3: Relative gene expression analyses of salt-induced genes and genes encoding components of photosystem I and II under control conditions and after ABA and salt treatment.	128

List of tables

Table 1: Protein sequence IDs and sources used to construct DCL phylogenetic tree.....	132
Table 2: Description of the generated <i>Mpdcl^{ge}</i> lines used in this study.....	134
Table 3: Oligonucleotides used in Question 1 (Supplementary Table 3)	135
Table 4: Overview of significant DE genes and their putative regulating DE miRNA and sRNA in <i>Mpdcl1a-6^{ge}</i> and WT treated with 100 mM NaCl.	137
Table 5: Overview of significant DE genes and their putative regulating DE miRNA and sRNA in <i>Mpdcl1b-6^{ge}</i> and WT treated with 100 mM NaCl.	138
Table 6: Overview of significant DE genes and their putative regulating DE miRNA and sRNA in <i>Mpdcl3-6^{ge}</i> and <i>Mpdcl4-1^{ge}</i>	139
Table 7: Oligonucleotides used in Question 2 (Supplementary Table 15)	140
Table 8: Significant differentially accumulated pigments in all <i>PpFLOT</i> mutant lines compared to the WT	142
Table 9: DE proteins in <i>PpFLOT</i> -OEX1, 2 and 3 compared to the WT	143
Table 10: List of all significant differentially accumulated lipids of all <i>PpFLOT</i> mutant lines compared to the WT (Supplementary Table 20).....	144

Summary

During the water-to-land transition, plants had to cope with drastic environmental changes such as fluctuating temperatures, drought and high soil salinity. To withstand these adverse environmental conditions, the ancestors of today's land plants had to undergo several structural and molecular adaptations. For example, expanded functions of small RNAs (sRNAs) enabled rapid changes in gene expression in response to changing environmental conditions. The diversification of the sRNA repertoire was accompanied by an expansion of DICER-LIKE (DCL) protein family essential for sRNA biosynthesis.

DCL proteins in the liverwort *Marchantia polymorpha* have received little attention compared to DCLs of other land plants and mosses, such as *Physcomitrium patens*. Therefore, the CRISPR/Cas9 system was used to generate reading frame mutants of the four MpDCLs: MpDCL1a, MpDCL1b, MpDCL3 and MpDCL4. These *Mpdc1^{ge}* mutants displayed either phenotypic deviations from the WT in response to long-term salt and phytohormone treatments or, in case of *Mpdc1a^{ge}*, impaired development under standard growth conditions. It is noteworthy that, with the exception of *Mpdc1b^{ge}*, all other *Mpdc1^{ge}* mutants were sterile, as no gametangioophores could be induced in these lines. However, the *Mpdc1b^{ge}* gametangioophores showed significantly reduced growth, suggesting that all MpDCLs play a role in gametangioophore induction and development. Detected changes in the sRNA and mRNA profiles of the *Mpdc1^{ge}* allow conclusions on the function of the individual MpDCLs. Thus, MpDCL1a is responsible for microRNA (miRNA) biogenesis, while MpDCL4 generates trans-acting small interfering RNAs (ta-siRNA) and MpDCL3 appears to be involved in the regulation of pathogen-induced genes and the synthesis of heterochromatic RNA (hcRNA).

Mpdc1b^{ge} mutants are able to tolerate higher salt concentrations than the WT. Salt-treated *Mpdc1b^{ge}* mutants show significantly reduced miRNA expression and fewer changes in their sRNA expression profile than the salt-treated WT. Interestingly, examination of the *Mpdc1b^{ge}* miRNA profile under standard growth conditions did not reveal any significant changes. This suggests that *M. polymorpha* possesses highly specific MpDCL1b-dependent mechanisms for miRNA regulation that are selectively activated in response to high salt concentrations. These newly discovered potential mechanisms for selective miRNA regulation are most likely evolutionarily conserved, as orthologs of MpDCL1b have been found in other moss and fern species.

Loss of a *PpDCL1a* regulatory feedback loop in *P. patens* results in salt hypersensitivity, ABA hyposensitivity, and increased expression of the band 7 protein FLOTILLIN (FLOT). At least one variant of this protein is present in most seed plants. FLOT generally associates with plasma membranes and is involved in clathrin-independent endocytosis. In contrast to most

seed plants, the only FLOT variant from *P. patens* does not associate with the plasma membrane but with thylakoid membranes, indicating a different function of this protein.

Overexpression of *PpFLOT* results in a reduced tolerance of *P. patens* to high salt concentrations. In addition, the protonemal filaments of *PpFLOT*-OEX lines develop brachyocyte-like cells, which show distinct discolorations with increasing *PpFLOT* expression that are most likely the result of necrotic events. It is worth noting that these necrotic events exclusively occur in the protonema stage of these lines and are absent in developed gametophores.

Overexpression of *PpFLOT* also leads to an increased photosynthetic rate, increased chlorophyll production and accumulation of reactive oxygen species (ROS). Metabolomics analyses revealed a general decrease in pigment levels and significant changes in the lipid profile of *PpFLOT* mutants. In particular, the changes in the lipid profile indicate an influence of *PpFLOT* on the biosynthesis of fatty acids. In contrast to the WT, the thylakoid membranes of *PpFLOT*-OEX lines also show a disordered structure and do not form grana. These structural changes are most likely a consequence of the different lipid composition.

Furthermore, proteomic analyses in the *PpFLOT*-OEX lines identified a number of differentially accumulated proteins that could contribute to the reduced salt tolerance. *PpFLOT* also indirectly affects the gene expression through its putative influence on ROS and Ca^{2+} homeostasis. The expression of *PpFLOT* *per se* can be repressed by ABA and light, follows a circadian rhythm and can most likely be regulated posttranscriptionally by miR167.

Zusammenfassung

Die ersten Landpflanzen sahen sich mit einer Reihe von Herausforderungen konfrontiert, wie z. B. schwankenden Temperaturen und salzhaltigen Böden. Um mit diesen widrigen Umweltbedingungen zurechtzukommen, mussten die Vorfahren der heutigen Landpflanzen einige strukturelle und molekulare Anpassungen durchlaufen. So ermöglichte die Evolution kleiner, nicht-kodierender RNAs (sRNAs) eine schnelle Regulation der Genexpression bei veränderten Umweltbedingungen. Diese Diversifizierung des sRNAs-Repertoires ging mit einer schrittweisen Erweiterung der DICER-LIKE (DCL) Proteinfamilie einher, die essentiell für die sRNA-Biosynthese ist.

Die Funktion der DCL-Proteine im Lebermoos *Marchantia polymorpha* wurde im Vergleich zu Samenpflanzen und dem Laubmoos *Physcomitrium patens* bisher nicht funktionell untersucht. Aus diesem Grund wurde das CRISPR/Cas9 System verwendet, um Leseraster-Mutanten von den vier MpDCLs, MpDCL1a, MpDCL1b, MpDCL3 und MpDCL4 zu erzeugen. Diese *Mpdcl^{pe}* Mutanten zeigten in ihrer Reaktion auf Salz- und Phytohormonbehandlungen phänotypische Abweichungen vom WT und *Mpdcl1a^{ge}* wies auch unter Standardwachstumsbedingungen deutliche Wachstumsanomalien und Entwicklungsstörungen auf. Interessanterweise waren mit Ausnahme von *Mpdcl1b^{ge}* alle *Mpdcl^{pe}* Mutanten steril, da in diesen Linien keine Gametangiophoren induziert werden konnten. Die Mutante *Mpdcl1b^{ge}* bildete Gametangiophoren mit deutlich reduziertem Wachstum, was darauf hindeutet, dass alle DCLs eine Rolle bei der Induktion und Entwicklung der Geschlechtsorgane spielen. Die sRNA- und mRNA-Profile der *Mpdcl^{pe}* lassen Rückschlüsse auf die Funktion der einzelnen MpDCL zu. So ist MpDCL1a für die Biogenese von microRNAs (miRNAs) verantwortlich, während MpDCL4 trans-acting small interfering RNAs (ta-siRNAs) generiert und MpDCL3 an der Regulation pathogen-induzierter Gene und der Synthese heterochromatischer RNAs (hcRNAs) beteiligt zu sein scheint.

Mpdcl1b^{ge} Mutanten sind im Vergleich zum WT in der Lage, höhere Salzkonzentrationen zu tolerieren. Salzbehandelte *Mpdcl1b^{ge}* Mutanten zeigen im Vergleich zum salzbehandelten WT eine deutlich reduzierte miRNA-Expression. Zudem weisen sie unter Standardwachstumsbedingungen im Vergleich zum WT ebenfalls nur geringe Änderungen in ihrem sRNA-Expressionsprofil auf. Dies deutet darauf hin, dass *M. polymorpha* über hochspezifische MpDCL1b-abhängige miRNA-Kontrollmechanismen verfügt, die selektiv als Reaktion auf hohe Salzkonzentrationen aktiviert werden. Diese neu entdeckten potenziellen Mechanismen der selektiven miRNA-Regulation sind höchstwahrscheinlich evolutionär konserviert, da Orthologe von MpDCL1b in anderen Moos- und Farnspezies gefunden wurden.

Der Verlust einer *PpDCL1a* regulierenden Rückkopplungsschleife in *P. patens* führt unter anderem zu einer Salz-Hypersensitivität, einer ABA-Hyposensitivität und einer erhöhten Expression des Band-7 Proteins *FLOTILLIN* (*FLOT*). Mindestens eine Variante dieses Proteins ist in den meisten Samenpflanzen vorhanden. *FLOT* ist in Samenpflanzen mit der Plasmamembran assoziiert und an der Clathrin-unabhängigen Endozytose beteiligt. Im Gegensatz dazu assoziiert die einzige *FLOT*-Variante von *P. patens* mit Thylakoidmembranen innerhalb der Plastiden, was auf eine andere Funktion dieses Proteins hinweist.

Die Überexpression von *PpFLOT* führt zu einer verminderten Toleranz von *P. patens* gegenüber hohen Salzkonzentrationen. Darüber hinaus entwickeln die Protonemafilamente der *PpFLOT*-OEX Linien Brachycyten-ähnliche Zellen, die mit zunehmender *PpFLOT*-Expression deutliche Verfärbungen aufweisen, bei denen es sich höchstwahrscheinlich um Nekrosen handelt. Interessanterweise treten diese Nekrosen nur im Protonema-Stadium dieser Linien auf und nicht in ausgebildeten Gametophoren.

Eine Überexpression von *PpFLOT* führt außerdem zu einer erhöhten Photosyntheserate, einer gesteigerten Chlorophyllproduktion und einer Anreicherung von reaktiven Sauerstoffspezies (ROS). Metabolomische Analysen zeigten zudem eine reduzierte Pigmentsynthese und deutliche Veränderungen im Lipidprofil von *PpFLOT*-OEX-Linien. Insbesondere die Veränderungen im Lipidprofil deuten auf einen Einfluss von *PpFLOT* auf die Biosynthese von Fettsäuren hin. Darüber hinaus zeigen die Thylakoidmembranen der *PpFLOT*-OEX Linien eine deutlich ungeordnete Struktur mit fehlender Ausbildung von Granastrukturen. Diese strukturellen Unterschiede sind sehr wahrscheinlich eine Folge der veränderten Lipidzusammensetzung.

Darüber hinaus wurden mittels Proteomanalysen der *PpFLOT*-OEX Linien eine Reihe differenziell akkumulierter Proteine identifiziert, die zur verminderten Salztoleranz beitragen könnten. Durch seinen mutmaßlichen Einfluss auf die ROS- und Ca^{2+} -Homöostase beeinflusst *PpFLOT* zudem indirekt die Genexpression. Die Expression von *PpFLOT* selbst kann durch ABA und Licht unterdrückt werden, folgt einem zirkadianen Rhythmus und wird vermutlich posttranskriptionell durch miR167 reguliert.

1 Introduction

1.1 Plant terrestrialization – an essential step for the evolution of modern life

Approximately 500 million years ago, the ancestors of modern plants began colonizing dry land, a new habitat (Morris et al., 2018; Rensing, 2018a; Lüttge, 2020; Rensing, 2020). This was a crucial step in the evolution of life, as it led to high biodiversity and provided the groundwork for the development of animal and human life (Rensing, 2018a). For example, photosynthetic activity by cyanobacteria and eukaryotic algae already led to the accumulation of oxygen (Martin and Allen, 2018), which led to the formation of the ozone layer and subsequent reduction in the intensity of ultraviolet (UV)-radiation (Rensing, 2018a). The spread of green non-vascular plants and later vascular plants on previously barren rock further enhanced these developments. Plants also weathered the rock and generated the biological soil crust covering most of the earth's surface (Rensing, 2018a; Lüttge, 2020) and supported a second wave of terrestrialization by vascular plants (Lüttge, 2020).

The first photosynthetic active organisms to adapt to the new environment were cyanobacteria, which spread on wet rocks and in shallow pools with no competitors (Lüttge, 2020). However, it is widely accepted that the common ancestor of all embryophytes belonged to the streptophyte green algae, more precisely to the Zygnematophyceae algae (de Vries and Archibald, 2018; Rensing, 2020) (Figure 1). Freshwater algae from this clade evolved into non-vascular land plants, best represented by the modern bryophytes (Rensing, 2018a). Bryophytes, including mosses, liverworts and hornworts, are a sister lineage to vascular plants (tracheophytes) (Rensing, 2018b; Degola et al., 2022; Pfeifer et al., 2022) (Figure 1). Recent studies suggest that bryophytes may be a monophyletic group rather than a paraphyletic one (Degola et al., 2022).

Bryophytes are ideal models for studying the adaptations necessary to survival on land, such as increased irradiance and the need to defend against UV damage. To defend against increased UV light intensity, land plants started accumulating phenylpropanoids like flavonoids (Rensing, 2018a; Degola et al., 2022). Flavonoids protect against UV damage by absorbing UV light and acting as reactive oxygen species (ROS) scavengers (Ferreyra et al., 2021). Furthermore, land plants need to tolerate external stressors such as extreme cold and drought due to their sessile lifestyle (de Vries and Archibald, 2018; Rensing, 2018a). These stressors require precise control over water management, leading to the development of morphological structures like stomata, roots and the cuticle layer to prevent uncontrolled water evaporation. Other morphological adaptations, including stems, rhizoids and leaves, are further signs of physical adaptations to the new environment (Bowles et al., 2022; Degola et al., 2022). Besides these physical changes, molecular changes also played a crucial role in land adaptation.

Similar to the accumulation of secondary metabolites, plant terrestrialization initiated the development of phytohormone-guided signaling and biosynthesis pathways. Components of auxin and cytokinin-related pathways are detectable in charophytes, while strigolactones (SL) are found in Charophyceae, and ethylene biosynthesis and response have been identified in Zygnematophyceae. Meanwhile, the abscisic acid (ABA) and jasmonate (JA) signaling pathways most likely evolved in the most recent common ancestor of land plants (Rensing, 2018a).

Land plants can also interact and form symbiotic relationships with microorganisms, particularly fungi. Bryophytes from all lineages possess the necessary components to form mycorrhizal symbioses, with the exception of a few species that lost this ability secondarily (Matsui et al., 2020; Degola et al., 2022). These symbiotic interactions are thought to have originated in freshwater environments during the water-to-land transition. They likely provided nutrients for the plants, especially considering the lack of roots and the high CO₂ concentration in the early terrestrial atmosphere (Rensing, 2018a; Delaux and Schornack, 2021; Degola et al., 2022). However, life on land also necessitated the development of defense mechanisms against pathogens. Bryophytes developed a wide range of secondary metabolites to defend against microbial attacks (Delaux and Schornack, 2021; Degola et al., 2022).

1.2 Phytohormone evolution enabled plant terrestrialization

Plant development, morphology, defense and abiotic and biotic stress responses are regulated by intricate pathways relying on phytohormones as signaling molecules (Wang et al., 2015). These phytohormone-driven signaling pathways, vital aspects of plant physiology, expanded greatly during plant terrestrialization. Core components of both auxin and cytokinin signaling have been identified in streptophyte algae, especially in Charophyceae and Zygnematophyceae (Wang et al., 2015; Carrillo-Carrasco et al., 2023) (Figure 1). Auxin guides plant development and growth by transcript regulation (Wang et al., 2015; Carrillo-Carrasco et al., 2023), while most streptophyte algae lack certain transcription factors, auxin transporters and the complete set of biosynthetic proteins found in bryophytes and tracheophytes (Bowman et al., 2017). The presence of endogenous indole-3-acetic acid (IAA) and responsiveness to IAA treatment suggest that auxin signaling exists in these species (Carrillo-Carrasco et al., 2023) (Figure 1). Similarly, core cytokinin signaling components have been found in *Klebsormidium flaccidum* and other streptophyte algae, although *Zygnema cylindricum* lacks major key components for biosynthesis and degradation, present in bryophytes. However, it still possesses histidine phosphotransfer proteins (HPt) and type-B response regulators (RRB) necessary for cytokinin signaling (Wang et al., 2015; Powell and Heyl, 2023). This indicates the development of cytokinin signaling in streptophyte algae. Both auxin and cytokinin primarily

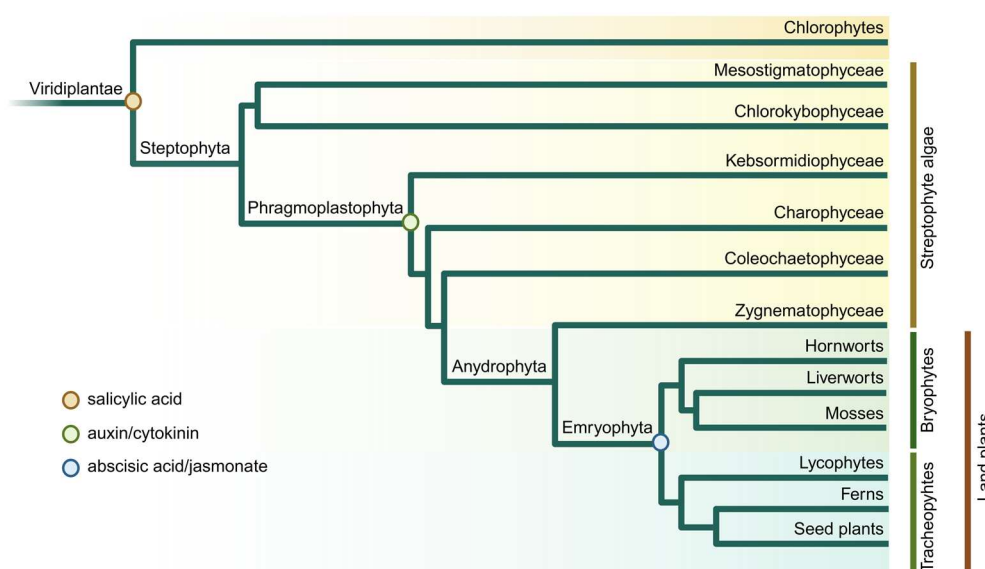


Figure 1: Evolution of land plants

The dendrogram illustrates the evolution of land plants by presenting the nested monophyletic clades of Streptophyta, Phragmoplastophyta, Anydrophyta and Embryophyta (Land plants) of the Viridiplantae lineage, as per Rensing (2020). The monophyletic Streptophyta clade comprises the paraphyletic streptophyte algae, while the land plant contains both monophyletic bryophytes and paraphyletic tracheophytes. Circles indicate the emergence of components of salicylic acid signaling according to Monte (2023), auxin signaling according to Carrillo-Carrasco et al. (2023), cytokinin signaling according to Powel and Heyl (2023) and abscisic acid and jasmonate signaling according to Bowman et al. (2017) and Monte (2023), respectively. Graphic was created with BioRender.com.

influence developmental processes like plant growth, cell division and morphological structure formation. Ancient plants required additional signaling systems to adapt to life on land, particularly to respond to environmental stresses, wounding and pathogen infection. These phytohormone-driven pathways emerged in the last common ancestor of embryophytes. ABA acts primarily in environmental stress signaling, while both JA and salicylic acid (SA) evolved in bryophytes to defend against pathogen infection and herbivores (Wang et al., 2015) (Figure 1). The core elements of the ABA signaling pathway, including ABA response/perception factors, transporters and metabolic genes, are present in both streptophyte algae and bryophytes (Wang et al., 2015; Bowman et al., 2017; Arif et al., 2018). While components for both SA and JA signaling have been identified in streptophyte algae and bryophytes (Wang et al., 2015; Bowman et al., 2017), the additional presence of SA in chlorophytes and charophytes suggests conserved SA biosynthesis and signaling since the last common Viridiplantae ancestor (Monte, 2023). Not all components of JA signaling pathways are present in bryophytes as they are unable to synthesize JA. However, JA-signaling is present in bryophytes as they produce the JA-precursor 12-oxo-phytodienoic acid (OPDA) instead (Bowman et al., 2017; Monte, 2023).

It is important to note that there are many different phytohormones regulating plant growth, development and stress signaling. Some well-known and extensively studied phytohormones are SL, cytokinin, ethylene, brassinosteroids (BR) and gibberellins (GA). While SLs are

primarily found in bryophytes and other land plants, streptophyte algae possess some genes for SL biosynthesis and signaling, though not the complete set. Therefore, SL signaling in streptophyte algae might only be possible through the use of SL-related precursors or related derivatives (Kyoizuka et al., 2022). Similarly, while only land plants possess all the necessary components for cytokinin perception, degradation and signal transduction, most streptophyte algae are cytokinin-responsive despite lacking the full set of cytokinin signaling genes (Powell and Heyl, 2023). Ethylene signaling, however, is considered ancient, with ethylene receptors even found in cyanobacteria. Yet, the components necessary for the ethylene sensing system of land plants emerged for the first time in streptophyte algae (Van de Poel and de Vries, 2023). Both BR and GA signaling detected in vascular plants most likely evolved in bryophytes. This was proposed because some key signaling and biosynthesis components of these phytohormones can be found in this clade, although the majority of the needed components are either absent or incomplete in bryophytes (Wang et al., 2015; Ferreira-Guerra et al., 2020; Hernandez-Garcia et al., 2021). In this thesis, I will mainly focus on the effects of auxin, ABA, SA and JA on the abiotic and biotic stress response, as well as plant growth and development in both *Physcomitrium patens* and *Marchantia polymorpha*. While other phytohormones will be mentioned in the following text, only auxin, ABA, SA and JA signaling will be described in detail in the next section.

1.2.1 Role of auxin during the development of bryophytes

Auxin, one of the evolutionary oldest plant hormones, plays a crucial role in plant growth and development (Wang et al., 2015; Carrillo-Carrasco et al., 2023). IAA is the primary type of auxin derivative found in plants, synthesized from tryptophan through TRYPTOPHAN AMINOTRANSFERASE (TAA) and YUCCA flavin monooxygenase (YUC) (Zhao, 2012; Carrillo-Carrasco et al., 2023). Auxin accumulation directly influences plant growth patterns, with growth occurring in areas with higher auxin concentrations. These gradients guide plant development (Teale et al., 2006; Ishizaki et al., 2012; Thelander et al., 2018; Carrillo-Carrasco et al., 2023). The auxin transport is mainly carried out by PIN-FORMED (PIN) transporters that also control the directional, also called “polar” auxin transport (Carrillo-Carrasco et al., 2023). Beyond distribution, auxin regulates gene expression related to development. Auxin activates auxin-responsive elements (ARE) in promoter regions, freeing auxin-responsive factors (ARF) and initiating growth factor expression. In their natural state, ARFs are bound and inactivated by binding Aux/IAA proteins. Skp1/Cul1/F-box complex (SCF)/ TRANSPORT INHIBITOR RESPONSE 1 (TIR) E3 ubiquitin ligase complexes ubiquitinate Aux/IAA proteins after auxin binds to the auxin receptors in this complex, for example, the F-box protein TIR1 and activates this complex. The Aux/IAA proteins are then degraded, freeing ARF and triggering the auxin-guided gene expression of growth factors (Teale et al., 2006; Leyser, 2018) (Figure 2A).

1.2.2 ABA regulates signaling pathways during salt, drought and cold stress

Plants face numerous challenges living on land, but abrupt fluctuations in temperature, desiccation and high salt concentrations are particularly severe. High salt concentrations disrupt ion balance, impacting plant metabolism and are potentially toxic. High salt concentrations also create osmotic stress by water deficiency, which is also a problem during prolonged periods of drought. Due to these challenges, plants respond to both of these abiotic stressors in a similar way: accumulating osmolytes, maintaining ion-homeostasis and scavenging ROS to combat these stress factors (Golldack et al., 2011; Haider et al., 2021). Both salt and drought stress lead to changes in cell wall composition and membrane integrity, initiating stress-sensing signals (Golldack et al., 2011; Haider et al., 2021; Shin et al., 2021; Gigli-Bisceglia et al., 2022). One example involves the influx of Ca^{2+} (Golldack et al., 2011; Zhang et al., 2022). However, hyperosmotic stress and water deficiency are not the only factors influencing cell wall and plasma membrane integrity. Cold stress, for instance, alters membrane fluidity (Guo et al., 2018) by modifying fatty acids (FA) composition, accumulating sugars, nitrogen compounds and proteins that help maintain membrane integrity during cold acclimation. These changes in membrane composition trigger Ca^{2+} -dependent signaling cascades in response to cold temperatures (Barrero-Sicilia et al., 2017; Guo et al., 2018).

Ca^{2+} signals are not the only signaling molecules activated by abiotic stress. Secondary messengers like ROS, nitric oxide and phospholipids also play a crucial role in stress-specific signal transduction. Posttranslational modifications of proteins, such as phosphorylation and de-phosphorylation, are also involved in this process (Zhang et al., 2022). One of the signaling pathways induced by abiotic stress involves ABA. ABA is induced by abiotic stress in a Ca^{2+} -dependent manner (Golldack et al., 2011; Zhang et al., 2022) and binds to the ABA receptor proteins PYRABACTIN RESISTANCE (PYR), PYRABACTIN RESISTANCE-LIKE (PYL) and REGULATORY COMPONENT OF ABSCISIC ACID RECEPTOR (RCAR). Then ABA activates PYR/PYL/RCARs, which in turn bind and inactivate TYPE 2C PROTEIN PHOSPHATASEs (PP2C), including ABA INSENSITIVE 1 (ABI1) and 2 (ABI2). Since PP2Cs inhibit SUBCLASS III SUCROSE NONFERMENTING 1 – RELATED PROTEIN KINASE 2 (SnRK2) kinases by dephosphorylation, their inactivation by ABA activates SnRK2s (Figure 2B). Activated SnRK2s relay the stress signal through downstream kinase activity and signal transduction (Golldack et al., 2011; Wang et al., 2015; Zhang et al., 2022). For instance, kinase-dependent activation of K^+ channels leads to ABA-mediated stomatal closure (Isner et al., 2018; Zhang et al., 2022). By activating SnRK2s, ABA indirectly regulates H_2O_2 production via RESPIRATORY BURST OXIDASE HOMOLOG (Rboh) D and F activity (Zhang et al., 2022).

Beyond signaling cascades, the ABA-PYR/PYL/RCAR-SnRK2 module also regulates gene transcription. ABA-activated SnRK2 can phosphorylate ABRE binding factors (ABF). These activated ABFs then bind to promoters containing ABA-responsive *cis*-elements (ABRE) and trigger ABA-induced gene expression (Sah et al., 2016; Fidler et al., 2022) (Figure 2B). However, ARBEs/ABF are not the only transcription factors capable of binding these regions. When phosphorylated by SnRK2, the basic region/leucine zipper (bZIP) transcription factor ABI5 can also regulate the transcription of ABA-responsive genes by binding to ABRE in promoters (Sah et al., 2016; Fidler et al., 2022). SnRK2 mediated phosphorylation can further induce or suppress various transcription factors, including APETALA 2 (AP2)/ETHYLENE RESPONSE FACTOR (ERF), MYELOCYTOMATOSIS ONCOGENE (MYC)/ V-MYB MYELOBLASTOSIS VIRAL ONCOGENE HOMOLOG (MYB), NO APICAL MERISTEM/ARABIDOPSIS THALIANA ACTIVATING FACTOR/CUP-SHAPED COTYPEDON (NAC) and basic HELIX-LOOP-HELIX (bHLH) transcription factors. This allows land plants to control multiple processes, including ion-homeostasis, ROS production and epigenetic and posttranscriptional modifications during stress adaptation (Golldack et al., 2011; Sah et al., 2016; Fidler et al., 2022).

1.2.3 Phytohormone regulation during pathogen defense and symbiotic infections

Plants transitioning from water to land faced the challenge of adapting to rocky terrain that lacked essential nutrients. Symbiotic relationships with other microorganisms were key to their success, as evidenced by the "mycorrhizal landing hypothesis" (Rensing, 2018a; Delaux and Schornack, 2021; Degola et al., 2022). However, this hypothesis requires two crucial abilities of plants: forming symbioses and defending against harmful pathogens. Phytohormones play a critical role in both the pathogen defense and mycorrhizal infection. The plant immune system depends on pattern recognition receptors (PRRs) recognizing microbe/pathogen/damage-associated molecular patterns (MAMP/PAMP/DAMP) or detecting factors trying to suppress these recognition mechanisms (Nishad et al., 2020). This recognition triggers an influx of Ca^{2+} and ROS, activating mitogen-activated protein kinase (MAPK) dependent signaling cascades (Figure 2C). These cascades lead to the production of two key phytohormones, SA and JA, essential for pathogen defense and symbiosis.

For instance, SA accumulates to establish systemic acquired resistance (SAR) in response to pathogen infection, primarily against tissue-dependent pathogens (Backer et al., 2019; Nishad et al., 2020; Vlot et al., 2021). SAR signals, the SA-dependent immune signals, spread from the infection site to the surrounding tissue, fortifying the entire plant against the pathogen attack for a prolonged period (Vlot et al., 2021). Interestingly, beneficial arbuscular mycorrhiza fungi (AMF) also induce SA, but in this case, JA is also upregulated to suppress SA-dependent defense reactions due to their antagonistic nature (Nishad et al., 2020; Monte, 2023). SA

regulates gene expression by binding to NONEXPRESSOR OF PATHOGENESIS RELATED PROTEIN 1 (NPR1), causing it to switch to a monomeric form. Monomerized NPR1 interacts with TGA transcription factors, leading to the expression of PATHOGENESIS-RELATED (PR) genes responsible for SAR (Backer et al., 2019; Pokotylo et al., 2019). JA activates its responsive genes by interacting with the SCF/CORINATINE INSENSITIVE 1 (SCF^{COI1}) complex. This complex targets JASMONATE-ZIM DOMAIN (JAZ) proteins for degradation by the proteasome 26S pathways, disbanding the gene suppressor complex of JAZ, TOPLESS

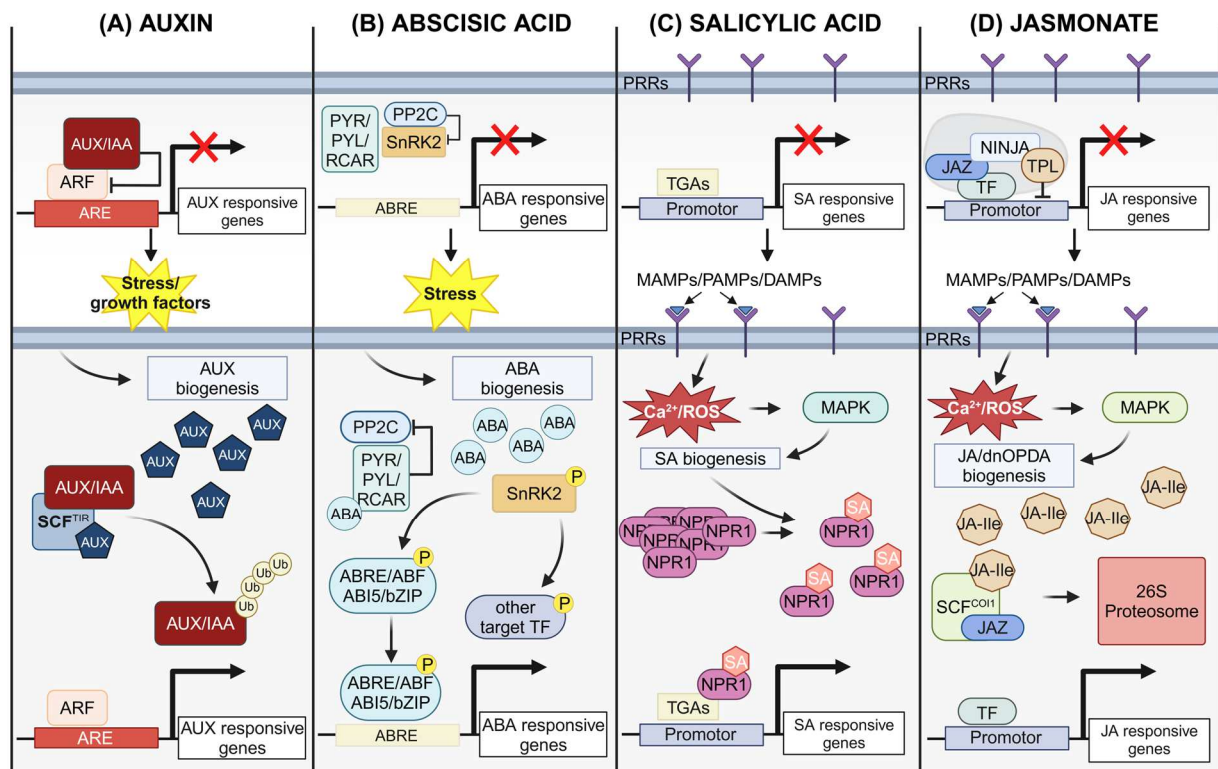


Figure 2: Phytohormone signaling in land plants

(A) Transcription of genes regulated by auxin is suppressed when AUX/IAA proteins inhibit AUXIN-RESPONSIVE FACTORS (ARF). In response to stress or growth factors, auxin biosynthesis increases and activates Skp1/Cul1/F-box complex (SCF)/ TRANSPORT INHIBITOR RESPONSE 1 (TIR) E3 ubiquitin ligase complexes (SCF^{TIR}). These complexes then ubiquitinate AUX/IAA proteins and ARF bound to auxin-responsive elements (ARE) in the promoter are activated, initiating gene expression. **(B)** ABA-responsive genes are activated by stress. ABA binds to PYRABACTIN RESISTANCE/ PYRABACTIN RESISTANCE-LIKE/ REGULATORY COMPONENT OF ABSCISIC ACID RECEPTOR (PYR/PYL/RCAR), activating these receptors and leading to the inactivation of TYPE 2C PROTEIN PHOSPHATASE (PP2C) proteins. By inactivating PP2C proteins, ABA activates SUBCLASS III SUCROSE NONFERMENTING 1 – RELATED PROTEIN KINASE 2 (SnRK2) kinases by phosphorylation. These kinases, in turn, phosphorylate transcription factors that bind to ABA-responsive *cis*-elements (ABRE) in the promoter, regulating the expression of ABA-responsive genes. **(C-D)** Pathogen infection leads to the recognition of microbe/pathogen/damage-associated molecular patterns (MAMP/PAMP/DAMP) by pattern recognition receptors (PRRs), which trigger ROS or Ca²⁺ influx. This activates mitogen-activated protein kinases (MAPK), which increases the expression of either SA or JA-Ile/dnOPDA. Increased SA biosynthesis leads to the monomerization of NONEXPRESSOR OF PATHOGEN-RELATED PROTEIN 1 (NPR1), which interacts with TGA transcription factors, leading to the expression of SA-regulated PATHOGENESIS-RELATED (PR) genes. Increased JA-Ile/dnOPDA biosynthesis leads to the activation of SCF/CORINATINE INSENSITIVE 1 (SCF^{COI1}) and degradation of JAZ by 26S proteasome. By degrading JAZ, the inhibitory complex containing JAZ, NOVEL INTERACTOR OF JAZ (NINJA) and TOPLESS (TPL) is dissolved, and transcription factors regulating JA-responsive genes are activated. Image was created with BioRender.com

(TPL) and NOVEL INTERACTOR OF JAZ (NINJA), removing their suppression of JA-responsive transcription factors, often MYC transcription factors (Li et al., 2022b) (Figure 2D). Bryophytes and some lycophytes lack the genetic tools to synthesize jasmonoyl-isoleucine (JA-Ile), the common JA derivative in plants, to activate JA-dependent signaling pathways (Wang et al., 2021b; Monte, 2023). However, these species produce OPDA ligands that fulfill a similar function and activate the complex containing COI1 to bind and degrade JAZ proteins, thus mirroring the effect of JA derivatives. Furthermore, the antagonistic relationship between SA and the JA-derivative dinor-*cis*-OPDA (dnOPDA) has been confirmed in *M. polymorpha* (Matsui et al., 2020). Therefore, by upregulating either JA or OPDA derivatives, early land plants most likely developed the tools for establishing and maintaining AMF symbiosis.

1.3 Small RNA biosynthesis and small RNA-dependent gene regulation

1.3.1 Evolution of sRNA signaling and DICER-LIKE proteins during plant terrestrialization

Plants have adapted to life on land through various changes, including an increased regulatory function of small non-coding RNAs (sRNA). These sRNAs of a size from approximately 20-24 nucleotides (nt) recognize reverse complementary RNA or DNA sequences, allowing them to mediate posttranscriptional and transcriptional gene silencing by either cleavage or sRNA-guided epigenetic alterations (Fattash et al., 2007; Khraiweh et al., 2010; Arif et al., 2013). To control the diversification of plant body plans, developmental mechanisms and adaptations to new abiotic and biotic stress factors, different classes of sRNAs, such as micro RNAs (miRNA) and small interfering RNA (siRNA), have evolved (Fattash et al., 2007). Proteins that act in sRNA biogenesis, including DICER-LIKE proteins (DCL), emerged through parallel evolution of the small RNA machinery in different Chlorophyta lineages (Margis et al., 2006; Fattash et al., 2007; Cui et al., 2017; Bélanger et al., 2023). The *DCL* gene family comprises multiple members, with the number varying across plant species. Seed plants typically have four to five *DCLs*, while most green algae possess at least one (Margis et al., 2006; Liu et al., 2009; Bélanger et al., 2023).

Seed plants have developed distinct pathways to generate sRNAs of specific sizes with dedicated functions, while the core function of DCLs remains evolutionarily conserved (Liu et al., 2009; You et al., 2017; Yu et al., 2017b; Tiwari et al., 2021). Previous studies proposed that DCL1 emerged in the last common ancestor of Klebsormidiophyceae and Streptophyta algae, while DCL2/3/4 diverged during the evolution of embryophytes (You et al., 2017; Wang et al., 2021a). The most common plant DCL1 protein evolved from an algae-typical DCL after the divergence of Klebsormidiophyceae and other Streptophyta lineages (Wang et al., 2021a). DCL2, another common DCL in seed plants, originated in the last common ancestor of fern and seed plants (You et al., 2017; Bélanger et al., 2023), while DCL3 and DCL4 emerged in

bryophyte lineages (You et al., 2017; Wang et al., 2021a; Bélanger et al., 2023). Additionally, most monocot plant lineages, such as rice and maize, express *DCL5* homologs (Patel et al., 2021; Bélanger et al., 2023).

Plant DCL proteins can be identified by specific protein domains: DEAD-box, Helicase-C, DUF283, PAZ (Piwi/Argonaute/Zwille), Ribonuclease 3 (RNase III) and double-stranded RNA binding (dsRBD) domains. However, not all DCLs possess every domain (Margis et al., 2006; Liu et al., 2009). This diversity suggests specific or interchangeable functions among DCLs, reflecting their complex evolutionary history in land plants (Margis et al., 2006). Studies indicate that a functional DCL protein requires an RNA binding site, a PAZ domain and two RNase III domains (RNase III a and b) located in close proximity to each other, forming the protein's active center. (Margis et al., 2006; Liu et al., 2009; Liu et al., 2012).

1.3.2 Role of DCL proteins during small RNA biosynthesis

The diversification of *DCL* genes, from one to four or five in some species, enabled the production of various sRNAs with different sizes and functions. These sRNAs include, among others, miRNAs, trans-acting small interfering RNAs (ta-siRNAs), heterochromatic small interfering RNAs (hc-RNAs) or repeat-associated small interfering RNAs (ra-siRNAs), phased small interfering RNAs (phasiRNAs) and natural antisense transcript-derived small interfering RNAs (nat-siRNAs) (Arif et al., 2013; Habermann et al., 2020; Tiwari et al., 2021).

DCL1, present in all land plants, plays a vital role in miRNA biogenesis and is highly conserved across species (Arif et al., 2013; Yu et al., 2017b; Manavella et al., 2019; Arif et al., 2022). MiRNAs, 20-22 nt sRNAs, are generated from *MIR* genes and can induce cleavage or translational inhibition as well as epigenetic modifications of complementary sequences (Khraiweh et al., 2010; Arif et al., 2013). The miRNA biogenesis in plants begins with the transcription of *MIR* genes by RNA polymerase II, which then folds into a hairpin-like structure and forms the primary miRNA (pri-miRNA). This pri-miRNA is recognized by a multiprotein microprocessor complex consisting of DCL1, RNA double-strand binding protein HYPONASTIC LEAVES 1 (HYL1) and the zinc finger protein SERRATE 1 (SER1). The complex processes the pri-miRNA into a precursor miRNA (pre-miRNA), after which DCL1 and HYL1 produce a specific miRNA/miRNA* (miRNA strand/passenger strand) duplex from the foldback region. The duplex is then 2'-O-methylated at the 3' ends by HUA ENHANCER 1 METHYLASE (HEN1) to protect it from degradation after transport into the cytoplasm (Baranauske et al., 2015; Pietrykowska et al., 2022). The ARGONAUTE 1 (AGO1) protein, which is part of the RNA-induced silencing complex (RISC), recruits the miRNA guide strand and is then exported into the cytoplasm with the help of CHROMOSOMAL MAINTENANCE 1 (CRM1) (Arif et al., 2013; Yu et al., 2017b; Bologna et al., 2018; Zhang et al., 2020; Tiwari et al., 2021). Once incorporated, the miRNA guides the RISC to complementary targets and

triggers posttranscriptional gene silencing (PTGS) through RNA cleavage and translational inhibition or transcriptional gene silencing (TGS) through DNA and/or histone modifications (Figure 3A).

MiRNAs themselves have a significant role in creating secondary siRNAs. In the beginning, phasiRNAs are generated when *PHAS* loci are transcribed into single-stranded (ss) long non-coding RNAs (lncRNA) by RNA polymerase II. These lncRNAs are then transported into the cytoplasm, where RNA-DEPENDENT RNA POLYMERASE 6 (RDR6) converts them into double-stranded (ds) RNAs. A RISC complex associated with SUPPRESSOR OF GENE SILENCING 3 (SGS3) and carrying the complementary miRNA sequence cleaves these dsRNAs (Liu et al., 2020; Zhan and Meyers, 2023). The resulting dsRNA pieces are processed by either DCL4 or DCL5 and diced into 21 nt or 24 nt large phasiRNAs. The phasing pattern of these phasiRNAs most likely depends on the DCL used for biogenesis (Liu et al., 2020; Zhan and Meyers, 2023). HEN1 then recruits the generated phasiRNAs into an AGO-containing RISC complex and performs PTGS (Zhan and Meyers, 2023). One type of these phasiRNAs are called ta-siRNAs. Ta-siRNAs originate from different *TAS* loci, whose presence varies from species to species. One of the evolutionary oldest *TAS* loci is *TAS3*, which is flanked by two binding sites for miR390 (Arif et al., 2013; Liu et al., 2020). This locus is transcribed into the *TAS3* dsRNA precursor, and the miRNA flanked section is processed by DCL4, assisted by DOUBLE-STRANDED RNA BINDING FACTOR 4 (DRB4), into 21 nt large ta-siRNAs (Arif et al., 2013; Liu et al., 2020). These ta-siRNAs are then loaded into AGO7-containing RISC complexes (Figure 3B).

In addition to dsRNAs generated from *PHAS/TAS* loci, siRNA can also be derived from inverted repeats, transposable regions of the genome, RDR transcription products and paired natural *cis*-antisense transcripts. Ra-siRNAs, for example, originate from dsRNAs generated from heterochromatic loci, which were first transcribed by RNA polymerase IV and then processed into dsRNA by RDR2 (Guleria et al., 2011; Arif et al., 2013). These dsRNAs are then processed by DCL into 22 - 24 nt long ra-siRNAs. Like phasiRNAs, the precise size and function of ra-siRNAs depends on the sequence origin and the processing dicer. However, ra-siRNA is typically processed by DCL3 and participates in transcriptional silencing. They are often also described as hc-siRNA (Guleria et al., 2011; Arif et al., 2013; Zhan and Meyers, 2023). The ra-siRNAs are loaded by AGO4/AGO6 into the RNA-induced transcriptional silencing (RITS) complex and transported back into the nucleus, where they guide DNA methylation (Arif et al., 2013; Zhan and Meyers, 2023) (Figure 3C).

Nat-siRNAs, on the other hand, are generated when two protein coding regions, arranged as convergent unit and with an anticorrelating sequence, are transcribed at the same time. The resulting RNA transcripts form dsRNA strands, which are recognized by DCLs and form one

nat-siRNA duplex. The remaining RNA strands, lacking a polyA tail, are recognized by RDR6 and further processed into dsRNA (Vaucheret and Voinnet, 2024). These dsRNAs are themselves further processed by DCLs. This type of siRNA is mostly generated in response to stress, as under normal circumstances, only one gene of the convergent unit is constitutively expressed while its partner is silenced. Only in response to external stressors is the expression of both genes activated and nat-siRNAs are generated (Vaucheret and Voinnet, 2024) to participate in PTGS (Figure 3D).

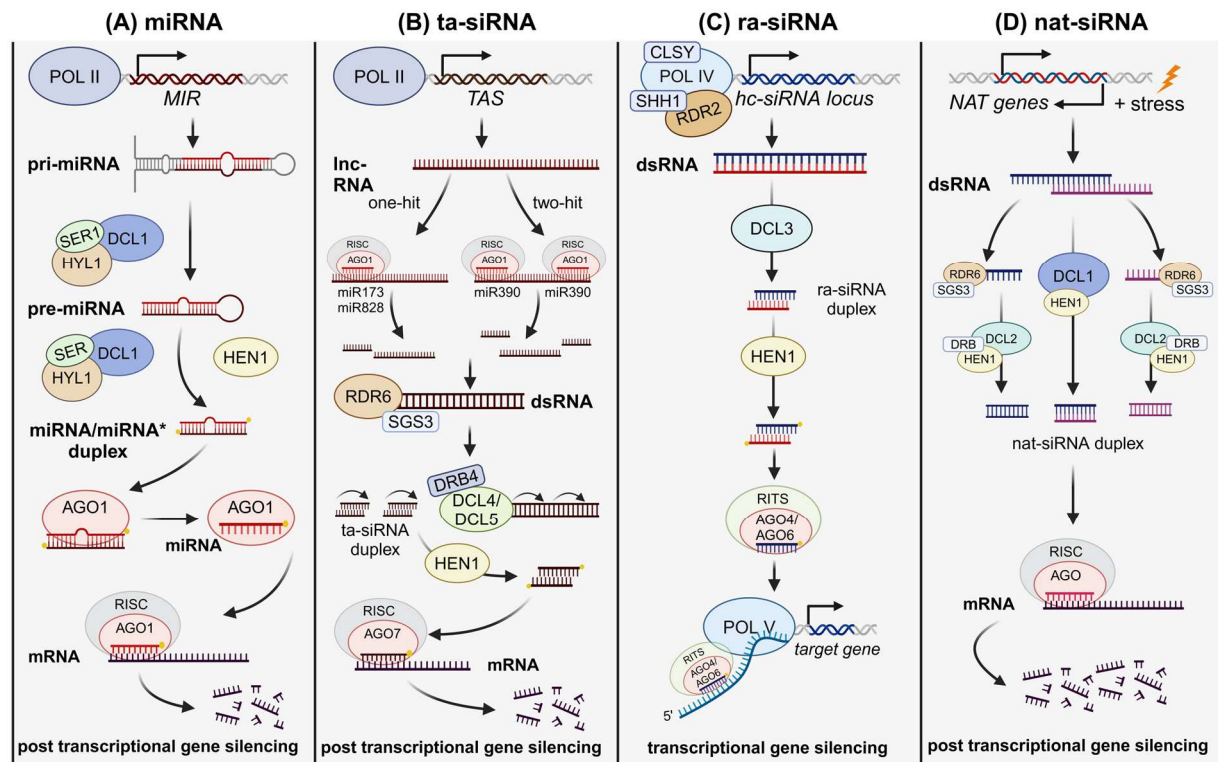


Figure 3: sRNA biogenesis in land plants

(A) miRNA biogenesis: *MIR* genes are transcribed by polymerase II and folded into pri-miRNAs. A complex of DICER-LIKE 1a (DCL1a), HYPONASTIC LEAVES 1 (HYL1) and SERRATE 1 (SER1) process the pri-miRNA first into pre-miRNAs and then into a miRNA/miRNA* duplex that is 2'-O-methylated by HUA ENHANCER 1 METHYLASE (HEN1) to protect the duplex from degradation. miRNA leading strand is recruited by ARGONAUTE 1 (AGO1) and implemented into the RNA-induced silencing complex (RISC) to perform posttranscriptional gene silencing (PTGS). **(B) ta-siRNA biogenesis:** *TAS* genes are transcribed by polymerase II into long non-coding RNAs (lncRNA). Depending on the number of intrinsic miRNA binding sites of the respective lncRNA, the lncRNAs are processed and cleaved by one (one hit (*A. thaliana*: miR173, miR828)) or two (two hits (*A. thaliana*: miRNA 390)) RISC. Cleaved sections are then processed by RNA-DEPENDENT RNA POLYMERASE 6 (RDR6) into dsRNA with the assistance of SUPPRESSOR OF GENE SILENCING 3 (SGS3). Depending on the species, this dsRNA is cleaved into multiple phased 21 nt ta-siRNA duplexes by DCL4 or DCL5. Ta-siRNA duplex is further processed by HEN1 and loaded into RISC to participate in PTGS. **(C) ra-siRNA biogenesis:** repetitive, transposable, or heterochromatic regions are transcribed by polymerase V and RDR2 with the assistance from CLASSY (CLSY) and SAWADEE HOMEODOMAIN HOMOLOG1 (SHH1) into dsRNA. This dsRNA is processed by DCL3 and HEN1 before the ra-siRNA leading strand is recruited by either AGO4 or AGO6 into RNA-induced transcriptional silencing (RITS) to participate in transcriptional gene silencing (TGS). **(D) nat-siRNA biogenesis:** In response to stress, the transcription of natural antisense (*NAT*) genes are both activated, resulting in dsRNA made of the complementary RNA strands. This dsRNA is processed by DCL1 into sRNA duplexes while the cleaved overhangs are transformed by RDR6 and SGS3 into dsRNAs that are processed by DCL2, DOUBLE-STRANDED RNA BINDING FACTOR (DRB) and HEN1 into nat-siRNA duplexes. These nat-siRNAs are recruited into RISC and lead to PTGS of *NAT* genes. Image was created with BioRender.com

The process of sRNA biogenesis is well-documented in *Arabidopsis thaliana* and other seed plants, but there are significant gaps in our knowledge regarding the sRNA biogenesis in bryophytes and lycophytes. While all four DCLs in *P. patens* have been studied in recent years (Cho et al., 2008; Khraiweh et al., 2010; Arif et al., 2012; Arif et al., 2022), the role and specific functions of DCLs in liverworts and hornworts remain largely unknown. By characterizing DCL-dependent sRNA biogenesis in *M. polymorpha* and comparing it to other bryophyte species, a better understanding of the evolution and functional diversification of DCLs in land plants can be gained. Not only will this study contribute to our understanding of DCL evolution, but it will also potentially reveal novel sRNA classes specific to *M. polymorpha*.

1.3.3 Influence of phytohormone signaling on miRNAs expression and vice versa

It has been previously shown that ABA-dependent signaling can alter the expression of miRNAs, which in turn changes the gene expression (Sunkar and Zhu, 2004; Golldack et al., 2011; Sah et al., 2016). For instance, in rice, 34 miRNAs were found to be significantly altered in response to ABA treatment (Shen et al., 2010; Sah et al., 2016), while in *A. thaliana* miR393, miR397b, miR402 and miR319c were upregulated after ABA treatment (Sunkar and Zhu, 2004). Abiotic stressors such as drought, cold and high light that induce ABA-guided stress responses have also been found to affect miRNA expression (Sunkar and Zhu, 2004; Tiwari et al., 2020; Tiwari et al., 2021). Interestingly, changes in the miRNA expression profile lead to changes in ABA sensing of the bryophyte moss *P. patens* (Arif et al., 2022), indicating a complex relationship between miRNA-guided regulation of ABA sensitivity and ABA-regulated miRNA expression.

ABA is not the only phytohormone that affects miRNA expression. Besides regulating the abiotic stress response (Barciszewska-Pacak et al., 2015; Tiwari et al., 2020; Tiwari et al., 2021), miRNAs also contribute to the regulation of plant development and organ formation (Willmann and Poethig, 2007). One of the phytohormones regulating plant development in both seed plants and bryophytes is auxin (Viaene et al., 2014; Wang et al., 2015; Kato et al., 2017; Flores-Sandoval et al., 2018a; Thelander et al., 2018). The expression of *ARFs* that participate in the root development of *A. thaliana* and the abiotic stress response are regulated by miR160, miR164, miR167, miR390 and miR393 (Meng et al., 2010). Furthermore, in *M. polymorpha*, the overexpression of miR160 leads to developmental aberrations due to altered auxin sensitivity, constitutive tropisms and faulty cell division during gemmae development due to the suppression of *MpARF3* activity (Flores-Sandoval et al., 2018a). MiR160 also regulates additional *ARF* in *Oryza sativa*, *A. thaliana* and *P. patens* (Arazi, 2012; Huang et al., 2016; Jodder, 2020). However, miRNAs are not the only small RNA class regulating auxin. For instance, a ta-siRNA-ARF module has been reported in *P. patens* that is capable of modulating the sensitivity and the robustness of auxin and nitrogen sensitivity (Plavskin et al., 2016).

The phytohormone cytokinin can also influence miRNA expression. For example, the expression of *PpMIR534a* in protonemal cells can be downregulated by exogenous cytokinin treatment (Saleh et al., 2011). MiR534a controls the expression of *BLADE-ON-PETIOLE (BOP) 1* and *2*, which initiate bud formation and the transition from protonema filament to the adult gametophyte. Therefore, cytokinin treatment of *P. patens* protonema leads to increased expression *PpBOP1* and *PpBOP2* and promotes budding (Saleh et al., 2011).

1.3.4 DCL1 feedback regulation in *A. thaliana* and *P. patens*

DCL1 is responsible for synthesizing miRNAs, which participate in PTGR and the biosynthesis of phasiRNAs. Due to their crucial role, it is essential to control their expression tightly. Previous studies on *A. thaliana* have proposed that *AtDCL1* undergoes a complex two-fold expression control. Firstly, miR162 targets the *AtDCL1* transcript, leading to a single feedback loop because miR162 expression depends on AtDCL1 abundance (Xie et al., 2003; Arif et al., 2022). Secondly, *AtDCL1* encodes the *MIR* sequence for miR838 in intron 14 of its sequence. Thus, high abundance of AtDCL1 leads to preferred processing of the intrinsic miRNA and less splicing of the *AtDCL1* transcript, generating increased amounts of truncated transcripts (Rajagopalan et al., 2006). Currently no functional analysis of these feedback loops has been conducted in *A. thaliana*.

However, these two feedback loops have also been found in other plant species, such as *P. patens*, where the *AtDCL1* homolog *PpDCL1a* encodes the *MIR* for miR1047 in intron seven of its genomic sequence and possesses a binding site for miR1217 (Axtell et al., 2007; Arif et al., 2022) (Figure 4). Disrupting the miR1047-driven autoregulatory feedback loop by deleting MIR1047 in a Δ MIR1047 line severely impacts the salt tolerance of *P. patens* and its ABA sensitivity. Furthermore, the resulting change in *PpDCL1a* expression leads to an altered miRNA profile and subsequent gene expression, leading to the observed phenotype (Arif et al., 2022). For instance, *PpFLOT*, a gene associated with vesicle formation and proposed to influence the ion balance under salt stress (Li et al., 2012; Baral et al., 2015), is upregulated in the Δ MIR1047 line (Arif et al., 2022). Interestingly, while such a feedback loop is also proposed for other seed plant species (Shao et al., 2015; Arif et al., 2022), the genomic sequence of *MpDCL1a* does not encode any intrinsic miRNAs, indicating a different method of DCL expression control in *M. polymorpha* compared to *P. patens*.

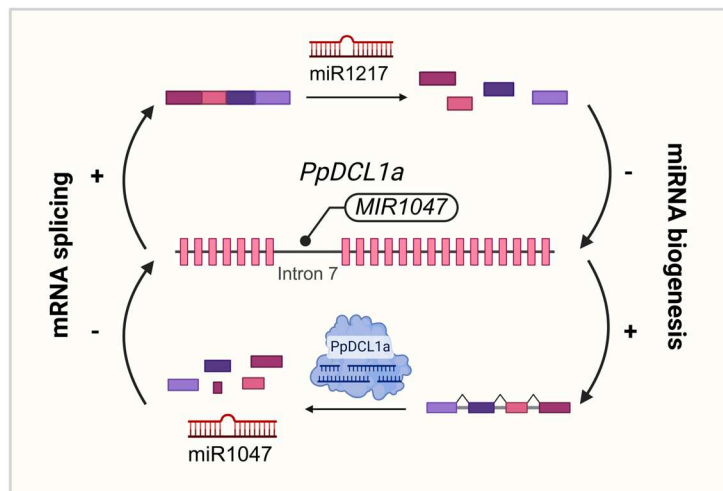


Figure 4: *PpDCL1a* autoregulatory feedback loop in *P. patens*

In *P. patens*, the *PpDCL1a* transcript is regulated by an autoregulatory feedback loop. At low abundance of *PpDCL1a*, mRNA splicing is preferred, leading to higher levels of *PpDCL1a* transcript that can be cleaved by miR1217. Cleavage by miR1217 leads to lower levels of *PpDCL1a* transcript, closing the first feedback loop. When miRNA biogenesis is favored over mRNA splicing of the *PpDCL1a* transcript at high *PpDCL1a* abundance, the intrinsic miR1047 is processed by *PpDCL1a*. This leads to higher levels of miR1047, truncated *PpDCL1a* mRNA and less *PpDCL1a* protein. Image was created with BioRender.com

1.4 The Band-7 protein family protein FLOTILLIN

The Stomatin/Prohibitin/Flotillin/HflK/C (SPFH) protein family, also known as Band-7 proteins, is widespread across evolutionary lineages (Rivera-Milla et al., 2006; Daněk et al., 2016; Martinière and Zelazny, 2021). The SPFH-protein family includes FLOTILLINS (FLOT), STOMATINS (STOM), PROHIBITINS (PHB), ERLINS (ER), the bacterial membrane-specific HflK and HflC proteins and the plant-specific HYPERSENSITIVE-INDUCED REACTION proteins (HIR). Despite differences in function, these proteins share the SPFH/Band-7 domain, ensuring cell membrane-associated localization and a common accumulation in micro/nanodomains in cell membranes (Daněk et al., 2016; Martinière and Zelazny, 2021). Enriched in detergent-resistant membrane fractions (DRM), these SPFH-proteins are proposed to actively participate in microdomain formation (Browman et al., 2007; Martinière and Zelazny, 2021). Among these SPFH-proteins, FLOT seems to have evolved independently in multiple lineages since plant and fungi FLOT do not encode a Flotillin domain or a PDZ3-binding motif that are characteristic for metazoan flotillin/reggie proteins (Rivera-Milla et al., 2006). A recent study suggests a horizontal gene transfer from fungi to plants, indicating FLOTs' role in the infection of nitrogen-fixing bacteria, endocytosis and seedling development evolved after this transfer (Ma et al., 2022). In plants, FLOT is sterol-dependently recruited into nanodomains, as demonstrated by altered dynamics in response to sterol-depleting agents like methyl- β -cyclodextrin (m β CD) and disturbances in sterol biosynthesis like in *cyclopropylsterol isomerase 1* (*cip-1*) mutant lines of *A. thaliana* which resulted in modified AtFLOT1 distribution in the root tissue (Li et al., 2012; Cao et al., 2020; Martinière and Zelazny, 2021). Studies on FLOT1 in *A. thaliana* revealed its crucial role in clathrin-independent endocytosis (Li et al., 2012; Hao et al., 2014; Daněk et al., 2016). AtFLOT2 interaction partners in *A. thaliana*, including aquaporins and carbonic anhydrase 2, an early-responsive

dehydration stress protein, have essential functions in biotic and abiotic stress response (Junková et al., 2018). Additionally, both FLOT2 and FLOT4 of *Medicago truncatula* are critical in the early stages of symbiotic bacterial infection, with the loss of these genes impairing nodule formation induced by *Sinorhizobium meliloti* infection (Haney and Long, 2010). Furthermore, Kroumanová et al. (2019) demonstrated increased expression of all three *AtFLOT* variants in response to Flagellin 22 (flg22) peptide treatment, while salt treatment suppressed *AtFLOT1* and *AtFLOT2* expression in *A. thaliana*. Notably, flg22 treatment increased trafficking of *AtFLOT1* into late endosomes, suggesting its advantageous degradation during the pathogen response (Yu et al., 2017a).

Suppression of *AtFLOT1* expression in *A. thaliana* leads to reduced seedling growth and root length (Li et al., 2012), while silencing *MtFLOT2*, *MtFLOT3* and *MtFLOT4* in *M. truncatula* alters root development (Haney and Long, 2010). Compared to *A. thaliana*, which encodes three FLOT variants, *AtFLOT1* (AT5G25250), *AtFLOT2* (AT5G25260) and *AtFLOT3* (AT5G64870), *P. patens* encodes only one (*PpFLOT*; Pp3c3_21910). This *PpFLOT* shares significant protein sequence similarity (73 – 75 %) with each of the three *AtFLOT* variants (Phytozome v.13; <https://phytozome-next.jgi.doe.gov>). Since *P. patens* is a model organism for land plant adaptation, the unique expression of a single FLOT, compared to the multiple variants in seed plants, suggests an evolutionarily conserved role potentially linked to plant terrestrialization. It is interesting to note that *PpFLOT* is among the genes that exhibit differential expression in the Δ *MIR1047* line (Arif et al., 2022). This suggests that *PpFLOT* may be regulated by miRNAs and may play a potential role in the response to ABA and salt, as the sensitivity to both conditions is significantly altered in this line (Arif et al., 2022).

1.5 Bryophytes – the ideal clade to study plant terrestrialization

Bryophytes are a clade of plants that are closely related to both streptophyte algae and tracheophytes, making them an ideal group for comparative studies. Analysis of molecular and physical changes in bryophytes can detect changes that occurred during the water-to-land transition (de Vries and Archibald, 2018; Nishiyama et al., 2018; Rensing, 2020; Rensing et al., 2020; Degola et al., 2022). Recent studies on plant evolution have revealed genetic changes in the bryophytes explaining prominent structures and mechanisms in seed plants (Bowman et al., 2017; Lang et al., 2018; Rensing et al., 2020; Bowles et al., 2022). For example, although plant stomata are common in most land plants, they were lost in liverworts despite possessing the necessary genes for stomata development in the last common ancestor of bryophytes and tracheophytes (Harris et al., 2020). Complete genome sequencing of two bryophyte species, *P. patens* and *M. polymorpha*, revealed key genes common in most land plants (Bowman et al., 2017; Lang et al., 2018; Fernandez-Pozo et al., 2022). *P. patens*, in particular, harbors a large number of genes with undiscovered functions (Cove, 2005; Lang

et al., 2018; Rensing et al., 2020), holding potential insight into water-to-land transitions and plant stress adaptation mechanisms. Therefore, these two model organisms will be used in this study to enhance our understanding of molecular mechanisms concerning DCL function and responses to abiotic and biotic stress.

1.5.1 The moss *Physcomitrium patens*

The moss *P. patens*, also known as spreading earth moss, inhabits regions in North America, Europe and East Asia (Rensing et al., 2020). Like all land plants, mosses alternate between diploid and haploid generations. During its sporophyte generation, *P. patens* is diploid and produces haploid spores via meiosis. Unlike seed plants, the dominant multicellular phase for mosses is the haploid generation, specifically the gametophyte generation. The haploid spores germinate into the protonemal stage of the gametophyte, consisting of filamentous cell structures. These structures differentiate into vegetative chloronema cells, densely packed with chloroplasts and elongated caulonema cells with fewer chloroplasts (Cove, 2005; Rensing et al., 2020) (Figure 5). *P. patens* can be easily maintained in liquid cell culture during this stage by regularly disrupting the growing cell filaments. Caulonema cells bud and develop into leafy shoots of the gametophores. Being dioecious, *P. patens* induces both antheridia and

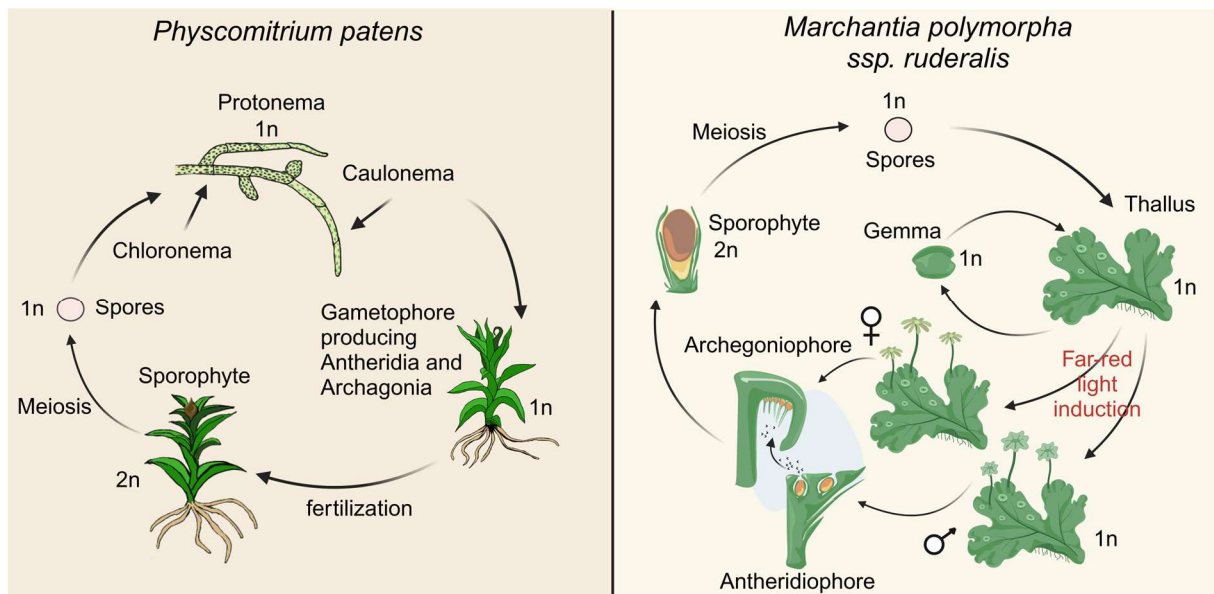


Figure 5: Life cycle of *P. patens* and *M. polymorpha*

In both *P. patens* and *M. polymorpha*, the haploid generation is dominant. *P. patens* first develops into a filamentous cell state called protonema, which can be differentiated into chloroplast-rich chloronema and elongated caulonema cells. Then, it develops into a leafy gametophore with rhizoids, shoots and leaves. *P. patens* is dioecious; thus, self-fertilization is possible. Both antheridia and archegonia develop at the apex of the gametophore. After fertilization, the diploid round sporophyte develops on top of the gametophore. When ripe haploid spores are released from the spore capsule, the life cycle starts anew. Similar to *P. patens*, *M. polymorpha* also develops from spores into mature thallus. On the dorsal side of the mature thallus gemma cups develop, containing the asexual propagules called gemmae. Since *M. polymorpha* is monocious, the antheridia and archegonia develop on different plants. Antheridiophores (♂) and archegoniophores (♀), respectively, can be induced in *M. polymorpha* after vernalization by far-red light. After water-promoted fertilization, the diploid sporophyte develops on the archegoniophores. The sporophyte itself produces haploid spores. Images were created with BioRender.com

archegonia at the apex of the same plant, facilitating self-fertilization (Cove, 2005). Spermatozoids travel to the archegonia via water as a medium and fertilize a zygote, which develops into a diploid sporophyte. This sporophyte grows into a short seta carrying a round spore capsule that, when ripe, bursts open to release haploid spores, initiating the life cycle anew (Cove, 2005; Rensing et al., 2020) (Figure 5). Besides sexual propagation, *P. patens* can also be easily propagated asexually by its tissues. Its dominant haploid generation makes *P. patens* suitable for easy genomic editing since it can be transformed by particle bombardment and PEG-mediated transformation of single protoplasts (Rensing et al., 2020). Due to its propensity for incorporating foreign DNA by homologous recombination, stably transformed lines can be obtained with high efficiency (Cove, 2005; Maronova and Kalyna, 2016; Lang et al., 2018; Naramoto et al., 2022).

1.5.2 The liverwort *Marchantia polymorpha*

The liverwort *M. polymorpha* ssp. *ruderalis* belongs to the *Marchantiales* and is distributed worldwide in regions with a temperate climate similar to *P. patens* (Shimamura, 2016). *M. polymorpha*, like many land plants, undergoes a change in generations. Its life cycle begins with a unicellular haploid spore and develops into short protonema cells with a rhizoid, which then grows into a prothallus and finally into a mature thallus (Shimamura, 2016; Naramoto et al., 2022) (Figure 5). Unlike *P. patens*, *M. polymorpha* is monoecious, with both male and female plants coexisting (Shimamura, 2016; Kohchi et al., 2021). Regardless of the sex, all plants develop asexual propagules in gemma cups that are formed on the dorsal side of the mature thallus. Meanwhile, sexual organs, the gametophores, can be induced by far-red light after vernalization. Male plants develop antheridophores and female plants develop archegoniophores. Water is necessary for transporting the spermatozoids during fertilization. The fertilized egg develops into the diploid sporophyte, which, upon maturity, releases haploid spores (Shimamura, 2016; Kohchi et al., 2021) (Figure 5). This indicates that, like *P. patens*, the dominant generation of *M. polymorpha* is haploid. Plants can be easily propagated by gemmae and transformations can be performed using *Agrobacterium tumefaciens*-guided sporeling or thallus transformation methods (Ishizaki et al., 2008; Kubota et al., 2013). However, the efficiency of genomic editing by homologous recombination is low (Ishizaki et al., 2013). Instead, genomic editing and the generation of stable mutant lines can be achieved using established CRISPR/Cas 9 protocols (Sugano et al., 2018). Therefore, the ease of propagation via thallus tissue or gemmae and the established molecular toolkit make *M. polymorpha* an intriguing new model organism for studying molecular similarities and differences among different bryophyte species.

1.6 Research Questions

The primary objective of this study is to elucidate the molecular adaptations that occurred in the last common ancestor of bryophytes, enabling their transition to terrestrial environments. Specifically, the study investigates the impact of DCL proteins in *M. polymorpha* and the single FLOT variant in *P. patens*, hypothesized to modulate salt tolerance and phytohormone responses in these bryophytes. Consequently, the study addresses the following two research questions:

1.6.1 Question 1 – How does the loss of DCL genes influence the phytohormone response, salt tolerance, gene expression and the sRNA profile of *M. polymorpha*? Does the function of MpDCLs differ from those in *P. patens*?

To investigate the role of DCL proteins in sRNA biogenesis and their evolutionary significance in *M. polymorpha*, I generated mutant lines for all four MpDCLs. To determine the phenotype of the generated mutant lines, I observed plant growth over a three week period and detected significant deviations from the WT phenotype by analyzing the complete thallus area. Given the known influence of DCL proteins and their derived sRNAs on salt tolerance and phytohormone sensitivity (section 1.3), I performed measurements under control conditions and in response to phytohormone treatments. Additionally, the salt tolerance of the generated mutant lines was evaluated by cultivating gemmae on solid medium for two weeks, followed by determination of the survival rate for each line. Subsequently, I analyzed changes in mRNA and sRNA profiles of the *Mpdc^{Pp}* mutant lines through next-generation sequencing to identify the underlying factors responsible for the observed phenotype. This comprehensive analysis enabled predictions about the functional role of DCL in *M. polymorpha* and provided insights into the evolution of plant DCL.

1.6.2 Question 2 – Does the Band-7 protein FLOT modulate stress tolerance in *P. patens*? How is the expression of *PpFLOT* regulated? Are there differences in the function of bryophyte and seed plant FLOT?

The increased expression of PpFLOT in the salt-sensitive and ABA hyposensitive $\Delta MIR1047$ line suggests that not only is PpFLOT expression regulated by miRNAs but also that PpFLOT is involved in the abiotic stress response of *P. patens* (Arif et al., 2022). To investigate the role of PpFLOT in the salt and phytohormone sensitivity of *P. patens*, I generated knockout and overexpression lines. The phenotype of $\Delta PpFLOT$ and *PpFLOT*-OEX lines was assessed under control conditions, high salt concentrations and phytohormone treatments. Besides the phenotypic changes, I examined molecular alterations through Pulse-Amplitude-Measurements (PAM), H₂O₂ detection and electrolyte leakage experiments. Localization studies were conducted to compare the function of PpFLOT with seed plant FLOTs. Additionally, proteomic and metabolomic analyses were performed to identify potential

differentially accumulated proteins that might elucidate the function of PpFLOT and explain the observed phenotype. Furthermore, I explored the regulation of *PpFLOT* through quantitative real-time PCR (qRT-PCR) in response to salt, phytohormones and altered light conditions.

2 Material and Methods

2.1 Experiments Question 1 - How does the loss of DCL genes influence the phytohormone response, salt tolerance, gene expression and the sRNA profile of *M. polymorpha*? Does the function of MpDCLs differ from those in *P. patens*?

2.1.1 Phylogenetic analysis of DCL protein sequences

To obtain homologous protein sequences of MpDCL1a (Mp7g12090), MpDCL1b (Mp6g09830), MpDCL3 (Mp1g02840) and MpDCL4 (Mp7g11720), their sequences were used as queries to search in the databases Phytozome v13 (phytozome-next.jgi.doe.gov), MarpolBase (marchantia.info), as well as UniProt (re 2022_04; uniprot.org) with BLASTp for reciprocal matches in the species *Anthoceros angustus*, *Anthoceros agrestis*, *Anthoceros punctatus*, *A. thaliana*, *Azolla filiculoides*, *Ceratodon purpureus*, *Ceratopteris richardii*, *Chara braunii*, *Chlamydomonas reinhardtii*, *Diphasiastrum complanatum*, *Klebsormidium nitens*, *M. polymorpha*, *M. truncatula*, *Mesotaenium endlicherianum*, *O. sativa japonica*, *P. patens*, *Salvinia cucullata*, *Selaginella moellendorffii*, *Spirogloea muscicola*, *Sphagnum fallax*, *Sphagnum magellanicum* and *Zea mays*. All protein sequences (for accession numbers, see Table 1, Supplementary Table 1) were aligned using CLC Genomics Workbench v20.0.4 (Qiagen) and the phylogenetic tree was constructed with the neighbor-joining method using Maximum likelihood parameters and 1000 bootstrap replicates in MEGA X (Kumar et al., 2018). Domain analysis was performed by the Pfam search function (Pfam-A v33.1) in CLC Genomics Workbench v20.0.4 (Qiagen).

2.1.2 Cultivation of *M. polymorpha*

M. polymorpha ssp. *ruderalis* ecotype BoGa obtained from the botanical garden of the University of Osnabrück (Germany) was used throughout this study. All plants were grown under sterile conditions on standard solid half-strength Gamborg B5 medium including vitamins (Duchefa) (pH 5.5, 1.4 % Agar-Agar, Kobe I) under long-day conditions (16 h light/8 h dark; LD 16:8) at 23°C and a light intensity of 85–100 $\mu\text{mol}/\text{m}^2\text{s}$ according to Althoff *et al.* (2014). Gametangiophore induction was performed according to Althoff *et al.* (2014) at 23°C. Male and female WT and *Mpdcl^{oe}* lines were simultaneously induced at the described conditions and observed for at least three months for signs of gametangiophore induction. Pictures were taken 11 weeks after start of far-red light treatment.

2.1.3 Generation of *M. polymorpha* DCL mutant lines

M. polymorpha mutant lines were generated following the double CRISPR/Cas 9 approach described by Sugano *et al.* (2018). Double-strand breaks were induced, resulting in sequence deletions or nucleotide insertions leading to frameshift mutations of the targeted gene loci

MpDCL1a, MpDCL1b and MpDCL3 and MpDCL4 (Table 2, Supplementary Table 2). All synthetic guide RNAs (gRNAs) were designed with CRISPOR (<http://crispor.org>) (Concordet and Haeussler, 2018) and are targeting the first two exons of the MpDCL locus or regions that code for functional domains. Cloning was carried out as described in Sugano *et al.* (2018) using the vectors pMpGE_EN03, pMpGE010 and pMpGE011, each encoding different gRNAs (for gRNAs, see Supplementary Table 2 and 3) and used in combination with each other (Sugano *et al.*, 2018). *A. tumefaciens* strain C58C1 pGV2260 mediated transformation was performed as previously described (Ishizaki *et al.*, 2008) with minor modifications. 7 d old WT sporelings were co-cultivated for 3 d with two *A. tumefaciens* lines, one carrying the first gRNA in pMpGE010 and the other carrying the second gRNA in pMpGE011, performing all transformations with two gRNAs for the same MpDCL in parallel. The transformed plants were plated on cellophane-covered standard medium supplemented with 0.5 μ M chlorosulfuron (Sigma), 10 mg/L hygromycin (Hygromycin B-solution; Roth) and 100 mg/L cefotaxime (Cefotaxime sodium; Duchefa) for two weeks before transferring the transformants to standard medium supplemented with 1 % glucose (Roth) and cultivating them for two weeks. Afterward, a second round of selection was performed for three weeks before further analysis. All transformed T₁ plants were screened by PCR (for oligonucleotides, see Table 3, Supplementary Table 3), and isogenic lines were obtained by propagating single gemmae to avoid potential chimeric lines. Regions that were targeted by the respective gRNAs were further sequenced to identify mutations and/or frameshifts caused by the CRISPR/Cas9 approach. With the exception of MpDCL1a (only female), one female and one male mutant line was chosen per MpDCL gene and the lines Mpdc1a-6^{ge}, Mpdc1b-6^{ge}, Mpdc1b-7^{ge}, Mpdc13-6^{ge}, Mpdc13-3^{ge}, Mpdc14-1^{ge} and Mpdc14-4^{ge} were used for all further analyses (Table 2, Supplementary Table 2).

2.1.4 DNA and RNA extraction

DNA extractions were performed with 0.5–1 cm² thallus pieces and 200 μ l of extraction buffer (100 mM Tris-HCl, 1 M KCl, 10 mM EDTA, pH 9.5). The tissue was disrupted with a Qiagen TissueLyser II and DNA was extracted according to Edwards *et al.* (1991). RNA extraction was performed with TRI-Reagent (Sigma) following the manufacturer's protocol out of 50–100 mg plant material. RNA samples were dissolved in nuclease-free water and stored at -80°C. RNA concentrations and quality were determined via NanoDrop™ 2000/2000c spectrophotometer (Invitrogen) and RNA integrity was confirmed by agarose gel electrophoresis.

2.1.5 qRT-PCR

In preparation for qRT-PCR, cDNA synthesis was performed as previously described (Arif *et al.*, 2022). The qRT-PCRs were performed in three biological replicates using the equivalent of 50 ng total RNA as template for EVAGREEN®DYE (Biotium) containing reaction mixes on

a CFX96 Real-Time system (Bio-Rad). Gene expression analysis was performed as described by Livak and Schmittgen (Livak and Schmittgen, 2001; Schmittgen and Livak, 2008) using ELONGATION FACTOR 1 α (*MpEF1 α* , *Mp3g23400*) as control. All oligonucleotides used are listed in Table 3 and Supplementary Table 3. Statistical analysis to determine change in expression was performed with R. Significance in the change in expression was determined by the Student's *t*-test.

2.1.6 Phenotypic analysis of *Mpdcl^{ge}* mutant lines

For phenotypic analyses, single gemmae were placed on standard solid medium (control conditions) or medium supplemented with 10 μ M 1-naphthylacetic acid (NAA) (1 mg/ml, Sigma-Aldrich) or 10 μ M 2-*cis*,4-*trans*-Absciscic acid (ABA) (Sigma-Aldrich), respectively. Images of at least five plants per mutant line were taken with a SMZ 1500 stereomicroscope and a DS-U3 camera (Nikon) at 0, 7, 14 and 21 days after gemmae germination (DAG). Images of complete plates were taken with the EOS 800D camera (Canon). Area measurements for all individual plants were performed using ImageJ (Schneider et al., 2012) with the area measurement tool set to limit to threshold. Area was measured after setting the threshold covering the visible thallus area of the respective plant. For statistical analysis, average values of the measured area from, when possible, at least two different mutant lines (male and female, for *Mpdcl1a^{ge}* only female) of the targeted genes *MpDCL1a*, *1b*, *3* and *4* were compared with at least two independent WT (male and female) lines with a sample size (*n*) of 20 before removing extreme outliers. For comparison, the thallus arm length of male and female WT and *Mpdcl3^{ge}* complete plant length at 14 DAG, starting and ending at the first branching point of either side, was measured with ImageJ. Measured thallus area values and thallus length of the respective *Mpdcl^{ge}* mutant lines were tested for normal distribution with the Shapiro-Wilk test, and equality of variances was tested with Levene's test. Statistical analysis of overall growth compared to the WT was performed using Student's *t*-test when samples were normally distributed and Wilcoxon-rank-sum test when the samples were not normally distributed. The statistical analysis was performed with R (ver. 4.2.2) using the 'rstatix' package (<https://CRAN.R-project.org/package=rstatix>).

2.1.7 Scanning electron microscopy of *Mpdcl1a-6^{ge}*

WT and *Mpdcl1a-6^{ge}* gemmae were cultivated under standard conditions for four weeks before the scanning electron microscopy was performed following a previously described protocol (Beheshti et al., 2021). Samples were imaged using a Zeiss Auriga Crossbeam station (Zeiss, Oberkochen, Germany) at an acceleration voltage of 1.5 kV.

2.1.8 Salt stress tolerance assay for *M. polymorpha*

To analyze the salt tolerance, gemmae of one male and one female WT line as well as gemmae from all mutant lines (*Mpdcl1a-6^{ge}*, *Mpdcl1a-8^{ge}*, *Mpdcl1b-6^{ge}*, *Mpdcl1b-7^{ge}*, *Mpdcl3-6^{ge}*, *Mpdcl3-3^{ge}*, *Mpdcl4-1^{ge}* and *Mpdcl4-4^{ge}*) were plated on standard solid medium supplemented with 250 mM NaCl (average of 118.9 gemmae/plate, SEM \pm 5.6, n = 6) for 14 d. Images of the plates were taken at 0 days and after 14 d. Surviving gemmae were counted with ImageJ (Schneider et al., 2012). A statistical comparison of the survival rate of male and female mutant lines and the WT lines was performed with Student's *t*-test. When no significant differences between male and female lines could be detected, survival rates of male and female lines were pooled (n = 12). Statistical analysis of the survival rate of mutant lines compared to the WT was performed with Student's *t*-test when normal distribution (Shapiro-Wilk test) and equality of variances (Levene's test) were met. When these conditions were not met, a Wilcoxon-rank-sum test was performed. All statistical analyses were performed with R (ver. 4.2.2) using the 'rstatix' package (<https://CRAN.R-project.org/package=rstatix>).

2.1.9 RNA sequencing of *Mpdcl^{ge}* lines

Female plants of *Mpdcl1a-6^{ge}*, *Mpdcl1b^{ge}*, *Mpdcl3^{ge}*, *Mpdcl4^{ge}* and WT control were cultivated on standard media in triplicates. Additionally, *Mpdcl1b^{ge}* and WT were cultivated on standard media supplemented with 100 mM NaCl. After two weeks, plant material was harvested, and RNA was extracted with Direct-zol™ RNA Microprep kit (Zymo Research) (Top et al., 2021). RNA integrity was checked by agarose gel electrophoresis and concentration and purity were determined spectrophotometrically. The libraries were prepared from 2 µg total RNA using the TruSeq® Stranded mRNA protocol (Illumina) by West German Genome Center (WGGC). Samples were sequenced strand-specifically as 150 bp paired-end reads on a NovaSeq™ 6000 (Illumina) platform with at least 30 million reads per library.

Due to the low abundance of sRNAs in *M. polymorpha*, 30 µg of total RNA was separated by 15 % denaturing polyacrylamide gel electrophoresis (PAGE) for 2 h at 120 V. The sRNA fractions with sizes ranging from 17-29 nt were excised from the gel and eluted using the ZR small-RNA™ PAGE recovery kit (Zymo Research). SRNA libraries were prepared with the Small RNA-Seq Library Prep Kit (Lexogen) and sequenced as 50 bp single-end reads on a NovaSeq™ 6000 (Illumina) with at least 20 million reads per library.

2.1.10 Bioinformatic analysis of RNA sequencing

For mRNA sequence analysis, the sequencing adapters were trimmed from the raw FASTQ files with Trimmomatic v0.4 (Bolger et al., 2014) by using the default parameters. To map the raw FASTQ files against the *M. polymorpha* reference genome v3.1 (Phytozome v13, phytozome-next.jgi.doe.gov), the STAR alignment tool was used at its default settings (Dobin

et al., 2013). The number of mapped reads to the reference genome (Mpolymorpha_320_v3.1.gene_exons.gff3) was then counted with the featureCounts tool v2.0.1 (Liao et al., 2014). The web-based GALAXY (Galaxy community, 2022) application DeSeq2 was used to identify differentially expressed genes (DEG) (Love et al., 2014). Transcripts were identified as differentially expressed (DE) at $\log_2(\text{Fold change (FC)}) \leq -1$ and $\geq +1$ and a false discovery rate (FDR) ≤ 0.05 when normalized against the generated WT transcriptome data under control conditions and WT after salt treatment, respectively. UpSet plots were generated by R using the 'UpSetR' (Conway et al., 2017) package. The GO enrichment analysis was performed by the web-based agriGO v2.0 application (Tian et al., 2017) by using the default parameters (Fisher Test, Yekutieli FDR < 0.05 , minimum number of mapped entries = 5) and visualized with R (v4.2.2) using the 'ggpubr' (<https://CRAN.R-project.org/package=ggpubr>) package. *M. polymorpha* reference genome v3.1 was initially used to enable the association of the mRNA sequencing data with the sRNA sequencing data. Nevertheless, newer gene IDs based on the *M. polymorpha* reference genome v6.1 (MarpolBase, <https://marchantia.info/nomenclature/>) were also provided.

Analysis of the sRNA sequencing was performed by clipping the sequence adapters with Trimmomatic v0.4 (Bolger et al., 2014) using the default settings. The ShortStack analysis package was used for advanced analysis of the sRNA sequences (Axtell, 2013) using the *M. polymorpha* v3.1 (Phytozome v13, phytozome-next.jgi.doe.gov) as reference genome. To identify mature miRNAs, aligned and clustered reads were mapped against a loci file, which was prepared using retrieved small RNA loci information available on Plant small RNA genes server [*Marchantia polymorpha* (Common Liverwort) genome build 3.0 (mpo-b3.0), https://plantsmallrnagenes.science.psu.edu/genomes.php?genomes_id=49]. As for the identification of potential ta-siRNAs, TAS3 locus info was obtained from Lin and Bowman (2018) and included in the loci file. DE sRNAs were identified with the GALAXY (Galaxy community, 2022) DeSeq2 (Love et al., 2014) application. sRNAs were classified as DE when $\log_2(\text{FC}) \leq -1$ and $\geq +1$ and $p \leq 0.05$ when compared to the sRNA expression of the generated respective WT control data set. Potential miRNA and siRNA targets were identified using the psRNAtarget (Dai et al., 2018) tool using the *M. polymorpha* 320_v3.1 genome as reference before assembling the sRNA and mRNA data sets to identify potential anticorrelating mRNA expression. Heatmaps were generated with R (v4.2.2) using the 'pheatmap' package (<https://CRAN.R-project.org/package=pheatmap>). To facilitate better comparison of the generated sRNA data with previous publications, the detected sRNA sequences were additionally annotated with miRNA IDs as proposed by Tsuzuki et al. 2016.

2.2 Experiments Question 2 - Does the Band-7 protein FLOT modulate stress tolerance in *P. patens*? How is the expression of *PpFLOT* regulated? Are there differences in the function of bryophyte and seed plant FLOT?

2.2.1 *PpFLOT::citrine* localization in *P. patens* protoplasts

The *PpFLOT* (*Pp3c3_21910*) transcript was tagged with citrine by cloning its CDS into a vector containing the Actin 5 promoter (ACT5_P), citrine sequence with required linkers for the tag (citrine) (Tian et al., 2004; Top et al., 2021) and a *nopaline synthase* terminator (NOS_T). The complete *PpFLOT* CDS was amplified using the oligonucleotides 5'-AGCTCTCGAGATGGCGTTCCATACCGC-3' and 5'-TCTAGATCTGGCTTGGGGAAGCTTGG-3', which generated a *PpFLOT* sequence flanked by two restriction enzyme sites for *Bgl*II and *Xho*I. This sequence was then ligated into a linearized Act5-citrineL vector using T4 ligase (Invitrogen) following manufacturer's instructions. The generated *PpFLOT::citrine* construct was transformed into *P. patens* protoplasts to generate lines that transiently express *PpFLOT::citrine*. Images of *PpFLOT::citrine* protoplasts were captured three days after transformation with a Stellaris 5 Point Scanning Confocal Microscope (Leica Microsystems) equipped with a turnable white light laser (485 - 685 nm) and five power hybrid HyD S detectors. The imaging was performed using the immersion oil objective HC PL APO CS2 63x/1.40. Chlorophyll autofluorescence (chl) served as a localization marker, excited at 405 nm and recorded at 623 nm–750 nm, while the fluorescent citrine protein (citrine) was excited at 512 nm and recorded at 524 nm–560 nm. Image processing was conducted using the LAS X Office software.

2.2.2 Phylogenetic analysis of FLOT homologs

To analyze the evolutionary relationship of *PpFLOT* to FLOT homologs in other species, query searches with the full-length amino acid sequence (AA) of *PpFLOT* in multiple plant species were performed. Reciprocal searches with the BLASTp function of Phytozome v13 (phytozome-next.jgi.doe.gov), UniProt (re_2024_01; uniprot.org) and MarpolBase (marchantia.info) databases revealed *PpFLOT* homologs in *A. thaliana*, *Asparagus officinalis*, *A. filiculoides*, *C. purpureus*, *C. braunii*, *Coccomyxa subellipsoidea*, *K. nitens*, *M. polymorpha*, *M. truncatula*, *O. sativa*, *S. cucullata*, *Spirodela polyrhiza*, *Synechocystis* sp. PCC 6803, *Z. mays* and *Zostera marina* revealed *PpFLOT* homologs. The full-length AA sequences of the detected *PpFLOT* homologs were aligned using CLC Genomics Workbench v20.0.4 (Qiagen), followed by phylogenetic analysis employing the Maximum Likelihood method with 1000 bootstrap replicates and the Jones-Taylor-Thornton method as the substitution model. The phylogenetic tree was generated using the Nearest-Neighbor-Interchange method in MEGA X (Kumar et al., 2018).

2.2.3 Generation of *PpFLOT* knockout and overexpression lines

To create $\Delta PpFLOT$ lines, exon 2 of the *PpFLOT* was replaced with a *neomycin phosphotransferase II* (*nptII*) selection cassette through homologous recombination. A *PpFLOT* CDS construct with the embedded *nptII* cassette was generated using Gibson assembly (NEB) (oligonucleotides listed in Supplementary Table 1) and then cloned into pJET1.2/blunt (Thermo Fisher Scientific) vector. After amplification, the construct was cut out of the plasmid via a *BglII* restriction site, separated from the pJET1.2 backbone by agarose gel electrophoresis and purified. The construct was transformed into *P. patens* protoplasts and transformed plants were selected by growing them on medium supplemented with 50 $\mu\text{g/ml}$ G418 sulfate. The correct integration of the *nptII* cassette was confirmed by amplifying the full-length *PpFLOT* genomic sequence containing the *nptII* cassette and the predicted integration sites by PCR (oligonucleotides listed in Supplementary Table 15, Table 7). Loss of the *PpFLOT* transcript was confirmed by qRT-PCR using primers located within the *PpFLOT* CDS (oligonucleotides listed in Supplementary Table 15, Table 7).

To create *PpFLOT* overexpression lines, the entire *PpFLOT* CDS was ligated into a vector carrying an ACT5_P sequence, a NOS_T sequence and a hygromycin selection cassette. ACT5_P-controlled *PpFLOT* CDS fragments encoding additional hygromycin resistance were transformed into *P. patens* protoplasts. The transformed plants were selected by cultivating them on hygromycin-containing medium and pre-screened by detecting the hygromycin resistance cassette by PCR (oligonucleotides listed in Table 7 and Supplementary Table 15) and by amplifying ACT5_P controlled *PpFLOT* CDS with primers spanning from the ACT5_P region to the NOS_T region of the newly inserted *PpFLOT* sequence. The overexpression of *PpFLOT* was confirmed by amplifying the *PpFLOT* transcript from cDNA using Pp_Flot_fwd and Pp_Flot_rev primers (oligonucleotides listed in Table 7 and Supplementary Table 15). The strength of the overexpression was determined by qRT-PCR with the primers Flot_qRT_fwd and Flot_qRT_rev (oligonucleotides listed in Table 7 and Supplementary Table 15).

2.2.4 Confirmation of single integration $\Delta PpFLOT$ lines by Southern blot analysis

Genomic DNA was extracted following the CTAB DNA extraction protocol as described by Inglis et al. (2018). From each $\Delta PpFLOT$ line, 10 μg DNA was digested overnight with *XhoI* and *NcoI*. After digestion, the genomic DNA was separated by agarose gel electrophoresis and then transferred to a Hybribond-N+ membrane (GE Healthcare) using an adapted alkaline desaturating blotting following the capillary method (Brown, 2001). After washing and pre-hybridization of the membrane, the hybridization probe was radioactively labeled with the Prime-a-Gene® Labeling System (Promega). A complementary probe against the *nptII* selection cassette was generated by PCR with the primers 5'-TCCATCATGGCTGATGCAAT-3' and 5'-GGCGATACCGTAAAGCACGA-3' using the *nptII* containing pUC-*nptII* vector (Top

et al., 2021) as template. After overnight hybridization and subsequent washing of the blot, radiation was detected with a phosphor image screen for at least 4 h before scanning the screen with the Typhoon Trio Variable Mode Imager (Amersham Biosciences). The brightness of the image was adjusted with the open-source program ImageJ (Schneider et al., 2012).

2.2.5 Cultivation of *P. patens* and following phenotypic analysis

P. patens ssp. *patens* (Hedwig) ecotype “Gransden” 2004 and all generated mutant lines were grown under long-day conditions (16 h light/ 8 h dark; LD 16:8) at 23 °C and a light intensity of 85–100 $\mu\text{mol}/\text{m}^2\text{s}$. Axenic cultivation was performed in liquid or on solid medium as previously described (Frank et al., 2005). Liquid cultures were homogenized and transferred to fresh media every 14 d. Plants were cultivated on solid medium supplemented with 250 mM NaCl, 300 mM NaCl, 700 mM mannitol, 10 μM 2-*cis*,4-*trans*-abscisic acid (ABA)(Sigma-Aldrich), 10 μM 1-naphthylacetic acid (NAA) (1mg/ml, Sigma-Aldrich), 10 μM 6- γ -(dimethylallylamino)-purine (2-ip) (Duchefa), respectively. For the phenotypic analysis, liquid cultures of all lines were adjusted to an equal density of 100 mg dry weight/L and 5 μl of the generated knockout, overexpression and WT control lines were spotted on solid medium. The phenotype assay was performed in triplicates and culture growth was observed and documented for 8 weeks. Pictures were taken with a SMZ 1500 stereomicroscope and a DS-U3 camera (Nikon).

2.2.6 Growth assay *P. patens* WT and $\Delta PpFLOT$ lines

To assess changes in the growth rate between the WT and the generated $\Delta PpFLOT$ lines under control conditions and salt treatment, protonema cultures were adjusted to an equal density of 100 mg dry weight/L in liquid medium, with and without supplementation of 250 mM NaCl. Cultures were monitored for 14 d, with dry weight measurements taken every two to three days. Culture pigmentation was documented using a DS-U3 camera (Nikon). These measurements were conducted in three independent experiments.

2.2.7 Analysis of circadian expression control of *PpFLOT*

To investigate whether *PpFLOT* expression is influenced by light or daytime, WT subcultures of 30 mg dry weight protonema were cultivated for three days under different light conditions: LD 16:8 photoperiod, continuous light (CL) and complete darkness (D). After three days, protonema cultures were harvested at 4 h intervals over a 24 h period (0, 4, 8, 12, 16, 20 and 24 h). Light intensity and temperature conditions were kept to standard cultivation conditions. RNA extraction, sample preparation and qRT-PCR were performed using EVAGREEN®DYE (Biotium) containing reaction mixes as previously described by Arif et al. (2022). To detect time-dependent changes in expression and differences between light treatments, normal distribution and equality of variances of the data sets were confirmed using Shapiro-Wilk and Levene’s tests before ANOVA analysis was performed. Statistically significant differences in

PpFLOT expression among light treatments and time points were determined using Tukey's HSD test. Cosinor analysis was additionally performed to determine potential rhythmicity in *PpFLOT* expression. All statistical analyses were performed in R (v. 4.2.2) (R Core Team, 2023) using the packaged "rstatix" (Kassambara, 2023b) a "cosinor2" (Mutak, 2018). Results were considered significant when $p < 0.05$.

2.2.8 Gene expression analysis after ABA and salt treatments in *PpFLOT* mutant lines

Liquid cultures of WT, $\Delta PpFLOT-1$ and *PpFLOT*-OEX1 were adjusted to a density of 0.4 mg dry weight/ml. The cultures were then divided into three groups per line: untreated control cultures and cultures treated with 10 μ M ABA and 250 mM NaCl, respectively. Samples were harvested from each line and treated in triplicates at 0, 1, 2, 4, 8 and 24 h. RNA extraction and qRT-PCR were performed as described above and statistical ANOVA analysis was performed to determine statistically significant differences between the analyzed lines under control conditions and after the treatment. When $p < 0.05$, a Tukey's HSD test was performed to identify the significantly different lines and the time points of treatment where these differences could be identified. The statistical analysis was conducted with R (v4.2.2) as previously described. MiRNA expression was analyzed using the stem-loop PCR method according to Kramer (2011) following the protocol described by Tiwari et al. (2021) adapted for *P. patens* and using *PpEF1 α* as cDNA synthesis control.

2.2.9 Analysis of photosynthetic activity of *PpFLOT* mutant lines

Pulse-amplitude-modulation (PAM) fluorometry was used to measure the photosynthetic activity of WT, $\Delta PpFLOT-1$, *PpFLOT*-OEX1, *PpFLOT*-OEX2 and *PpFLOT*-OEX3 during their gametophore and protonema life stages. For the analysis of photosynthetic activity in the gametophores, liquid cultures of all lines were standardized to a density of 100 mg/L dry weight and spotted in triplicate 5 μ l spots on solid medium before cultivating them for three months to ensure densely grown moss colonies. Three independent experiments were prepared for the gametophores ($n = 9$ per analyzed line). To measure the fluorescence in protonema, liquid cultures of all lines were adjusted to a concentration of 1 mg dry weight/ml. Five ml of the liquid cultures were filtered through Miracloth (Merck) tissue and placed into six-well plates ($n = 9$ per analyzed line). All plates were dark adapted for 3 h before PAM measurements were performed with the IMAGING PAM M-Series chlorophyll fluorescence imaging system (Walz GmbH) and the ImagingWinGigE V2.56zn software program. Actinic light of 450 nm (IMAG-Max/L) was used at an intensity of 55 μ mol/m²s photosynthetically active radiation (PAR) to mimic normal growth conditions, and the saturation pulse was given for 240 ms to determine maximal fluorescence after dark adaptation. After 40 s, the steady-state fluorescence (F) levels were determined. The steady-state F levels were measured at actinic light intensities of 55 μ mol/m²s PAR in 20 intervals for 315 s. Since protonema cultures of *PpFLOT*-OEX3 displayed

low fluorescence signals and fluorescence could not be detected with these parameters, the measuring light intensity was adjusted, resulting in an actinic light intensity of 60 $\mu\text{mol}/\text{m}^2\text{s}$ PAR. Due to these adjustments, PAM measurements of *PpFLOT*-OEX3 protonema cultures were not considered during the statistical evaluation. PSII quantum yield [Y(II)] was calculated as $(F_m' - F)/F_m'$ (Genty et al., 1989) and the non-photochemical quenching (NPQ/4) as $((F_m - F_m')/F_m')/4$ (Kramer et al., 2004; Gao et al., 2022). To detect statistically significant differences between the analyzed lines, ANOVA analysis was performed, and when $p < 0.05$, then the statistical analysis was followed up with a Tukey's HSD test to determine which lines show significant differences. Statistical analysis for all parameters was performed with R (v. 4.2.2) using the "rstatix" (Kassambara, 2023b) package and graphs were generated with R using the "ggpubr" (Kassambara, 2023a) package.

2.2.10 H₂O₂ detection by 3,3-diaminobenzidine staining

Accumulation of H₂O₂ in all mutant lines was analyzed by harvesting 15 ml of WT, $\Delta PpFLOT$ -1, *PpFLOT*-OEX1, *PpFLOT*-OEX2 and *PpFLOT*-OEX3 protonema cultures grown under standard conditions. The harvested protonema was equally divided into samples treated with sterile MilliQ H₂O (mock), 1 mg/ml 3,3-diaminobenzidine (DAB) pH 3.8 (Rea et al., 2004) and medium (control) for each line before incubating the samples for 18 h at CL. Subsequently, the solutions of the mock and DAB samples were replaced with 99.9 % ethanol, boiled for 10 min and stored in fresh ethanol while the control remained untreated. Microscopy images of mock, DAB and untreated control of all lines were taken with an Axiophot light microscope (Carl Zeiss Microscopy GmbH). Reddish-brown colorations are indicating the sites of H₂O₂ accumulation.

2.2.11 Evaluation of chlorophyll content of *PpFLOT* mutant lines

To evaluate the chlorophyll content of WT, $\Delta PpFLOT$ -1 and all *PpFLOT* overexpression lines, 0.4 g protonema fresh weight was harvested in triplicates for each line and immediately frozen in liquid nitrogen. The harvested plant material was homogenized with metal beads in a TissueLyser™ (Qiagen) to obtain a fine powder, and chlorophyll was extracted by adding 1.5 ml of 80% (v/v) acetone to all samples. The samples were then mixed at 300 rpm for 5 min before centrifugation at 14,000 g for 5 min to obtain cell-free chlorophyll solutions. Chlorophyll content was determined by measuring the absorbance of the supernatant at 645 and 663 nm. Subsequently, the supernatant was transferred back into the reaction tube containing the cell debris of the respective lines and the samples were dried in a speed-vac centrifuge at room temperature overnight. Finally, the samples were dried for 2 h at 105°C to obtain the dry weight for all samples. The chlorophyll content was then calculated after the following method:

$$\text{chlorophyll}/g \text{ dry weight} = [(A_{663})(0.0082) + (A_{645})(0.0202)] \times 1.5/\text{dry weight}$$

2.2.12 Electrolyte leakage assay for WT and *PpFLOT*-OEX lines

To assess electrolyte leakage in WT and all three *PpFLOT*-OEX lines, 5 mg of gametophores grown on solid medium for 8 weeks were collected without damaging the tissue and placed into clean round glass tubes. A clean, adjusted cell sieve was placed into each glass tube without damaging the harvested plant material to serve as physical barrier between the plant material and the electrode of the conductivity meter during measurements. Glass tubes were filled with 5 ml ddH₂O and incubated in a cryostat for 1 h at 0 °C. Ice formation was induced by introducing a metal wire pre-cooled in liquid nitrogen to the water surface without disturbing the plant material. Samples were returned to the cryostat and every 30 min the temperature was decreased by 1 °C. Incubation was stopped for all lines in triplicates at 0, -1, -2, -3, -5 and -7 °C. Samples were left to thaw while gently shaking overnight at 4 °C until all ice crystals were completely dissolved. After adding 5 ml ddH₂O, samples were gently shaken additional 30 min before measuring their conductivity with an inoLab® Cond 7110 (Xylem Inc.) conductivity meter. Samples were autoclaved for 20 min, cooled for 30 min at 4 °C and then allowed to adjust to room temperature by gently shaking at room temperature for 45 min before measuring total conductivity. The relative conductivity was calculated as follows:

$$relative\ conductivity\ [\%] = \frac{sample\ conductivity\ [\mu s/cm]}{total\ conductivity\ [\mu s/cm]} \times 100$$

2.2.13 *PpFLOT*-OEX proteomics analysis

DE protein expression in *PpFLOT*-OEX1, *PpFLOT*-OEX, and *PpFLOT*-OEX3 lines was analyzed by generating total protein extracts from 50 mg protonema (fresh weight) for these lines and the WT control in four replicates. Protein extraction and trypsin digestion were performed as described in (Marino et al., 2019) and Liquid chromatography-tandem mass spectrometry (LC-MS/MS) was performed following the protocol described by Espinoza-Corral et al. (2023), with the exception that peptides were separated over a 90 min linear gradient of 5 – 80% (v/v) acetonitrile (ACN). Raw files were processed using the MaxQuant software version 2.1.0.0 (Cox and Mann, 2008), annotating detected peaks against the *P. patens* reference proteome (UniProt, www.uniprot.org) using the “match-between-runs” setting. Proteins were quantified via label-free quantification method (LFQ) previously described by Cox et al. (2014) and subsequent analysis utilized Perseus version 2.0.1.1. (Tyanova et al., 2016; Tyanova and Cox, 2018). Contaminants, reverse hits and proteins identified solely by site modifications were excluded from further analysis. Only protein groups quantifiable by LFQ algorithm in at least three out of four technical replicates of one of the analyzed lines were used. LFQ intensities were log₂-transformed and missing values were imputed from a normal distribution using default settings. ANOVA tests in Perseus identified statistically significant protein groups between all tested lines ($p < 0.05$, permutation-based FDR $q < 0.05$). Z-scores

of significant \log_2 -transformed LFQ intensities were used to generate a clustered heatmap for easy comparison. GO term enrichment analysis of differentially expressed protein groups (DEP) was performed using web-based shinyGO v0.8 application (Ge et al., 2020). Additional Student's *t*-tests between all *PpFLOT*-OEX lines and the WT control identified significant DEP (all $p < 0.05$, permutation-based FDR $q < 0.05$ and $\log_2(\text{LFQ intensities}) < -1$ and $> +1$). Heatmaps, UpSet plots and Volcano plots were generated with R v4.3.1 using the "pheatmap" (Kolde, 2019), "UpSetR" (Gehlenborg, 2019) and "ggplot2" (Wickham, 2016) packages, respectively.

2.2.14 Metabolomics analysis of *PpFLOT* mutant lines

Approximately 50 mg (fresh weight) of liquid nitrogen frozen and pulverized protonema tissue of WT, $\Delta PpFLOT-1$ and all *PpFLOT*-OEX lines was mixed with 700 μL of basic acetone (acetone: 0.2 M NH_4OH , 9:1 v/v) containing 2 μL corticosterone (2 mg/mL) per sample as an internal standard, in a 2 ml Eppendorf tube. Samples were stored at -20°C for 20 min with gentle mixing every 5 min, then centrifuged for 10 min at 4°C at maximum speed. The supernatant was transferred to a new tube and the pellet was extracted a second time using 300 μL of basic acetone. Both supernatants were combined and mixed before 750 μL of the mixture was vacuum-dried (Concentrator 5301; Eppendorf). Sample preparation was performed under low light and the dried supernatant was stored at -80°C until further analysis, with argon added to prevent oxidation. The dry pellet was resuspended in 100 μL methanol and subsequent LC-MS/MS was performed using a Dionex Ultimate 3000 UHPLC with a diode array detector (DAD) (Thermo Fisher Scientific). For pigment analysis, a 5 μL injection volume was separated at a flow rate of 500 $\mu\text{L min}^{-1}$ on a C30 reversed-phase column (Acclaim C30, 3 μm , 2.1 x 150 mm, Thermo Fisher Scientific) at 15°C . ACN (solution A) and a mixture of methanol and ethyl acetate (50/50; v/v) (solution B), both containing 0.1 % formic acid, were used to form a solvents gradient. The gradient started with 14.5 % solution B, followed by a ramp to 34.5 % solution B within 15 min that was then maintained for 10 min before returning to 14.5 % solution B with an additional 5 min of re-equilibration. Pigments were quantified by DAD. Analysis of the lipid composition was performed by separating 5 μL injection volume at a flow rate of 500 $\mu\text{L min}^{-1}$ on a C30 reversed-phase column (Acclaim C30, 3 μm , 2.1 x 150 mm, Thermo Fisher Scientific) at 15°C . The solvent used for lipid separation was water (solution C) and an ACN:isopropanol mixture (7:3; v/v) (solution D), both including 1 % ammonium acetate and 0.1 % (v/v) acetic acid. The 26 min gradient started at 55 % solution D, followed by a ramp to 99 % solution D within 15 min. After a 5 min washing step at 99 % solution D, the gradient was returned to 55 % solution D and kept constant for 5 min equilibration. For lipid detection, an electrospray ionization (ESI) source was used in positive mode and negative mode to detect FA. Nitrogen was used as the dry gas, at 8 L min^{-1} , 8 bar and 200°C . Mass spectra were recorded in MS mode from 50 m/z to 1300 m/z with 40.000 resolution, 1 Hz scan speed and

0.3 ppm mass accuracy using the timsTOF (Bruker) mass spectra were recorded in MS mode. Compounds were compared to reference standards or annotated in a targeted approach using DAD data as well as the specific mass (m/z) at retention time and the isotopic pattern. Data were acquired by OTOF Control 4.0 and evaluated using DataAnalysis 5.0 and MetaboScape 4.0. All software tools were provided by Bruker. All analyses were performed in four replicates and extreme outliers were removed while ensuring that at least three replicates per line remained for statistical analysis. To identify significant enriched or depleted pigments and lipids, \log_2 transformation of the DAD data was performed and the fold change compared to the WT was calculated. Subsequently, statistical analysis was conducted using Perseus v 2.0.1.1. (Tyanova et al., 2016; Tyanova and Cox, 2018). A two-sample Student's t -test was performed for all generated mutant lines using the WT as the control group. Metabolites were considered statistically significant when $p < 0.05$ and permutation-based FDR $q < 0.05$. All presented heatmaps and UpSet plots were generated using R v4.3.1 with the "pheatmap" (Kolde, 2019) and "UpSetR" (Gehlenborg, 2019) packages, respectively.

2.2.15 Transmission electron microscopy

Protonema cultures of WT, $\Delta PpFLOT-1$ and all $PpFLOT$ -OEX lines were harvested and fixed for three days in fixation buffer made of 75 mM cacodylate, 2 mM $MgCl_2$ (pH = 7.0) and 2.5 % glutaraldehyde. Subsequently, the samples underwent sequential washing steps in fresh fixation buffer for 5, 20, 40 and 60 min. Following this, samples were incubated for 90 min in fixation buffer supplemented with 1% OsO_4 , followed by washing in fresh buffer for 25 min. After overnight incubation in fresh buffer, the samples underwent additional washing steps in ddH₂O for 5, 15 and 30 min. The samples were then gradually dehydrated by incubating them for 20 min in 10 % acetone, 20 min in a 20 % acetone/ 1% UrAc mixture, 110 min in 40 % acetone and for 15 min in 60 % acetone, 80 % acetone. Prior to embedding in 100 % resin, the samples were subjected to a final incubation in 100 % acetone in three steps. Ultrathin sections were prepared and the slides were analyzed using a Zeiss EM912 (Carl Zeiss Microscopy GmbH) equipped with a 2k x 2k Tröndle slow-scan CCD camera (TRS, Tröndle Restlichtverstärkersysteme, Moorenweis, Germany) operated at 80 kV.

2.3 Additional Methods

2.3.1 AI assist for writing in a non-native language

As a non-native English speaker, I used Grammarly to enhance the quality of the text. The text was improved with the assistance of Grammarly responding to various AI prompts such as "Improve it", "Paraphrase it", "Make it engaging", "Sound formal" and "Make it sound academic".

3 Results

3.1 Results Question 1 - How does the loss of DCL genes influence the phytohormone response, salt tolerance, gene expression and the sRNA profile of *M. polymorpha*? Does the function of MpDCLs differ from those in *P. patens*?

3.1.1 *In silico* analysis of *M. polymorpha* DCL proteins reveals differences in their domain architecture

All four MpDCLs were initially annotated by Lin and Bowman (Lin et al., 2016; Lin and Bowman, 2018) but were re-annotated by Bélanger *et al.* (2023), who used recently released databases for the comparative analyses of DCLs from different plant species (Bélanger et al., 2023). The number of putative DCLs for each species, either identified by me or already known, is parenthesized. These analyses were extended by searching for putative DCLs in additional species (*A. agrestis*, *C. braunii*, *C. purpureus* (1), *D. complanatum*, *A. punctatus*, *A. angustus*, *S. cucullata* (2)). The four *M. polymorpha* DCLs, MpDCL1a (Mp7g12090), MpDCL1b (Mp6g09830), MpDCL3 (Mp1g02840) and MpDCL4 (Mp7g11720) that all encode the essential DCL domains, were used as queries to search for DCL homologs in established and newly emerging model organisms. Through this, I identified all known DCLs as well as putative DCLs in established and newly emerging model organisms: *A. thaliana* (4), *M. truncatula* (6), *O. sativa japonica* (6), *Z. mays* (5) as well as DCL homologs in the lycophytes *S. moellendorffii*, *D. complanatum* (5), in the Polypodiophyta species *A. filiculoides* (4) and *S. cucullata* (5), *C. richardii* (5), the bryophytes *P. patens* (5) and *A. agrestis* (4), *A. punctatus* (4), *A. angustus* (4), *S. magellanicum* (5), *S. fallax* (5), *C. purpureus* (4), *M. polymorpha* (5), the streptophyte algae species *C.* (3), *K. nitens* (2), *M. endlicherianum* (1), *S. muscicola* (3) and a chlorophyte algae species *C. reinhardtii* (3) (Figure 6, Table 1, Supplementary Table 1). All obtained full-length protein sequences were used to generate a phylogenetic tree using the CLC Main Workbench (v20), applying the neighbor-joining tree method using Maximum likelihood parameters to create an unrooted cladogram. This method confirmed that *M. polymorpha* does not encode a DCL2 homolog but harbors two related DCL1 proteins (MpDCL1a and MpDCL1b). Based on sequence similarities, the renaming of Mp7g12090 into MpDCL1a, Mp6g09830 into MpDCL1b, Mp1g02840 into MpDCL3 and Mp7g11720 into MpDCL4, as proposed by Bélanger *et al.* (2023) and Pietrykowska *et al.* (2022) was also confirmed. Notably, these results show that *C. reinhardtii*, *C. braunii*, *K. nitens* and *M. endlicherianum* harbor DCLs with a reduced set of functional domains. Domain analysis via Pfam search (Pfam-A v33.1) with the *C. reinhardtii* DCL revealed the presence of two RNase III, one Dicer-dimer and one Helicase C domain. While CrDCL1 encodes one additional DEAD/DEAH-box domain, the DCL homologs of *K. nitens* encode, in addition to these domains, the RES III and Dead end protein 1 homologous

to double-strand RNA binding (DND1_DSRM) domain. Kfl00265.0060 also encodes one PAZ domain. Similar domain compositions are also present in the single *M. endlicherianum* DCL homolog. (Figure 6, Supplementary Table 1). These structural differences support the origin of embryophytic DCL differentiation as suggested by Wang *et al.* (2021). On the other hand, *C. braunii* DCL G24199, unlike the hypothesis of embryophytic DCL differentiation, harbors two adjacent RNase III domains, while G34091 encodes a Dicer-dimer domain and PAZ domain. Moreover, G34093 lacks RNase III domains but contains two RNase H-like domains and a Helicase C domain (Figure 6, Supplementary Table 1). According to the biochemical properties of DCL proteins and the essential domains involved in sRNA biogenesis, additional copies of *DCLs* may exist in *C. braunii* that escaped the detection using current databases. Interestingly, all three detected DCLs of *S. muscicola* are not clustered together with the DCL1 orthologs in other species but show a close relation to the DCL3 of other species. They all encoded one DEAD/DEAH box helicase, one Dicer-dimer, one Helicase C domain, one PAZ, two RESIII and two dsRBD motifs. Thus, they not only encode all domains necessary for DCL function but also show very little variation between the three DCL homologs of this streptophyte algae species.

Detailed domain analysis of all four MpDCLs revealed that MpDCL1a, MpDCL3 and MpDCL4 encode domains of RESIII, Helicase C, Dicer-dimer, PAZ and two adjacent RNase III domains. In addition to these five different domains, MpDCL1a and MpDCL4 also harbor the DND1_DSRM domain, hence they contain all six important domains reported in diverse plant lineages (Margis *et al.*, 2006; Liu *et al.*, 2009; Liu *et al.*, 2012). On the contrary, MpDCL1b contains only the PAZ domain and two adjacent RNase III domains (Figure 6, Supplementary Table 1). The lack of other functional domains raises the question of whether or not MpDCL1b is a pseudogene. Based on the phylogenetic analysis, DCLs that lack some of the aforementioned six different domains were found. More importantly, through reciprocal BLAST searches using the full-length MpDCL1b protein sequence as query potential DCL homologs that also encode one PAZ and at least one RNase III domain could be found in *A. agrestis* (AagrOXF_evm.model.utg000049l.134.1), *A. punctatus* (Apun_evm.model.utg000162l.37.1), *S. fallax* (Sphfalx14G057500.1; Sphfalx17G041800.1), *S. magellanicum* (Sphmag17G038700.1; Sphmag14G056800.1), *C. purpureus* (CepurR40.3G117100.1), *P. patens* (Pp3c24_9630V3.1), *D. complanatum* (Dicom.06G085000.1), *A. filiculoides* (Azfi_s0335.g06552), *S. cucullata* (Sacu_v1.1_s0089.g018689) and *C. richardii* (Ceric.13G041700.1) (Figure 6A, 1B, Supplementary Table 1). Interestingly, this type of MpDCL1b could only be identified in moss and fern species and not in seed plants or in the tested streptophyte algae, implying that this type of DCL might be important for the initial stage of plant terrestrialization and was later lost in seed plants. Consequently, due to the presence of similar DCL proteins in early land plants,

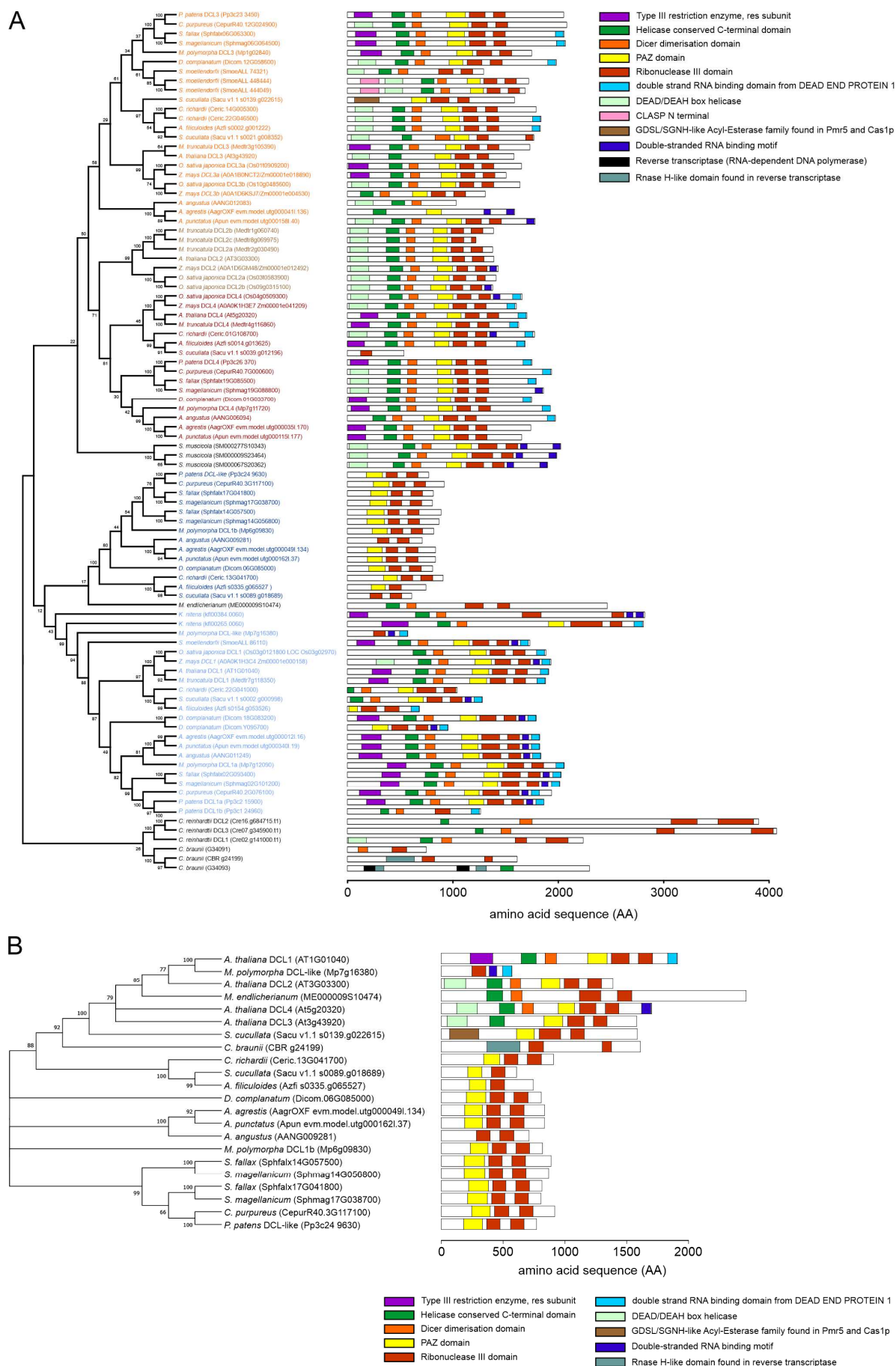


Figure 6: Phylogenetic analysis of DCL proteins and their functional domains

(A) Cladogram of MpDCL homologs from the following species: *A. angustus*, *A. agrestis*, *A. punctatus*, *A. thaliana*, *A. filiculoides*, *C. purpureus*, *C. richardii*, *C. braunii*, *C. reinhardtii*, *D. complanatum*, *K. nitens*, *M. polymorpha*, *M. truncatula*, *M. endlicherianum*, *O. sativa japonica*, *P. patens*, *S. cucullata*, *S. moellendorffii*, *S. fallax*, *S. magellanicum*, *S. muscicola* and *Z. mays*. The accession number of the amino acid (AA) sequences is provided for sequences that have not been annotated previously. The cladogram was generated by comparing AA sequence using CLC Genomics Workbench (Qiagen) through neighbor end joining with Maximum likelihood parameters and 1000 bootstrap replicates in MEGA X. Common plant DCL variants are color-coded: DCL1 homologs in light blue, MpDCL1b homologs in dark blue, DCL2 homologs in brown, DCL3 homologs in orange, DCL4 homologs in red and algae specific DCLs and non-annotated clades in black. Protein domain analysis of the plant DCLs listed according to their phylogenetic relationship. Functional domains were identified after PAM domain search (Pfam-A v33.1) with CLC Genomics Workbench v20.0.4 (Qiagen). The functional domains are marked in different colors and the domain position in their respective AA sequence is listed in Supplementary Table 1. **(B)** Cladogram of closest MpDCL1b homologs detected in *A. agrestis*, *A. punctatus*, *A. filiculoides*, *C. purpureus*, *C. richardii*, *C. braunii*, *D. complanatum*, *M. polymorpha*, *P. patens*, *S. cucullata*, *S. fallax*, *S. magellanicum* and with added *A. thaliana* and *M. endlicherianum* DCL for outgroup comparison.

MpDCL1b is most likely not a pseudogene but might have a different role than its paralogs in sRNA biogenesis. Besides MpDCL1b, there might be other ribonucleases in *M. polymorpha* with similar functions. For instance, during reciprocal BLAST searches using known MpDCL1b, Mp7g16380, which could belong to this new class of DCLs, was also identified as a potential DCL homolog. However, this homolog only encodes one RNase III and two dsRBD sites, lacking a PAZ domain, hence it was excluded from this analysis.

3.1.2 Effects of MpDCL mutations on thallus development

To characterize all four MpDCLs, loss-of-function mutants using the CRISPR/Cas9 system described by Sugano *et al.* (2018) were generated. Two gRNAs (Supplementary Table 2) were designed to target either the first exon or regions encoding functionally important domains of the respective MpDCL gene and used these gRNAs in pairs during transformation to ensure large deletions and/or frameshift mutations. As a result, lines with large deletions and indels that introduced premature stop codons in MpDCL1b, MpDCL3 and MpDCL4 and prevent the generation of functional proteins, were obtained. Furthermore, this way, both male and female lines for Mpdc1b^{ge}, Mpdc13^{ge} and Mpdc14^{ge} were obtained. The positions of induced double-strand breaks within these genes, as well as mutated regions, are shown in Figure 7A and 2B, respectively. From the gRNA pair used to generate Mpdc14^{ge}, only one was effective (Supplementary Table 2). The use of various gRNAs in pairs (two gRNAs in each transformation event) targeting MpDCL1a failed to cause large genomic fragment deletions, frameshift mutations, or the generation of a premature stop codon. Analysis of all viable mutant lines displayed that only gRNA2, which did not target a genomic region encoding a functional DCL domain, induced a double-strand break resulting in short deletions and, in some cases, insertions of short sequences, but none of the plants surviving the selection obtained a frameshift mutation adversely affecting the encoded AA sequence (Figure 7A, 7B, Supplementary Table 2, Supplementary Figure 1). It has been previously shown that DCL1 is an essential protein for miRNA biogenesis and is required for normal plant development. The *Atdcl1* null mutants are embryo-lethal (Henderson *et al.*, 2006) and the Δ PpDCL1a mutant

lines display severe developmental disorders with altered cell size, shape and arrested development at the filamentous protonema stage (Khraiwesh et al., 2010). Hence, failure in generating a *MpDCL1a* mutant line with large genomic arrangements may indicate that *MpDCL1a*, like its homologs in *P. patens* and *A. thaliana*, is essential for plant development and transformants harboring a non-functional *MpDCL1a* protein may not be viable. Additionally, most of the designed gRNAs were targeted to regions encoding functional DCL domains. The observed phenotypic aberrations in *Mpdc11a^{ge}* mutant lines correlate with the type of the genomic alterations (Supplementary Figure 1). The mutant line *Mpdc11a-6^{ge}* displayed the most severe phenotypic abnormalities and sequencing of the mutated region revealed the insertion of “TTG” at position 1015 and substitution of T to A (position 1014) and G to T (position 1015) (Figure 7B, Table 2, Supplementary Table 2). These changes result in an exchange of aspartic acid (D) by glutamic acid (E) at position 338 and the insertion of leucine and cysteine (LC) at the positions 339–340 in the primary AA of *MpDCL1a*. Based on the detailed analysis of the expected *MpDCL1a* AA using Phyre² (Kelley et al., 2015), a potential change in the secondary structure of the protein (position 280–390) was detected due to comparison of the aforementioned mutations to the *MpDCL1a* wild-type sequence. For further analyses, this study focuses on *Mpdc11a-6^{ge}*, as it exhibited severe developmental aberrations due to the genomic alteration that most likely affected the proper folding of *MpDCL1a* protein. The RES III domain of *MpDCL1a* (position 379–557) is predicted to be involved in endonucleolytic cleavage to generate double-stranded fragments and any change in the AA affecting the secondary protein structure might impair the function of *MpDCL1a* and lead to faulty pri-miRNA processing.

Sequencing of mutated sites using plants from the G2 generation (Figure 7B) confirmed the likely generation of premature stop codons in *Mpdc11b^{ge}*, *Mpdc13^{ge}* and *Mpdc14^{ge}* lines (Table 2, Supplementary Table 2). These lines, along with *Mpdc11a-6^{ge}*, were further examined phenotypically. For this purpose, single gemmae from one male and one female line of *Mpdc11b^{ge}*, *Mpdc13^{ge}*, *Mpdc14^{ge}* and WT control were plated on standard medium and observed for at least 21 DAG. Only a female line of *Mpdc11a-6^{ge}* was used in phenotypic analysis, as no male line with the aforementioned mutations in the *MpDCL1a* gene could be obtained. While *Mpdc11a-6^{ge}* displayed pleiotropic developmental alterations compared to the WT, *Mpdc13^{ge}* lines showed severe changes in their body plan. In contrast, both *Mpdc11b^{ge}* and *Mpdc14^{ge}* grew similarly to the WT (Figure 7C). A closer look at the development of the *Mpdc11a-6^{ge}* mutant revealed that it grows drastically slower than WT at 7 DAG and does not exhibit typical dichotomous thallus branching but instead forms a callus-like structure even after 21 DAG (Figure 7C, 8A). Under control conditions, *Mpdc11a-6^{ge}* also showed stunted growth and failed to develop gemmae cup walls, although the dorsal epidermis still produces gemmae (Figure

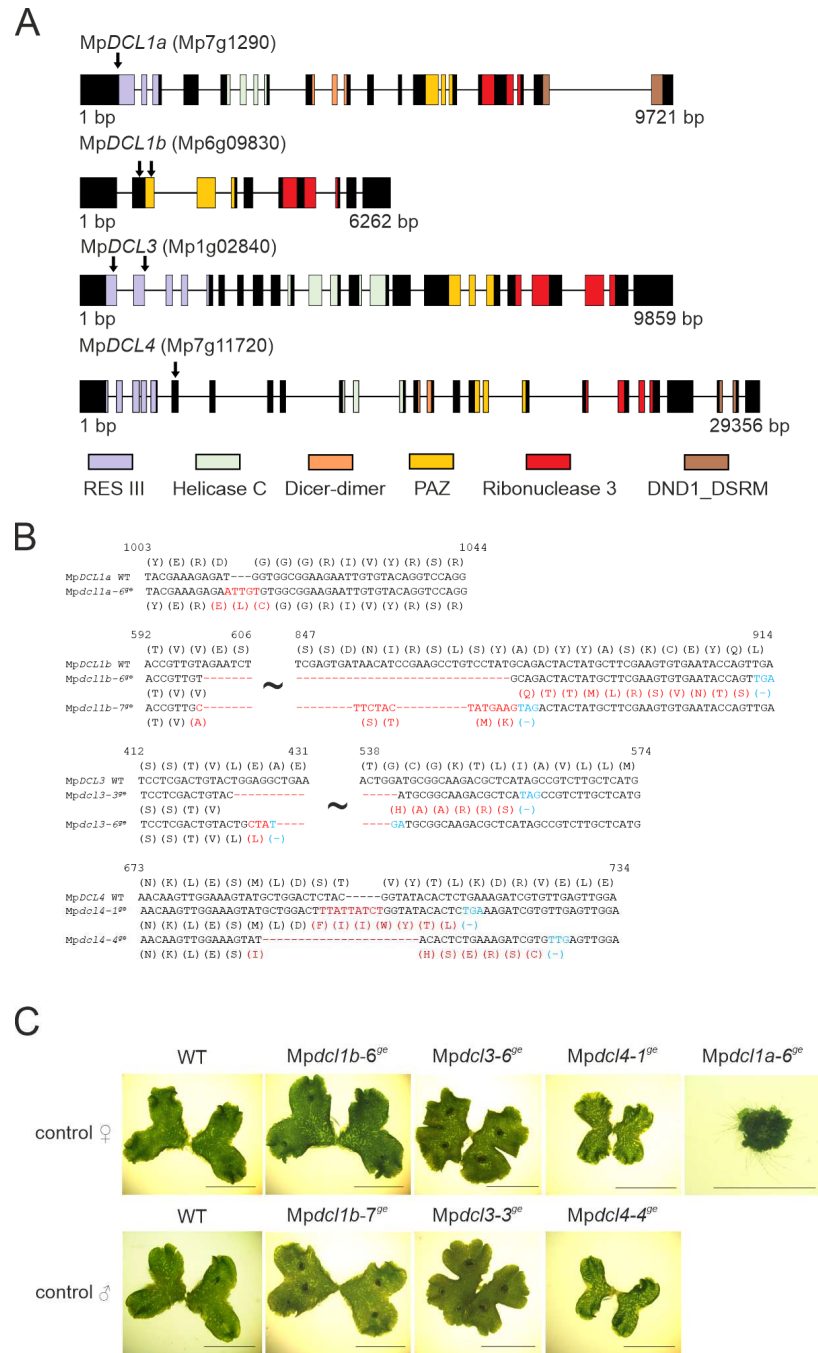


Figure 7: Generation of *Mpdcl*^{oe} mutant lines

(A) Schematic representation of all MpDCL genomic sequences without 3' and 5' UTRs. The colored sections indicate encoded domains characteristic for DCL proteins. Arrows mark the targeting sites of gRNAs successfully used to generate the respective *Mpdcl*^{oe} mutant line. (B) Alignment of WT MpDCL coding sequences (CDS) and mutated CDS of ♀ *Mpdcl1a*^{oe} mutant line as well as ♀ and ♂ mutant lines of *Mpdcl1b*^{oe}, *Mpdcl3*^{oe} and *Mpdcl4*^{oe}; only mutated regions are shown and mutations are highlighted in red. Deletions are indicated by dashes. WT amino acid (AA) sequence is displayed above the alignment and the mutated AA sequences are displayed below the mutated CDS. Premature stop codons are highlighted in blue. (C) Phenotypic comparison of ♀ and ♂ WT with mutant lines *Mpdcl1b*^{oe}, *Mpdcl3*^{oe}, *Mpdcl4*^{oe} and *Mpdcl1a-6*^{oe}, 21 days after gemmae germination (DAG) and grown on standard medium under control conditions; scale bar 1 cm.

8B). Scanning electron microscopy of the dorsal epidermal layer revealed exposed gemmae floor cells on the thallus surface of *Mpdcl1a-6^{ge}* in areas where the gemmae cup initiation occurs. However, the cup is unable to fully develop (Figure 8C). Furthermore, development of cell clusters near the gemmae floor cells was observed, which likely contributes to the observed callus-like growth.

Additionally, *Mpdcl3^{ge}* also exhibited slightly stunted thallus growth and an increase in thallus branching events, resulting in a distinct rosette shape at 21 DAG (Figure 8D). Although the decrease in thallus arm length of *Mpdcl3^{ge}* at 14 DAG was statistically significant ($p < 0.001$) (Figure 8E), the difference in thallus area between *Mpdcl3^{ge}* (mean $1.71 \text{ cm}^2 \pm \text{SEM } 0.159$) and WT (mean $1.57 \text{ mm}^2 \pm \text{SEM } 0.158$) was no longer statistically significant ($p = 0.427$) at 21 DAG (Figure 8F). Further statistical analysis of all *Mpdcl^{ge}* mutant lines at 21 DAG revealed that the thallus area of *Mpdcl1a-6^{ge}* was significantly reduced to an average of 0.167 cm^2 (SEM ± 0.012) compared to WT ($p < 0.01$) (Figure 8F).

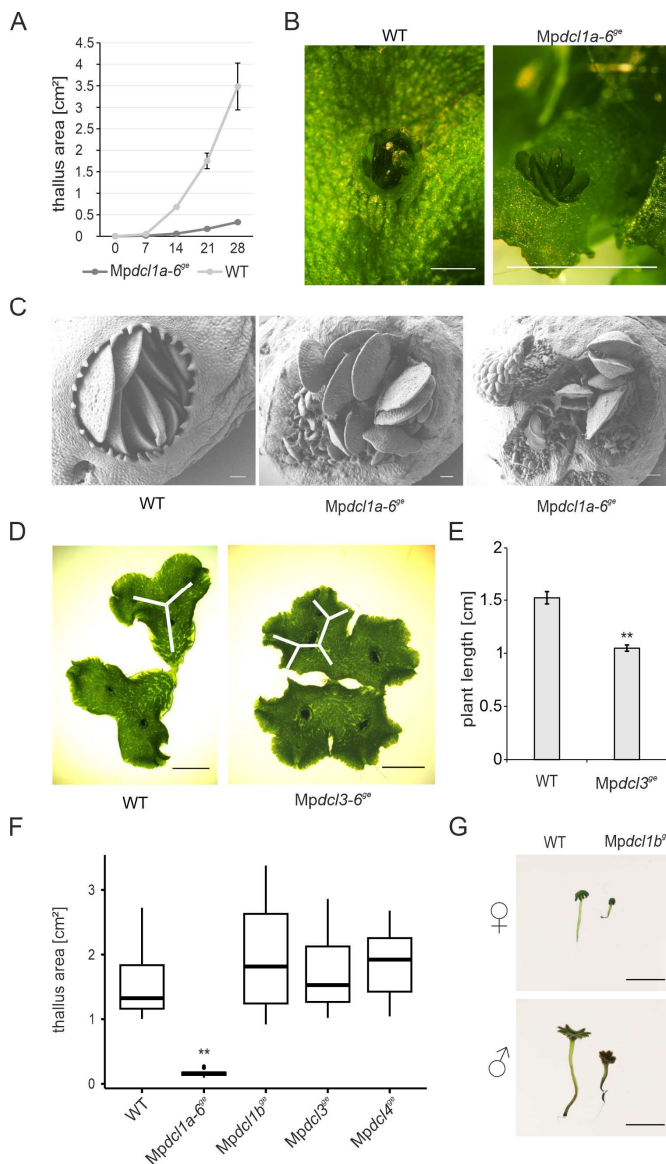


Figure 8: Phenotypic analysis of *Mpdcl^{ge}* mutant lines

(A) Thallus area of WT (♀/♂; 50/50) and *Mpdcl1a-6^{ge}* (♀) grown on standard medium under control conditions at 0, 7, 14, 21 and 28 days after gemmae germination (DAG), ($n = 10$, error bars indicate \pm SEM). **(B)** Close-up of a WT gemmae cup and gemmae from *Mpdcl1a-6^{ge}* (♀) that develop on the dorsal thallus side from 7 weeks old plants grown under control conditions on standard medium; scale bar 1 mm. **(C)** Scanning electron microscopy analysis of 28 DAG WT (♀) and *Mpdcl1a-6^{ge}* (♀) gemmae cup after first gemmae and gemmae cup formation. Left panel shows WT gemmae in gemmae cups, middle panel shows close-ups of epidermal layer of *Mpdcl1a-6^{ge}* with unsheltered gemmae cup floor cells developing gemmae, right panel shows multiple areas of gemmae development and formation of cell clusters. Scale bar: 100 μm . **(D)** Branching of WT and *Mpdcl3^{ge}*, 21 DAG grown on standard medium under control conditions; scale bar 5 mm. **(E)** Total plant length (cm) of WT and *Mpdcl3^{ge}* ($n = 20$; ♀/♂; 50/50) 14 DAG. Statistically significant Student's *t*-test ($p < 0.001$) is marked by two asterisks, error bars depict \pm SEM. **(F)** Box plot of the thallus area of 21 DAG *Mpdcl1a-6^{ge}* (♀) as well as ♀ and ♂ (50/50) WT, *Mpdcl1b^{ge}*, *Mpdcl3^{ge}*, *Mpdcl4^{ge}* lines grown on standard medium under control conditions, $n = 14$. Statistically significant results of Student's *t*-test between WT and mutant lines ($p < 0.001$) are marked with two asterisks. **(G)** Gametangiophores from WT, *Mpdcl1b^{ge}* after 11 weeks growth in far-red light conditions. Upper panel: archegoniophores, lower panel: antheridiophores; scale bar 1 cm.

The thallus growth of *Mpdcl1b^{ge}* (mean 1.95 cm² ± SEM 0.214) and *Mpdcl4^{ge}* (mean 1.85 cm² ± SEM 0.148) lines showed no significant changes compared to WT (mean 1.57 cm² ± SEM 0.158) under control conditions (Figure 8F) (*Mpdcl1b^{ge}* *p* = 0.265; *Mpdcl4^{ge}* *p* = 0.178).

Consequently, these phenotypic analyses suggest an important function for *MpDCL1a*, through sRNAs processed by *MpDCL1a*, in gemmae germination, thallus development and gemmae cup formation. Even though *Mpdcl3^{ge}* did not exhibit any significant changes compared to WT at 21 DAG, the accelerated branching of *Mpdcl3^{ge}* in early developmental stages and different branching patterns suggest an essential role for *MpDCL3* and associated sRNAs during thallus development. However, *Mpdcl1b^{ge}* and *Mpdcl4^{ge}*, despite higher phenotypic variation, did not display any alterations in thallus development compared to WT. While *MpDCL1b* and *MpDCL4* are expressed at low levels in sporelings, gemmalings and adult thallus, they are both expressed at high levels in the antheridium and at mid-tier levels in the antheridiophores and archegoniophores (eFP browser, http://bar.utoronto.ca/efp_marchantia/cgi-bin/efpWeb.cgi). Thereby, rather than developmental aberrations in sporelings or gemmalings, defects may be expected in gametangiophore development or antheridium formation due to mutations in *Mpdcl1b^{ge}* and *Mpdcl4^{ge}*. To evaluate gametangiophore development in the *Mpdcl^{ge}* lines, vernalized gemmae from all lines and male and female WT controls were cultivated under LD 16:8 photoperiod conditions supplemented with far-red light. The cultures were observed weekly for up to three months. Attempts to induce gametangiophores in all *Mpdcl^{ge}* mutant lines resulted in smaller and deformed gametangiophores in the *Mpdcl1b^{ge}* lines that were induced simultaneously to the WT control (Figure 8G) whereas no gametangiophores could be induced in *Mpdcl1a^{ge}*, *Mpdcl3^{ge}* and *Mpdcl4^{ge}*. Hence, it can be suggested that all *MpDCL*, through associated sRNAs, play important roles in gametangiophore induction.

3.1.3 Mutation in *MpDCL1b* causes increased salt tolerance

Unlike *P. patens*, which tolerates high salt concentrations, *M. polymorpha* exhibits lower salt tolerance. The survival rate of *M. polymorpha* significantly decreases when grown on solid medium supplemented with 50 mM NaCl (Frank et al., 2005; Tanaka et al., 2018). A recent publication showed that abolishing the *PpDCL1a*/miR1047 autoregulatory feedback loop leads to salt hypersensitivity in *P. patens*, indicating the importance of DCLs and sRNAs in salt stress tolerance (Arif et al., 2022). Previous reports also revealed that sRNAs are crucial for abiotic stress tolerance mechanisms in various plant species (Fu et al., 2017; Habermann et al., 2020; Tiwari et al., 2020; Tiwari et al., 2021). Therefore, it was hypothesized that plants with mutated *MpDCLs* would have altered abiotic stress tolerance due to the anticipated adjustment or misregulation of sRNA biogenesis and sRNA-directed gene regulatory networks.

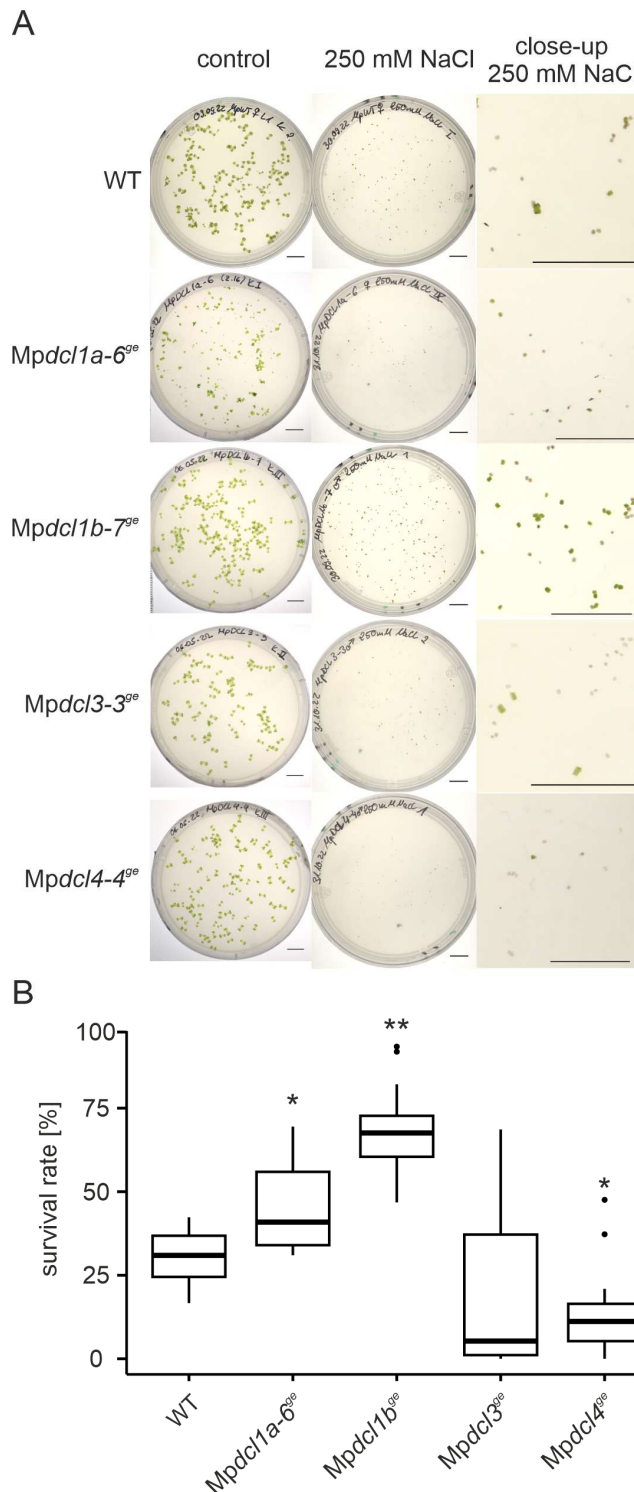


Figure 9: Growth of WT and *Mpdcl^{ge}* mutant lines on high salt concentration

(A) WT, *Mpdcl1a-6^{ge}*, *Mpdcl1b-7^{ge}*, *Mpdcl3-3^{ge}* and *Mpdcl4-4^{ge}* grown for 14 days after gemmae germination (DAG) on standard medium (left) and medium supplemented with 250 mM NaCl (middle). The right column depicts close-ups of plates with the NaCl-supplemented medium; scale bar 1 cm. (B) Box plot of survival rates of *Mpdcl1a-6^{ge}* (♀), as well as ♀ and ♂ (50/50) WT, *Mpdcl1b^{ge}*, *Mpdcl3^{ge}*, *Mpdcl4^{ge}* lines on medium containing 250 mM NaCl 14 DAG. Statistically significant results of Student's *t*-test between WT and the respective *Mpdcl^{ge}* mutant lines with $p < 0.001$ are marked with two asterisks and $p < 0.05$ with one asterisk, $n = 12$.

To test whether mutations in *MpDCL* genes affect salt stress responses, multiple gemmae (Ø 118.9 gemmae per plate) from *Mpdcl1a-6^{ge}*, male and female *Mpdcl1b^{ge}*, *Mpdcl3^{ge}* and *Mpdcl4^{ge}* lines as well as male and female WT lines, were plated on standard medium supplemented with 250 mM NaCl and grown for 14 d under standard conditions (Figure 9A). At the end of the cultivation period, all plants showing growth and chlorophyll production on each plate were counted and the survival rate of the respective lines was calculated. At 14

DAG, male and female WT lines showed an average survival rate of 30.03 % (Figure 9B), which is in line with a previous study (Tanaka et al., 2018). However, an overall decrease in survival rates to 20.84 % and 14.30 % was observed for *Mpdcl3^{ge}* and *Mpdcl4^{ge}* lines, respectively (Figure 9B). Despite the observed decrease in both lines, only the decrease in *Mpdcl4^{ge}* lines upon salt treatment was statistically significant ($p = 0.006$). On the other hand, both *Mpdcl1a-6^{ge}* and *Mpdcl1b^{ge}* displayed an enhanced salt stress tolerance compared to WT and the other mutant lines, with average survival rates of 45.03 % ($p = 0.003$) and 68.90 % ($p < 0.001$), respectively (Figure 9B). To sum up, mutations in *MpDCL1a*, *MpDCL1b* and *MpDCL4* resulted in altered survival rates upon salt treatment. While *MpDCL4* and its associated sRNAs positively regulate salt stress adaptation in *M. polymorpha*, *MpDCL1a*, *MpDCL1b* and the sRNAs they control are most likely negative regulators of salt stress adaptation. In particular, this might explain why *M. polymorpha* WT, which harbors functional *MpDCL1a*, *MpDCL1b* and *MpDCL4*, does not tolerate high levels of salt stress and further investigations are required to understand how these mechanisms evolved during the water-to-land-transition.

3.1.4 *Mpdcl1a-6^{ge}*, *Mpdcl3^{ge}* and *Mpdcl4^{ge}* lines display ABA hypersensitivity

Numerous miRNAs are differentially regulated in response to phytohormone treatment and abiotic stress (Khraiweh et al., 2010; Khraiweh et al., 2012). ABA is the central mediator of stress signaling responses (Hauser et al., 2011; Arif et al., 2018), hence alterations in the various sRNA biogenesis pathways due to mutations in *MpDCL* genes might affect ABA signaling and the sensitivity of the mutant lines to ABA treatment. I analyzed whether the response to ABA in the *Mpdcl1a-6^{ge}*, *Mpdcl1b-6^{ge}*, *Mpdcl1b-7^{ge}*, *Mpdcl3-3^{ge}*, *Mpdcl3-6^{ge}*, *Mpdcl4-1^{ge}* and *Mpdcl4-4^{ge}* lines would be affected by the loss of the respective functional DCL protein and the subsequent changes in the sRNA and mRNA repertoire upon exogenous ABA treatments. Single gemmae ($n = 20$, *Mpdcl1a^{ge}* $n = 15$) of the respective *MpDCL* mutant lines (both male and female lines, with the exception of *Mpdcl1a^{ge}*, together with WT) were inoculated on standard medium supplemented with 10 μ M ABA. Gemmae were grown under standard conditions for at least 21 DAG before thallus area was measured and compared with WT controls. In response to ABA, WT showed reduced growth at 21 DAG (mean 0.718 cm²; SEM \pm 0.088) and a 2.19-fold decrease in thallus area compared to the untreated WT (Figure 10A). These observations are in accordance with a previous study where ABA treatment led to a delay in gemmae germination and stunted growth (Eklund et al., 2018). Even though *Mpdcl1a-6^{ge}* displayed stunted growth under normal conditions, its growth (i.e., thallus area) decreased further by 3.4-fold in response to ABA. This decrease in growth in comparison to ABA treated WT is statistically significant ($p < 0.01$) (Figure 10A, 10B). While *Mpdcl1b^{ge}* mutant lines showed reduced growth compared to untreated *Mpdcl1b^{ge}* lines, this ABA sensitivity was not statistically significant ($p = 0.285$) (Figure 10B). Moreover, *Mpdcl3^{ge}* and *Mpdcl4^{ge}* lines showed ABA hypersensitivity like *Mpdcl1a-6^{ge}*: 4.5-fold and 4.07-fold decreases in thallus area

were recorded in *Mpdcl3^{ge}* ($p = 0.00123$) and *Mpdcl4^{ge}* ($p = 0.0304$), respectively (Figure 10B). Consequently, it can be proposed that all MpDCLs except MpDCL1b and those sRNAs associated with these proteins are involved in ABA signaling and stress response in *M. polymorpha*.

3.1.5 *Mpdcl3^{ge}* phenotype is rescued by auxin treatment

Auxin regulates plant growth and differentiation through coordinated changes in gene expression and assists the transition from 2D to 3D growth in *M. polymorpha* (Flores-Sandoval et al., 2015). In response to exogenous auxin, while thallus growth is inhibited, rhizoidal initiation and elongation are observed in the liverwort *M. polymorpha* (Ishizaki et al., 2012; Kato et al., 2017). Similar changes can be observed in various plant species upon auxin treatment. For instance, auxin induces chloronema to caulonema transition, inhibits bud formation and controls rhizoid and gametophore development in *P. patens* (Jang and Dolan, 2011; Thelander et al., 2018). Moreover, miRNAs have been shown to modulate auxin signaling and, thereby, plant development and stress responses (Navarro et al., 2006; Jodder, 2020). To investigate whether mutations in MpDCLs and an altered sRNA repertoire result in impaired auxin response and developmental aberrations, the mutant as well as wild-type plants were treated with exogenous NAA. Twenty gemmae were grown on standard medium supplemented with 10 μ M NAA and the visible thallus area was measured 21 DAG. In wild-type, exogenous NAA treatment induced enhanced rhizoid formation and inhibited thallus growth significantly ($p < 0.001$, in comparison with untreated WT) (Figure 10A), which is in line with previous findings in *M. polymorpha* (Ishizaki et al., 2012; Flores-Sandoval et al., 2015; Kato et al., 2017). Upon exogenous NAA treatment, *Mpdcl1a-6^{ge}* plants grew significantly slower ($p < 0.001$) than untreated *Mpdcl1a-6^{ge}* plants (21 DAG). In addition, *Mpdcl1a-6^{ge}* showed increased rhizoid production like auxin-treated wild-type plants (Figure 10A) and the reduction in thallus area in *Mpdcl1a-6^{ge}* plants after NAA treatment was statistically significant ($p < 0.001$) when compared to WT plants (Figure 10C). Treatment of *Mpdcl3^{ge}* with NAA led to overall growth inhibition ($p < 0.001$) that was not significantly different from WT ($p = 0.213$), even though thallus measurements of NAA-treated *Mpdcl3^{ge}* indicated high levels of variance between individuals (Levene's test $p < 0.001$ compared to the WT). Rather than inducing rhizoid formation at the expense of inhibited thallus growth, most *Mpdcl3^{ge}* plants showed an increase in thallus length compared to their control counterparts. By cultivating multiple *Mpdcl3^{ge}* plants on one plate, this effect could be enhanced and the resulting body plan resembled the WT under control conditions, indicating a NAA-insensitive phenotype for these mutants (Figure 10A, 10C, 10D).

Reduced thallus growth ($p < 0.001$) and increased rhizoid formation were also observed in *Mpdcl1b^{ge}* and *Mpdcl4^{ge}* upon exogenous NAA treatment (Figure 10A, 10C), but they did not exhibit NAA hypo- or hypersensitivity as reductions in thallus growth in these mutant lines were

not statistically significant compared to the growth reduction in WT (*Mpdcl1b^{ge}* $p = 0.387$; *Mpdcl4^{ge}* $p = 0.337$). Only *Mpdcl1a^{ge}* showed a significant ($p < 0.001$) reduction in thallus area in reaction to NAA treatment when compared to the treated WT. In conclusion, due to the NAA insensitivity observed in the *Mpdcl3^{ge}* mutant and the NAA hypersensitivity observed in the *Mpdcl1a^{ge}* mutant, I propose that MpDCL3 as well as MpDCL1a and their associated sRNAs are involved in auxin signaling, essential for *M. polymorpha* development.

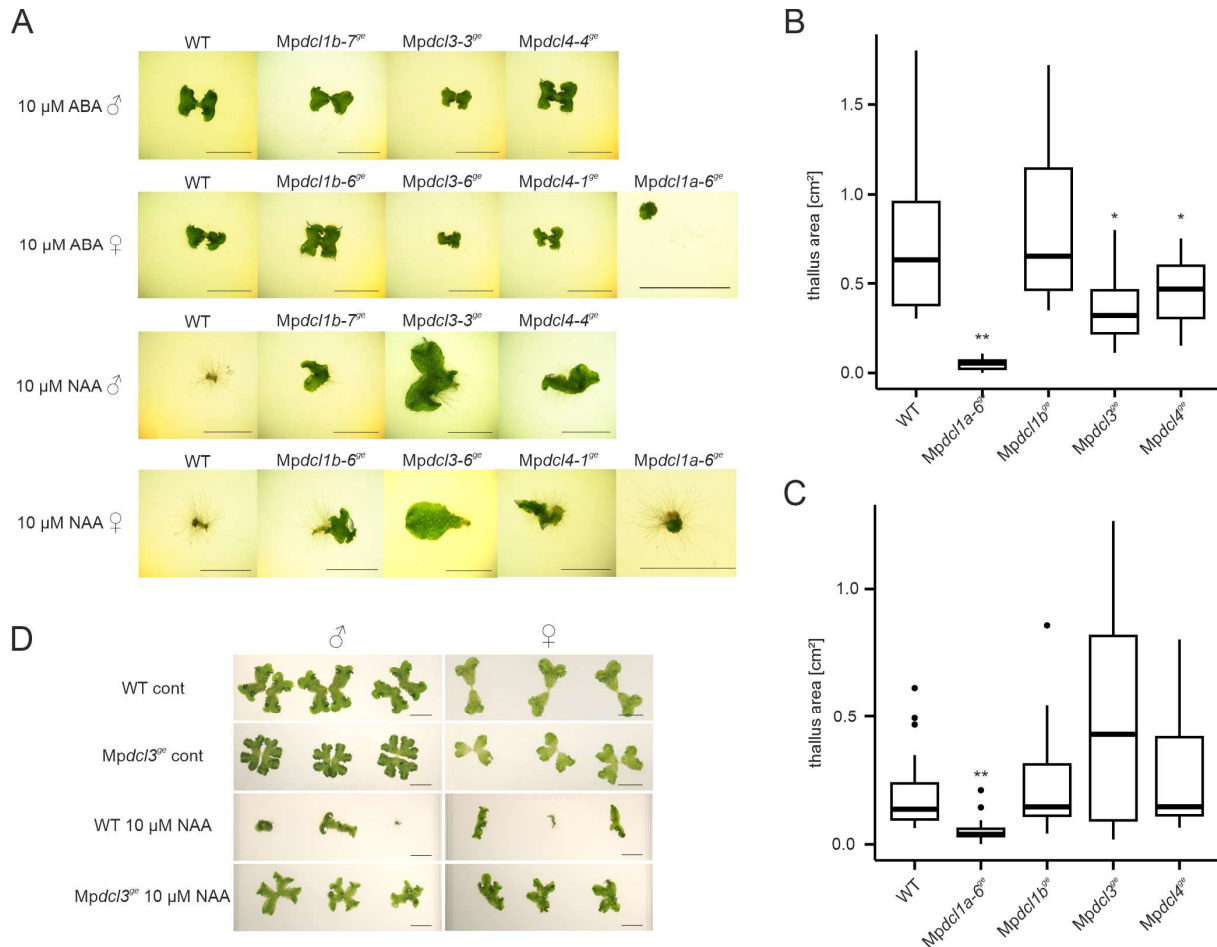


Figure 10: Phytohormone treatment of mutant *Mpdcl^{ge}* lines

(A) Male and female lines of WT and *Mpdcl1b^{ge}*, *Mpdcl3^{ge}* and *Mpdcl4^{ge}* lines as well as the *Mpdcl1a-6^{ge}* female line grown for 21 days after gemmae germination (DAG) on medium supplemented with 10 μ M ABA or 10 μ M NAA; scale bar 1 cm. For control grown on standard medium, see Figure 7C and Figure 8F. **(B)** Box plot of thallus area (cm^2) of male and female (50/50) WT, *Mpdcl1a^{ge}*, *Mpdcl1b^{ge}*, *Mpdcl3^{ge}* and *Mpdcl4^{ge}* lines grown on standard medium supplemented with 10 μ M ABA for 21 DAG under control conditions $n=20$ (10 ϕ and 10 σ per line) except for *Mpdcl1a-6^{ge}* ($n = 15$ all ϕ). Statistically significant results of Student's *t*-test between WT and the respective mutant line are marked with two asterisks ($p < 0.001$) or one asterisk ($p < 0.05$). **(C)** Box plot of thallus area (cm^2) of male and female (50/50) WT, *Mpdcl1a^{ge}*, *Mpdcl1b^{ge}*, *Mpdcl3^{ge}* and *Mpdcl4^{ge}* lines grown on standard medium supplemented with 10 μ M NAA for 21 DAG under control conditions $n=20$ (10 ϕ and 10 σ per line) except for *Mpdcl1a-6^{ge}* ($n = 15$ all ϕ). Statistically significant results of Student's *t*-test between WT and the respective mutant line are marked with two asterisks ($p < 0.001$) or one asterisk ($p < 0.05$). **(D)** Three male (left panel) and female (right panel) plants of WT and *Mpdcl3^{ge}* cultivated under control conditions for 28 DAG on standard medium and on medium supplemented with 10 μ M NAA on the same plate (upper section WT, lower section *Mpdcl3^{ge}*), scale bar 1 cm.

3.1.6 MpDCL1a is responsible for the miRNA biogenesis

To gain insight into the pathways responsible for the biogenesis of the different sRNA classes, especially miRNAs, an in-depth sRNA sequencing analysis for all generated *Mpdc^{pe}* mutants was conducted. To elucidate the sRNA composition found in each of the generated *Mpdc^{pe}* mutants, multiple gemmae of the female line of each mutant and a female WT control were grown for two weeks under standard conditions and used for sequencing. Additionally, WT and *Mpdc1b-6^{ge}* plants were cultivated on media supplemented with 100 mM NaCl to analyze potential changes in sRNA expression between these two lines that might explain the observed high salt tolerance of *Mpdc1b-6^{ge}*. Triplicates for each line and condition were used to generate sRNA libraries of at least 20 million reads that were mapped to the *M. polymorpha* reference genome v3.1. Loci identified as rRNA, tRNA and degraded mRNA, as well as loci identified as near miRNA by ShortStack (Axtell, 2013) were excluded from the analysis. Subsequently, DE sRNAs were identified between the salt-treated or untreated *Mpdc^{pe}* lines and their respective WT control using DeSeq2 applying the $\log_2(\text{FC}) \geq \pm 1$ with a Benjamini-Hochberg corrected p-value of 0.05 as limiting parameters. Using this method, 927 DE sRNA loci in *Mpdc1a-6^{ge}*, 217 in *Mpdc1b-6^{ge}*, 623 in *Mpdc3-6^{ge}* and 423 in *Mpdc4-1^{ge}* (Figure 11A, Supplementary Table 4) were identified. The four generated *Mpdc^{pe}* lines show a slight overlap in their DE sRNA loci between each other, with 21,3% (184 DE sRNA loci) of the overlap occurring between *Mpdc3-6^{ge}* and *Mpdc4-1^{ge}* (Figure 11A, Supplementary Tables 4 and 5). Interestingly, the analysis of sRNA loci that are DE in the *Mpdc1b-6^{ge}* and WT when cultivated in a high salinity environment showed barely any overlap between these two genotypes. When compared to their respective untreated control group, the number of DE sRNA loci in the salt-treated WT is considerably larger than in *Mpdc1b-6^{ge}*, with 177 loci in the WT compared to only 15 in *Mpdc1b-6^{ge}* (Supplementary Tables 4 and 5). Furthermore, when the salt-treated *Mpdc1b-6^{ge}* is compared with the salt-treated WT, then 514 sRNA loci are DE, indicating that in terms of their sRNA expression, these two lines show a drastically different response to cultivation in a high salinity environment (Figure 11B, Supplementary Tables 4 and 5).

When only the mature miRNAs were analyzed, 59 DE miRNAs in *Mpdc1a-6^{ge}*, 19 in *Mpdc1b-6^{ge}*, 26 in *Mpdc3-6^{ge}* and 17 in *Mpdc4-1^{ge}* were detected. *Mpdc1a-6^{ge}* showed the highest number of DE mature miRNAs and a significantly greater number of miRNAs that did not overlap with the DE miRNAs of the other three *Mpdc^{pe}* mutants (Figure 11C, Supplementary Tables 6 and 7). Among the known conserved miRNAs in *M. polymorpha* (Tsuzuki et al., 2016), I observed a downregulation of miR166a (mpo-b3.0r1-16303), miR166b (mpo-b3.0r1-4561) and miR536 (mpo-b3.0r1-4273) precursors as well as a downregulation of the mature miR1030

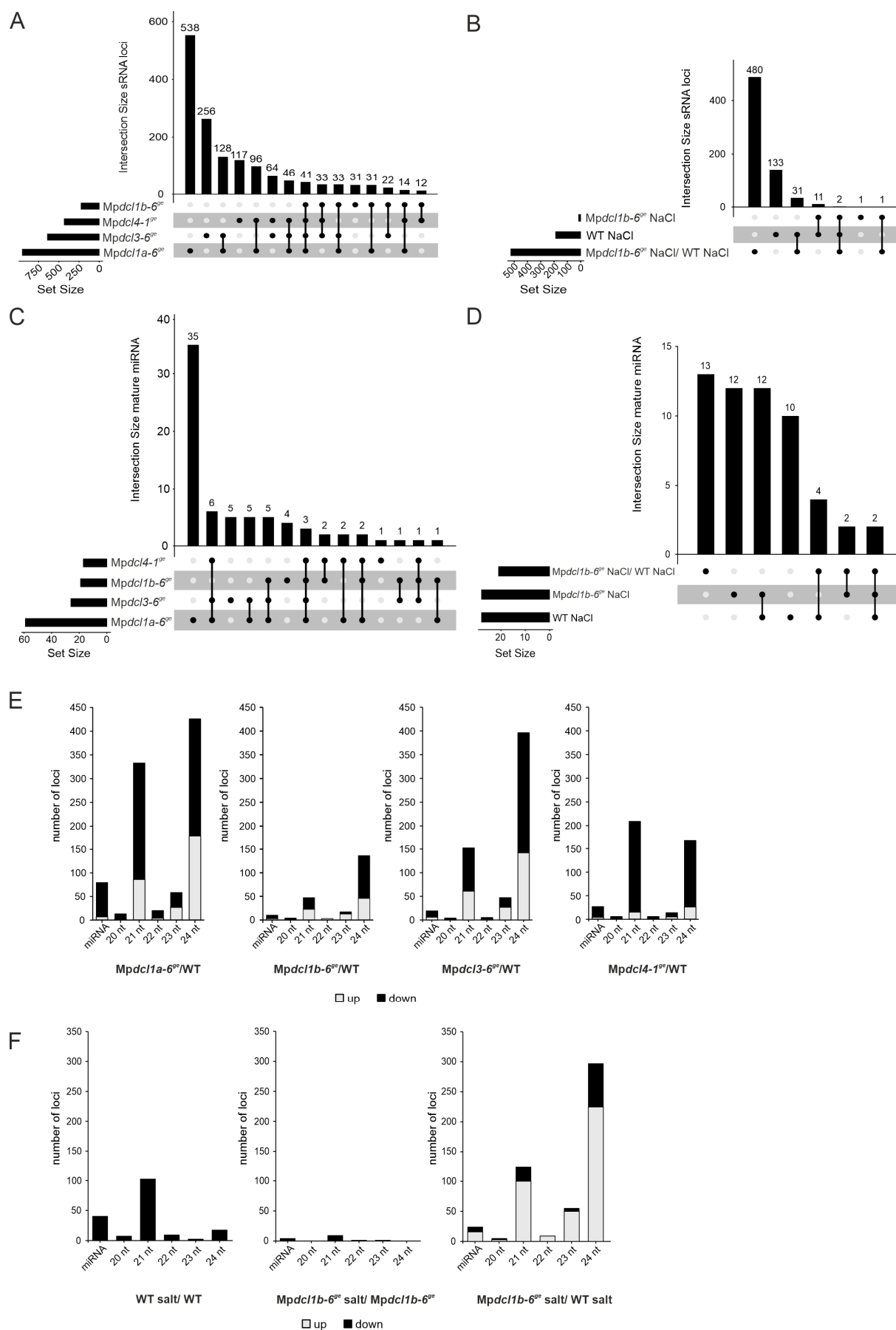


Figure 11: Expression analysis of miRNAs and sRNAs in mutant *Mpdcl^{oe}* lines grown under standard and salt stress conditions

(A) UpSet plot of differentially expressed (DE) sRNA precursors (Benjamini-Hochberg adjusted p-value < 0.05, $\log_2(\text{Fold change}) < \pm 1$) in *Mpdcl1a-6^{ge}*, *Mpdcl1b-6^{ge}*, *Mpdcl3-6^{ge}* and *Mpdcl4-1^{ge}* compared to the wild type (WT) when cultivated for two weeks under standard conditions. (B) DE sRNA precursors of WT and *Mpdcl1b-6^{ge}* when grown for two weeks on standard medium supplemented with 100 mM NaCl. (C) Expression of DE mature miRNAs depicted in an UpSet plot for *Mpdcl1a-6^{ge}*, *Mpdcl1b-6^{ge}*, *Mpdcl3-6^{ge}* and *Mpdcl4-1^{ge}* compared to the wild type (WT) when cultivated for two weeks on standard medium and (D) in WT and *Mpdcl1b-6^{ge}* when cultivated on 100 mM NaCl under control conditions. (E) Number of DE sRNA loci split according to their size distribution (miRNA, 20-24 nt sRNAs) of *Mpdcl1a-6^{ge}*, *Mpdcl1b-6^{ge}*, *Mpdcl3-6^{ge}* and *Mpdcl4-1^{ge}* compared to the wild type (WT) when cultivated for two weeks on standard medium and (F) WT and *Mpdcl1b-6^{ge}* when cultivated on salt. In (E) and (F): Upregulated sRNAs are depicted in grey and downregulated sRNAs in black.

(mpo-b3.0r1-10150) and upregulation of miR390 (mpo-b3.0r1-12192) in the *Mpdcl1a-6^{ge}* mutant line (Supplementary Tables 4 and 6). In contrast, none of the conserved miRNAs were DE in the *Mpdcl1b-6^{ge}* or the *Mpdcl3-6^{ge}* mutant line while in *Mpdcl4-1^{ge}* only the miR529c (mpo-b3.0r1-2332) precursor was downregulated. This further supports the idea that MpDCL1a is the major contributor to miRNA biogenesis. Furthermore, miRNAs appear to play a significant role in gene regulation during salt stress in *M. polymorpha* since 177 miRNA precursors and 28 mature miRNAs were DE in WT upon salt treatment (Figures 6B and 6D, Supplementary Tables 5 and 7). Among these, a downregulation of miR160 (mpo-b3.0r1-941) precursor, mature miR536 and an upregulation of mature miR408 (mpo-b3.0r1-15745) in response to salt treatment was detected. Interestingly, 28 mature miRNAs were also DE in the salt-treated *Mpdcl1b-6^{ge}* when compared to their expression under standard conditions. However, only 33.3 % of these 28 DE miRNAs overlap with the DE miRNAs of the salt-treated WT. Notably, miR536 is the only conserved mature miRNA that remains downregulated in the salt-treated *Mpdcl1b-6^{ge}* while miR160 precursor and mature miR408 are no longer DE in response to salt treatment in this line (Figure 11D, Supplementary Tables 4, 6 and 7). An additional 21 mature miRNAs are DE in the salt-treated *Mpdcl1b-6^{ge}* compared to the salt-treated WT. Consequently, this suggests that both MpDCL1a and MpDCL1b contribute to the salt stress response in *M. polymorpha*, with MpDCL1b influencing miRNA expression during salt treatment.

3.1.7 sRNA size composition reveals distinct roles of MpDCLs on sRNA biogenesis

It was previously shown that the majority of sRNAs in *M. polymorpha* are 21 nt long, followed by the 22 and, at last, 24 nt sRNA populations (Lin et al., 2016; Tsuzuki et al., 2016). In *Mpdcl1a-6^{ge}* an increase in DE miRNAs, 21 nt sRNAs and 24 nt sRNAs was detected. While *Mpdcl1a-6^{ge}* exhibited the most significant changes in miRNA and 21 nt sRNA expression, both *Mpdcl3-6^{ge}* and *Mpdcl4-1^{ge}* also displayed changes in their 21 nt and 24 nt sRNA populations. These changes were more pronounced in *Mpdcl3-6^{ge}* than in *Mpdcl4-1^{ge}*. In *Mpdcl3-6^{ge}*, the number of DE 24 nt sRNAs was significantly higher than that of the detected DE 21 nt sRNAs, whereas in *Mpdcl4-1^{ge}* more 21 nt sRNAs were DE than 24 nt sRNAs. *Mpdcl4-1^{ge}* also exhibited a noticeably higher ratio of downregulated sRNAs in all populations compared to its counterparts in the other three *Mpdcl^{ge}* mutants. In contrast, only a small proportion of the 21

nt population in *Mpdcl1b-6^{ge}* was DE and most DE sRNAs belonged to the 24 nt population (Figure 11E, Supplementary Tables 4 and 8). Among all sRNA populations in *M. polymorpha*, the 20 and 22 nt sRNA populations appear to be the least affected by the mutation and knockout of the respective MpDCL, while significant changes were detected in the 21 nt and 24 nt populations of all *Mpdcl^{ge}* mutants. Interestingly, none of the analyzed *Mpdcl^{ge}* mutants exhibited a significant change in the expression of 22 nt sRNAs, whereas all of them displayed changes in terms of 24 nt sRNA accumulation. In *P. patens*, the accumulation of 22-24 nt sRNAs is dependent on PpDCL3 (Cho et al., 2008). While a change in the expression of 24 nt sRNA in *Mpdcl3-6^{ge}* could be detected, their expression was not completely abolished. Furthermore, a significant number of downregulated 24 nt sRNAs in *Mpdcl4-1^{ge}* and *Mpdcl1a-6^{ge}* were also detected. However, the change in 24 nt sRNA expression, as well as the increase DE 21 nt sRNAs in *Mpdcl1a-6^{ge}*, is possibly a secondary effect due to faulty processing of pri-miRNAs due to misfolded MpDCL1a protein.

In the salt-treated WT, the miRNA and 21 nt sRNA populations are the most altered ones. All detected DE 21 nt sRNAs are downregulated in the WT in response to salt treatment. In contrast, the salt-treated *Mpdcl1b-6^{ge}* shows no significant DE sRNA populations compared to growth under standard conditions. This leads to a drastic change in sRNA populations in salt-treated *Mpdcl1b-6^{ge}* compared to the salt-treated WT, as an increase in DE 21, 23 and 24 nt sRNA populations could be detected. These DE sRNA populations have a higher ratio of upregulated sRNAs to downregulated sRNAs (Figure 11F, Supplementary Table 8), indicating that the *Mpdcl1b^{ge}* lines are salt-hyposensitive. The sRNA composition of *Mpdcl1b^{ge}* barely changes in response to the salt treatment, and it might be this salt insensitivity that results in increased salt tolerance in these lines.

3.1.8 *Mpdcl^{ge}* lines display distinct differences in mRNA expression leading to altered plant growth

To identify differentially regulated genes and putative miRNA target genes that might explain the altered phenotype of the generated *Mpdcl^{ge}* lines, mRNA sequencing was performed. I sequenced triplicates of the WT and all *Mpdcl^{ge}* mutants, as well as salt-treated WT and *Mpdcl1b-6^{ge}* lines grown under the same conditions as the plants used to generate sRNA libraries. Sequencing of these mRNA libraries yielded at least 30 million reads per replicate. After mapping the reads to a *M. polymorpha* reference genome, DeSeq2 was used to identify DEG compared to the respective WT controls (Love et al., 2014). Transcripts were identified as DE when $\log_2(\text{FC}) \leq -1$ and $\geq +1$, Benjamini-Hochberg adjusted *p*-value with $\text{FDR} \leq 0.05$. Out of all generated *Mpdcl^{ge}* lines, *Mpdcl1a-6^{ge}* showed the highest deviation in gene expression, with 1262 DEG, from which 998 do not overlap with any of the other *Mpdcl^{ge}* mutants. This further indicates that MpDCL1a is a crucial component for miRNA biogenesis in

M. polymorpha. I also identified 415 and 357 DEG for *Mpdc13-6^{ge}* and *Mpdc14-1^{ge}*, respectively, with an overlap of 142 DEG (22.5 %) between these two mutant lines. In the *Mpdc11b-6^{ge}* line 157 genes are DE and 35 of these are only DE in this *Mpdc^{ge}* mutant (Figure 12A, Supplementary Table 9 with heatmaps of shared DEG included). After salt treatment, 83 genes are DE in the *Mpdc11b-6^{ge}* mutant compared to the untreated line, while 856 DEG could be identified in the WT upon salt treatment, supporting the hypothesis that the *Mpdc11b^{ge}* lines are salt hyposensitive. It is also interesting that none of the 22 shared DEG between the salt-treated WT and salt-treated *Mpdc11b-6^{ge}* is anticorrelated in these two genotypes. However, all these DEG are less responsive in the *Mpdc11b-6^{ge}* (Figure 12B, Supplementary Table 9 with heatmaps of shared DEG included). Comparison between the 856 DEG in the salt-treated WT and the 157 DEG of the untreated *Mpdc11b^{ge}* revealed an overlap of 59 genes. Interestingly, out of these, 44 are not annotated and might be potential candidates for further study of the salt stress response in bryophytes (Supplementary Table 9).

To gain an overview of the affected physiological components and processes, a gene ontology (GO) enrichment analysis of the detected DEG was performed using AgriGO v2.0 (Tian et al., 2017). GO terms with an FDR value ≤ 0.05 were designated as significantly enriched and categorized them into biological process, cellular components and molecular function (Figure 12C, Supplementary Table 10). Among all analyzed mutant lines, DEG in the *Mpdc11a-6^{ge}* line contained the highest number of GO terms. In *Mpdc11a-6^{ge}*, the biological processes response to stress (69), response to oxidative stress (57) and oxidation-reduction (125) were primarily affected by the mutation. Meanwhile, the significant affected molecular functions included antioxidant activity (57), peroxidase activity (57), oxidoreductase activity (131), catalytic activity (317), tetrapyrrole (82) and heme binding (82) (Figure 12C, Supplementary Table 10). *Mpdc11b-6^{ge}* displayed a significant enrichment of cellular components, including cytoskeleton (6), cytoskeleton parts (6), microtubule cytoskeleton (6), organelle parts (8) and intracellular organelle parts (8). Interestingly, *Mpdc11b-6^{ge}* does not share any significantly enriched GO terms with any of the other *Mpdc^{ge}* mutants, suggesting that MpDCL1b is the only DCL modulating these cellular components and may also fulfill a distinct function (Figure 12C, Supplementary Table 10). In the salt-treated *Mpdc11b-6^{ge}*, no significantly enriched GO terms were detected, while the salt-treated WT showed a significant enrichment of the following GO terms: single-organism metabolic process (128), oxidation-reduction process (90), response to stimulus (68), response to stress (64), response to oxidative stress (50), antioxidant activity (51), oxidoreductase activity (92), peroxidase activity (50), catalytic activity (201), tetrapyrrole (57) and heme binding (57) (Supplementary Table 10). Interestingly, some of these GO terms partially overlap with those enriched in the *Mpdc11a-6^{ge}* mutant, suggesting an involvement of MpDCL1a in the salt stress response of *M. polymorpha*. The overlapping significant GO terms between *Mpdc13-6^{ge}* and *Mpdc14-1^{ge}* suggest potential redundancy in the functions of these

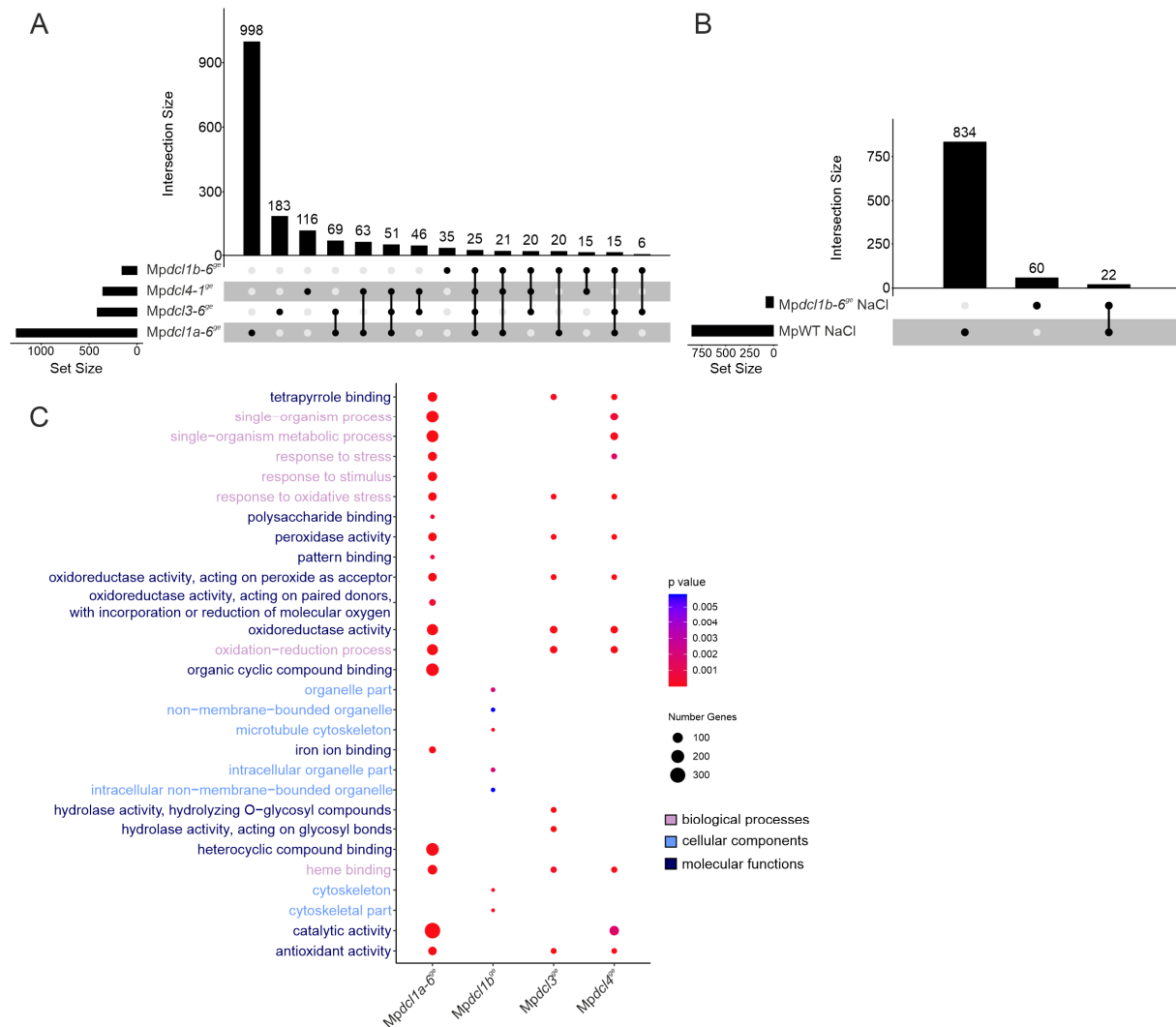


Figure 12: Expression of protein-coding transcripts in the *Mpdcl9e* mutant lines when grown under standard and salt stress conditions

(A) UpSet plot depicting differentially expressed genes (DEG) in *Mpdcl1a-6^{ge}*, *Mpdcl1b-6^{ge}*, *Mpdcl3-6^{ge}* and *Mpdcl4-1^{ge}* compared to the wild type (WT) when cultivated for two weeks on standard medium and **(B)** in WT and *Mpdcl1b-6^{ge}* when cultivated for two weeks on standard medium supplemented with 100 mM NaCl (FDR < 0.05, log₂(Fold change) < ± 1) **(C)** Gene ontology analysis (GO) of all significantly enriched (default settings, Yekutieli FDR ≤ 0.05) GO terms for all DEG in *Mpdcl1a-6^{ge}*, *Mpdcl1b-6^{ge}*, *Mpdcl3-6^{ge}* and *Mpdcl4-1^{ge}* compared to the wild type (WT) when cultivated for two weeks on standard medium. Dot size represents the number of enriched genes of the respective GO term and the color the Fishers test p-value ≤ 0.05. Categorical separation of GO terms into biological processes, cellular components and molecular functions is color-coded.

two MpDCLs. In both *Mpdcl3-6^{ge}* and *Mpdcl4-1^{ge}*, the following processes are affected: oxidation-reduction process (37/35), response to oxidative stress (15/15), antioxidant activity (16/14), oxidoreductase activity (39/37), tetrapyrrole binding (20/19) and heme binding (20/19). While hydrolase activity acting on glycosyl bonds (18) and hydrolyzing O-glycosyl compounds (16) are affected in *Mpdcl3-6^{ge}* but not in *Mpdcl4-1^{ge}*, catalytic activity (80) is influenced by the loss of *MpDCL4*. Furthermore, *Mpdcl4-1^{ge}* exhibits DEG related to single organism processes (49), single organism metabolic processes (43) and the response to stress (16) (Figure 12C, Supplementary Table 10).

To examine the influence of the MpDCLs on phytohormone-regulated signaling pathways, I checked the expression of auxin, ABA, cytokinin and ethylene-related genes in *M. polymorpha* for differential expression in all *Mpdc^{pe}* mutants under control conditions. In *Mpdc1a-6^{ge}*, the auxin-related genes including *MpTAA* (*Mp5g14320*), *SHORT INTERNODES* (*MpSHI*) (*Mp3g19510*), *GRETCHEN HAGEN 3B* (*MpGH3B*) (*Mp2g14010*), *ATP-BINDING CASSETTE B1* (*MpABCB1*) (*Mp2g02920*), *SMALL AUXIN UPREGULATED 8* (*MpSAUR8*) (*Mp1g27980*), *IAA CARBOXYLMETHYLTRANSFERASE 1* (*MpIAMT1*) (*Mp7g11980*) and *S-PHASE KINASE-ASSOCIATED PROTEIN 2A* (*MpSKP2A*) (*Mp8g10660*) are DE, revealing that altered sRNA expression in *Mpdc1a-6^{ge}* influences auxin signaling and homeostasis. These alterations most likely contribute to the observed phenotype of this line (Eklund et al., 2015; Flores-Sandoval et al., 2015; Eklund et al., 2018; Flores-Sandoval et al., 2018a). Furthermore, the *CYTOKININ OXIDASE 1* (*MpCKX1*) (*Mp5g03090*), the ethylene-responsive MAP-kinase *CONSTITUTIVE TRIPLE RESPONSE 1* (*MpCTR1*) (*Mp8g15840*) and the ethylene-responsive AP2/ERF transcription factor *MpERF15* (*Mp7g09350*) and *MpERF7* (*Mp6g04880*) were all downregulated in *Mpdc1a-6^{ge}* (Table 4, Supplementary Table 9 with heatmaps of shared DEG included).

However, *MpTAA* and *MpCKX1* are the only phytohormone-related genes that are upregulated in *Mpdc13-6^{ge}* and *Mpdc14-1^{ge}*, respectively (Table 6). Similarly, no phytohormone-related DEG, except slight upregulation of *MpCKX1*, were identified in *Mpdc1b-6^{ge}* (Table 5), further indicating that MpDCL1a, through associated sRNAs, is a major modulator of gemmae development and phytohormone-regulated cell differentiation.

An analysis of transcription factors in *Mpdc1a-6^{ge}* revealed a downregulation of the auxin-responsive *CLASS II HOMEODOMAIN-LEUCINE ZIPPER* (*MpC2HDZ*) (*Mp2g24200*), *GLUTAMIC ACID-RICH-PROTEIN 2* (*MpGARP2*) (*Mp4g08700*), while *FEMALE GAMETOPHYTE-SPECIFIC MYB* (*MpFGMYB/ MpR2R3-MYB1*) (*Mp1g17210*), NAC transcription factor *MpNAC8* (*Mp6g02670*) and the basic helix–loop–helix transcription factor *MpbHLH37* (*Mp2g04200*) were all upregulated. In both *Mpdc13-6^{ge}* and *Mpdc14-1^{ge}*, the *MpR2R3-MYB5* (*Mp8g11870*) transcription factor was downregulated, while in *Mpdc14-1^{ge}*, the expression of another AP2/ERF transcription factor (*MpERF18*, *Mp5g12480*) was increased (Table 4, Supplementary Table 9 with heatmaps of shared DEG included). High salinity is one of the most severe abiotic stresses that induces global transcriptomic changes and adversely affects plant growth and development (Golldack et al., 2011; Fu et al., 2017; Tanaka et al., 2018). For example, transcription factors of the MYB, bHLH and bZIP families are DE upon salt treatment in *A. thaliana* (Golldack et al., 2011) and *M. polymorpha* (Tanaka et al., 2018). Due to the overlap of significantly enriched GO terms between the salt-treated WT and *Mpdc1a-6^{ge}*, the expression of previously reported transcription factors (Tanaka et al., 2018)

was also checked. Among these transcription factors, 23 were also DE in *Mpdcl1a-6^{ge}* when cultivated under standard conditions and belonged to the MYB, WRKY, bHLH, ERF/AP2 and ASLBD transcription factor families (Table 4).

To validate the generated mRNA sequencing data, I measured the transcript levels of genes encoding the transcription factors *MpERF7*, *MpGARP2*, *MpNAC8*, as well as the *CATALASE 4* (*MpCAT4*) (*Mp5g07320*) and *Mp3g25440*, a gene of unknown function, in *Mpdcl1a-6^{ge}* by qRT-PCR (Supplementary Table 11). The detected expression levels confirmed the reliability and validity of the generated sequencing data.

While phytohormone signaling and gene expression regulation were only significantly affected in *Mpdcl1a-6^{ge}*, the expression of multiple protein kinase families was affected in all *Mpdcl^{ge}* mutant lines as well as in salt-treated *Mpdcl1b-6^{ge}* and WT. These kinases included Receptor-Like-Kinase/*Pelle* (RLK/*Pelle*) protein kinases, MAPK and cyclin-dependent kinases. Fourteen of these kinases were DE in *Mpdcl1a-6^{ge}*, four in *Mpdcl1b-6^{ge}* and *Mpdcl3-6^{ge}* and five in *Mpdcl4-1^{ge}* (Tables 4, 5 and 6). Upon salt treatment seven were DE in the WT and only two in *Mpdcl1b-6^{ge}*. Interestingly, the cyclin kinases *MpCYCA* (*Mp2g25500*), *MpCYCB_1* (*Mp5g10030*) and CELL DIVISION CYCLE 25 (*MpCDC25_1*; *Mp4g01900*) were all upregulated in *Mpdcl1b-6^{ge}*, only *MpCYCB_1* showed a significant repression in response to salt treatment (Table 5). Since cyclin kinases regulate cell cycle progression and have been shown to be suppressed in response to salt treatment (Kitsios and Doonan, 2011; Qi and Zhang, 2019), the overexpression of these kinases, as well as the unchanged expression of RLK/*Pelle* kinases that are suppressed in the salt-treated WT, might contribute to the increased salt tolerance of *Mpdcl1b-6^{ge}*. Additionally, this analysis identified *Mp3g16740*, a leucine-rich protein kinase and the *RGF insensitive-like* (*MpRGI-like*) (*Mp1g04830*) leucine-rich repeat (LRR) protein kinase as putative miR390 targets (Table 5, Supplementary Tables 12 and 13). Both kinases show decreased expression levels in correlation with an increased miR390 level. Leucine-rich protein kinases in plants contribute to the regulation of cell proliferation, hormone perception, stem cell maintenance and more.

A noticeable difference between the analyzed genotypes pertains to genes involved in the pathogen response of *M. polymorpha*. The class of *PATHOGENESIS RELATED PROTEIN 1* (*PR-1*), which belongs to the CAP protein superfamily, plays an essential role in plant defense against pathogens (Backer et al., 2019). Overexpression of *PR-1* genes has been shown to enhance pathogen resistance in plants (Han et al., 2023). In *Mpdcl3-6^{ge}* seven *MpPR-1* genes were upregulated, while one *MpPR-1* gene was downregulated (Table 6, Supplementary Table 9 with heatmaps of shared DEG included). Interestingly, none of the other *Mpdcl^{ge}* displayed such a significant alteration in the expression of *MpPR-1* genes. *Mpdcl3-6^{ge}* also showed downregulation of five DIRIGENT (*MpDIR*), 16 DE PEROXYGENASE (*MpPOD*) and three DE

LIPOXYGENASE (MpLOX) genes (Table 6, Supplementary Table 9). These gene families are induced during the pathogen response of plants and are part of the dnOPDA-guided pathogen response in *M. polymorpha* (Blée, 2002; Jaiti et al., 2009; Paniagua et al., 2017; Li et al., 2022a). Furthermore, their general downregulation indicates a potential suppression due to a putative increased activity of SA since SA can act antagonistic to dnOPDA (Gimenez-Ibanez et al., 2019; Matsui et al., 2020; Li et al., 2022a). Interestingly, 14 MpPOD in *Mpdcl4-1^{ge}* were DE as well. In contrast to *Mpdcl3-6^{ge}*, in which the majority (12) of DE MpPOD were downregulated, in *Mpdcl4-1^{ge}* 12 of their DE MpPOD showed increased expression (Table 6).

3.1.9 DEG is a direct consequence of the altered sRNA biogenesis of all mutant lines

To prove that the differential gene expression in the *Mpdcl1a-6^{ge}* mutant is the result of altered miRNA expression, the psRNATarget was used to determine the putative targets of DEG miRNAs. This approach identified 344 potential targets in *Mpdcl1a-6^{ge}*, from which 157 showed an anticorrelated expression to their cognate mature miRNA (Supplementary Tables 12 and 13). Additional analysis of the salt-treated WT revealed that 51 of the 95 putative targets DE in response to high salinity were also anticorrelated to their associated miRNAs. Analysis of DE sRNAs and their putative targets revealed similar results. 4805 potential sRNA:mRNA modules were detected in *Mpdcl1a-6^{ge}*, 150 in *Mpdcl1b-6^{ge}*, 963 in *Mpdcl3-6^{ge}* and 156 in *Mpdcl4-1^{ge}*. In the salt-treated *Mpdcl1b-6^{ge}*, only 6 such modules were DE, while in the salt-treated WT, 547 sRNA:mRNA modules were DE compared to their respective control, resulting in 734 DE modules between these two lines when salt-treated (Supplementary Table 14). Out of the detected DE miRNA:mRNA modules in *Mpdcl1a-6^{ge}* MpFGMYB, MpERF7, MpGARP2, MpR2R3-MYB8 (*Mp3g23170*), MpbHLH37 (*Mp2g04200*), MpERF15 and MpC2HDZ were all anticorrelated with respect to their cognate miRNAs (Table 4, Supplementary Tables 12 and 13). MiRNAs putatively targeting MpFGMYB were mpo-b3.0r1-10692 and mpo-MIR11802 (mpo-b3.0r1-3564), from which mpo-MIR11802 was downregulated. MpFGMYB is crucial during the development of sexual dimorphism, as knockout of this transcription factor leads to female plants developing antheridiophores (Hisanaga et al., 2019; Cui et al., 2023). Typically, this transcription factor remains undetectable in the apical notch of mature thalli before induction by far-red light (Cui et al., 2023). However, the mature thalli of *Mpdcl1a-6^{ge}* displayed an upregulation of MpFGMYB (Table 4, Supplementary Table 9 with heatmaps of shared DEG included). This ectopic expression of the transcription factor, potentially regulated by mpo-MIR11802, could be a contributing factor to the observed phenotype in *Mpdcl1a-6^{ge}*. The miRNAs that putatively mediate the downregulation of MpC2HDZ are mpo-MIR11741 (mpo-b3.0r1-4187), mpo-MIR11768a (mpo-b3.0r1-17058) and mpo-b3.0r1-2510, respectively, from which only mpo-MIR11768a is upregulated. The MpC2HDZ transcription factor has been reported to be upregulated by auxin (Mutte et al., 2018) and to be co-expressed with other auxin-regulated genes in *M. polymorpha* (Flores-Sandoval et al., 2018b). Its potential miRNA-

related suppression might correlate to the detected increased salt tolerance of this line, as HD-ZIP proteins have been reported to be DE in response to salt stress (Romani et al., 2016; Li et al., 2022c). Furthermore, 12 DE *ATP-BINDING CASSETTE TRANSPORTERS* (MpABCG) transporters could be identified in *Mpdcl1a-6^{ge}*, five of which are putatively regulated by miRNAs (Table 4). ABCG transporters have been shown to play a role in intracellular ABA signaling, as *AtABCG25* exports and *AtABCG40* imports ABA across cell membranes (Kuromori and Shinozaki, 2010). The DE of these transporters in *Mpdcl1a-6^{ge}* most likely contributes to the altered ABA sensitivity in this line. A closer look at other putative miRNA:mRNA targets also showed potential regulation of *Mp6g16160*, *Mp1g06050*, *Mp4g16040* and the late embryogenesis abundant (LEA) protein *MpLEA-like18* (Mp4g05730) by miR1030 in *Mpdcl1a-6^{ge}* (Table 4, Supplementary Tables 12 and 13). LEA-like proteins accumulate in both *P. patens* and *M. polymorpha* in response to cold and desiccation stress, as well as exogenous ABA treatment (Bhyan et al., 2012; Jahan et al., 2019). In *Mpdcl1a-6^{ge}*, the expression of *MpLEA-like18* increased due to the low levels of miR1030. The ectopic accumulation of MpLEA-like proteins might be favorable for *Mpdcl1a-6^{ge}* during the salt stress response and contribute to its slightly increased salt tolerance and observed ABA sensitivity. Interestingly, suppression of *MpLEA-like46* and *MpLEA-like48* in *Mpdcl4^{ge}* might also influence the salt tolerance of this line.

This potential role of MpDCL1a in the salt stress response further enhances the involvement of MpDCL1b. Examination of mRNA and miRNA expression in the *Mpdcl1b-6^{ge}* line revealed that only nine mRNAs showed anticorrelation with their targeting miRNAs upon salt treatment. Thus, the salt-treated plants did not experience major alterations in their transcriptome compared to plants grown under standard conditions. Since MpDCL1a is responsible for miRNA biogenesis, this suggests either a supporting role of MpDCL1b during miRNA processing that is crucial during prolonged salt stress response, or that the few miRNAs and sRNAs that are already DE in *Mpdcl1b-6^{ge}* are major contributors of salt stress adaptation in *M. polymorpha*.

3.1.10 Examination of ta-siRNA biogenesis

With increasing miR390 levels, the *MpTAS3* (scaffold_154:327227-327462) expression in *Mpdcl1a-6^{ge}* (Supplementary Table 6) increased as well. This *TAS3* encoding locus was proposed as origin of 21 nt long ta-siRNA in *M. polymorpha* by Tsuzuki et al. (2016). Since the *MpTAS3* precursor harbors confirmed miR390 binding sites elevated miR390 levels most likely lead to enhanced *TAS3* processing and a subsequent increase in the amount of ta-siRNAs in *Mpdcl1a-6^{ge}*. As *MpTAS3* contains a ta-siAP2 site (Krasnikova et al., 2013; Tsuzuki et al., 2016) the downregulation of target mRNAs encoding AP2/ERF transcription factors might be due to the upregulation of ta-siRNAs in *Mpdcl1a-6^{ge}*. Interestingly, a drastic decrease in

MpTAS3 transcript in *Mpdc14-1^{ge}* was detected. In *P. patens* the TAS3 precursor is cleaved by miR390 and subsequently processed by PpRDR6 and PpDCL4 into phasing ta-siRNAs (Arif et al., 2012; Arif et al., 2013). Coupled with the pronounced decrease in 21 nt sRNAs in *Mpdc14-1^{ge}*, I propose that MpDCL4 is also responsible for the ta-siRNA biogenesis in *M. polymorpha*. Interestingly, the loss of PpDCL4 leads to severe phenotypical defects due to an accumulation of 22-24 nt sRNAs, as PpDCL3 compensates for this loss by processing the TAS3 precursor, leading to altered size and function of the resulting siRNAs (Arif et al., 2012). Even though the high overlap of DEG mRNA and similarity in GO enrichment analysis in the *Mpdc13-6^{ge}* and *Mpdc14-1^{ge}* lines indicate a similar functional redundancy for both DCLs, a loss of MpDCL4 neither leads to a significant increase in 22-24 nt sRNAs nor to a significantly altered phenotype, with the exception of the inability to develop gametangiophores.

3.2 Results Question 2 - Does the Band-7 protein FLOT modulate stress tolerance in *P. patens*? How is the expression of *PpFLOT* regulated? Are there differences in the function of bryophyte and seed plant FLOT?

3.2.1 Single FLOT variant in *P. patens* is localized in chloroplasts

Even though all SPFH-proteins are associated with cell membranes, their association is notably specific and determined by the N-terminus region of the protein. The N-terminal of SPFH-proteins, housing transmembrane domains or hydrophobic regions in conjunction with the Band-7 protein domain, facilitates interaction with cell membranes (Rivera-Milla et al., 2006; Browman et al., 2007; Daněk et al., 2016). Previous studies in human cells have demonstrated that the membrane association of FLOT is determined by its N-terminal region (Daněk et al., 2016). Localization studies in *A. thaliana* identified all three FLOT variants in the plasma membrane of root epidermal cells (Li et al., 2012; Danek et al., 2020) and for AtFLOT1 and AtFLOT2 in epidermal cotyledon cells (Junková et al., 2018; Cao et al., 2020). AtFLOT1 was also detected in the tonoplast of root epidermal cells (Danek et al., 2020), most likely due to its primary role in clathrin-independent endocytosis (Li et al., 2012). To determine the localization of FLOT in *P. patens* I constructed a *PpFLOT* CDS construct with an added citrine tag in-frame by cloning it into an empty ACT5 vector containing the linked citrine sequence (Top et al., 2021). *P. patens* WT protoplasts were transformed with this construct to generate transient *PpFLOT::citrine* lines. Three days after transformation the localization of *PpFLOT::citrine* was traced by confocal microscopy. In contrast to all three FLOT variants in *A. thaliana*, *PpFLOT::citrine* did not localize to the plasma membrane of the protoplast but clearly colocalized with chlorophyll autofluorescence signals in the chloroplasts (Figure 13A). Close-up images further disclosed the accumulation of *PpFLOT::citrine* in thylakoids, suggesting the formation of nanodomains similar to the accumulation of AtFLOTs in plasma membranes.

3.2.2 Analysis of the evolutionary relationship and the domain structure of *PpFLOT*

Phylogenetic analysis of *PpFLOT* was conducted through reciprocal BLAST of full-length peptide sequences from various plant species, *A. officinalis*, *A. thaliana*, *A. filiculoides*, *C. purpureus*, *C. braunii*, *C. subellipsoidea*, *K. nitens*, *M. polymorpha*, *M. truncatula*, *O. sativa*, *P. patens*, *S. cucullata*, *S. polyrhiza*, *Synechocystis* sp. PCC 6803, *Z. mays* and *Z. marina*. Results indicated a high similarity between bryophyte FLOT homologs, with *PpFLOT* showing a closer relationship to homologs in ferns, green algae and cyanobacteria than to seed plant homologs (Figure 13B). Notably, *PpFLOT* homologs in monocotyledons (*O. sativa*, *Z. mays*, *Z. marina* and *A. officinalis*) exhibit higher similarity compared to homologs in dicotyledonous species like *A. thaliana* and *M. truncatula* (Figure 13B). Interestingly, both *O. sativa* and *Z.*

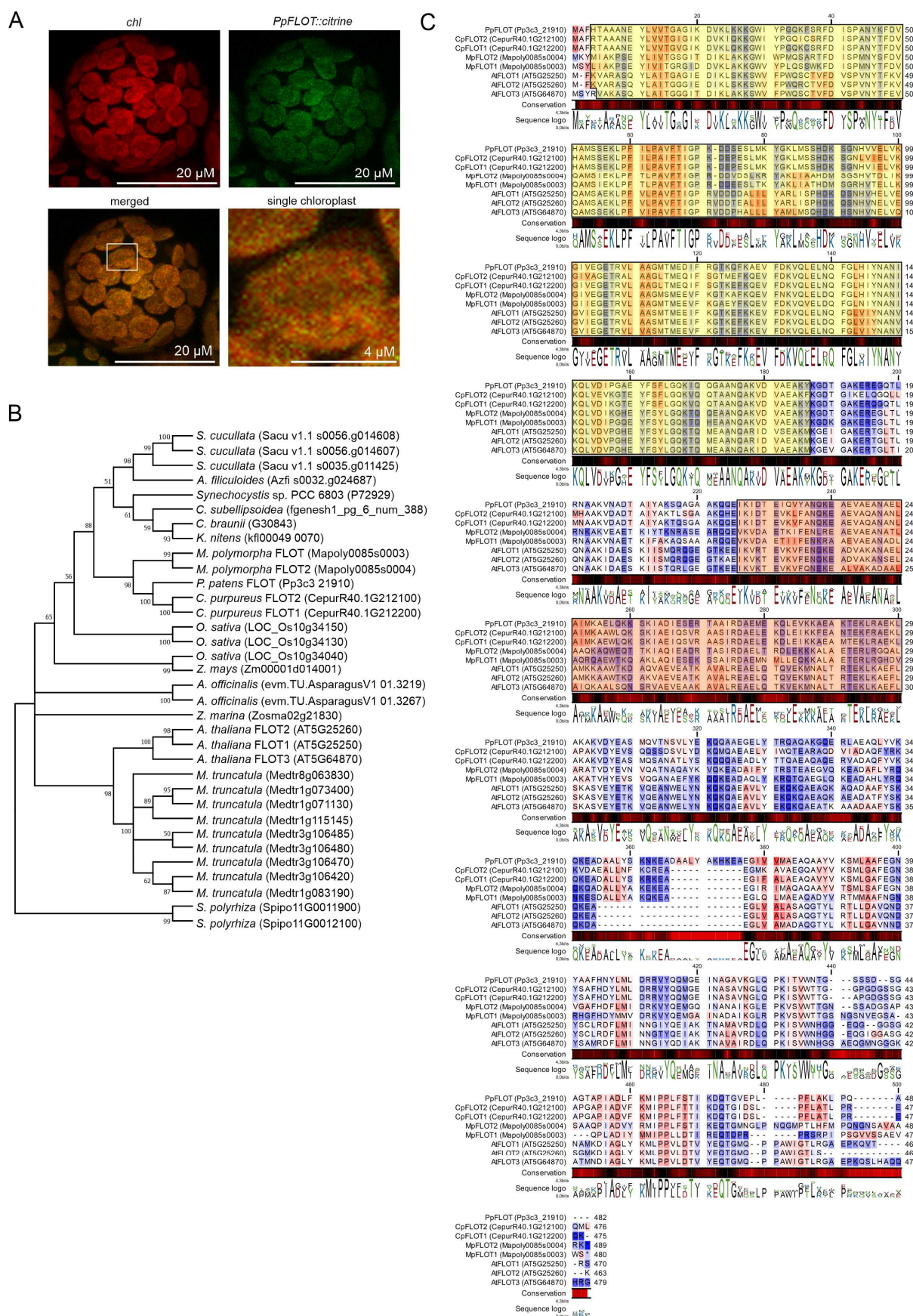


Figure 13: Localization of PpFLOT::citrine and comparison of its peptide sequence to homologs in other plant species

(A) Confocal microscopy images of a *P. patens* protoplast transiently transformed with the *PpFLOT::citrine* construct showing chlorophyll (chl) autofluorescence (red), *PpFLOT::citrine* (green) and a merged (orange) image. A close-up of a single chloroplast of the merged image is also presented. Scale bars are indicated in the respective images. **(B)** Phylogenetic tree generated by MEGA X using the maximum likelihood method, depicting relationships among PpFLOT homologs in various plant species: *Asparagus officinalis*, *A. thaliana*, *A. filiculoides*, *C. purpureus*, *C. braunii*, *C. subellipsoidea*, *K. nitens*, *M. polymorpha*, *M. truncatula*, *O. sativa*, *P. patens*, *S. cucullata*, *S. polyrhiza*, *Synechocystis* sp. PCC 6803, *Z. mays* and *Z. marina*. The alignment was generated with the CLC workbench v20.0.4. Only branches with bootstrap values > 50 are shown. **(C)** Protein sequence alignment of all FLOT variants from *A. thaliana*, *C. purpureus*, *P. patens* and *M. polymorpha* generated by CLC workbench v20.0.4. Sequence conservation is color-coded, from 0 % (red) to 100 % (black) and a sequence logo is provided below the alignment. Protein sequence hydropathicity is marked according to Kyte-Doolittle (Kyte and Doolittle, 1982) from minimal (blue) to maximal (red). SPFH/Band-7 protein domain regions are highlighted in yellow and regions of potential coiled-coil structures are highlighted in orange.

marina, which grow submerged or partially submerged in water, share higher similarity with PpFLOT. Given *P. patens*' ability to be cultivated in submerged conditions, this suggests that PpFLOT's function may have evolved during the water-to-land transition and remains beneficial for plants regularly encountering anoxic environments.

To examine the potential impact of AA sequence variations on the distinct locations of PpFLOT and its *A. thaliana* variants full-length homologs of PpFLOT were identified through reciprocal BLAST searches in *A. thaliana*, *C. purpureus* and *M. polymorpha*. Alignment and analysis using CLC workbench v20.0.4 (Qiagen) revealed minimal changes in the AA sequence, with a generally high conservation among the FLOT variants, except for the last 100 AA at the C-terminus. Additionally, PpFLOT exhibited 22 AA from a repeated DAALY*K*K*KEA motif at positions 354 to 375 (Figure 13C). This conserved motif, also present in related bryophyte species, was absent in all three AtFLOT variants (Figure 13C). These minimal changes within an otherwise conserved sequence support a common origin of FLOT across all plant species. Evolutionary alterations in the FLOT peptide sequence might have occurred in the last common ancestor of bryophytes and tracheophytes, potentially resulting in an altered function of FLOT in bryophytes. The analyzed proteins encode an SPFH/Band-7 protein domain in the N-terminal region, beginning at position three, or position four in AtFLOT3, and ending at position 185/6 (Figure 13C). This region, crucial for membrane association, contains hydrophobic regions, displaying slight changes in hydrophobicity between bryophyte FLOT and the three *A. thaliana* FLOTs (Figure 13C). Another characteristic feature of FLOTs are coiled-coil domains that serve as recognition sites for interaction partners and facilitate oligomerization with themselves or other FLOT variants at the plasma membrane (Rivera-Milla et al., 2006; Frick et al., 2007; Solis et al., 2007; Daněk et al., 2016). Interaction studies with truncated AtFLOT1/3 proteins in yeast demonstrated oligomerization between AtFLOT1 and AtFLOT3 (Yu et al., 2017a). These studies showed that AtFLOT1 aggregated at plasma membranes (Yu et al., 2017a). Further confirmation of the crucial role of coiled-coil regions in oligomerization was provided when truncated AtFLOT1/3 variants lacking these regions (position 201 - 470) (Figure 13C) failed to interact (Yu et al., 2017a). Using the Galaxy-based (ver. 5.0.0.1) (Galaxy

community, 2022) application Pepcoil (Rice et al., 2000; Blankenberg et al., 2007) and the web-based application CoCoNat (Madeo et al., 2023), a search for coiled-coil regions in PpFLOT identified putative structures between positions 226 to 300 (Figure 13C). Given the presence of these structures, it is likely that PpFLOT undergoes homo-oligomerization, leading to the formation of PpFLOT scaffolds in thylakoid membranes, providing anchoring points for protein complex formation and interactions.

3.2.3 Generation of Δ PpFLOT knockout and PpFLOT-OEX lines

To probe the potential role of PpFLOT in *P. patens* development, Δ PpFLOT lines were generated by replacing exon 2 of the PpFLOT CDS with a *nptII* selection cassette via homologous recombination (Figure 14A) (Schaefer, 2001; Frank et al., 2007). Following protoplast transformation with the linearized construct and subsequent selection via G418 sulfate (50 μ g/ml), transformed plants were screened by amplifying the complete genomic

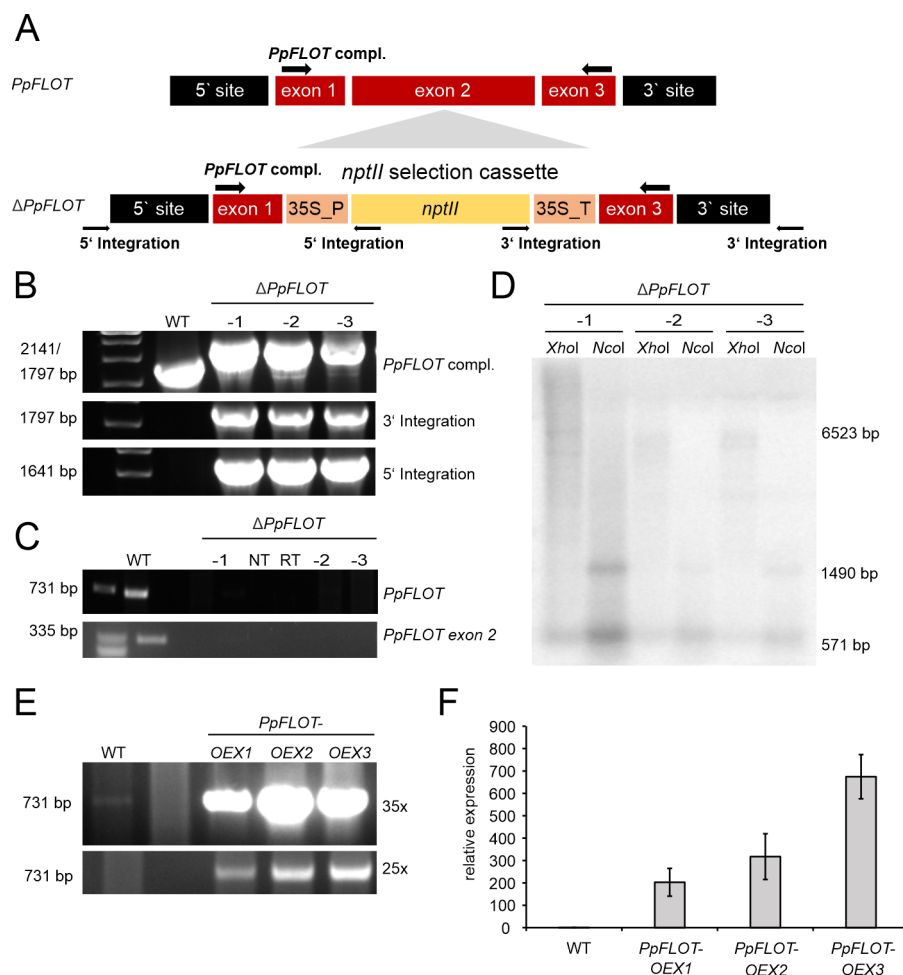


Figure 14: Generation of Δ PpFLOT and PpFLOT-OEX lines

(A) Schematic representation of the transformation construct. The upper panel illustrates the WT *PpFLOT* coding sequence (CDS), while the lower panel displays the construct for Δ PpFLOT generation, involving exon 2 replacement with a *nptII* selection cassette. Arrows indicate primer positions during screening (B) Screening of Δ PpFLOT lines via PCR, amplifying the complete *PpFLOT* sequence and the 5' and 3' integration sites using

genomic DNA **(C)** Transcript analysis of *PpFLOT* by PCR from cDNA, amplifying both the *PpFLOT* transcript sequence and exon 2 sequence. **(D)** Southern blot analysis for all three identified $\Delta PpFLOT$ lines, confirming single construct integration in moss genome. In case of single integration, digestion of total genomic DNA with *XhoI* and detection of the *nptII* selection cassette with a complementary probe results in a band of 6523 bp since *XhoI* does not cut within the selection marker sequence. For better validation, the experiment was repeated with *NcoI*, an enzyme that cuts within the *nptII* selection cassette and produces two bands (1490 bp and 571 bp) upon single integration. **(E)** Confirmation of *PpFLOT*-OEX lines by PCR amplification of *PpFLOT* transcript from cDNA at 35 and 25 cycles, comparing band intensities to WT **(F)** qRT-PCR results of relative *PpFLOT* expression compared to the WT, normalized to *PpEF1 α* expression, following Schmittgen and Livak (2008). Mean values with error bars indicating \pm SEM ($n = 3$) are presented. Oligonucleotide sequences are listed in Supplementary Table 15 and Table 5.

PpFLOT sequence (Figure 14B). Examination of 3' site and 5' site integration of the construct (Figure 14B), along with confirming *PpFLOT* transcript loss (Figure 14C), identified three independent $\Delta PpFLOT$ lines, $\Delta PpFLOT$ -1, $\Delta PpFLOT$ -2 and $\Delta PpFLOT$ -3, with a single integration confirmed by Southern blot analysis (Figure 14D). Given the previous observation of increased *PpFLOT* expression linked to salt sensitivity and ABA hyposensitivity in *P. patens* (Arif et al., 2022), *PpFLOT* overexpression lines were also generated. To generate the *PpFLOT*-OEX lines a construct in which the *PpFLOT* CDS was under the control of an *Act5* promoter was created for constitutive expression and the respective construct also harbored a hygromycin resistance cassette for plant selection. After protoplast transformation, screening and confirmation of construct insertion in the genome, an enhanced expression was confirmed by amplifying the *PpFLOT* transcript from cDNA for 25 and 35 cycles by PCR (Figure 14E). This approach identified three *PpFLOT*-OEX lines, *PpFLOT*-OEX1, *PpFLOT*-OEX2 and *PpFLOT*-OEX3 that showed a relative expression of 202.79 (SEM \pm 62.01), 317.61 (SEM \pm 102.18) and 674.49 (SEM \pm 98.6), respectively, compared to the WT and normalized against the expression of *PpEF1 α* (Figure 14F).

3.2.4 $\Delta PpFLOT$ display enhanced salt tolerance

Liquid cultures of *P. patens* WT and all three generated $\Delta PpFLOT$ lines were grown for 14 d under control conditions and in medium supplemented with 250 mM NaCl. To detect potential changes in the accumulation of biomass and their salt sensitivity every two to three days, the dry weight of the equalized cultures was determined and images of the cultures were taken. Despite reported stunted growth in *AtFLOT1* amiRNA lines (Li et al., 2012), no changes in accumulated biomass over time were observed in the $\Delta PpFLOT$ lines compared to the WT, both under control conditions and in salt-treated cultures (Figure 15A and B). Interestingly, unlike the WT, the $\Delta PpFLOT$ lines did not display bleaching in response to the salt treatment. Bleaching in plant cultures typically results from decreased chlorophyll content (Benavides et al., 2000; Taïbi et al., 2016) to avoid ROS accumulation and oxidative damage (Verma and Mishra, 2005). The apparent lack of chlorophyll suppression in response to salt treatment suggests a potential role for *PpFLOT* in detecting or regulating ROS or in chlorophyll biogenesis regulation, a function that may be impaired in $\Delta PpFLOT$ lines.

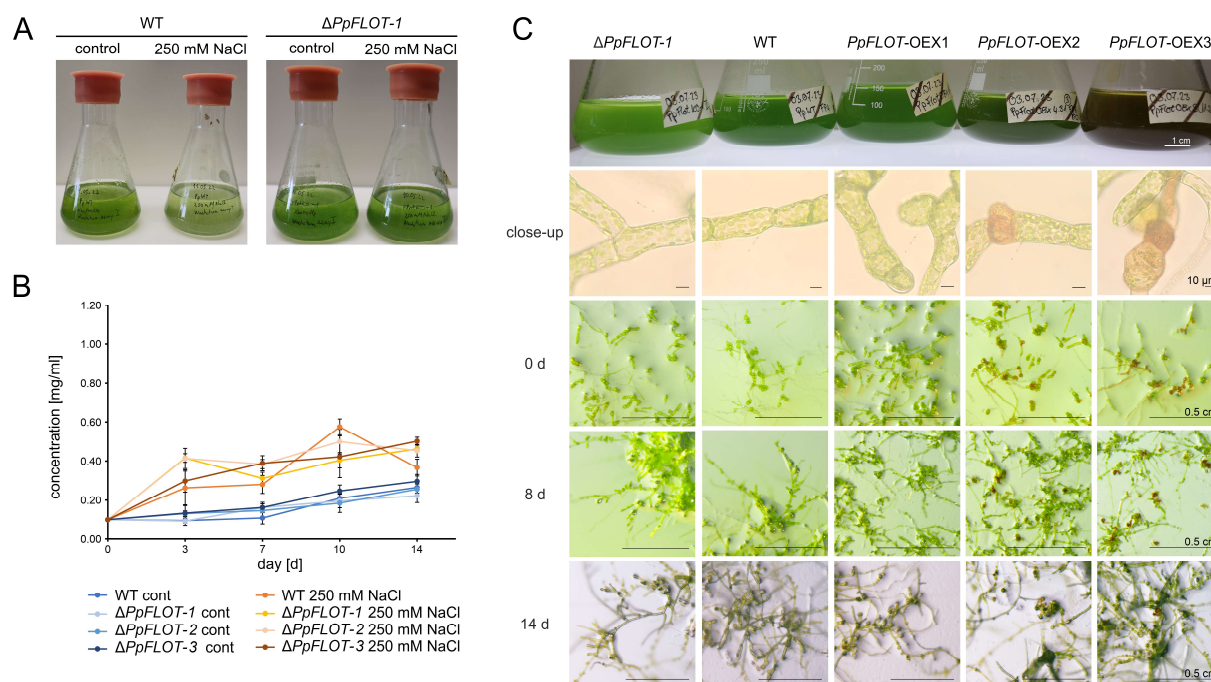


Figure 15: Growth phenotype of $\Delta PpFLOT$ and $PpFLOT$ -OEX lines

(A) Comparison of WT and $\Delta PpFLOT-1$ liquid protonema cultures with an initial density of 0.1 mg/ml after 14 d of treatment with 250 mM NaCl (right) and an untreated control (left). **(B)** Growth curves of $\Delta PpFLOT-1$ lines and WT determined by dry weight measurements, three to four days for 14 d. Cultures were initially inoculated with an equal density of 0.1 mg/ml dry weight. Measurements were taken during treatment with 250 mM NaCl and under control conditions for $\Delta PpFLOT$ lines and a WT control. **(C)** Upper panel displays liquid protonema cultures starting with an equal density of 100 mg/L and grown for 16 weeks (left to right) of $\Delta PpFLOT-1$, WT, $PpFLOT$ -OEX1, $PpFLOT$ -OEX2 and $PpFLOT$ -OEX3 at a density of ~ 1 mg/ml dry weight. The second panel presents close-ups of protonema cells from the respective lines when cultivated in standard liquid medium. Diaspore-like cells with brown coloration develop in $PpFLOT$ -OEX2 and 3. Panels three to five show the development of the respective lines when cultivated for 0, 8 and 14 d on solid growth medium. Scale bars are indicated in the respective images.

3.2.5 Increased $PpFLOT$ overexpression strongly affects protonema growth

Long-term cultivation of liquid protonema cultures from all generated $PpFLOT$ mutant lines (including $\Delta PpFLOT-1$ and $PpFLOT$ -OEX1, 2, 3 lines) resulted in changes of the coloration of the liquid protonema cultures. The in Figure 3C depicted cultures were started with an equal density of 100 mg/L and cultivated for 16 weeks before dry weight was measured again and images were taken. A comparison of the $PpFLOT$ mutant lines with a WT control grown with the same density revealed subtle changes, with a discernible color gradient depending on the $PpFLOT$ expression level (Figure 15C). This gradient ranged from light green in $\Delta PpFLOT-1$ to dark brown-green in $PpFLOT$ -OEX3 (Figure 15C) and close examination of single protonema cells indicated that increased $PpFLOT$ expression led to the development of small round cells in addition to the characteristic cell filaments. These cells resemble vegetative diaspores or brachyocytes observed in *P. patens* under exogenous ABA treatments or ABA-mediated stress responses (Arif et al., 2019). These brachyocytes are released from the protonema cell network by transforming the surrounding cells into empty tmema cells (Arif et al., 2019), which could not be detected in the $PpFLOT$ -OEX lines. These round cells, in

contrast to these diaspores, turned reddish-brown with increasing *PpFLOT* levels, contributing to the observed change in culture coloration, especially in the strongest *PpFLOT*-OEX lines. Notably, this coloration expands to the surrounding cell filaments as well (Figure 15C). Interestingly, when *PpFLOT*-OEX protonema was plated on solid media, these structures receded, and after two weeks, they mostly recovered, developing WT-typical gametophores (Figure 15C). Additionally, mature gametophores submerged in liquid media without tissue disruption showed no changes in pigmentation (Supplementary Figure 2).

3.2.6 Salt and phytohormone sensitivity in *P. patens* are modulated by *PpFLOT* expression levels

To evaluate the responses of the generated mutant lines to elevated salt concentrations, increased osmotic pressure and exogenous phytohormone treatment, protonema cultures of an equal density (100 mg/L dry weight) were spotted on standard solid medium supplemented with 250 mM NaCl, 300 mM NaCl, 700 mM mannitol, 10 μ M ABA, 10 μ M of the auxin analog NAA and 10 μ M of the cytokinin derivate 2-ip. The spotted colonies were cultivated for eight weeks. Under control conditions and 250 mM NaCl treatment, Δ *PpFLOT-1* and *PpFLOT*-OEX lines showed no significant changes in development compared to the WT (Figure 16). However, at a salt concentration of 300 mM, the *PpFLOT*-OEX lines were unable to form colonies whereas both Δ *PpFLOT-1* and the WT exhibited colony formation (Figure 16). To assess the impact of increased osmotic pressure on the *PpFLOT*-OEX lines, which exhibit reduced salt tolerance, protonema cultures of all lines were placed on plates supplemented with 700 mM Mannitol. This concentration was chosen to simulate the osmotic pressure equivalent to 300 mM NaCl for *P. patens*, following observations described by Saavedra et al. (2006). All tested lines were able to develop colonies and exhibited growth similar to the WT. However, consistent with observations in liquid culture, a gradient of pigmentation was observed in the colonies, shifting to a green-brownish hue with increased *PpFLOT* expression (Figure 16). The findings suggest that increased expression of *PpFLOT* is detrimental to the salt tolerance of *P. patens*, implying that *PpFLOT* most likely acts as a negative regulator in abiotic stress response, either directly or indirectly. Notably, qRT-PCR measurements of the *PpFLOT* expression in WT protonema cultures treated with 250 mM NaCl over 24 h showed a decrease in the expression levels (Figure 17A) at 8 and 24 h. However, this decrease in expression was not statistically significant (ANOVA, $p = 0.075$) due to a high variance among the biological replicates. Conversely, the expression levels in the salt-treated *PpFLOT*-OEX1 line did not exhibit significant decrease (ANOVA, $p = 0.26$) (Figure 17A). During ABA treatment of the respective lines, a further improved ABA sensitivity was observed and correlated with *PpFLOT* expression, as evidenced by larger *PpFLOT*-OEX3 colonies compared to the Δ *PpFLOT-1* or the WT control (Figure 16). Interestingly, 10 μ M ABA treatment of WT proto-

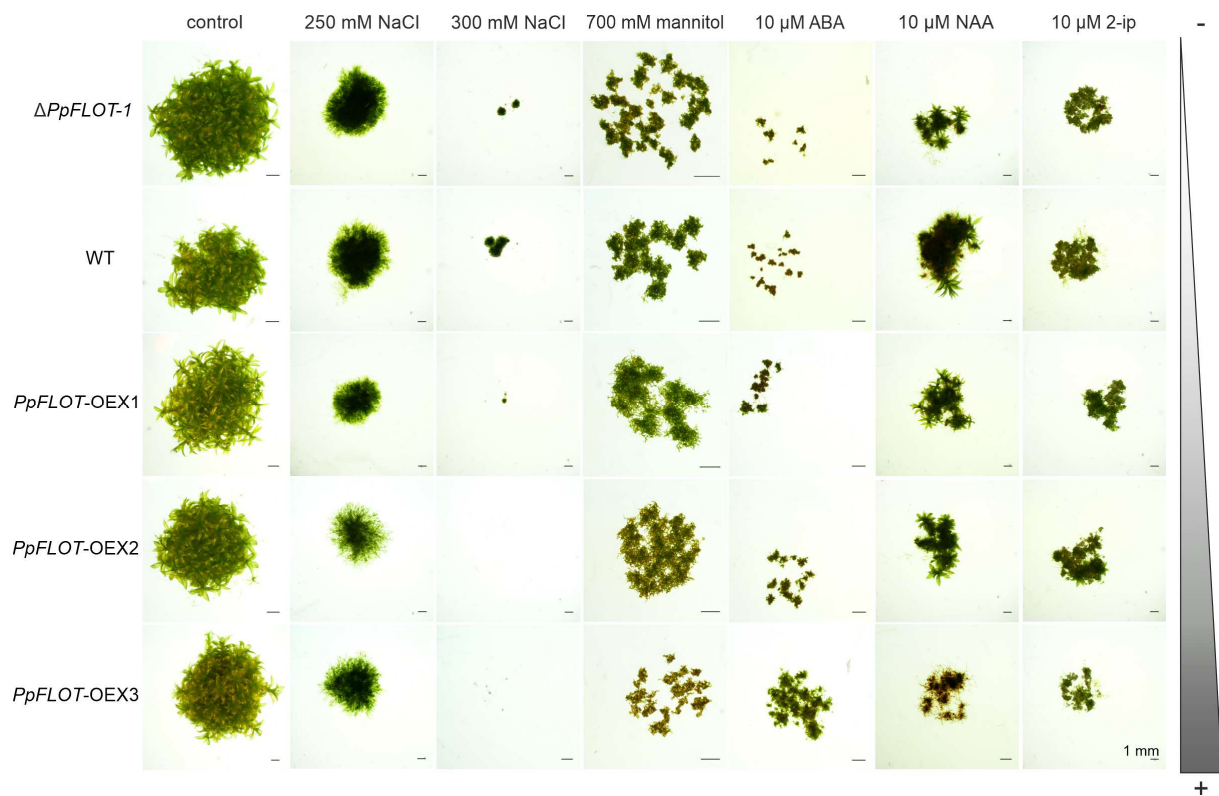


Figure 16: Phenotypic analysis of $\Delta PpFLOT-1$ and all *PpFLOT*-OEX lines

$\Delta PpFLOT-1$, WT, *PpFLOT*-OEX1, *PpFLOT*-OEX2 and *PpFLOT*-OEX3 were inoculated with an equal density (100 mg/L dry weight) on standard solid medium (control) and media supplemented with 250 mM NaCl, 300 mM NaCl, 700 mM mannitol, 10 μ M ABA, 10 μ M NAA and 10 μ M 2-ip and grown for 8 weeks. The scale bar in all images represents 1 mm. The strength of *PpFLOT* expression is indicated on the right.

nema cultures led to a statistically significant decrease in *PpFLOT* transcript levels over time (ANOVA, $p < 0.01$) (Figure 17A). Starting from 1 h after ABA treatment, *PpFLOT* expression significantly decreased and continued to decrease steadily, reaching a relative expression of 0.01 after 24 h (Figure 17A). Treatment with NAA or 2-ip did not result in phenotypic changes for $\Delta PpFLOT-1$, *PpFLOT*-OEX1, or *PpFLOT*-OEX2 compared to the treated WT control (Figure 16). In both cases the lines exhibited a similar growth pattern as the wild type, except line *PpFLOT*-OEX3. Upon NAA treatment this line failed to develop gametophores and formed reddish colonies. When treated with 2-ip *PpFLOT*-OEX3 exhibited slightly reduced growth compared to the other lines (Figure 16). Overall, the observed phenotypic alterations in response to all treatments were correlated with the levels of *PpFLOT* expression.

3.2.7 The *PpFLOT* transcript is regulated by multiple pathways

The phenotypic analysis of the generated *PpFLOT* mutant lines suggests a putative regulatory function for *PpFLOT* during abiotic stress responses in *P. patens*. Furthermore, the expression of WT *PpFLOT* is suppressed in response to ABA and salt treatment. Examination of the *PpFLOT* 5'UTR and 1.5 kb the genomic sequence upstream genomic sequence for *cis*-acting regulatory elements using PlantPAN 4.0 (Chow et al., 2019) identified potential binding sites

for various transcription factors, AP2, bHLH, CG-1 DNA-binding domain containing transcription factors (CG-1), ETHYLENE INSENSITIVE 3 (EIN3), GATA transcription factors, DNA binding with ONE FINGER (DOF), LATERAL ORGAN BOUND (LOB) domain transcription factors, MYB/ SWITCH_DEFECTIVE PROTEIN 2 (SWI3), ADAPTOR 2 (ADA2), NUCLEAR RECEPTOR COREPRESSOR (N-CoR), TRANSCRIPTION FACTOR III B (TF) (SANT), NAC, WRKY, MINI CHROMOSOME MAINTENANCE1/AGAMOUS/DEFICIENCY/ SERUM RESPONSE FACTOR (MADS) box, bZIP, TATA BINDING PROTEIN (TBP) transcription factors as well as C2H2, TCR, homeodomain and AT-hook motifs. The diverse array of identified putative transcription factor binding sites suggests the involvement of *PpFLOT* in various biological processes.

Interestingly, bHLH, NAC and WRKY, as well as, in some instances, MYB, AP2, DOF and bZIP transcription factors, are recognized regulators of the abiotic stress response or are themselves regulated by ABA (Golldack et al., 2011; Mizoi et al., 2012; Ambawat et al., 2013; Phukan et al., 2016; Das et al., 2019; Zou and Sun, 2023). Meanwhile, the presence of CG-1 and GATA binding sites suggests potential circadian or light-dependent regulation (da Costa e Silva, 1994; Reyes et al., 2004). Previous studies in rice indicate that AT-hook motifs may interact with light-sensitive phytochromes (Nieto-Sotelo et al., 1994). Subsequently, the *PpFLOT* expression was investigated for light-dependent or circadian regulation. WT protonema cultures were analyzed for putative circadian regulation by measuring *PpFLOT* transcript levels every 4 h over 24 h. The experiment was conducted under standard growth conditions (LD 16:8), complete darkness (D) and continuous light (CL), with all samples pre-adapted to their respective photoperiods for 3 days. ANOVA analysis of the *PpFLOT* expression over 24 h revealed significant changes ($p < 0.01$) in LD, D and CL cultivated samples. LD samples showed a peak expression at time point (TP) 12, with the lowest *PpFLOT* expression at TP 16, while D samples peaked at TP 20 and TP 0 showed the lowest expression (Figure 17B). In contrast to the other two photoperiod conditions, CL did not display a single maximum or minimum of the expression (Figure 17B). While the overall expression levels of *PpFLOT* in LD and CL samples oscillated between a normalized relative expression of 0.5 – 3, D samples exhibited a higher overall expression level, fluctuating between a normalized relative expression of 10 – 50 (Figure 17B).

Intriguingly, the highest *PpFLOT* expression in the LD samples coincided with the beginning of the dark period (Figure 17B), suggesting that *PpFLOT* expression is generally enhanced in the absence of irradiation. To assess if the observed oscillations follow a circadian rhythmicity, a cosinor-based *rhythmometry* analysis (Cornelissen, 2014) was conducted for all three groups. Both LD and D expression levels could be fitted to a cosinor curve, meeting the criteria for circadian rhythmicity with $p < 0.01$.

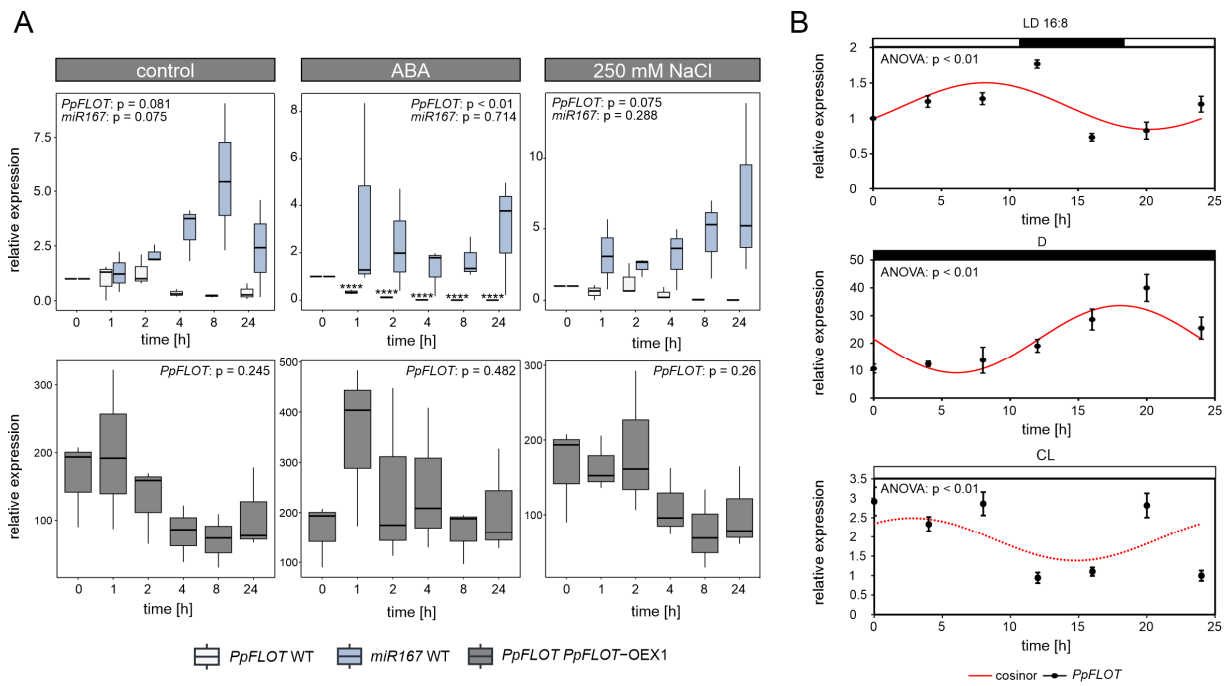


Figure 17: *PpFLOT* expression is regulated by daytime, light, ABA and salt

(A) Depiction of relative gene expression of *PpFLOT* and *miR167* in *P. patens* WT protonema (upper panel) and expression of *PpFLOT* in *PpFLOT*-OEX1 (lower panel) measured over 24 h under control conditions and in response to 10 μ M ABA and 250 mM NaCl in triplicates. Analysis performed according to Schmittgen and Livak (2008). ANOVA analysis was conducted to identify statistically significant differences between time points, with p-values provided in the respective boxes. Asterisks denote time points with statistically significant changes in expression identified by Tukey's HSD test compared to 0 h treatment. * $p < 0.05$, ** $p < 0.01$, **** $p < 0.0001$. **(B)** Relative gene expression of *PpFLOT* in *P. patens* WT protonema observed over 24 h under long-day conditions (LD 16:8), complete darkness (D) and continuous light (CL) after adapting for three days to the respective light conditions. Mean values of biological triplicates are depicted with \pm SEM ($n = 3$). Bars above the graphs indicate light conditions at the respective time points (black = light off, white = light on). Light intensity in all conditions was 85–100 μ mol/m²s. P-values of the ANOVA analyses are given in the respective graphs. Cosinor curve calculated from acrophase, mesor and amplitude is indicated by a red line. A continuous line indicates statistically significant rhythmicity ($p < 0.05$) while an interrupted line indicates non-significant rhythmicity ($p > 0.05$).

However, the CL group did not fulfill these conditions ($p = 0.205$). The detected arrhythmicity under CL is likely attributed to a dysfunctionality of the *P. patens* circadian clock at CL conditions, as proposed and demonstrated by Okada et al. (2009) for clock-related genes in *P. patens* (Ichikawa et al., 2004; Ichikawa et al., 2008; Okada et al., 2009; Petersen et al., 2022). Due to the overall higher expression levels, a shift in amplitude and acrophase between the LD and NL samples (Figure 17B) was observed. Additionally, a phase delay in D samples compared to LD samples was likely caused by the absence of irradiation impulses (Fukuda et al., 2013). It is noteworthy that in mammals, stress and changes in hormone levels can induce a shift in the expression of genes regulated by the circadian clock (Ota et al., 2021). Therefore, during stress, a delay in the circadian clock of *P. patens* could occur due to increased expression of *PpFLOT* or alterations in phytohormone profiles throughout the day.

In a previous study, altered miRNA biogenesis led to an increase in *PpFLOT* transcript levels (Arif et al., 2022). Subsequently, the genomic *PpFLOT* sequence was searched for a putative miRNA binding site with psRNATarget (Dai et al., 2018), identifying miR167 as the best match with an expectation score of 3.5 and a putative cleavage site in the third exon of the *PpFLOT* sequence located at bp 1898-1918. Relative miR167 expression detected by stem-loop PCR revealed anticorrelating expression between miR167 and *PpFLOT* in WT protonema under control conditions and in response to salt treatment (Figure 17A). However, statistical analysis did not confirm the detected changes in miRNA expression as significant, likely due to high variance between replicates. While these changes in expression were not statistically significant, they suggest a potential regulation of *PpFLOT* on the transcript level.

Overall, four potential regulatory mechanisms controlling the *PpFLOT* transcript levels could be identified in *P. patens* protonema. The evidence suggests that the expression of *PpFLOT* can be suppressed by ABA-responsive transcription factors. Additionally, *PpFLOT* is circadian regulated, with increased expression when cultivated without light impulses. Moreover, it cannot be dismissed that miR167 may regulate the *PpFLOT* transcript, although further experiments are necessary to confirm this type of regulation. I propose that *PpFLOT*, located in the chloroplasts of *P. patens*, serves as a scaffolding protein in various biological processes, particularly during the response to abiotic stress and in processes related to the day-night transition of chloroplasts. The diverse methods identified to regulate *PpFLOT* levels transcriptionally or posttranscriptionally in chloroplasts highlight its importance in multiple cellular functions.

3.2.8 Detection of slight ROS accumulation in *PpFLOT*-OEX lines

All generated *PpFLOT*-OEX lines, displaying lower salt tolerance than the WT or $\Delta PpFLOT-1$, potentially attributed to increased ROS accumulation (Pandey et al., 2017) underwent DAB staining to detect H₂O₂ overaccumulation. Protonema samples were incubated for 18 h in the staining solution under CL photoperiod conditions and subsequent microscopic examination revealed higher H₂O₂ levels in *PpFLOT*-OEX lines compared to the WT and $\Delta PpFLOT-1$ (Figure 18A). Notably, *PpFLOT*-OEX2 and *PpFLOT*-OEX3 exhibited cells with persistent pigmentation, suggesting potential challenges in destaining by boiling in ethanol, making it challenging to ascertain the origin of H₂O₂ overaccumulation in these structures. However, a general comparison of stained, normal grown protonema cells across all *PpFLOT*-OEX lines and the WT demonstrated a correlation between *PpFLOT* expression levels and H₂O₂ accumulation (Figure 18A).

Elevated H₂O₂ levels, indicative of stress in *P. patens*, prompted an examination of transcript levels of abiotic stress-induced genes (Boursiac et al., 2005; Saavedra et al., 2006; Frank et al., 2007; Hauser et al., 2011; Li et al., 2011; Li et al., 2012). These measurements were

performed under control conditions and when treated with either 250 mM NaCl or 10 μ M ABA in WT, $\Delta PpFLOT-1$ all *PpFLOT*-OEX1. Interestingly, the expression of *AQUAPORINE TIP* (*Pp1s44_31/ Pp3c20_15350*), 9'-cis *EPOXYCAROTENOID DIOXIGENASE (NCED)* (*Pp1s412_7/ Pp3c25_4810*), *TRANSLOCATOR PROTEIN 1 (PpTSPO1)* (*Pp1s281_123/ Pp3c2_17540*) and *DEHYDRIN B (DHNB)* (*Pp1s442_22/ Pp3c5_11880*) barely showed any significant changes in the gene expression among the tested genotypes (Supplementary Figure 3). Specifically, only *PpTSPO1* displayed slightly lower expression in *PpFLOT*-OEX1 compared to the WT and $\Delta PpFLOT-1$ (ANOVA $p = 0.04$) in response to salt treatment (Supplementary Figure 3).

Conversely, the expression of a mRNA encoding an AP2/ERF domain transcription factor *Pp1s8_127/ Pp3c8_7340* changed significantly between the genotypes under control conditions (ANOVA, $p = 0.02$) since *Pp3c8_7340 (AP2/ERF)* exhibited significantly (Tukey's HSD, $p = 0.0235$) higher expression in *PpFLOT*-OEX1 compared to $\Delta PpFLOT-1$. Significant upregulation of *Pp3c8_7340 (AP2/ERF)* was observed at 0 h of salt treatment (Tukey's HSD, $p = 0.0429$) and at 8 h of ABA treatment (Tukey's HSD, $p = 0.0229$) in *PpFLOT*-OEX1 compared to the WT. Notably, both the WT and $\Delta PpFLOT-1$ samples treated with ABA for 1, 2 and 4 h exhibited a significant increase in *Pp3c8_7340 (AP2/ERF)* expression compared to untreated samples (ANOVA, $p < 0.01$). Statistically significant differences in expression levels between the genotypes were observed at 2 h (Tukey's HSD $\Delta PpFLOT-1$ vs WT, $p < 0.01$) and 8 h (Tukey's HSD *PpFLOT*-OEX1 vs WT, $p = 0.0295$). However, the overall changes in expression between the tested genotypes in response to ABA treatment were not statistically significant (ANOVA, $p = 0.09$) (Figure 18B). Similarly, upon salt treatment, the overall change in expression between the tested genotypes was not significant (ANOVA, $p = 0.187$). At 0 h, a significantly higher expression of *Pp3c8_7340 (AP2/ERF)* was detected in *PpFLOT*-OEX1 (Tukey's HSD *PpFLOT*-OEX1 vs WT, $p = 0.0429$) (Figure 18B). This upregulation in untreated samples of *PpFLOT*-OEX1 is most likely an attempt to suppress the ectopic *PpFLOT* expression.

Heavy metal-associated domain (HMA) containing proteins, vital for heavy metal transport and detoxification in plants, respond to various stresses (Li et al., 2020; Barr et al., 2023). Proteins in this family are upregulated in response to drought, cold, hypoxia and bacterial infection (Barr et al., 2023). The gene expression of the copper transport protein *Pp1s296_27/Pp3c3_6890*, encoding such an HMA domain, exhibited significant differences in expression between the three genotypes upon ABA and salt treatment (ANOVA, $p < 0.01$). For instance, while all genotypes showed increasing *Pp3c3_6890* levels in response to ABA, this upregulation was extreme in *PpFLOT*-OEX1 1 h after ABA treatment compared to the other two lines (Tukey's HSD, $p < 0.05$) (Figure 18B).

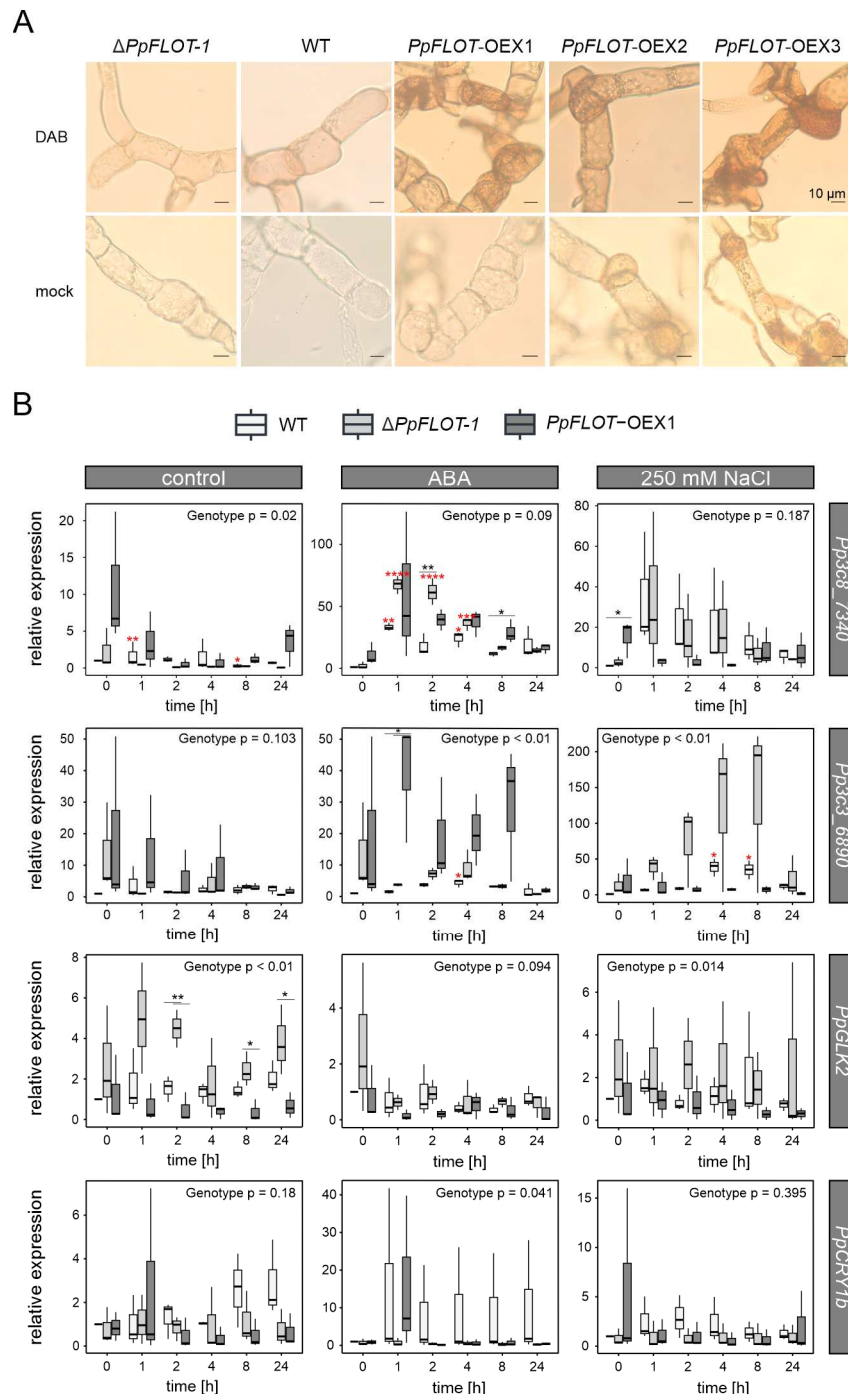


Figure 18: Changes in H_2O_2 levels and gene expression corresponding to changes in *PpFLOT* expression

(A) H_2O_2 levels were visualized in $\Delta PpFLOT-1$, WT and all three *PpFLOT*-OEX lines through staining with 3, 3'-diaminobenzidine. The upper panel depicts images of treated protonema cells, while the lower panel exhibits images of untreated mock controls. The scale bar in all images represents 10 μm . **(B)** Box plots present qRT-PCR results of relative gene expression for (top to bottom) AP2/ERF domain transcription factor *Pp3c8_7340*, copper transport HMA domain protein *Pp3c3_6890*, GOLDEN 2-LIKE PROTEIN 2 (*PpGLK2*) and CRYPTOCHROME 1b (*PpCRY1b*), comparing expression levels to WT at 0 h of treatment and normalized against *PpEF1a* following the method by Schmittgen and Livak (2008). The depicted relative gene expression of the respective genes in $\Delta PpFLOT-1$, WT and *PpFLOT*-OEX1 protonema is shown under control conditions (left), upon ABA (middle) and salt (right) treatment measured over 24 h in triplicates. ANOVA was used to determine statistically significant changes in expression between the three genotypes, with p-values indicated in the respective graphs (black asterisk). Tukey's HSD results for time-dependent expression in one line are marked by red asterisk when significant compared to 0 h of treatment. * $p < 0.05$, ** $p < 0.01$, *** $p < 0.001$, **** $p < 0.0001$

On the other hand, in response to salt $\Delta PpFLOT-1$ displayed an extreme upregulation of *Pp3c3_6890* (*Cu-HMA*) compared to both WT (Tukey's HSD, $p < 0.01$) and *PpFLOT-OEX1* (Tukey's HSD, $p < 0.01$). Comparatively, *Pp3c3_6890* (*Cu-HMA*) expression is subdued in *PpFLOT-OEX1* in response to salt (Figure 18B).

Despite the salt-sensitive phenotype of *PpFLOT-OEX* lines, only minor changes in the expression levels of salt and ABA-induced genes were detected upon induction. For instance, *Aquaporine TIP* exhibited slight repression in *PpFLOT-OEX1* at all TP compared to 0 h under control conditions. Comparatively, *PpFLOT-OEX1* showed a peak in *Aquaporine TIP* expression at 2 h instead of 24 h (Supplementary Figure 3). In the WT, *NCED* expression significantly increased in response to ABA (ANOVA, $p = 0.015$) and salt treatment (ANOVA, $p < 0.01$). While this change in expression was also detected in *PpFLOT-OEX1* and $\Delta PpFLOT-1$, it was not statistically significant (*PpFLOT-OEX1*: ANOVA salt $p = 0.585$, ABA $p = 0.427$ and $\Delta PpFLOT-1$: ANOVA salt $p = 0.629$; ABA $p = 0.078$) (Supplementary Figure 3). Similarly, no changes in the expression of *PpDHNB* were detected among the three genotypes (ANOVA, $p = 0.865$) over 24 h. However, at 24 h, *PpDHNB* expression was significantly upregulated in the WT compared to $\Delta PpFLOT-1$ and *PpFLOT-OEX1* (Tukey's HSD, $p < 0.01$). Additionally, the peak expression of *PpDHNB* upon salt treatment for both WT and *PpFLOT-OEX1* occurred at 2 h, while in $\Delta PpFLOT-1$, it peaked at 24 h (Supplementary Figure 3). Most abiotic stress markers behaved similarly to the WT, suggesting no upregulation of ABA biosynthesis or other known abiotic stress-sensing pathways in $\Delta PpFLOT-1$ and *PpFLOT-OEX* lines.

Abnormal expression of stress-induced genes and increased H_2O_2 levels may impact retrograde signaling pathways involving chloroplast-to-nucleus communication using ROS as signaling molecules (Locato et al., 2018; Li and Kim, 2022). The gene *GOLDEN 2-LIKE PROTEIN 2* (*Pp3c11_21140*) (*GLK2*), associated with retrograde signaling (Sun et al., 2022; Zeng et al., 2023), exhibited significant expression changes under control conditions and salt treatment in WT, $\Delta PpFLOT-1$ and all *PpFLOT-OEX* lines (ANOVA, salt $p = 0.014$, cont $p < 0.01$). $\Delta PpFLOT-1$ displayed consistently higher *PpGLK2* expression than WT and *PpFLOT-OEX1* under control conditions (Tukey's HSD, $p < 0.01$) (Figure 18B). In response to salt treatment, *PpFLOT-OEX1* showed significantly lower *PpGLK2* expression (Tukey's HSD, $p < 0.0119$) compared to $\Delta PpFLOT-1$ but not compared to the WT (Tukey's HSD, $p = 0.581$) (Figure 18B). Another retrograde signaling gene, *CRYPTOCHROME 1b* (*Pp3c7_20480*) (*PpCRY1b*), displayed a statistically significant expression change (ANOVA, $p = 0.041$) between the genotypes upon ABA treatment. *PpCRY1b* was generally expressed at higher levels in WT than $\Delta PpFLOT-1$ (Tukey's HSD, $p < 0.0356$) except at 1 h. However, under control conditions, *PpCRY1b* showed higher transcript levels at 8 and 24 h after start of the

measurements compared to $\Delta PpFLOT-1$ and $PpFLOT-OEX1$, with no statistically significant differences under control conditions (Figure 18B).

3.2.9 Increased chlorophyll a/b content correlates with strength of *PpFLOT* expression

The total chlorophyll content of WT, $\Delta PpFLOT-1$, $PpFLOT-OEX1$, $PpFLOT-OEX2$ and $PpFLOT-OEX3$ was assessed to determine if the observed *PpFLOT*-dependent change in pigmentation resulted in altered chlorophyll content in the *PpFLOT* mutant lines. Chlorophyll a and b were extracted using 80 % acetone from equal amounts of protonema harvested per line. After separating cell debris, chlorophyll absorption was measured and total chlorophyll content was calculated following the method outlined by Frank et al. (2005). Significant changes (ANOVA, $p < 0.01$) in the chlorophyll content were observed between *PpFLOT* mutant lines and the WT control. $\Delta PpFLOT-1$ exhibited only half as much chlorophyll as the WT, with 0.4 mg chl/g dry weight (Figure 19A). Surprisingly, the $PpFLOT-OEX1$ line exhibited a similar amount of chlorophyll (0.49 mg chl/g dry weight). In contrast, both $PpFLOT-OEX2$ and $PpFLOT-OEX3$ had significantly higher chlorophyll content, with 2.6 and 2.5 mg chl/g dry weight, respectively (Figure 19A). This suggests an enhanced chlorophyll biosynthesis, potentially leading to increased photosynthetic activity.

To assess this, PAM measurements were performed to quantify the chlorophyll fluorescence and calculate the quantum yield of the PSII activity and non-photochemical quenching during photosynthesis activation by light. As previously mentioned, the pigmentation between *PpFLOT* mutant lines grown in liquid cultures and those cultivated on solid media displayed massive differences. Therefore, separate measurements for mature gametophores grown on solid medium and protonema liquid cultures with the same number of biological replicates ($n = 9$) were conducted using identical parameters. Interestingly, while statistical analysis of PSII activity among all tested genotypes in the gametophores revealed significant differences (ANOVA, $p = 0.023$), only $PpFLOT-OEX1$ displayed a lower PSII activity compared to WT and $\Delta PpFLOT-1$, while $PpFLOT-OEX2$ and 3 showed no differences in activity compared to the WT. During non-photochemical quenching, no changes between the WT, $\Delta PpFLOT-1$ and all *PpFLOT-OEX* lines could be found in the gametophores (ANOVA, $p = 0.34$) (Figure 19B).

To ensure comparability between the gametophore and the protonema samples, fluorescence was measured at 450 nm and an actinic light intensity of 55 $\mu\text{mol}/\text{m}^2\text{s}$ PAR for all samples. However, $PpFLOT-OEX3$ protonema displayed no detectable fluorescence under these conditions and the measuring light parameter had to be adjusted to an intensity of 60 $\mu\text{mol}/\text{m}^2\text{s}$ PAR to detect a fluorescence signal. Therefore, PAM measurements of $PpFLOT-OEX3$ protonema were excluded from the analysis to maintain comparability between all measurements. In contrast to the fluorescence measurements in gametophores, statistically significant differences could be detected in the Y(II) and NPQ/4 (ANOVA, $p < 0.01$) between

$\Delta PpFLOT-1$ and $PpFLOT$ -OEX1 and 2 protonema cultures. Compared to the WT samples, neither the $\Delta PpFLOT-1$ nor the two $PpFLOT$ -OEX lines showed any significant differences in the calculated photosynthetic activity (Tukey's HSD, $\Delta PpFLOT-1$ vs WT $p = 0.898$, $PpFLOT$ -OEX1 vs WT $p = 0.0719$, $PpFLOT$ -OEX1 vs WT $p = 0.165$). However, a comparison between the $\Delta PpFLOT-1$ and the $PpFLOT$ -OEX lines revealed a significantly higher quantum yield in PSII of the $PpFLOT$ -OEX lines (Tukey's HSD, $PpFLOT$ -OEX1 vs $\Delta PpFLOT-1$ $p < 0.01$, $PpFLOT$ -OEX2 vs $\Delta PpFLOT-1$ $p = 0.0298$) compared to the knockout line (Figure 19B).

This change in activity was also detected during non-photochemical quenching. For instance, both $PpFLOT$ -OEX lines process less energy by non-photochemical quenching than $\Delta PpFLOT-1$ (ANOVA, $p < 0.01$; Tukey's HSD, $PpFLOT$ -OEX1/2 vs $\Delta PpFLOT-1$ $p < 0.01$) (Figure 19B). The level of photosynthetic activity in protonema cultures slightly increases in correlation with the increased expression of $PpFLOT$. However, a statistical comparison between the WT and all $PpFLOT$ mutant lines did not yield any significant results. Interestingly, $\Delta PpFLOT-1$ displayed a significantly higher (ANOVA, $p < 0.01$) NPQ/4 signal compared to $PpFLOT$ -OEX1 and 2 (Tukey's HSD, $p < 0.01$). The absence of $PpFLOT$ in the knockout line results in lower photosynthetic activity and increased non-photochemical quenching, potentially due to reduced chlorophyll levels. By adjusting the amount of $PpFLOT$ in chloroplasts of protonema cells the photosynthetic activity can most likely be fine-tuned to accommodate the specific needs of the respective cells. This seems to be relevant only during the protonema life stage of *P. patens* as $PpFLOT$ overexpression, with the exception of $PpFLOT$ -OEX1, has barely an effect on the photosynthetic activity of the gametophores.

Since photosynthetic activity is slightly altered in the $PpFLOT$ mutant protonema liquid cultures these lines display changes in the chlorophyll biosynthesis rate. Thus, transcript levels of photosystem I (PSI) and PSII-related components were measured. Under control conditions the expression of the *LIGHT-HARVESTING COMPLEX B1* (*LHCB1*) (*Pp3c2_35930*) displayed significant (ANOVA, $p < 0.01$) differential expression when compared between WT, $\Delta PpFLOT-1$ and $PpFLOT$ -OEX1 over 24 h. $\Delta PpFLOT-1$ showed significantly higher *PpLHCB1* expression compared to the WT (Tukey's HSD, $p = 0.0347$) and $PpFLOT$ -OEX1 (Tukey's HSD, $p < 0.0347$). Although not statistically significant, *PpLHCB1* expression appears subdued in the $PpFLOT$ -OEX1 line in general (Figure 19C).

Meanwhile, the expression of the *LIGHT-HARVESTING COMPLEX A1.1* (*LHCA1.1*) (*Pp3c13_14980*) not only changes under control conditions (ANOVA, $p < 0.01$) (Figure 19C) but also in response to salt (ANOVA, $p = 0.031$) and ABA treatment (ANOVA, $p < 0.01$) (Supplementary Figure 3). Under all conditions, *PpLHCA1.1* showed a lower expression in the $PpFLOT$ -OEX1 line compared to both the WT and $\Delta PpFLOT-1$ (Figure 19C, Supplementary Figure 3).

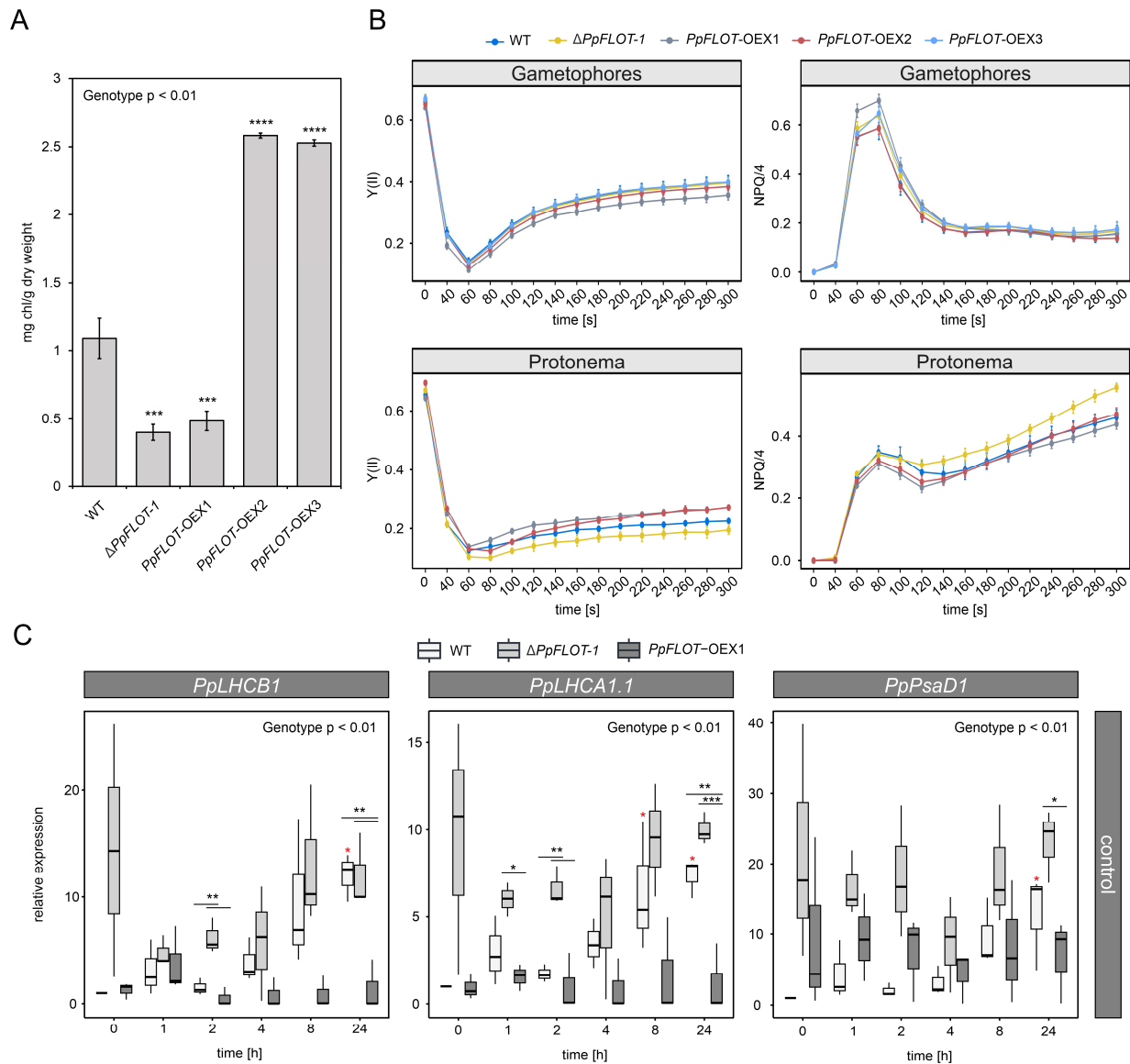


Figure 19: Effects of changes in *PpFLOT* expression on chlorophyll content and photosynthetic activity

(A) Chlorophyll content of 0.4 g protonema from WT, $\Delta PpFLOT-1$ and all *PpFLOT*-OEX lines. Mean values \pm SEM ($n = 3$) are shown. ANOVA results are provided and statistically significant ($p < 0.05$) differences in the *PpFLOT* mutants compared to the WT were determined by Tukey's HSD test and are indicated by asterisks. * $p < 0.05$, ** $p < 0.01$, *** $p < 0.001$, **** $p < 0.0001$ **(B)** Effect of *PpFLOT*'s expression on Y(II) and NPQ/4 in the gametophore and protonema life stage of *P. patens*. Mean values \pm SD ($n = 9$) are shown. Measurements were performed after 3 h of dark adaptations and actinic light of $55 \mu\text{mol}/\text{m}^2\text{s}$ at 450 nm for 315 s after saturation pulse stimulation. **(C)** qRT-PCR results shown as box plots of relative gene expression of *PpLHCB1* (*Pp3c2_35930*), *PpLHCA1.1* (*Pp3c13_14980*), *PpPsaD1* (*Pp3c16_23780*) over 24 h relative to WT expression at 0 h, normalized against *PpEF1a* as described by Schmittgen and Livak (2008). Depicted is the relative gene expression of the respective genes in $\Delta PpFLOT-1$, WT and *PpFLOT*-OEX1 protonema under control conditions measured in biological triplicates. Statistically significant changes in expression between the three genotypes were determined by ANOVA, with p-values provided in the respective graphs. Significant differential gene expression at a specific time point is marked by black asterisks. Results of the Tukey's HSD for the time-dependent expression within the same genotype are marked by red asterisks when significant compared to 0 h of treatment. * $p < 0.05$, ** $p < 0.01$, *** $p < 0.001$, **** $p < 0.0001$

A similar trend was observed for the expression of the *PSI SUBUNIT D1* (*PsaD1*) (*Pp3c16_23780*). Comparison among the three tested lines revealed a statistically significant

change in expression under control conditions (ANOVA, $p < 0.01$) (Figure 19C), ABA (ANOVA, $p = 0.013$) and salt treatment (ANOVA, $p = 0.019$) (Supplementary Figure 3). Under control conditions, *PpPsaD1* expression was significantly higher in the $\Delta PpFLOT-1$ line compared to the WT (Tukey's, $p < 0.01$) and *PpFLOT-OEX1* (Tukey's, $p < 0.01$). Overall, the alterations in chlorophyll content, photosynthetic activity of PSII and the expression of PS antenna-complex components in correlation with *PpFLOT* expression indicate an involvement of *PpFLOT* in the photosynthesis of *P. patens*.

3.2.10 Zeaxanthin level is depleted in correlation to *PpFLOT* expression

The observed color change in the *PpFLOT-OEX* liquid cultures may result from specific alterations in the pigment profile compared to the WT. Thus, the pigment composition of $\Delta PpFLOT-1$, all *PpFLOT-OEX* lines and a WT control was analyzed by LC-MS in four replicates. Among 24 detected pigments, 19 could not be identified. To identify differentially accumulated pigments, statistical analysis was conducted using Perseus v 2.0.11 (MaxQuant) (Tyanova et al., 2016). Pigments were classified as DE when both the p -value and the permutation-based FDR (q -value) of the Student's t -test of $\Delta PpFLOT-1$ and all *PpFLOT-OEX* lines using the WT as a control group were less than 0.05. The analysis employed the \log_2 transformed FC of the relative pigment abundance. It was found that two detected pigments, lutein and unknown pigment 16, were differentially accumulated in all groups.

Additionally, zeaxanthin and unknown pigment 10 displayed an altered abundance in the *PpFLOT-OEX* lines (Figure 20A, Table 8 and Supplementary Table 16) that correlates with *PpFLOT* expression. Notably, all shared differentially accumulated pigments of the *PpFLOT* mutant lines were downregulated compared to the WT (Figure 20A, Table 8 and Supplementary Table 16). However, while the detected amount of these pigments decreased in the *PpFLOT* mutant lines, only zeaxanthin and unknown pigment 10 decreased in correlation with the *PpFLOT* expression (Figure 20A). As zeaxanthin is part of the xanthophyll cycle, the accumulation of its other main components alongside lutein in the *PpFLOT* mutant lines was further analyzed (Figure 20B). It is noteworthy that the lycopene pool was significantly depleted in $\Delta PpFLOT-1$, *PpFLOT-OEX1* and 3 when compared to the WT (Figure 20A, Table 8 and Supplementary Table 16). β -carotene also showed a slight depletion in *PpFLOT-OEX1* and 2 but recovered in *PpFLOT-OEX3*. The abundance of violaxanthin exhibited only minor changes in the *PpFLOT* mutant lines compared to the WT (Figure 20B). No other differentially accumulated components of the xanthophyll cycle were detected or identified. Interestingly, unknown pigments 6, 12, 19 and 25 all showed increased abundance in at least three *PpFLOT* mutant lines compared to the WT.

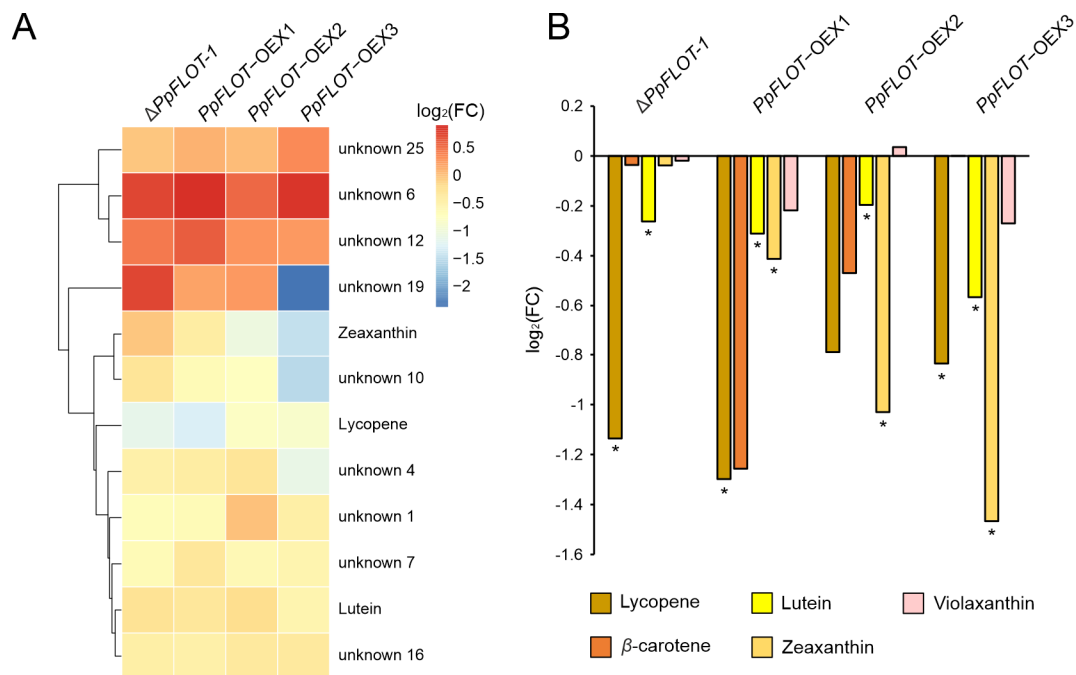


Figure 20: Pigment composition of all *PpFLOT* mutant lines

(A) The clustered heatmap displays $\log_2(\text{FC})$ values of identified pigments, which were deemed differentially accumulated by Student's *t*-test ($p < 0.05$) and the permutation-based false discovery rate (FDR) ($q < 0.05$) in at least one *PpFLOT* mutant line in comparison to the WT. **(B)** The $\log_2(\text{FC})$ of key xanthophyll cycle components, including lycopene, lutein, violaxanthin, β -carotene and zeaxanthin is shown for $\Delta PpFLOT-1$ and all *PpFLOT*-OEX lines compared to the WT. Differentially accumulated pigments identified by Student's *t*-test and FDR are denoted with an asterisk.

Identification of these unknown pigments may elucidate the molecular processes responsible for the observed change in culture coloration. It is also interesting to note that with the exception of zeaxanthin no gradual change in the analyzed pigment levels can be detected since *PpFLOT*-OEX2 seems to behave differently from *PpFLOT*-OEX1 and 3. These differences most likely occurred due to a higher variability between the technical replicates and extreme outliers in this group compared to the other *PpFLOT* mutant lines.

3.2.11 Changes in the proteome of *PpFLOT*-OEX lines convey influence on metabolic pathways in chloroplasts

A proteomics analysis was carried out to identify potential proteins that could explain the observed phenotype and altered salt tolerance. Since the change in protonema cell shape and coloration, as well as the altered salt tolerance, was limited to *PpFLOT*-OEX lines the proteomics profiles of the three *PpFLOT*-OEX and a WT control were analyzed. For this analysis 50 mg fresh weight protonema liquid culture of WT control and all *PpFLOT*-OEX lines were harvested in four replicates and LC-MS was conducted. First analysis of the generated proteomics data confirmed that the increase of *PpFLOT* transcript in all three *PpFLOT*-OEX lines translated into correspondingly higher protein levels. The detected $\log_2(\text{FC})$ of *PpFLOT* abundance in *PpFLOT*-OEX 1, 2 and 3 lines compared to the WT amounted to 8.12, 8.88 and

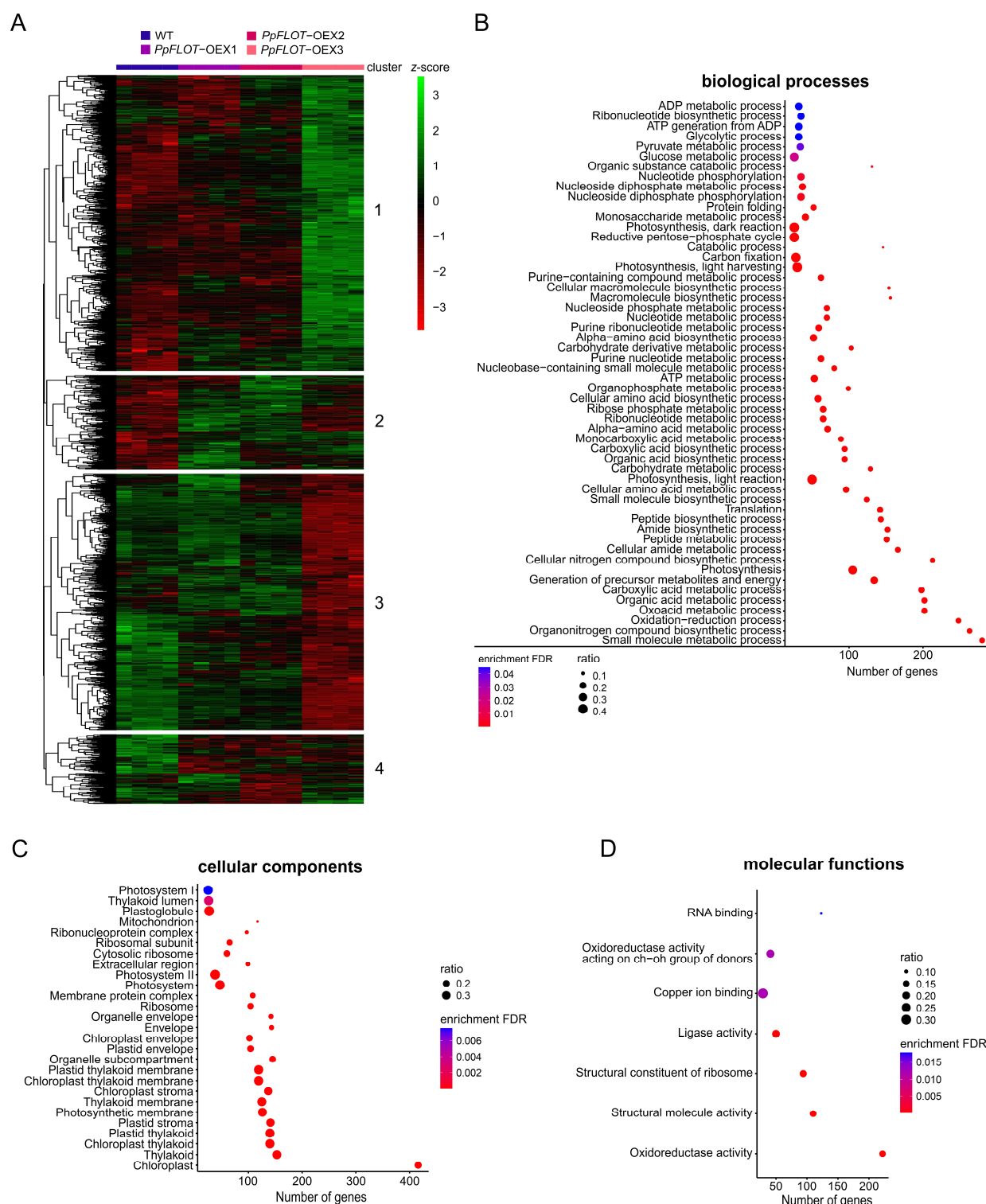


Figure 21: Proteomics and GO term analysis of all *PpFLOT*-OEX lines compared to *P. patens* WT

(A) Clustered heatmap of z-score transformed \log_2 (LFQ intensities) values of all differentially expressed protein groups (DEP) identified by ANOVA ($p < 0.05$) and a significant permutation-based false discovery rate (FDR) ($q < 0.05$). The depicted protein groups are DEP between at least two of the analyzed genotypes. Clusters are numbered and proteins contained in each cluster are listed in Supplementary Table 17. (B - D) Results of the GO term analysis performed by shinyGO (Ge et al., 2020) and sorted after (B) biological processes, (C) cellular components and (D) molecular functions. Shown are the significant ($p < 0.05$) GO terms also displaying a significant enrichment (FDR) $q < 0.05$. The number of detected proteins and the ratio between total genes of a pathway and the detected genes/proteins of that pathway are given.

9.79, respectively. The statistical analysis of the generated proteomics data was performed with Perseus (Tyanova et al., 2016). To identify statistically significant differentially expressed protein groups (DEP), an ANOVA analysis using the permutation-based FDR of 0.05 as threshold was performed.

A total of 2163 detected protein groups were identified, with 1484 showing significant DE between at least two of the analyzed genotypes (Supplementary Table 17). By visualizing the z-scores of the DEP using a clustered heatmap, a shift in the protein expression correlated with the amount of synthesized PpFLOT (Figure 21A) was shown. Cluster one contained proteins whose expression increased with enhanced PpFLOT expression, while the expression of protein groups in cluster three was suppressed (Figure 21A, Supplementary Table 17). Interestingly, clusters two and four both showed changes in protein abundance in *PpFLOT*-OEX1 and 2 compared to the WT while the protein expression profile of *PpFLOT*-OEX3 was WT-like (Figure 21A, Supplementary Table 17).

To identify the molecular functions, cellular components and biological processes influenced by *PpFLOT* overexpression, a GO enrichment analysis was performed using shinyGO v 0.8 (Ge et al., 2020). The majority of affected cellular components are part of the thylakoids and the chloroplasts, supporting the localization of *PpFLOT* associated to thylakoid membranes. This implies a function during photosynthetic or photosynthesis-related processes, most likely by assisting protein complex assembly (Figure 21B). Interestingly, among the affected GO terms in the category molecular function were copper ion binding, structural molecular activity and oxidoreductase activity, particularly focusing on oxidoreductase activity when acting on CH-OH groups (Figure 21B). The detected enriched biological processes also suggest an involvement of PpFLOT in photosynthesis and biosynthesis of carbohydrates, amides, organic acids and peptides (Figure 21B, Supplementary Tables 17 and 18).

To identify DEP in each *PpFLOT*-OEX line compared to the WT specifically, a Student's *t*-test was performed for each overexpression line. Protein groups with a p-value and a permutation-based FDR of 0.05 and a $\log_2(\text{FC}) \leq -1$ and $\geq +1$ were identified as DEP (only main IDs shown). This way, 89 DEP in *PpFLOT*-OEX1 (76 up and 13 down), 92 in *PpFLOT*-OEX2 (62 up and 30 down) and 216 in *PpFLOT*-OEX3 (135 up and 81 down) (Figure 22A, 22B, Supplementary Table 19) could be identified. It was further demonstrated that the increase of *PpFLOT* transcript translates to the protein level and continues to correlate with the strength of *PpFLOT* expression. The majority of these DEP are upregulated in all three overexpression lines and only a fraction of them are downregulated (Figure 22C).

However, the number of downregulated DEP increases with the strength of *PpFLOT* expression (Figure 22C, Supplementary Table 19). This analysis shows that *PpFLOT*-OEX3

displays the largest modification in its proteomics profile with 160 DEP, compared to *PpFLOT-OEX1* and *PpFLOT-OEX2*, which display 36 and 31 DEP, respectively, which are specific to these lines and do not overlap with any of the other two overexpression lines. However, 20 DEP were found to be differentially accumulated in all three lines (Figure 22B, Supplementary Table 19). Notably, among these, 14 proteins (including *PpFLOT*) displayed either a $\log_2(\text{FC}) \leq -2$ and $\geq +2$ or a correlated DE to the strength of *PpFLOT* expression (Figure 22D, Table 9 and Supplementary Table 19). THIOREDOXIN Y2 (*PpTRX-Y2*) (Pp3c26_10440/A0A2K1IC14), HEAT SHOCK COGNATE PROTEIN 70-1 (*PpHSP70-1*) (Pp3c4_21500/ A9TRK2) and one unknown protein (A0A7I4CH40) showed decreased protein levels.

TRX-Y2 plays a role in oxidative stress response signaling pathways in chloroplasts (Geigenberger et al., 2017; Wittmann et al., 2021), while *PpHSP70-1* is a cytosolic HSP70 involved in protein trafficking and maintenance (Cazalé et al., 2009; Shi and Theg, 2010; Leng et al., 2017). Double mutants of functionally redundant HSP70-1 and -4 in *A. thaliana* exhibited salt hypersensitivity and ABA hyposensitivity (Leng et al., 2017). Conversely, HSP70-1 overexpression lines showed increased tolerance to abiotic stress, including salinity stress (Cazalé et al., 2009). Therefore, the downregulation of both *PpTRX-Y2* and *PpHSP70-1* might contribute to the altered salt sensitivity and response to enhanced osmotic pressure in *PpFLOT-OEX* lines.

Additionally, a homolog to *A. thaliana* PECTIN METHYLESTERASE 53 (*PpPME53*) (Pp3c5_12660/ A0A2K1KJF2) and EXPANSIN A9 (*PpEXPA9*) (Pp3c12_4560/Q84V44) are both upregulated in all *PpFLOT-OEX* lines. Since both proteins are involved in restructuring the cell wall (Li et al., 2002; Cosgrove, 2015; Gigli-Bisceglia et al., 2022) and cell wall integrity is an important factor during salt sensing (Shin et al., 2021; Gigli-Bisceglia et al., 2022), these differences in expression might influence the salt sensing capability of the *PpFLOT-OEX* lines. Besides these cell wall-related proteins, two proteins related to electron transport in mitochondria, NADH DEHYDROGENASE UBIQUINONE IRON-SULFUR PROTEIN 8 (*PpNDUFS8*) (Pp3c15_4330 /A9SIS3) and NADH-ubiquinone oxidoreductase B8 subunit (*PpNDUFA2/B8*) (Pp3c20_8510 /A0A2K1IUJ9) were upregulated, indicating increased respiration due to *PpFLOT* overexpression (Klodmann and Braun, 2011; Domergue et al., 2022). Also, the *A. thaliana* MATERNAL EFFECT EMBRYO ARREST 51 (*MEE51*) homolog (Pp3c2_11980/A0A2K1L177) is upregulated. *PpMEE51* belongs to the phosphofructokinase family and its upregulation might indicate an increasingly anoxic environment in the *PpFLOT-OEX* lines since both ATP-dependent phosphofructokinases (PFK) and pyrophosphate-fructose-6-phosphotransferases (PFP) are upregulated in *O. sativa* upon anoxia (Mustroph et al., 2013). Furthermore, knockout of *PpNDUFS8* homolog in *A. thaliana* led to increased lipid

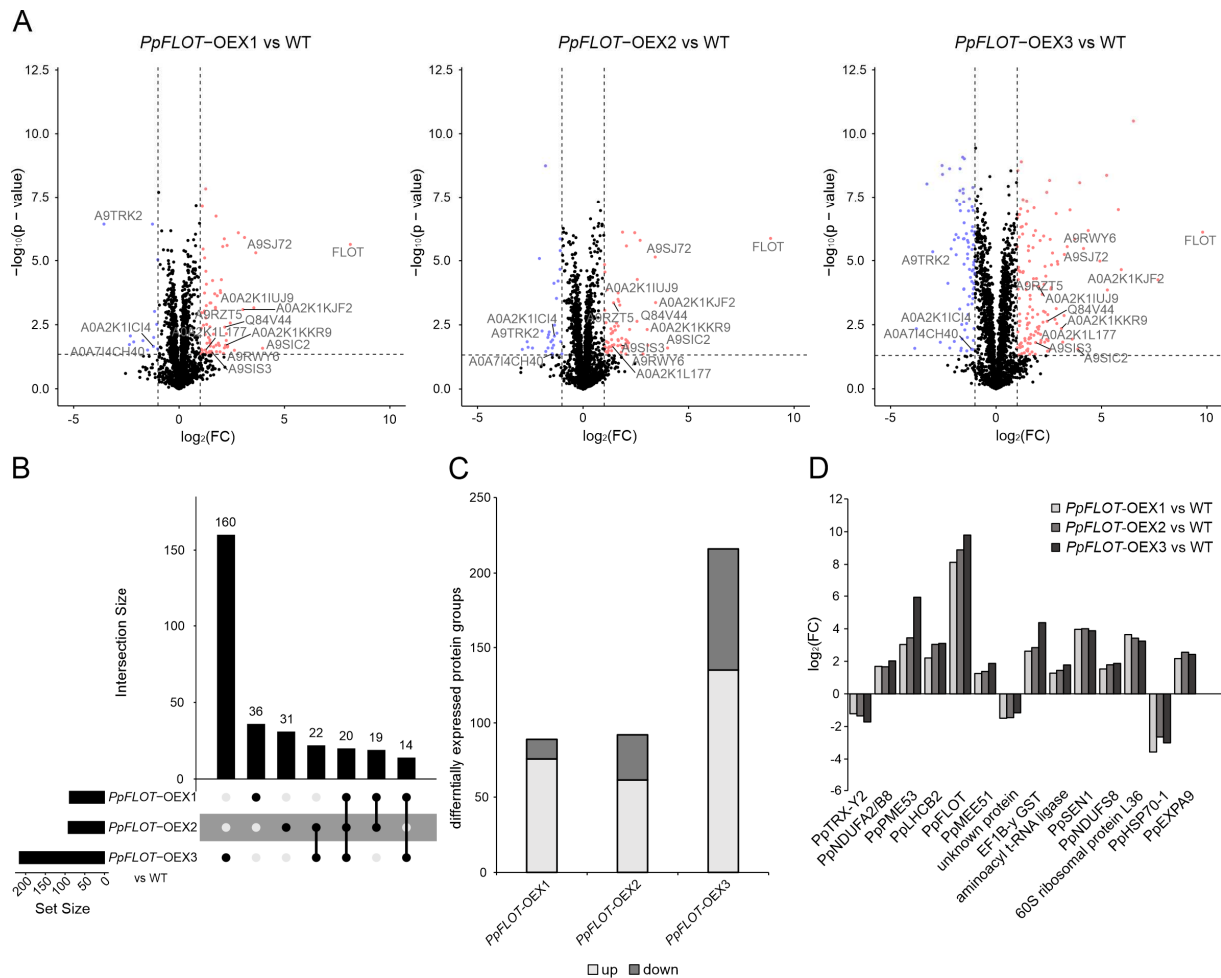


Figure 22: Identification of differentially expressed protein groups in all *PpFLOT*-OEX lines

(A) Volcano plots of all differentially expressed protein groups (DEP) identified by Student's *t*-test with $p < 0.05$ and permutation-based false discovery rate (FDR) $q < 0.05$ using WT expression as the control group. All DEP exhibited a $\log_2(\text{FC})$ of < -1 and > 1 . UniProt protein ID was added to the DEP common in all *PpFLOT*-OEX lines and either correlating with the *PpFLOT* expression or showing a $\log_2(\text{FC})$ of < -2 and > 2 . Downregulated DEPs are denoted in blue and upregulated DEPs are denoted in red. (B) UpSet plot of all identified DEP in the three *PpFLOT*-OEX lines. (C) Bar chart showing the amount of up- or downregulated DEP in all three *PpFLOT*-OEX lines. (D) Bar chart shows 14 common DEP between the three *PpFLOT*-OEX lines, either showing a *PpFLOT* correlating expression or a $\log_2(\text{FC})$ of < -2 and > 2 . DEP: PpTRX-Y2 (A0A2K11C14); PpNDUFA2/B8 (A0A2K11UJ9); PpPME53 (A0A2K1KJF2); PpLHCB2 (A0A2K1KKR9); PpFLOT (A0A2K1KVH5); PpMEE51 (A0A2K1L177); unknown protein (A0A7I4CH40); EF1B- γ Glutathione S-transferase (A9RWY6); aminoacyl t-RNA ligase (A9RZT5); PpSEN1 (A9SIC2); PpNDUFS8 (A9SIS3); 60S ribosomal protein L36 (A9SJ72); PpHSP70-1 (A9TRK2); PpEXPA9 (Q84V44).

content, suggesting that its higher expression in *P. patens* might also lead to changes in the lipid profile (Domergue et al., 2022).

An EF1B- γ Glutathione S-transferase (GST) (Pp3c18_20060/A9RWY6) is also upregulated. In plants, GSTs are not only involved in the abiotic but also in the biotic stress response (Gullner et al., 2018; Hernández Estévez and Rodríguez Hernández, 2020). Interestingly, while the transcript expression analysis in *PpFLOT*-OEX1 revealed a suppression of *PpLHCB1* and *PpLHCA1.1*, PpLHCB2 (Pp3c5_22920/A0A2K1KKR9) displayed increased levels in all three *PpFLOT*-OEX lines.

It is noteworthy that PpLHCB2 was the sole PS antenna component that displayed a change in protein level. Additionally, a Rhodanese-containing protein, homologous to *A. thaliana* SENESCENCE 1 (AtSEN1), also known as DARK INDUCIBLE 1 (AtDIN1) (Pp3c16_18500/A9SIC2), exhibited elevated protein levels. Similar to *PpFLOT*, *AtSEN1* expression is induced in darkness and exhibits increased transcript levels in response to bacterial infection (Schenk et al., 2005; Fernandez-Calvino et al., 2016). Furthermore, *AtSEN1* participates in senescence (Fernandez-Calvino et al., 2016). Thus, the dependence of PpSEN1 accumulation on PpFLOT suggests a role for PpFLOT in the pathogen response.

3.2.12 Overexpression of *PpFLOT* leads to changes in the fatty acid profile and increases monogalactosyldiacylglycerol (MGDG) accumulation

Chloroplasts do not only serve as the site of photosynthesis, but also for multiple metabolic pathways, including FA biosynthesis (Block et al., 2007; Eberhard et al., 2008; Johnson, 2016; He et al., 2020). FA are essential building blocks for many metabolic compounds, including the cuticle layer that covers the outer cell wall of *P. patens* and plasma membrane components (Renault et al., 2017; Resemann et al., 2019; Batsale et al., 2021). Previous studies have shown that plasma membrane fluidity and cell wall structure are crucial factors during the abiotic stress tolerance, particularly during drought and cold stress of *P. patens* and *A. thaliana* (Bhyan et al., 2012; Barrero-Sicilia et al., 2017; Batsale et al., 2021). Moreover, increased salt concentrations lead to changes in the cell wall composition, which, in turn, activate the salt stress response (Gigli-Bisceglia et al., 2022). Since the salt tolerance of the *PpFLOT*-OEX lines is severely impaired, the relative conductivity for all *PpFLOT*-OEX lines and a WT control was measured during cold stress. Observations of the relative conductivity in a temperature range of 0 °C to -7 °C for all tested genotypes revealed that the electrolyte leakage, and in turn, relative conductivity, increased in correlation with increased *PpFLOT* expression (Figure 23A). However, the variances between the measured replicates were too high to make a statistically significant statement on the data distribution.

LC-MS Analysis of the lipid profile of $\Delta PpFLOT-1$ and all *PpFLOT*-OEX lines revealed significant changes in their respective lipid levels with 27 differentially accumulated lipid classes in $\Delta PpFLOT-1$, 13 in *PpFLOT*-OEX1, 17 in *PpFLOT*-OEX2 and 26 in *PpFLOT*-OEX3 (Table 10 and Supplementary Table 20). Interestingly, there was little overlap of the differentially abundant lipid classes among the four *PpFLOT* mutant lines. Only one lipid class, FA 20:4 (arachidonic acid), displayed significantly altered accumulation levels in all tested lines (Figure 23B, Table 10 and Supplementary Table 20). When comparing the *PpFLOT*-OEX lines, only digalactosyldiglyceride (DGDG) 34:6 and arachidonic acid were found to be differentially abundant in all lines (Figure 23B, 23C, Table 10 and Supplementary Table 20), with DGDG 34:6 decreasing and arachidonic acid increasing in the three overexpression lines correlating

with the level of *PpFLOT* expression (Figure 23C). Similar to the results of the pigment and protein profile analyses, *PpFLOT*-OEX3 showed the greatest alterations in its lipid profile with 10 additional differentially accumulated lipid classes compared to the other *PpFLOT* mutant lines. Interestingly, when looking for lipid classes that display altered levels in at least one *PpFLOT*-OEX line and show a change in the abundance correlating with the *PpFLOT* expression, one linolenic acid (FA 18:2) derivate displayed both. Similarly, the FA heptadecane acid (FA 17:0), ethyl linoleate (FA 20:2), heneicosanoic acid (FA 21:0) and triacontanoic acid

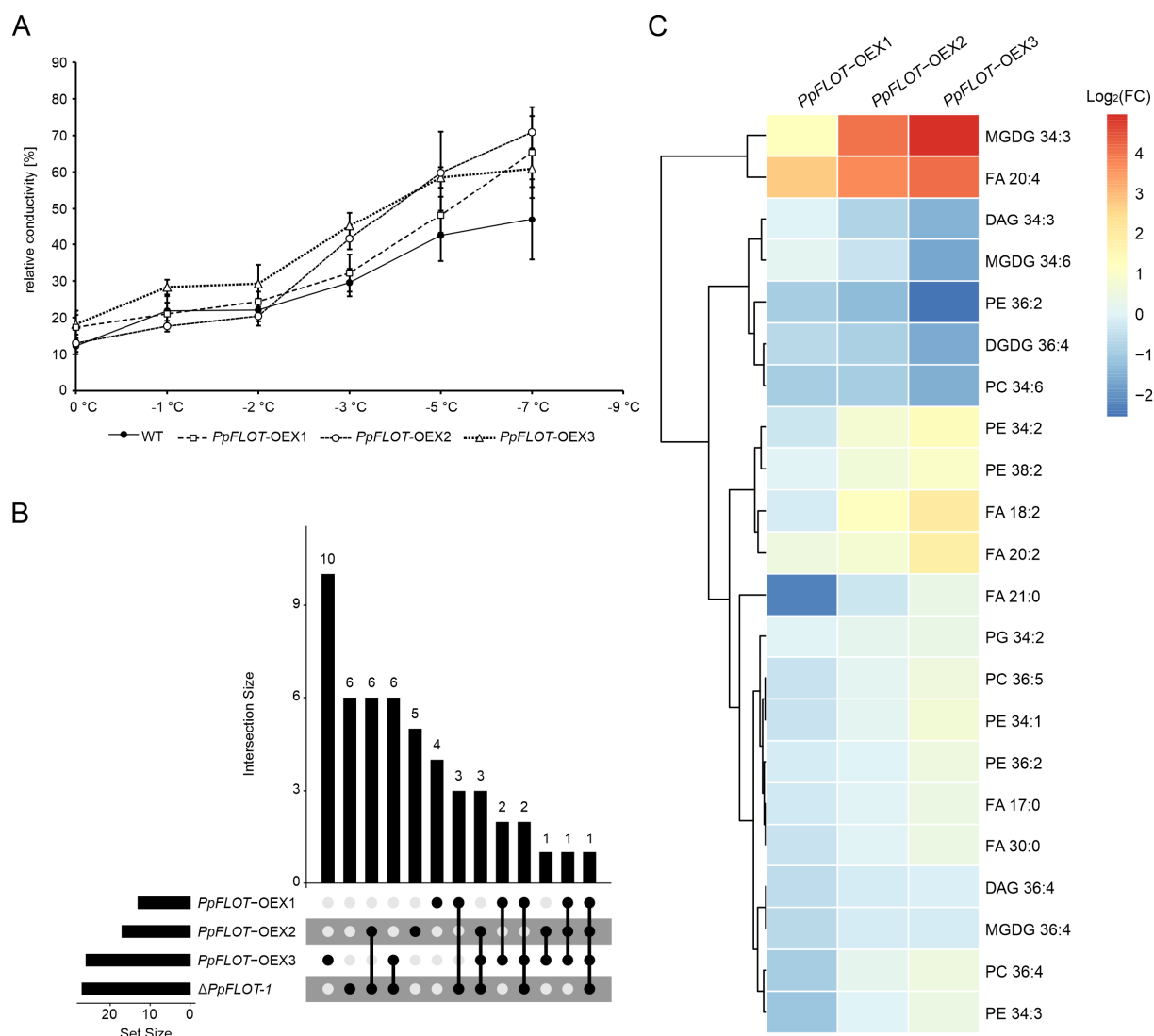


Figure 23: Analysis of changes in the lipid profile of *PpFLOT* mutant lines

(A) Conductivity measurements of 5 mg WT and *PpFLOT*-OEX gametophores cultivated for 11 weeks on solid medium at decreasing temperatures. Mean values \pm SEM ($n = 3$) of the relative conductivity are shown. **(B)** Upset plot depicting the overlap of all identified differentially expressed (DE) lipids between $\Delta PpFLOT-1$ and all *PpFLOT*-OEX lines compared to the WT. Lipid levels are labeled as differentially accumulated when Student's *t*-test using WT expression as control yielded $p < 0.05$ and the permutation-based false discovery rate (FDR) $q < 0.05$. **(C)** Clustered heatmap showing the $\log_2(FC)$ of DE lipids of all *PpFLOT*-OEX lines. Lipids that show altered abundance in at least one line correlating to the amount of PpFLOT are displayed.

(FA 30:0) showed their lowest abundance in the *PpFLOT*-OEX1 and their highest abundance in *PpFLOT*-OEX3 (Figure 23C). In addition to the FA, the glycerophosphoglycerol (PG) PG 34:2, glycerophosphocholines (PC) and phosphatidylethanolamine (PE) displayed similar behavior with the exception of PC 34:6 and PE 36:2, whose levels decreased with increasing *PpFLOT* expression (Figure 23C). Besides decreased DGDG 36:4 levels, MGDG 34:6 and 36:4 also displayed a low abundance. However, MGDG 36:4 shows higher levels in *PpFLOT*-OEX3 compared to *PpFLOT*-OEX1 and 2.

Although these MGDG species displayed lower levels in all three *PpFLOT*-OEX lines compared to the WT, MGDG 34:3 was upregulated and correlated with the *PpFLOT* expression. This, combined with the general increase in the arachidonic acid pool, demonstrates the strongest effect of increasing *PpFLOT* expression on the lipid profile. These changes in the lipid profiles in the *PpFLOT*-OEX lines indicate alterations in the composition of thylakoid membranes, attributed to variations in the abundance of DGDG and MGDG classes, which are primary constituents of thylakoid membranes. Additionally, the levels of FAs, crucial for cell wall component biosynthesis, potentially impacting the cell wall composition and subsequently, the sensitivity of these lines to abiotic stress, appear to be influenced by *PpFLOT* expression. Furthermore, the accumulation of arachidonic acid in *PpFLOT*-OEX plants suggests a potential role in plant defense mechanisms, as low concentrations can induce systemic resistance against pathogens, while high concentrations may lead to necrosis and phytoalexin accumulation (Dedyukhina et al., 2014). Arachidonic acid serves as precursor for oxylipins, oxygenated derivatives involved in plant defense, implying potential alterations in oxylipin biosynthesis and pathogen response, thus highlighting the involvement of *PpFLOT* not only in abiotic stress responses but also in pathogen defense mechanisms (Blée, 2002).

3.2.13 *PpFLOT*-OEX affects grana stack assembly and enlarges the thylakoid lumen

Since *PpFLOT* localizes to the thylakoid membrane and alterations in thylakoid-membrane-related proteins were observed in response to changes in the *PpFLOT* expression, it was hypothesized that chloroplast structure might be impacted by *PpFLOT* overexpression. Transmission electron microscopy (TEM) analysis of chloroplast structures revealed significant deviations in the *PpFLOT*-OEX lines compared to WT and $\Delta PpFLOT-1$, characterized by disordered thylakoid membranes, disrupted grana stacks and enlarged thylakoid lumens (Figure 24). Interestingly, similar thylakoid alterations have been reported under high-light stress in chlorophyte species and in seed plants during cold stress adaptation and salt treatment (Gorelova et al., 2019; Venzhik et al., 2019). Furthermore, examination of cell wall structure revealed a potential increase in cuticle layer density with increasing *PpFLOT* levels

(Figure 24), possibly indicating changes induced by *PpFLOT* expression, supported by observed alteration in relative conductivity and FA abundance in *PpFLOT*-OEX lines.

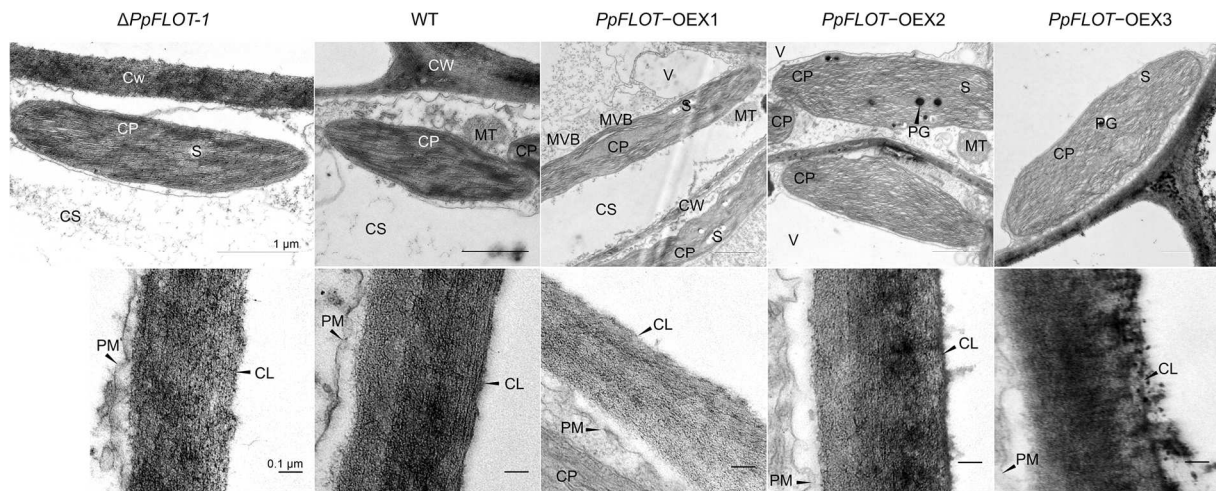


Figure 24: Altered *PpFLOT* expression leads to changes in the chloroplast thylakoid structure

Transmission electron microscopy (TEM) images of complete chloroplasts (upper panel) in protonema cells of *ΔPpFLOT-1*, WT and all three *PpFLOT*-OEX lines, along with close-up images of the cell wall in the respective lines (lower panel), are shown. Structural abbreviations include: chloroplast (CP), cytosol (CS), mitochondria (MT), cell wall (CW), plasma membrane (PM), vacuole (V), starch granula (S), plastoglobuli (PG), cuticle layer (CL) and multivesicular bodies (MVB). Scale bars represent 1 μm (upper panel) and 0.1 μm (lower panel), respectively.

4 Discussion

4.1 Discussion Question 1 - How does the loss of DCL genes influence the phytohormone response, salt tolerance, gene expression and the sRNA profile of *M. polymorpha*? Does the function of MpDCLs differ from those in *P. patens*?

4.1.1 Phylogenetic analysis reveals new bryophyte- and fern-specific DCL class

DCL proteins are functionally conserved proteins and play crucial roles during the water-to-land transition. Adaptation to challenging environments increased and diversified DCLs in land plants (Wang et al., 2021a). While DCL1a, DCL2, DCL3 and DCL4 are major members present in most land plants, some monocots also encode DCL5 (Wang et al., 2021a). Consistent with previous studies, this phylogenetic analysis confirmed that *M. polymorpha* harbors four DCLs: MpDCL1a, MpDCL1b, MpDCL3 and MpDCL4. With the exception of MpDCL1b, these MpDCLs harbor RESIII, Helicase C, PAZ, Dicer-dimer, two adjacent RNase III and at least one double-strand RNA binding domain. These three DCLs show high similarity to homologs in *P. patens*. While MpDCL1a and MpDCL3 have the same domain structure as their counterparts, PpDCL1a and PpDCL3, in *P. patens*, MpDCL4 contains an additional DND1_DSRM domain compared to PpDCL4. Interestingly, MpDCL1b harbors RESIII, PAZ and two adjacent RNase III domains, whereas PpDCL1b contains additional Helicase C, Dicer-dimer and DND1_DSRM domains. With the phylogenetic analysis, potential ancestry DCLs that only encode some of the domains otherwise present in land plants could be identified. Furthermore, this analysis identified DCL1, DCL3 and DCL4 homologs in all analyzed hornwort species. The comparative phylogenetic analysis revealed that additional moss and fern species encode DCLs that lack important domains, similar to MpDCL1b. Interestingly, this type of MpDCL1b homolog could only be identified in moss and fern species and not in seed plants or in the tested algae species, implying that this type of DCL might be important for the initial stage of plant terrestrialization and may then be lost during the course of evolution. Furthermore, this type of DCL was detected in *P. patens* as well. Hence, I propose that MpDCL1b and PpDCL1b evolved independently from each other and MpDCL1b might serve different roles in sRNA biogenesis.

4.1.2 Altered MpDCL1a guided miRNA biogenesis leads to severe developmental defects

DCL1 homologs, such as PpDCL1a and AtDCL1, are essential for miRNA biogenesis, the generation of *DCL1* null mutants results in either developmentally arrested plants, as seen in *P. patens* (Khraiweh et al., 2010) and *O. sativa* (Liu et al., 2005) or embryonic lethality, as observed in *A. thaliana* (Henderson et al., 2006; Arif et al., 2013). Since no *Mpdc1a^{ae}* mutant line with large genomic rearrangements or early stop codons could be identified, it is highly probable that *MpDCL1a* null mutants are lethal. The detected mutations in the *MpDCL1a* gene,

which led to specific amino acid exchanges and additions, resulted in severe developmental abnormalities, including stunted growth and inhibition of gemmae cup formation. This is similar to the drastic phenotypic abnormalities in the $\Delta PpDCL1a$ mutant line (Khraiwesh et al., 2010; Arif et al., 2022). The phylogenetic analysis and the observed phenotypic aberrations in the mutant lines suggest that MpDCL1a is a PpDCL1a homolog and most likely modulates miRNA biogenesis in *M. polymorpha*. This observation is supported by the sequencing analysis, which shows the highest number of DE mature miRNAs and subsequently also the highest number of DEG in *Mpdc1a^{ge}*. Furthermore, these identified DEG also contained the highest ratio of putative miRNA-regulated genes compared to the other *Mpdc^{ge}*. However, due to the mutations in regions encoding the restriction enzyme subunit (RESIII domain) within MpDCL1a, miRNA biogenesis is likely not completely abolished but severely altered. I hypothesize that error-prone cleavage of sRNA precursors occurs in this line, contributing to the detected DE of certain miRNAs and their potential targets. Moreover, an unexpected rise in the 24 nt sRNA populations of *Mpdc1a^{ge}* was detected, supporting the hypothesis that error-prone cleavage of sRNA precursors occurs in this line. This faulty cleavage most likely contributes to the detected DE of certain miRNAs and their potential targets. For instance, the constitutive expression of MpTAA has been reported to lead to slight growth inhibition, similar to the effects of exogenous auxin treatment (Eklund et al., 2015). Thus, its 2.8-fold upregulation in *Mpdc1a^{ge}* most likely contributes to the observed stunted growth. Auxin acts in the establishment of the dorsoventral polarity, rhizoid and gemmae cup formation, developmental stage transition and determines the overall body plan as well as branching patterns in *M. polymorpha* (Flores-Sandoval et al., 2015; Flores-Sandoval et al., 2018b). Interestingly, the auxin-related transcription factor MpC2HDZ, that displayed decreased levels in *Mpdc1a^{ge}*, is positively regulated by MpARF3 (Flores-Sandoval et al., 2018a) and can be induced by auxin (Flores-Sandoval et al., 2018b, Mutte et al., 2018). I identified putative miRNAs that regulate MpC2HDZ, one of which was expressed in an anticorrelated manner. Even though MpTAA is upregulated, MpC2HDZ expression is suppressed due to the DE of its putative regulating miRNAs. Since HD-ZIP transcription factors also regulate plant response to abiotic stresses, the miRNA-dependent downregulation of MpC2HDZ most likely contributes to the observed increased salt tolerance of *Mpdc1a^{ge}* (Romani et al., 2016, Li et al., 2022b). Moreover, even though most of the detected DEG could be annotated, many of them had to be classified as genes of unknown function due to limited publicly available bioinformatic resources. Validation of these genes might further elucidate the connection between MpDCL1a miRNA processing and auxin signaling in *M. polymorpha*.

In addition to the auxin-related genes, cytokinin- and ethylene-related genes were also affected. Suppression of cytokinin severely impairs the development of gemmae cup initiation (Aki et al., 2019; Aki et al., 2022). The suppression of MpCKX1 in *Mpdc1a-6^{ge}*, one of the

inactivators of cytokinin by catalyzing its degradation (Frebortova, 2010; Avalbaev et al., 2012), most likely indicates disturbed cytokinin levels or response, which might contribute to the inability of this line to develop gemmae cups.

One of the miRNAs that was upregulated together with *MpTAS3* in *Mpdcl1a-6^{ge}* is miR390. MiR390 targets and mediates the processing of *MpTAS3* precursors to enable the generation of AP2 ta-siRNAs by *MpDCL4* (Krasnikova et al., 2013; Tsuzuki et al., 2016). An increase in DE 21 nt sRNAs was also detected in *Mpdcl1a-6^{ge}*. This increase, in addition to the altered miRNA expression, is most likely the result of increased ta-siRNA production due to higher miR390 levels. As a consequence, a range of mRNAs coding for AP2/ERF transcription factors are downregulated in *Mpdcl1a-6^{ge}*, which might contribute to the increased salt tolerance and enhanced phytohormone sensitivity of this line.

In the *Mpdcl1a-6^{ge}* mutant multiple DE *MpABCG* transporters were identified and their corresponding miRNAs showed an anticorrelated expression. Since these transporters are part of the intracellular ABA signaling in *A. thaliana* (Kuromori and Shinozaki, 2010), their DE might contribute to the increased ABA sensitivity of *Mpdcl1a-6^{ge}*. In addition to these transporters, the transcription factors *MpGARP2*, *MpbHLH30*, *MpbHLH37* and *MpR2R3-MYB8* were all DE and are potentially regulated by at least one anticorrelating miRNA, further confirming that *MpDCL1a* is the main contributor to miRNA biogenesis.

Previous reports showed that altered miRNA expression can influence the normal gametangiophore development of *M. polymorpha* (Tsuzuki et al., 2019; Yamaoka et al., 2021). Therefore, in *Mpdcl1a-6^{ge}*, DE miRNAs might contribute to the observed inability of this line to develop sexual reproductive organs. Interestingly, *MpFGMYB* levels increased and one putative miRNA, mpo-MIR11802 (mpo-b3.0r1-3564), was expressed in an anticorrelated manner. *MpFGMYB* is the main driver of the female sexual dimorphism in *M. polymorpha* as its deletion in the female lines leads to development of sterile antheridiophores, while ectopic expression in male individuals results in the development of archegoniophores (Hisanaga et al., 2019; Cui et al., 2023). Typically, *MpFGMYB* is barely expressed under white light as its expression is activated by far-red light irradiation in the apical notch (Cui et al., 2023). However, two weeks old vegetative thalli displayed increased levels of *MpFGMYB* without prior far-red light induction. Thus, its ectopic expression might not only contribute to the observed developmental alterations but also hinder proper gametangiophore induction.

4.1.3 Alterations in the miRNA levels of *Mpdcl1b^{ge}* lead to an increased salt tolerance

Mutations in the *MpDCL1b* gene did not affect gemmae germination or thallus development, but they increased salt stress tolerance compared to the WT and the other *MpDCL* mutant lines. Interestingly, the expression data taken from the Marchantia Atlas eFP browser

(http://bar.utoronto.ca/efp_marchantia/cgi-bin/efpWeb.cgi) show that *MpDCL1b* and *MpDCL1a* are slightly downregulated upon salt treatment in the analyzed Tak-1 plants cultivated for 15 DAG under the respective stress condition (Tan et al., 2023). While these measurements were conducted in the TAK genotype and the BoGa line used in this study might display a slightly different abiotic stress response, these reports support the hypothesis that both *MpDCL1a* and *MpDCL1b* play a role in the salt stress response. The enriched GO terms of *Mpdc1a-6^{ge}* showed an overlap with the enriched GO terms of the salt-treated WT, which might explain the increased salt tolerance of *Mpdc1a-6^{ge}*. In contrast, sRNA expression was barely altered in the *Mpdc1b^{ge}* lines in response to salt treatment. While mature miRNAs were DE upon salt treatment, they did not overlap with the DE miRNAs in the salt-treated WT. Moreover, among all *Mpdc^{ge}* mutants, the *Mpdc1b^{ge}* lines showed the lowest number of DEG under control conditions and when treated with salt, the number of DEG was significantly lower than in the salt-treated WT. However, one notable change in the gene expression profile in *Mpdc1b^{ge}* is the upregulation of cyclin kinases. Reduced cyclin kinase expression is one of the growth-limiting factors during salt and drought stress in plants. Therefore, the elevated expression of cyclin kinases in salt-treated *Mpdc1b^{ge}* might contribute to its enhanced salt tolerance (Qi and Zhang, 2019).

I have extensively investigated the role of *PpDCL1a* on salt tolerance. For instance, the abolishment of the miR1047-dependent autoregulatory feedback loop of *PpDCL1a* leads to increased *PpDCL1a* expression, altered miRNA levels and salt hypersensitivity (Arif et al., 2022). While an increased expression of *MpDCL1a* in the *Mpdc1b^{ge}* lines could not be confirmed, the loss of *MpDCL1b* clearly affects the *MpDCL1a*-guided miRNA biosynthesis in response to elevated salt concentrations. Furthermore, both *Mpdc1a^{ge}* and *Mpdc1b^{ge}* lines show increased salt tolerance compared to the WT. Since *Mpdc1b^{ge}* displayed minimal changes in the expression of sRNA and miRNAs compared to *Mpdc1a^{ge}*, I propose that under standard conditions, *MpDCL1b* does not affect the *MpDCL1a*-guided miRNA biosynthesis. However, during the salt stress response *MpDCL1b*-dependent pathways are activated, directly or indirectly regulating *MpDCL1a* activity, thereby leading to the observed changes in sRNA and mRNA expression in the salt-treated WT, which are absent in the salt-treated *Mpdc1b^{ge}*.

MpDCL1b might not only play a crucial role in the salt stress response but also in the response to other abiotic stresses like drought, cold, high light, flooding and heavy metal concentration, making an interesting point of study in the future. A phylogenetic analysis revealed homologs of *MpDCL1b* were identified in *A. punctatus*, *S. fallax*, *S. magellanicum*, *C. purpureus*, *P. patens*, *D. complanatum*, *A. filiculoides*, *S. cucullata*, *C. richardii*, *A. agrestis* and in *S. cucullata*. All these homologs encode one PAZ and two adjacent RNase III domains,

suggesting some degree of evolutionary conservation in bryophytes and ferns. Interestingly, *A. filiculoides* exhibits high tolerance to heavy metal accumulation (Chen, 2022) and shows a similar sensitivity to elevated salt concentrations as *M. polymorpha* as the growth of *A. filiculoides* is adversely affected when cultivated at 30 mM NaCl (Masood et al., 2006).

However, the abiotic stress tolerance of these species still requires extensive study. Nonetheless, the identified DCL-like ribonucleases might fulfill similar functions to MpDCL1b in *M. polymorpha*. An in-depth investigation of MpDCL1b and its homologs in other species might further elucidate the evolutionary relationships of bryophytes and tracheophytes.

To gain indications of the potential function of MpDCL1b, which might have been lost in seed plants, I searched for salt-induced or salt-sensitive Ribonucleases in other species. It is possible that MpDCL1b and its homologs are responsible for generating an entirely different sRNA class capable of regulating miRNA expression, which lost its importance during the plant terrestrialization. Recently, it was shown that *cis*-encoded antisense RNAs (asRNAs) modules in the cyanobacterium *Synechocystis* sp. PCC 6803 can be activated by salt stress. These asRNAs can act as regulators for their target mRNAs or sRNAs (Klahn et al., 2021). While that study predominantly focused on asRNA-guided regulation of protein-coding transcripts activated by salt, a similar regulatory mechanism might exist for miRNAs or sRNAs in *M. polymorpha*. Whether such specific salt-activated asRNAs are generated in *M. polymorpha* and other bryophytes remains to be seen and needs to be the subject of intensive studies before any definitive conclusion can be drawn. However, barely any detected 22-24 nt sRNAs were DE in salt-treated *Mpdcl1b^{ge}* when compared to the untreated control. Especially, the 24 nt sRNA populations show a peculiar behavior in the salt-treated *Mpdcl1b^{ge}* with no DE candidates, indicating vastly different sRNA expression compared to the salt-treated WT. This marks the DE 24 nt sRNAs in salt-treated *Mpdcl1b^{ge}* compared to the salt-treated WT as candidates for a potentially salt-induced, miRNA-regulating sRNA class that has not yet been defined in land plants.

4.1.4 MpDCL3 loss of function leads to altered expression of pathogenesis-related genes

DCL3 is responsible for generating siRNAs derived from repetitive regions and transposable elements in land plants and these siRNAs participate in transcriptional silencing through the regulation of epigenetic modifications such as RNA-dependent DNA methylation or histone modifications (Henderson et al., 2006; Moura et al., 2019). In *P. patens*, PpDCL3 is required for the accumulation of 22–24 nt siRNAs and $\Delta PpDCL3$ gene deletion mutants display accelerated gametophore development (Cho et al., 2008). Similarly, *Mpdcl3^{ge}* lines developed shorter thallus branches and showed accelerated branching compared to the WT. Moreover, the aberrant phenotype observed in *Mpdcl3^{ge}* was reverted to a wild-type-like growth pattern

by exogenous auxin treatment, suggesting a potential role of MpDCL3 and its associated sRNAs in modulating auxin-responsive genes. Surprisingly, a search for known auxin-related genes revealed MpTAA as the only candidate potentially responsible for this phenotype. MpTAA is upregulated in *Mpdcl3^{ge}* lines and is a crucial component during tryptophan-dependent auxin biosynthesis (Zhao, 2012). Moreover, ectopic expression of MpTAA inhibits plant growth in *M. polymorpha*, similar to exogenous auxin treatments (Eklund et al., 2015). However, if the observed rosette-shaped body plan is the result of enhanced auxin production, exogenous auxin treatments should not revert plant development to the WT body plan but enhance it. Interestingly, cultivating multiple plants on auxin-containing medium enhances the reversion to the WT body plan. Recent reports have shown that cultivating *A. thaliana* seedlings on medium containing RNA extracts from *miR399* and *miR156* overexpression plants leads to repression of their targets in the treated seedlings. Moreover, when the WT was cultivated in close proximity to a miRNA overexpression plant, their targets were suppressed in the WT as well (Betti et al., 2021). This demonstrates that communication with neighboring plants by miRNA secretion is possible. Thus, the enhanced phenotype of *Mpdcl3^{ge}* when cultivated at higher densities on auxin-containing medium might be the result of the excretion of miRNAs or other sRNA classes that are overexpressed in these lines. Another possible explanation for the observed phenotype might be that among the identified DEG of unknown function in *Mpdcl3^{ge}* are factors that influence the auxin homeostasis and contribute to the observed phenotype.

Mpdcl3^{ge} showed an overall upregulation of *PR-1* genes. *PR-1* genes are typically upregulated during viral and pathogen infections (Backer et al., 2019; Han et al., 2023) by MpNPR, which are SA-responsive (Backer et al., 2019). Altered endogenous SA levels in plants can lead to changes in growth phenotype in plants; for example, multiple *A. thaliana* mutants with increased SA levels exhibit overall stunted growth (Li et al., 2022a). High SA levels can also accelerate cell division in the root apical meristem of *A. thaliana*. Importantly, the effect of SA levels on plant growth varies among species (Li et al., 2022a). *M. polymorpha* encodes all the key components necessary for SA biosynthesis (Bowman et al., 2017; Gimenez-Ibanez et al., 2019) and exogenous SA treatment results in inhibited growth in *M. polymorpha* (Gimenez-Ibanez et al., 2019). The stunted thallus growth and accelerated branching observed in *Mpdcl3^{ge}*, resulting in a rosette-shaped body plan, could be attributed to increased endogenous SA levels. This is further supported by the observation that exogenous auxin treatment of *Mpdcl3^{ge}* leads to elongation of the thallus branches. Since SA is known to antagonize auxin (Alazem and Lin, 2015; Li et al., 2022a) the upregulation of MpTAA might indicate an attempt to increase the auxin production to counter elevated SA levels and the subsequent suppression of the auxin response. Furthermore, no change in expression of the MpNRP gene was detected in *Mpdcl3^{ge}*. Since it was recently reported that MpNRP is most likely not the only

regulator responsible for SA-induced transcriptional reprogramming in *M. polymorpha* (Jeon et al., 2023) the upregulation of MpPR-1 genes in Mp*dcl3^{ge}* is likely to be MpNRP independent. Interestingly, Mp*DIR*, Mp*LOX* and Mp*POD* genes were also downregulated in Mp*dcl3^{ge}*. Mp*LOX* genes are crucial for the biogenesis of JAs, including dnOPDA in *M. polymorpha* (Li et al., 2022a) and their suppression in the Mp*dcl3^{ge}* mutant might also be due to increased SA activity (Gimenez-Ibanez et al., 2019; Matsui et al., 2020; Li et al., 2022a). Furthermore, downregulation of *DIR* genes is also part of the pathogen defense mechanism in plants since selective suppression of *DIR* genes leads to reduced lignin biosynthesis, which in turn activates the expression of defense response genes (Paniagua et al., 2017). Resulting modifications of the lignin biogenesis in Mp*dcl3^{ge}* might further contribute to the observed rosette-shaped phenotype. One essential mechanism of the SA-guided defense mechanism is the initial accumulation of ROS. SA acts as a regulator of the ROS homeostasis during the pathogen defense. Moreover, this ROS accumulation is accomplished by inhibiting ROS-decomposing enzymes like ascorbate peroxidases (APX), CAT and POD (Hernández et al., 2016; Saleem et al., 2021). Thus, an artificially induced SA-guided pathogen-response in Mp*dcl3^{ge}* might also explain the detected 12 downregulated Mp*POD*. DCL proteins also contribute to antiviral defense. For instance, AtDCL2 and AtDCL3 generate siRNA from viral transcripts (Akbergenov et al., 2006) and AtDCL3 contributes to the AtAGO4 and AtDRB3-guided hypermethylation of the viral genome as part of the plant virus defense mechanism (Raja et al., 2014). AtDCL4 is a major producer of 21 nt viral-derived sRNAs in the plant viral defense (Bouche et al., 2006; Qu et al., 2008; Alvarado and Scholthof, 2009). Notably, when comparing the SA-mediated pathogen response to cucumber mosaic virus (CMV) in *A. thaliana* WT and *Atdcl2/3/4* triple mutants, no differences were observed in their immune defenses. This led to the proposition of the existence of DCL-independent SA-mediated pathogen defense mechanisms (Lewsey and Carr, 2009; Alazem and Lin, 2015). In Mp*dcl3^{ge}*, it is likely that the plant erroneously interprets the loss of MpDCL3 function as viral siRNA suppression, thus amplifying the SA-guided DCL-independent pathogen defense. This results in the observed growth phenotype as a secondary effect of SA on plant growth. Furthermore, the loss of DCL3 is not compensated by DCL4 as no DE of MpDCL4 was detected in the mRNA sequencing data from Mp*dcl3^{ge}*. Thus, MpDCL3 is most likely essential during viral infection and pathogen defense in *M. polymorpha* and might contribute to epigenetic regulation by processing repetitive transposable elements into hc-RNA and nat-siRNA, similar to its function in *A. thaliana* and *P. patens* (Cho et al., 2008; Arif et al., 2012; Wei et al., 2014).

The inability of Mp*dcl3^{ge}* to induce gametangiophore development might also be related to its contribution to methylation and epigenetic regulation through nat-siRNAs and hc-siRNAs. For instance, mutations in the RNA-directed DNA methylation (RdDM) pathway in rice can lead to plant sterility (Wang et al., 2022) and sRNA-dependent epigenetic programming is necessary

for proper female gamete development of *A. thaliana* (Olmedo-Monfil et al., 2010; You et al., 2022).

4.1.5 MpDCL4 is the major driver of ta-siRNA biogenesis

Phenotypic analyses of *Mpdcl4^{ge}* mutant lines under control conditions and upon exogenous phytohormone treatment did not reveal any differences compared to the WT. This is in stark contrast to *P. patens*, where the loss of the *PpDCL4* gene resulted in severe developmental defects, gravitropism insensitivity and sterility (Arif et al., 2012). A detailed analysis using the available Marchantia Atlas eFP browser (http://bar.utoronto.ca/efp_marchantia/cgi-bin/efpWeb.cgi) revealed that *MpDCL4* is barely expressed during thallus development but highly expressed in gametangiophores, especially in spermatid mother cells and the antheridial cavity. This tissue-specific expression suggests a possible function of *MpDCL4* and its associated sRNAs during gametangiophore induction.

On the other hand, ta-siRNAs regulate bud formation and the transition from 2D to 3D growth in *P. patens* (Cho et al., 2012). The discrepancy in phenotypic aberrations between *Mpdcl4^{ge}* and $\Delta PpDCL4$ lines may be due to the role and importance of *MpDCL4* in ta-siRNA biogenesis in *M. polymorpha*. Three miRNAs responsible for ta-siRNA biogenesis, as well as four *TAS* gene families, are present in *A. thaliana* (Allen et al., 2005; Arif et al., 2012), while all ta-siRNAs originate from four *TAS3* precursors in *P. patens* (Axtell et al., 2006; Arif et al., 2012). In contrast, only one *TAS* locus with two miR390 binding sites and expressing tasiR-AP2 has been identified in *M. polymorpha* (Tsuzuki et al., 2016) and its expression was drastically decreased in the *Mpdcl4-1^{ge}* line. In the same study, the authors detected high levels of 20–21 nt siRNA in antheridiophores derived from two additional loci without complementary miRNAs triggering their processing. These ta-siRNAs are designated as sex-specific phasing siRNAs (SS-phasiRNAs) and their processing is proposed to be executed by *MpDCL4* (Tsuzuki et al., 2016). The lack of detectable ta-siRNAs, together with the lack of phenotypic alterations under normal growth conditions in *Mpdcl4^{ge}* mutants, suggests that ta-siRNAs are not required to control *M. polymorpha* development but are crucial during the induction of the sexual organs. *Mpdcl4^{ge}* mutants displayed an increase in DE 21 nt sRNA, even though no changes in the expression of SS-phasiRNAs were detected. However, both the decreased salt stress tolerance and increased ABA sensitivity in *Mpdcl4^{ge}* mutant lines are most likely a result of the DE of ta-siRNA-regulated AP2/ERF transcription factors. Since ethylene promotes abiotic stress tolerance in *M. polymorpha* (Bharadwaj et al., 2022), the DE of *MpERFs* might impair ethylene signaling. Additionally, the GO term response to stress was significantly enriched and such DE factors might influence the salt response of *Mpdcl4^{ge}*. This GO term includes the previously mentioned 16 DE peroxidases. Since peroxidases are responsible for processing ROS (Pandey et al., 2017; Kidwai et al., 2020), a general upregulation might

indicate increased oxidative stress in *Mpdcl4^{ge}* under control conditions, which can no longer be tolerated when salt stressed. Another possibility is that altered sRNA expression in *Mpdcl4^{ge}* results in altered expression of sRNA-dependent salt-responsive genes, including peroxidases. In *A. thaliana*, 24 nt nat-siRNAs are produced by AtDCL2 to regulate Δ^1 -pyroline-5-carboxylate dehydrogenase (*AtP5CDH*) expression and subsequent proline and ROS accumulation during the stress response (Borsani et al., 2005). Since *M. polymorpha* does not encode an AtDCL2 homolog, similar functions might possibly be fulfilled by MpDCL4. I propose that MpDCL4 fulfills functions similar to PpDCL4, but the role and importance of ta-siRNAs and other MpDCL4 derived sRNAs differ between the moss *P. patens* and the liverwort *M. polymorpha*.

4.1.6 Influence of DE receptor kinases on ABA sensitivity

Treatment of all generated *Mpdcl^{pe}* lines with ABA revealed an increased ABA sensitivity in *Mpdcl1a^{ge}*, *Mpdcl3^{ge}* and *Mpdcl4^{ge}*. The increased ABA sensitivity in *Mpdcl1a^{ge}* can partially be explained by miRNA-dependent misregulation of MpABCG transporters. However, in *Mpdcl3^{ge}*, only one MpABCG transporter is DE and none in *Mpdcl4^{ge}*. This suggests that additional factors are influencing the ABA sensitivity of these lines. The ROOT MERISTEM GROWTH FACTORS /RGF INSENSITIVE-SOMATIC EMBRYOGENESIS RECEPTOR-LIKE KINASE (RGF/RGI-SERK) complex, in particular, regulates cell proliferation and root meristem maintenance in plants (Torii, 2004; Gou and Li, 2020; Furumizu and Sawa, 2021). Decreased expression of these growth regulators is the most likely driver of the stunted growth observed in *Mpdcl1a-6^{ge}*. Since some RLK protein kinases are also known to be ABA sensitive in *A. thaliana*, and some are crucial to relay the ABA signal (Jose et al., 2020), the aberrant expression of these kinases in *Mpdcl1a^{ge}*, *Mpdcl3^{ge}* and *Mpdcl4^{ge}* most likely leads to the observed ABA sensitivity of these lines. Interestingly, in all three lines, LRR-kinases and RLK/Pelle kinases are also DE. Since RLK is necessary for ABA-induced signal transduction (Ye et al., 2017; Jose et al., 2020), the DE of LRR and RLK kinases most likely increases their ABA sensitivity as well. However, a range of still uncharacterized genes were also DE. These genes might contribute to the ABA-sensitive phenotype and require extensive additional analysis.

4.2 Discussion Question 2 - Does the Band-7 protein FLOT modulate stress tolerance in *P. patens*? How is the expression of *PpFLOT* regulated? Are there differences in the function of bryophyte and seed plant FLOT?

4.2.1 Putative switch of function of bryophyte and seed plant FLOT

As mosses were among the first plants to adapt to life on land, the segregation of bryophyte FLOT in terms of function and localization from other plant FLOT is intriguing in the context of adapting to the new environment. The previously described observations suggest that both loss and overexpression of *PpFLOT* are less detrimental in the gametophore than in the protonema life stage of *P. patens*, indicating the involvement of *PpFLOT* in the water-to-land transition. Whether at least one FLOT variant is positioned in the chloroplasts of other bryophyte, fern or green algae species and what might have caused a shift in localization remains to be seen. To determine the most probable position of FLOT in the last common ancestor of land plants, further investigations in streptophyte algae, bryophytes and seed plants are required. However, it is suggested that FLOT was acquired through horizontal gene transfer from fungi into ancient plant lineages (Ma et al., 2022), supported by the localization of the fungus FLOT homolog, FloA of *Aspergillus nidulans*, to plasma membranes (Takeshita et al., 2012). Thus, it is highly likely that a change in FLOT localization was driven by exaptation of FLOT function in *P. patens* and potentially in other bryophytes. At the protonema stage, *PpFLOT*-OEX lines showed altered pigmentation when grown in liquid culture under normal growth conditions. No such changes were detected in the leafy gametophores grown on solid medium, implying greater importance of FLOT under either submerged conditions or at the developmental stage of protonema cells. Indeed, changes in the cell shape were observed in response to *PpFLOT* overexpression, reminiscent of ABA-induced brachyocytes that develop in *P. patens* as a survival mechanism in response to abiotic stress conditions (Arif et al., 2019). However, no significant changes were detected in the transcript expression of the ABA biosynthesis rate-limiting enzyme *PpNCED* (Hauser et al., 2011).

4.2.2 FLOT influences ABA sensitivity and might change Ca^{2+} signaling patterns

The accumulation of ABA levels to counter the increased *PpFLOT* levels is unlikely to be the only source of these changes, especially since 100 μM ABA is necessary to induce brachyocytes (Arif et al., 2019). However, accumulation of *PpLHCB2* correlated with increased *PpFLOT* levels. A study in 2012 showed that altered *LHCB* expression can influence ABA sensing and signaling (Xu et al., 2012), potentially affecting the ABA response in *PpFLOT*-OEX lines without impacting the ABA biosynthesis rate. Meanwhile, in *M. truncatula*, increased expression of *MtFLOT2* and 4 is crucial during nodule initiation upon infection with nitrogen-fixing bacteria (Haney and Long, 2010) and artificially activating Ca^{2+} /calmodulin-dependent protein kinase-interacting protein of DMI3 (CCaMK-IPD3) module in *P. patens* results in

constitutively developed brood cells (Kleist et al., 2022). The CCaMK-IPD3 module is activated by symbiotic infection and oscillating calcium signals (Lévy et al., 2004; Miller et al., 2013; Kleist et al., 2022), suggesting that the formation of round, brachyocyte-like cells in response to *PpFLOT* overexpression may involve slightly increased ABA levels and changes in Ca^{2+} signaling. Additionally, slight changes in *PpCRY1b* expression were detected and since Ca^{2+} waves in *P. patens* can be induced by light and altered by changes in cryptochrome expression (Tucker et al., 2005), the circadian-regulated putative scaffolding protein PpFLOT might be involved in light-dependent Ca^{2+} signaling. External signals such as light-dark cycle, salt, mannitol treatment and oxidative stress can influence Ca^{2+} dynamics between plastids and the cytosol (Sello et al., 2016; Martí Ruiz et al., 2020; Navazio et al., 2020).

4.2.3 PpFLOT's putative role in ion-homeostasis

It has been proposed that FLOT regulates the positioning of *A. thaliana* AQUAPORINE PIP1;2 (AtAPIP1;2) by initiating lipid rafts since AtAPIP1;2 colocalizes with AtFLOT1 (Browman et al., 2007; Li et al., 2011; Martinière and Zelazny, 2021). Thus, by altering the composition of the thylakoid membrane, FLOT may putatively regulate the positioning of ion channels. For instance, PpFLOT might be involved in altering membrane fluidity or colocalize with Ca^{2+} channels, determining their position in thylakoid membranes. Moreover, Ca^{2+} transporters might not be the only ion channels affected by this. The transcript expression analysis of the copper transport and HMA protein *Pp3c3_6890* showed a different response to ABA and salt treatment in *PpFLOT*-OEX1 than in both the WT and $\Delta PpFLOT-1$. The GO term analysis of all identified significant protein groups between WT and all *PpFLOT*-OEX lines also detected an effect of PpFLOT abundance on copper ion binding molecular function. Maintaining Cu homeostasis in chloroplasts is crucial, as Cu is a cofactor for the electron transporter plastocyanin (PCY), polyphenol oxidases (PPO) and Cu/Zinc superoxide dismutase (Cu/ZnSOD). PPO and Cu/ZnSOD participate in the biotic and oxidative stress protection, respectively (Aguirre and Pilon, 2015; Printz et al., 2016; Schmidt et al., 2020). Interestingly, no significant change in the abundance of these Cu-dependent proteins was detected. Nonetheless, the expression levels of other copper transporters similar to *Pp3c3_6890* might be affected, leading to changes in the copper homeostasis in *PpFLOT*-OEX lines. Further examination is necessary to determine if PpFLOT influences both Ca^{2+} signaling and copper transport.

4.2.4 PpFLOT is a negative regulator of the salt response

As a scaffolding protein, PpFLOT is likely involved in multiple pathways and can oligomerize with multiple proteins (Garbett and Bretscher, 2014; Daněk et al., 2016). However, overexpression of *PpFLOT* impairs the high tolerance of *P. patens* against salinity and osmolarity stress (Frank et al., 2005), suggesting an additional function as a negative regulator

during salt stress response. In response to long-term salt treatment, *PpFLOT* expression in WT is suppressed, likely due to elevated ABA levels since ABA is a signaling molecule initiating the abiotic stress response (Hauser et al., 2011) and suppressing *PpFLOT* expression. Interestingly, *PpTRX-Y2* and *PpHSP70-1* are both suppressed in correlation to elevated *PpFLOT* levels. *AtHSP70-1* participates in abiotic stress response regulation in *A. thaliana* (Cazalé et al., 2009; Leng et al., 2017), while *AtTRX-Y2* is a known regulator of the light-dependent (Valerio et al., 2011; Seung et al., 2013; Geigenberger et al., 2017) and osmotic stress-induced starch degradation via amylases (Valerio et al., 2011). *AtTRX-Y2* is also a crucial component of the antioxidative defense system in chloroplasts (Geigenberger et al., 2017). Hence, suppression of both proteins likely contributes to the observed altered salt tolerance (Figure 25). Although causality between *PpFLOT* expression and subsequent suppression of these two proteins is currently unknown, one can speculate about their relationship to *PpFLOT*. For example, HSP-70 proteins in plants drive protein translocation into organelles, including mitochondria and plastids (Shi and Theg, 2010; Berka et al., 2022). Downregulation of *PpHSP70-1* might be a way for the cells to impede *PpFLOT* transportation in the chloroplasts of *PpFLOT*-OEX lines. Furthermore, *AtTRX-Y2* reduces antioxidant enzymes, including peroxiredoxins (Collin et al., 2004; Jurado-Flores et al., 2020), glutathione peroxidases and methionine sulfoxide reductases (Vieira Dos Santos et al., 2007; Laugier et al., 2013; Vanacker et al., 2018). Thus, changes in *PpTRX-Y2* levels likely lead to the elevated ROS levels in response to elevated *PpFLOT* protein expression (Figure 25). Previous studies also showed that the LON DOMAIN-CONTAINING PROTEIN 1 suppresses *TRX-Y2* activity and regulates ROS levels by controlling *TRX-Y2* activity in *A. thaliana* (Shin et al., 2020). *PpFLOT* might putatively activate a similar protein in *P. patens*, and thus its overexpression leads to suppression of *PpTRX-Y2* and increased ROS levels.

4.2.5 *PpFLOT* has a putative role in biotic stress response

Upon detection of pathogens, ROS production within the chloroplast increases that activates stress signaling pathways to induce the plant defense against pathogens (Bleau and Spoel, 2021). Overexpression of *PpFLOT* leads to the accumulation of ROS, which is linked to the pathogen defense response (Hernández et al., 2016; Bleau and Spoel, 2021). Therefore, *PpFLOT* may have a putative role in the pathogen defense. In *A. thaliana*, treatment with flg22 alters the mobility of *AtFLOT1* and *AtFLOT1* overexpression increases callose deposition. Flg22 also induces *AtFLOT* aggregation (Yu et al., 2017a; Junková et al., 2018). The described findings suggest that the cuticle layer and cell wall composition in the *PpFLOT*-OEX lines are altered due to an altered FA profile. These changes of the cell wall components may be due to increased *PpEXPA9* and *PpPME53* accumulation in response to *PpFLOT* activated or guided pathogen defense mechanisms in *P. patens* (Figure 25). For example, an increase in Ca^{2+} -dependent PME activity can lead to cell wall remodeling during abiotic stress response

and pectin fragments can be used as damage-associated signals (Shin et al., 2021). Moreover, PME activity increases after pathogen treatment in *A. thaliana* (Bethke et al., 2014). Increased PpFLOT expression not only leads to changes in the cell wall composition, but also to a higher abundance of linoleic acid derivatives and the accumulation of arachidonic acid. Pathogen defense signaling pathways depend on unsaturated fatty acids (UFA), such as linoleic acid derivatives (He and Ding, 2020). These UFA function not only as constituents for components of the cuticle layer, such as cutin and suberin, but also as intermediates in the biosynthesis of JAs and other active biomolecules of pathogen defense (Resemann et al., 2019; He and Ding, 2020). During pathogen defense, one way to counter the rising ROS is the oxidation of C18 UFAs into oxylipins, which themselves are building blocks of JA biosynthesis (Blée, 2002; Resemann et al., 2019; He and Ding, 2020). The increase in the arachidonic acid pool further supports this hypothesis. Arachidonic acid is an elicitor of plant pathogen defense and depending on its abundance, its accumulation can also lead to either systemic resistance or to accumulation of phytoalexins and necrosis of plant tissues (Dedyukhina et al., 2014). There is a distinct possibility that the detected changes in coloration of *PpFLOT*-OEX cultures are the result of increased necrotic events (Figure 25). Interestingly, PpSEN1 also displayed increased levels in all three *PpFLOT*-OEX lines. SEN1 not only shows increased expression in *A. thaliana* in response to infection events, but also triggers the senescence response resulting in necrosis upon pathogen infection (Schenk et al., 2005; Fernandez-Calvino et al., 2016). A senescent phenotype in *P. patens* can also lead to changes in the FA composition, including arachidonic acid (Chen et al., 2020). Changes in culture coloration of *PpFLOT*-OEX lines might thus be attributed to necrosis rather than changes in pigments of the xanthophyll cycle. Even though these pigments displayed an overall low abundance in *PpFLOT*-OEX lines, changes in coloration due to altered expression of the unidentified pigments are still a distinct possibility. Curiously, no changes in coloration were detected in the gametophores of *PpFLOT*-OEX lines.

I propose that the increased production of ROS triggers SEN1 accumulation (Schenk et al., 2005) and may cause enhanced hypoxia in chloroplasts (Pucciariello and Perata, 2021), which cannot be compensated by *P. patens* protonema cells in an already anoxic environment. The molecular changes that enable 3D growth of *P. patens* may help the plant to counteract this effect. For example, *PpFLOT* expression in the WT gametophore is lower compared to its expression in rhizoids, caulonema cells and protoplasts (eFP browser, https://bar.utoronto.ca/efp_physcomitrella/cgi-bin/efpWeb.cgi) (Winter et al., 2007).

Other regulators of SAR in response to pathogen infection include DGDG and MGDG (Gao et al., 2014). DGDG promotes SAR by regulating NO and SA synthesis, while MGDG regulates signals downstream of NO-guided SAR, such as azelaic acid and glycerol-3-phosphate (Gao et al., 2014). Although proteomics and metabolomics analysis did not detect any DE of these

signals, overexpression of *PpFLOT* severely altered MGDG and DGDG levels. Therefore, overexpressed MGDG species may be beneficial during the pathogen response of *PpFLOT*-OEX lines.

4.2.6 High *PpFLOT* expression enhances photosynthesis rate in protonema cells

In addition to its proposed contribution to pathogen defense, *PpFLOT* seems to be involved in chlorophyll biosynthesis. An increase in *PpLHCB2* protein levels was detected in correlation with *PpFLOT* levels, and the two *PpFLOT*-OEX lines with the highest *PpFLOT* and *PpLHCB2* expression also showed elevated chlorophyll levels. *PpLHCB2* could potentially be a direct interaction partner of *PpFLOT*, but it is also a chlorophyll-binding molecule and its overexpression could be due to a need for binding excessive chlorophyll (Eberhard et al., 2008; Johnson, 2016). Even slight changes in the expression of one LHCB influence the expression and overall composition of the light-harvesting antenna of PSII (Xu et al., 2012). Furthermore, LHCB expression takes part in regulating both ABA and ROS homeostasis (Xu et al., 2012), and high ABA levels can induce LHCB expression (Liu et al., 2013). Interestingly, ROS is one of the signaling molecules used for plastid-to-nucleus communication the retrograde signaling (Eberhard et al., 2008; Li and Kim, 2022). *GLK2*, a gene involved in retrograde signaling and chlorophyll biosynthesis regulation (Yasumura et al., 2005; Kim et al., 2023; Lee et al., 2023), is upregulated in response to *PpFLOT* knockout, but downregulated in *PpFLOT*-OEX lines. This gene acts as a transcription factor for photosynthetic genes, and its knockout in *A. thaliana* leads to diminished chlorophyll content, while *AtGLK2* overexpression results in higher chlorophyll levels (Yasumura et al., 2005; Kim et al., 2023). Both knockout and overexpression of *PpFLOT* lead to changes in the expression of *PpGLK2*, suggesting a role of *PpFLOT* in chlorophyll biosynthesis. However, no changes in the protein levels of known factors participating in chlorophyll biosynthesis could be detected, suggesting a regulating function rather than a direct involvement. Since the chlorophyll content is decreased in $\Delta PpFLOT-1$ and increases with the *PpFLOT* expression, the anticorrelating expression of *PpGLK2* to the respective chlorophyll content suggests an attempt to regulate *PpFLOT*-dependent changes in the chlorophyll biosynthesis via *PpGLK2*. *PpFLOT* most likely participates in the recruitment of protein complexes involved in chlorophyll biosynthesis to the thylakoid membrane. Due to the circadian nature of *PpFLOT* and its inducibility by darkness, one of its functions might contribute to the light-dependent regulation of chlorophyll biosynthesis. For instance, FLUORESCENT IN BLUE LIGHT (FLU) suppresses the chlorophyll biosynthesis in the dark by inactivating the GLUTAMYL-tRNA-REDUCTASE (GluTR) and repressing the 5-aminolevulinic acid (ALA) synthesis (Meskauskiene and Apel, 2002; Kaus et al., 2012; Fang et al., 2016; Hou et al., 2019; Wittmann et al., 2021). ALA is an intermediate compound during chlorophyll biosynthesis, and its decline during the night prevents the accumulation of phototoxic products (Wittmann et al., 2021). How GluTR is recruited into a complex together

with the membrane-bound FLU and other components of the Mg^{2+} branch of the chlorophyll biosynthesis is unclear (Wittmann et al., 2021). The described findings suggest, that at least in *P. patens*, PpFLOT might fulfill such a role. Since, in this case, the activity of FLU would be dependent on PpFLOT abundance, chlorophyll biosynthesis might be suppressed in the *PpFLOT*-OEX1, leading to the detected lower chlorophyll levels. In this case, both *PpFLOT*-OEX2 and 3, as well as the $\Delta PpFLOT-1$ lines, might depend on other ways to regulate the chlorophyll synthesis under changing light conditions, leading to higher and lower chlorophyll levels, respectively. However, concrete evidence supporting this hypothesis is still lacking. It is possible that PpFLOT influences chlorophyll biosynthesis in another way. However, altered chlorophyll levels are the most likely explanation for the detected changes in the Y(II) of *PpFLOT*-OEX1 and 2 and the NPQ/4 of $\Delta PpFLOT-1$. In $\Delta PpFLOT-1$, excess energy that cannot be processed due to inefficient chlorophyll levels is redistributed and redirected into non-photochemical quenching (Eberhard et al., 2008). On the other hand, an excess of chlorophyll leads to a higher photorespiration in *PpFLOT*-OEX lines. This increase in photorespiration most likely also leads to an increase in respiration, supported by the measured increase in PpNDUFS8 and PpNDUFA2/B8 expression (Figure 25). Previous studies showed that the thylakoid lumen enlarges in response to abiotic stresses (Gorelova et al., 2019; Venzhik et al., 2019) to increase the travel distance and diffusion rate of electron carriers to the photosystems, thus slowing down the photosynthesis rate (Mullineaux, 2008; Kirchhoff et al., 2011; Jarvi et al., 2013; Gorelova et al., 2019). Such a reaction would also explain the observed lumen enlargement in *PpFLOT*-OEX chloroplasts. Increased PpFLOT expression most likely contributes to this effect.

4.2.7 PpFLOT influences lipid composition of thylakoid membranes

Detected changes in the lipid composition of thylakoid membranes could also explain the increase in thylakoid lumen and structural changes in these membranes. Thylakoid membranes mainly consist of the glycolipids MGDG, DGDG and sulfoquinoyl-diacylglycerol (SQDG), with MGDG making up more than 50 % of the total lipid content while DGDG makes up about 30 % (Rast et al., 2015; Garab et al., 2016). Unlike DGDG, MGDG is a non-bilayer lipid that is forced into a bilayer by interaction with LHCII proteins (Garab et al., 2016). PpFLOT may be involved in the localization or transport of PpLHCB2 to the PS II antenna complexes along the thylakoid membranes, which could affect the structure of the thylakoid membrane. Meanwhile, DGDG is the main driver behind the bilayer formation and changes in the MGDG/DGDG ratio affect both membrane organization and protein complex stability (Pribil et al., 2014; Rast et al., 2015; Garab et al., 2016). Although the exact mechanism behind increased PpFLOT levels and subsequent changes in thylakoid membrane composition are unknown, it can be assumed that this change in lipid composition contributes to the detected alterations in the thylakoid structure of the *PpFLOT*-OEX lines. Interestingly, increased levels

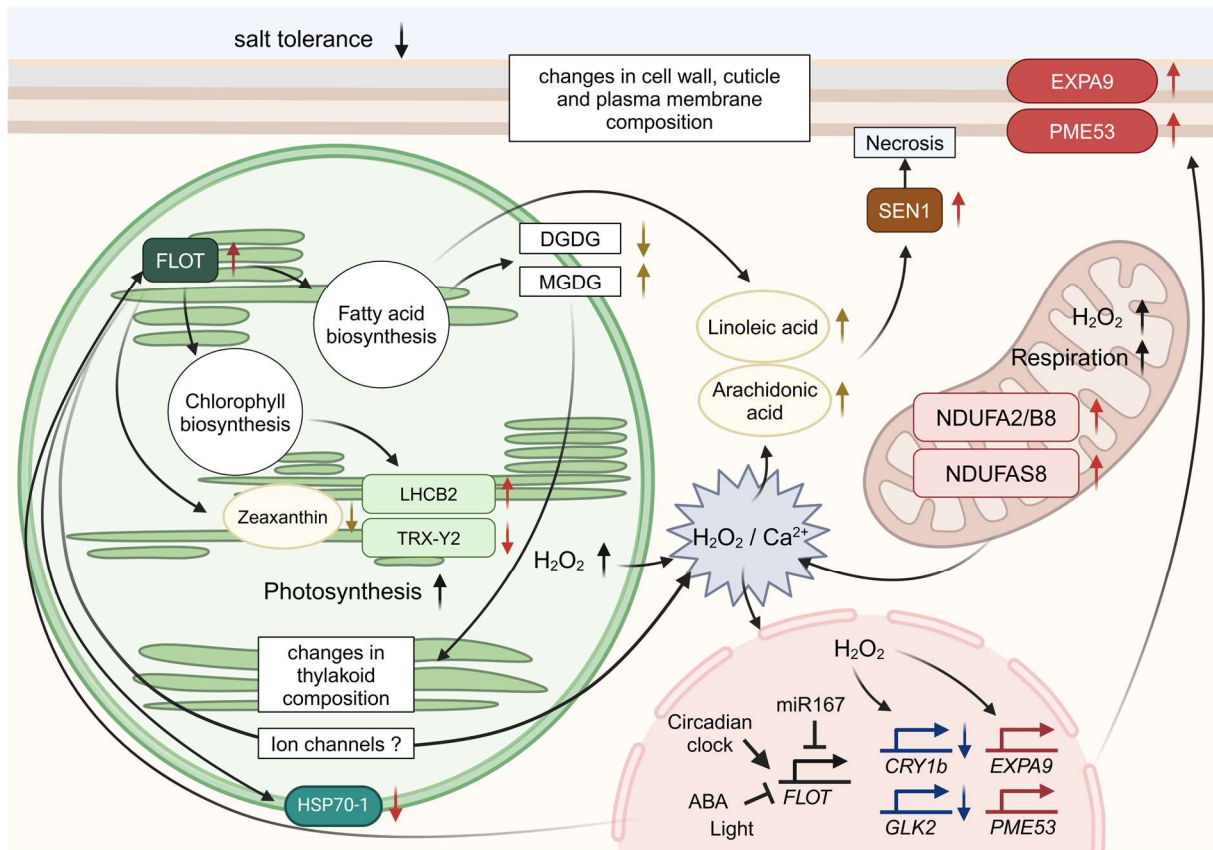


Figure 25: Effect of *PpFLOT* overexpression in protonema cells

The expression of *PpFLOT* is regulated by the circadian clock, ABA, light stimuli and potentially by miR167. Elevated *PpFLOT* levels in chloroplasts alter fatty acid (FA) biosynthesis, increase chlorophyll biosynthesis, decrease *PpHSP70-1* levels and likely impact ion channel activity or localization. Moreover, high *PpFLOT* levels increase *PpLHC2* while reducing zeaxanthin and *PpTRX-Y2* levels. Changes in FA biosynthesis affect thylakoid membrane composition due to increase in MGDG and decrease in DGDG levels. These changes enlarge the lumen and impair grana formation in the thylakoid membrane, thus enhancing photosynthesis, H_2O_2 production and possibly Ca^{2+} signaling. Elevated photosynthesis affects metabolic processes including respiration, as evidenced by upregulated *PpNDUFA2/B8* and *NDUFAS8*. H_2O_2 accumulation triggers retrograde signaling, increasing the expression of *PpEXPA9* and *PpPME53* and suppressing the expression of *PpCRY1b* and *PpGLK2*. Increased *PpEXPA1* and *PpPME53* levels alter cell wall, plasma membrane and cuticle composition. Together with low levels of *PpHSP70-1*, *PpTRX-Y2* and the overall increased metabolic activity changes in these components are reducing the salt tolerance. Altered FA biosynthesis leads to linoleic acid and arachidonic acid accumulation, potentially mimicking molecular patterns initiated by pathogens. This most likely includes the accumulation of *PpSEN1*, leading to necrotic events. The arrows in the graph denote experiments validating changes in expression levels or protein abundance. Blue: qRT-PCR measurements, red: Proteomics analysis, yellow: Metabolomics analysis, black: PAM and DAB staining. This graphical representation was generated using BioRender.

of MGDG can also lead to a higher photosynthetic activity (Zhou et al., 2009; Pribil et al., 2014). One way that *PpFLOT* could adjust the lipid composition of thylakoid membranes directly is by participating in the formation of stromal vesicles that transport lipids generated in the chloroplast envelope to the thylakoid membranes.

Vesicle formation has been observed in proplastids and developing chloroplasts (Pribil et al., 2014; Mechela et al., 2019), potentially playing a crucial role in early thylakoid membrane development (Mechela et al., 2019). While *AtFLOT1* has been implicated in clathrin-

independent endocytosis (Li et al., 2012; Cao et al., 2020) and vesicle formation, it is challenging to extrapolate the molecular function of PpFLOT from AtFLOT due to their differing locations. Besides, the absence of evidence for chloroplast-related FLOT in other plant species, coupled with the lack of observable changes in thylakoid structure in $\Delta PpFLOT-1$, suggests that FLOT may not significantly contribute to chloroplastic vesicle formation outside of *P. patens*.

It is difficult to distinguish between direct and indirect effects of PpFLOT overexpression since no claims can be made about its direct interaction partners. However, this study has revealed a few important points. PpFLOT is more versatile than previously assumed, and while its association with thylakoid membranes may be unique to bryophytes, the differences in the gametophore and protonema phenotype suggest a change in function during the transition of plant terrestrialization. Although the exact function of PpFLOT is still a mystery, this study has shed light on a few pathways in chloroplast metabolism where PpFLOT appears to be crucial. High concentrations of PpFLOT are detrimental during salt adaptations and to cope with elevated osmotic pressure. However, evidence gathered suggests a potential role of PpFLOT in pathogen defense response, chlorophyll biosynthesis and involvement in Ca^{2+} signaling.

4.3 Outlook

Given the changing climate, it is imperative for crop plants to adapt to extreme environmental conditions. Soil salinization, projected to escalate in the 21st century, poses a significant challenge to crop cultivation (Hassani et al., 2021). Therefore, enhancing our comprehension of the fundamental principles underlying plant adaptation to such harsh environments is crucial. The field of land plant evolution is well-suited to advance this understanding, as it elucidates the foundational mechanisms established during the transition to terrestrial life.

This study aims to enhance our understanding of the evolutionary origins of DCL proteins in land plants by comparing their function in *P. patens* and *M. polymorpha*. The data generated will also contribute to our knowledge of how sRNA-guided mechanisms and gene regulatory networks evolved in *M. polymorpha*. By comparing the phenotypes of all *Mpdcl*^{ge} mutants with their counterparts in *P. patens*, I was able to detect distinct differences suggesting variations in DCL function between these two bryophyte species. Particularly, the *Mpdcl1b*^{ge}, *Mpdcl3*^{ge} and *Mpdcl4*^{ge} mutant lines exhibited the most striking differences, highlighting the functional specialization of DCL-like proteins. For instance, the here gathered data suggests a putative involvement of MpDCL4 and MpDCL3 in pathogen defense in *M. polymorpha*, though further investigation is needed to confirm this hypothesis. If confirmed, it would signify a notable difference in the function of MpDCL compared to *P. patens*. Additionally, my findings suggest that all MpDCL proteins contribute to gametangiophore development to a greater extent than observed in other bryophyte species.

Through comparisons of evolutionary relationships among DCL homologs across species, I was able to identify a distinct set of proteins similar to DCL in mosses and ferns, suggesting uniqueness to these plant species. MpDCL1b, representing a member of this newly discovered DCL class, along with its associated sRNAs, likely influences the salt sensitivity of *M. polymorpha* most likely by regulating miRNA expression. This novel regulatory mechanism has not been observed in other plant species to date. These findings shed light on the molecular mechanisms of gene expression in *M. polymorpha* and related plant species, and they also offer insights for potential approaches to enhance the salt tolerance in seed plants.

Further studies are required to fully elucidate the proposed mechanism. However, the identification of specific sRNA:miRNA modules regulating salt tolerance could significantly advance our understanding of salt adaptation in bryophytes. Moreover, such insights may pave the way for the development of molecular tools capable of enhancing the salt tolerance of land plants.

Although I focused exclusively on mRNA and sRNA expression in young developing gemmalings, investigating the involvement of DCLs in other life stages of *M. polymorpha* could

be of interest. Nonetheless, the sequencing data generated here provide a valuable resource for studying sRNA expression at this developmental stage within the *M. polymorpha* community.

DCL and sRNAs are not the sole regulators of salt tolerance in bryophytes. This study demonstrates that elevated PpFLOT levels adversely affect the salt tolerance of *P. patens*. Intriguingly, it also suggests a potential role of PpFLOT in plant terrestrialization. While previous studies hint at FLOT's involvement in establishing symbiotic infections beneficial to the ancestors of modern bryophytes, this study provides evidence for a potential role of FLOT during the pathogen defense. By contributing to both processes, FLOT might have ultimately facilitated plant transition to terrestrial habitats.

In this study, I have demonstrated the presence of PpFLOT in chloroplasts of *P. patens*, a phenomenon unprecedented in other land plant species. The reasons underlying this localization shift remain elusive and require further investigation. Exploring FLOT in other bryophyte, fern, or seed plant species is likely to enhance our understanding of FLOT evolution and function.

The influence of PpFLOT on ROS signaling, metabolic pathways and its putative influence on ion- and heavy metal transport requires further analysis. Such investigations could involve identifying direct interaction partners of PpFLOT through pull-down assays and confirming interactions via Förster resonant energy transfer (FRET) analysis. Potential accumulations of metal ions might contribute to observed coloration changes and further elucidate PpFLOT's involvement in pathogen defense.

Currently, the underlying principles governing the effects of PpFLOT on metabolic pathways and photosynthesis remain only partially understood. Continued research in this area promises valuable insights into plant stress tolerance and may yield novel contributions to our understanding of salt tolerance and defense mechanisms against plant pathogens in both bryophytes and land plants.

References

- Aguirre, G., and Pilon, M. (2015). Copper delivery to chloroplast proteins and its regulation. *Front Plant Sci* 6, 1250.
- Akbergenov, R., Si-Ammour, A., Blevins, T., Amin, I., Kutter, C., et al. (2006). Molecular characterization of geminivirus-derived small RNAs in different plant species. *Nucleic Acids Res* 34, 462-471.
- Aki, S.S., Mikami, T., Naramoto, S., Nishihama, R., Ishizaki, K., et al. (2019). Cytokinin signaling is essential for organ formation in *Marchantia polymorpha*. *Plant Cell Physiol* 60, 1842-1854.
- Aki, S.S., Morimoto, T., Ohnishi, T., Oda, A., Kato, H., et al. (2022). R2R3-MYB transcription factor GEMMA CUP-ASSOCIATED MYB1 mediates the cytokinin signal to achieve proper organ development in *Marchantia polymorpha*. *Sci Rep* 12, 21123.
- Alazem, M., and Lin, N.S. (2015). Roles of plant hormones in the regulation of host-virus interactions. *Mol Plant Pathol* 16, 529-540.
- Allen, E., Xie, Z., Gustafson, A.M., and Carrington, J.C. (2005). microRNA-directed phasing during trans-acting siRNA biogenesis in plants. *Cell* 121, 207-221.
- Althoff, F., Kopischke, S., Zobel, O., Ide, K., Ishizaki, K., et al. (2014). Comparison of the MpEF1 α and CaMV35 promoters for application in *Marchantia polymorpha* overexpression studies. *Transgenic Res* 23, 235-244.
- Alvarado, V., and Scholthof, H.B. (2009). Plant responses against invasive nucleic acids: RNA silencing and its suppression by plant viral pathogens. *Semin Cell Dev Biol* 20, 1032-1040.
- Ambawat, S., Sharma, P., Yadav, N.R., and Yadav, R.C. (2013). MYB transcription factor genes as regulators for plant responses: an overview. *Physiol Mol Biol Plants* 19, 307-321.
- Arazi, T. (2012). MicroRNAs in the moss *Physcomitrella patens*. *Plant Mol Biol* 80, 55-65.
- Arif, M.A., Alseekh, S., Harb, J., Fernie, A., and Frank, W. (2018). Absciscic acid, cold and salt stimulate conserved metabolic regulation in the moss *Physcomitrella patens*. *Plant Biol (Stuttg)* 20, 1014-1022.
- Arif, M.A., Fattash, I., Ma, Z., Cho, S.H., Beike, A.K., et al. (2012). DICER-LIKE3 activity in *Physcomitrella patens* DICER-LIKE4 mutants causes severe developmental dysfunction and sterility. *Mol Plant* 5, 1281-1294.
- Arif, M.A., Frank, W., and Khraiweh, B. (2013). Role of RNA interference (RNAi) in the Moss *Physcomitrella patens*. *Int J Mol Sci* 14, 1516-1540.
- Arif, M.A., Hiss, M., Tomek, M., Busch, H., Meyberg, R., et al. (2019). ABA-induced vegetative diaspore formation in *Physcomitrella patens*. *Front Plant Sci* 10, 315.
- Arif, M.A., Top, O., Csicsely, E., Lichtenstern, M., Beheshti, H., et al. (2022). DICER-LIKE1a autoregulation based on intronic microRNA processing is required for stress adaptation in *Physcomitrium patens*. *Plant J* 109, 227-240.
- Avalbaev, A.M., Somov, K.A., Yuldashev, R.A., and Shakirova, F.M. (2012). Cytokinin oxidase is key enzyme of cytokinin degradation. *Biochemistry (Mosc)* 77, 1354-1361.
- Axtell, M.J. (2013). ShortStack: comprehensive annotation and quantification of small RNA genes. *RNA* 19, 740-751.
- Axtell, M.J., Jan, C., Rajagopalan, R., and Bartel, D.P. (2006). A two-hit trigger for siRNA biogenesis in plants. *Cell* 127, 565-577.
- Axtell, M.J., Snyder, J.A., and Bartel, D.P. (2007). Common functions for diverse small RNAs of land plants. *Plant Cell* 19, 1750-1769.
- Backer, R., Naidoo, S., and Van Den Berg, N. (2019). The NONEXPRESSOR OF PATHOGENESIS-RELATED GENES 1 (NPR1) and related family: mechanistic insights in plant disease resistance. *Front Plant Sci* 10, 102.
- Baral, A., Shruthi, K.S., and Mathew, M.K. (2015). Vesicular trafficking and salinity responses in plants. *IUBMB Life* 67, 677-686.
- Baranauske, S., Mickute, M., Plotnikova, A., Finke, A., Venclovas, C., et al. (2015). Functional mapping of the plant small RNA methyltransferase: HEN1 physically interacts with HYL1 and DICER-LIKE 1 proteins. *Nucleic Acids Res* 43, 2802-2812.
- Barciszewska-Pacak, M., Milanowska, K., Knop, K., Bielewicz, D., Nuc, P., et al. (2015). *Arabidopsis* microRNA expression regulation in a wide range of abiotic stress responses. *Front Plant Sci* 6, 410.
- Barr, Z.K., Werner, T., and Tilsner, J. (2023). Heavy metal-associated isoprenylated plant proteins (HIPPs) at plasmodesmata: exploring the link between localization and function. *Plants (Basel)* 12, 3015.
- Barrero-Sicilia, C., Silvestre, S., Haslam, R.P., and Michaelson, L.V. (2017). Lipid remodelling: unravelling the response to cold stress in *Arabidopsis* and its extremophile relative *Eutrema salsugineum*. *Plant Sci* 263, 194-200.
- Batsale, M., Bahammou, D., Fouillen, L., Mongrand, S., Joubes, J., et al. (2021). Biosynthesis and functions of very-long-chain fatty acids in the responses of plants to abiotic and biotic stresses. *Cells* 10, 1284.
- Beheshti, H., Strotbek, C., Arif, M.A., Klingl, A., Top, O., et al. (2021). PpGRAS12 acts as a positive regulator of meristem formation in *Physcomitrium patens*. *Plant Mol Biol* 107, 293-305.
- Bélanger, S., Zhan, J., and Meyers, B.C. (2023). Phylogenetic analyses of seven protein families refine the evolution of small RNA pathways in green plants. *Plant Physiol* 192, 1183-1203.
- Benavides, M.P., Marconi, P.L., Gallego, S.M., Comba, M.E., and Tomaro, M.L. (2000). Relationship between antioxidant defence systems and salt tolerance in *Solanum tuberosum*. *Functional Plant Biology* 27, 45-50.
- Berka, M., Kopecka, R., Berkova, V., Brzobohaty, B., and Cerny, M. (2022). Regulation of heat shock proteins 70 and their role in plant immunity. *J Exp Bot* 73, 1894-1909.

- Bethke, G., Grundman, R.E., Sreekanta, S., Truman, W., Katagiri, F., et al. (2014). Arabidopsis PECTIN METHYLESTERASEs contribute to immunity against *Pseudomonas syringae*. *Plant Physiol* 164, 1093-1107.
- Betti, F., Ladera-Carmona, M.J., Weits, D.A., Ferri, G., Iacopino, S., et al. (2021). Exogenous miRNAs induce post-transcriptional gene silencing in plants. *Nat Plants* 7, 1379-1388.
- Bharadwaj, P.S., Sanchez, L., Li, D., Enyi, D., Van De Poel, B., et al. (2022). The plant hormone ethylene promotes abiotic stress tolerance in the liverwort *Marchantia polymorpha*. *Front Plant Sci* 13, 998267.
- Bhyan, S.B., Minami, A., Kaneko, Y., Suzuki, S., Arakawa, K., et al. (2012). Cold acclimation in the moss *Physcomitrella patens* involves abscisic acid-dependent signaling. *J Plant Physiol* 169, 137-145.
- Blankenberg, D., Taylor, J., Schenck, I., He, J., Zhang, Y., et al. (2007). A framework for collaborative analysis of ENCODE data: making large-scale analyses biologist-friendly. *Genome Res* 17, 960-964.
- Bleau, J.R., and Spoel, S.H. (2021). Selective redox signaling shapes plant-pathogen interactions. *Plant Physiol* 186, 53-65.
- Blée, E. (2002). Impact of phyto-oxylipins in plant defense. *Trends Plant Sci* 7, 315-322.
- Block, M.A., Douce, R., Joyard, J., and Rolland, N. (2007). Chloroplast envelope membranes: a dynamic interface between plastids and the cytosol. *Photosynth Res* 92, 225-244.
- Bolger, A.M., Lohse, M., and Usadel, B. (2014). Trimmomatic: a flexible trimmer for Illumina sequence data. *Bioinformatics* 30, 2114-2120.
- Bologna, N.G., Iselin, R., Abriata, L.A., Sarazin, A., Pumplin, N., et al. (2018). Nucleo-cytosolic shuttling of ARGONAUTE1 prompts a revised model of the plant microRNA pathway. *Mol Cell* 69, 709-719 e705.
- Borsani, O., Zhu, J., Verslues, P.E., Sunkar, R., and Zhu, J.K. (2005). Endogenous siRNAs derived from a pair of natural cis-antisense transcripts regulate salt tolerance in *Arabidopsis*. *Cell* 123, 1279-1291.
- Bouche, N., Laressergues, D., Gascioli, V., and Vaucheret, H. (2006). An antagonistic function for *Arabidopsis* DCL2 in development and a new function for DCL4 in generating viral siRNAs. *EMBO J* 25, 3347-3356.
- Boursiac, Y., Chen, S., Luu, D.T., Sorieul, M., Van Den Dries, N., et al. (2005). Early effects of salinity on water transport in *Arabidopsis* roots. Molecular and cellular features of aquaporin expression. *Plant Physiol* 139, 790-805.
- Bowles, A.M.C., Paps, J., and Bechtold, U. (2022). Water-related innovations in land plants evolved by different patterns of gene cooption and novelty. *New Phytol.* 235, 732-742.
- Bowman, J.L., Kohchi, T., Yamato, K.T., Jenkins, J., Shu, S., et al. (2017). Insights into land plant evolution garnered from the *Marchantia polymorpha* genome. *Cell* 171, 287-304 e215.
- Browman, D.T., Hoegg, M.B., and Robbins, S.M. (2007). The SPFH domain-containing proteins: more than lipid raft markers. *Trends Cell Biol* 17, 394-402.
- Brown, T. (2001). Southern blotting. *Curr Protoc Protein Sci* Appendix 4.
- Cao, Y., He, Q., Qi, Z., Zhang, Y., Lu, L., et al. (2020). Dynamics and endocytosis of Flot1 in *Arabidopsis* require CPI1 function. *Int J Mol Sci* 21, 1552.
- Carrillo-Carrasco, V.P., Hernandez-Garcia, J., Mutte, S.K., and Weijers, D. (2023). The birth of a giant: evolutionary insights into the origin of auxin responses in plants. *EMBO J* 42, e113018.
- Cazalé, A.C., Clement, M., Chiarenza, S., Roncato, M.A., Pochon, N., et al. (2009). Altered expression of cytosolic/nuclear HSC70-1 molecular chaperone affects development and abiotic stress tolerance in *Arabidopsis thaliana*. *J Exp Bot* 60, 2653-2664.
- Chen, Z.-H. (2022). Unveiling novel genes in Fern genomes for the design of stress tolerant crops. *Crop Design* 1, 100013.
- Chen, Z., Wang, W., Pu, X., Dong, X., Gao, B., et al. (2020). Comprehensive analysis of the *Ppatg3* mutant reveals that autophagy plays important roles in gametophore senescence in *Physcomitrella patens*. *BMC Plant Biol* 20, 440.
- Cho, S.H., Addo-Quaye, C., Coruh, C., Arif, M.A., Ma, Z., et al. (2008). *Physcomitrella patens* DCL3 is required for 22-24 nt siRNA accumulation, suppression of retrotransposon-derived transcripts, and normal development. *PLoS Genet* 4, e1000314.
- Cho, S.H., Coruh, C., and Axtell, M.J. (2012). miR156 and miR390 regulate tasiRNA accumulation and developmental timing in *Physcomitrella patens*. *Plant Cell* 24, 4837-4849.
- Chow, C.N., Lee, T.Y., Hung, Y.C., Li, G.Z., Tseng, K.C., et al. (2019). PlantPAN3.0: a new and updated resource for reconstructing transcriptional regulatory networks from ChIP-seq experiments in plants. *Nucleic Acids Res* 47, D1155-D1163.
- Collin, V., Lamkemeyer, P., Miginiac-Maslow, M., Hirasawa, M., Knaff, D.B., et al. (2004). Characterization of plastidial thioredoxins from *Arabidopsis* belonging to the new y-type. *Plant Physiol* 136, 4088-4095.
- Concordet, J.P., and Haeussler, M. (2018). CRISPOR: intuitive guide selection for CRISPR/Cas9 genome editing experiments and screens. *Nucleic Acids Res* 46, W242-W245.
- Conway, J.R., Lex, A., and Gehlenborg, N. (2017). UpSetR: an R package for the visualization of intersecting sets and their properties. *Bioinformatics* 33, 2938-2940.
- Cornelissen, G. (2014). Cosinor-based rhythmometry. *Theor Biol Med Model* 11, 16.
- Cosgrove, D.J. (2015). Plant expansins: diversity and interactions with plant cell walls. *Curr Opin Plant Biol* 25, 162-172.
- Cove, D. (2005). The moss *Physcomitrella patens*. *Annu Rev Genet* 39, 339-358.
- Cox, J., Hein, M.Y., Luber, C.A., Paron, I., Nagaraj, N., et al. (2014). Accurate proteome-wide label-free quantification by delayed normalization and maximal peptide ratio extraction, termed MaxLFQ. *Mol Cell Proteomics* 13, 2513-2526.

- Cox, J., and Mann, M. (2008). MaxQuant enables high peptide identification rates, individualized p.p.b.-range mass accuracies and proteome-wide protein quantification. *Nat Biotechnol* 26, 1367-1372.
- Cui, J., You, C., and Chen, X. (2017). The evolution of microRNAs in plants. *Curr Opin Plant Biol* 35, 61-67.
- Cui, Y., Hisanaga, T., Kajiwara, T., Yamaoka, S., Kohchi, T., et al. (2023). Three-dimensional morphological analysis revealed the cell patterning bases for the sexual dimorphism development in the liverwort *Marchantia polymorpha*. *Plant Cell Physiol* 64, 866-879.
- Da Costa e Silva, O. (1994). CG-1, a parsley light-induced DNA-binding protein. *Plant Mol Biol* 25, 921-924.
- Dai, X., Zhuang, Z., and Zhao, P.X. (2018). psRNATarget: a plant small RNA target analysis server (2017 release). *Nucleic Acids Res* 46, W49-W54.
- Danek, M., Angelini, J., Malinska, K., Andrejch, J., Amlerova, Z., et al. (2020). Cell wall contributes to the stability of plasma membrane nanodomain organization of *Arabidopsis thaliana* FLOTILLIN2 and HYPERSENSITIVE INDUCED REACTION1 proteins. *Plant J* 101, 619-636.
- Daněš, M., Valentová, O., and Martinec, J. (2016). Flotillins, Erlins, and HIRs: From animal base camp to plant new horizons. *Crit Rev Plant Sci* 35, 191-214.
- Das, P., Lakra, N., Nutan, K.K., Singla-Pareek, S.L., and Pareek, A. (2019). A unique bZIP transcription factor imparting multiple stress tolerance in Rice. *Rice (N Y)* 12, 58.
- De Vries, J., and Archibald, J.M. (2018). Plant evolution: landmarks on the path to terrestrial life. *New Phytol* 217, 1428-1434.
- Dedyukhina, E.G., Kamzolova, S.V., and Vainshtein, M.B. (2014). Arachidonic acid as an elicitor of the plant defense response to phytopathogens. *Chem. Biol. Technol. Agric* 1, 18.
- Degola, F., Sanita Di Toppi, L., and Petraglia, A. (2022). Bryophytes: how to conquer an alien planet and live happily (ever after). *J Exp Bot* 73, 4267-4272.
- Delaux, P.M., and Schornack, S. (2021). Plant evolution driven by interactions with symbiotic and pathogenic microbes. *Science* 371, eaba6605.
- Dobin, A., Davis, C.A., Schlesinger, F., Drenkow, J., Zaleski, C., et al. (2013). STAR: ultrafast universal RNA-seq aligner. *Bioinformatics* 29, 15-21.
- Domergue, J.B., Bocca, C., De Paepe, R., Lenaers, G., Limami, A.M., et al. (2022). Mitochondrial complex I disruption causes broad reorchestration of plant lipidome including chloroplast lipids. *Int J Mol Sci* 24, 453.
- Eberhard, S., Finazzi, G., and Wollman, F.A. (2008). The dynamics of photosynthesis. *Annu Rev Genet* 42, 463-515.
- Edwards, K., Johnstone, C., and Thompson, C. (1991). A simple and rapid method for the preparation of plant genomic DNA for PCR analysis. *Nucleic Acids Res* 19, 1349.
- Eklund, D.M., Ishizaki, K., Flores-Sandoval, E., Kikuchi, S., Takebayashi, Y., et al. (2015). Auxin produced by the indole-3-pyruvic acid pathway regulates development and gemmae dormancy in the liverwort *Marchantia polymorpha*. *Plant Cell* 27, 1650-1669.
- Eklund, D.M., Kanei, M., Flores-Sandoval, E., Ishizaki, K., Nishihama, R., et al. (2018). An evolutionarily conserved abscisic acid signaling pathway regulates dormancy in the liverwort *Marchantia polymorpha*. *Curr Biol* 28, 3691-3699 e3693.
- Espinoza-Corral, R., Schwenkert, S., and Schneider, A. (2023). Characterization of the preferred cation cofactors of chloroplast protein kinases in *Arabidopsis thaliana*. *FEBS Open Bio* 13, 511-518.
- Fang, Y., Zhao, S., Zhang, F., Zhao, A., Zhang, W., et al. (2016). The *Arabidopsis* glutamyl-tRNA reductase (GluTR) forms a ternary complex with FLU and GluTR-binding protein. *Sci Rep* 6, 19756.
- Fattash, I., Voss, B., Reski, R., Hess, W.R., and Frank, W. (2007). Evidence for the rapid expansion of microRNA-mediated regulation in early land plant evolution. *BMC Plant Biol* 7, 13.
- Fernandez-Calvino, L., Guzman-Benito, I., Del Toro, F.J., Donaire, L., Castro-Sanz, A.B., et al. (2016). Activation of senescence-associated *Dark-inducible (DIN)* genes during infection contributes to enhanced susceptibility to plant viruses. *Mol Plant Pathol* 17, 3-15.
- Fernandez-Pozo, N., Haas, F.B., Gould, S.B., and Rensing, S.A. (2022). An overview of bioinformatics, genomics, and transcriptomics resources for bryophytes. *J Exp Bot* 73, 4291-4305.
- Ferreira-Guerra, M., Marques-Bueno, M., Mora-Garcia, S., and Cano-Delgado, A.I. (2020). Delving into the evolutionary origin of steroid sensing in plants. *Curr Opin Plant Biol* 57, 87-95.
- Ferreira, M.L.F., Serra, P., and Casati, P. (2021). Recent advances on the roles of flavonoids as plant protective molecules after UV and high light exposure. *Physiol Plant* 173, 736-749.
- Fidler, J., Graska, J., Gietler, M., Nykiel, M., Prabucka, B., et al. (2022). PYR/PYL/RCAR receptors play a vital role in the abscisic-acid-dependent responses of plants to external or internal stimuli. *Cells* 11, 1352.
- Flores-Sandoval, E., Eklund, D.M., and Bowman, J.L. (2015). A simple auxin transcriptional response system regulates multiple morphogenetic processes in the liverwort *Marchantia polymorpha*. *PLoS Genet* 11, e1005207.
- Flores-Sandoval, E., Eklund, D.M., Hong, S.F., Alvarez, J.P., Fisher, T.J., et al. (2018a). Class C ARFs evolved before the origin of land plants and antagonize differentiation and developmental transitions in *Marchantia polymorpha*. *New Phytol* 218, 1612-1630.
- Flores-Sandoval, E., Romani, F., and Bowman, J.L. (2018b). Co-expression and transcriptome analysis of *Marchantia polymorpha* transcription factors supports class C ARFs as independent actors of an ancient auxin regulatory module. *Front Plant Sci* 9, 1345.
- Frank, W., Baar, K.M., Qudeimat, E., Woriedh, M., Alawady, A., et al. (2007). A mitochondrial protein homologous to the mammalian peripheral-type benzodiazepine receptor is essential for stress adaptation in plants. *Plant J* 51, 1004-1018.

- Frank, W., Ratnadewi, D., and Reski, R. (2005). *Physcomitrella patens* is highly tolerant against drought, salt and osmotic stress. *Planta* 220, 384-394.
- Frebortova, J. (2010). Function of plant defense secondary metabolite in cytokinin degradation. *Plant Signal Behav* 5, 523-525.
- Frick, M., Bright, N.A., Riento, K., Bray, A., Merrified, C., et al. (2007). Coassembly of flotillins induces formation of membrane microdomains, membrane curvature, and vesicle budding. *Curr Biol* 17, 1151-1156.
- Fu, R., Zhang, M., Zhao, Y., He, X., Ding, C., et al. (2017). Identification of salt tolerance-related microRNAs and their targets in maize (*Zea mays* L.) using high-throughput sequencing and degradome analysis. *Front Plant Sci* 8, 864.
- Fukuda, H., Murase, H., and Tokuda, I.T. (2013). Controlling circadian rhythms by dark-pulse perturbations in *Arabidopsis thaliana*. *Sci Rep* 3, 1533.
- Furumizu, C., and Sawa, S. (2021). The RGF/GLV/CLEL family of short peptides evolved through lineage-specific losses and diversification and yet conserves its signaling role between vascular plants and bryophytes. *Front Plant Sci* 12, 703012.
- Galaxy Community (2022). The Galaxy platform for accessible, reproducible and collaborative biomedical analyses: 2022 update. *Nucleic Acids Res*, 50, W345-W351.
- Gao, Q.M., Yu, K., Xia, Y., Shine, M.B., Wang, C., et al. (2014). Mono- and digalactosyldiacylglycerol lipids function nonredundantly to regulate systemic acquired resistance in plants. *Cell Rep* 9, 1681-1691.
- Gao, S., Pinnola, A., Zhou, L., Zheng, Z., Li, Z., et al. (2022). Light-harvesting complex stress-related proteins play crucial roles in the acclimation of *Physcomitrella patens* under fluctuating light conditions. *Photosynth Res* 151, 1-10.
- Garab, G., Ughy, B., and Goss, R. (2016). Role of MGDG and Non-bilayer lipid phases in the structure and dynamics of chloroplast thylakoid membranes. *Subcell Biochem* 86, 127-157.
- Garbett, D., and Bretscher, A. (2014). The surprising dynamics of scaffolding proteins. *Mol Biol Cell* 25, 2315-2319.
- Ge, S.X., Jung, D., and Yao, R. (2020). ShinyGO: a graphical gene-set enrichment tool for animals and plants. *Bioinformatics* 36, 2628-2629.
- Gehlenborg, N. (2019). _UpSetR: A more scalable alternative to venn and euler diagrams for visualizing intersecting sets_. R package version 1.4.0, URL <https://CRAN.R-project.org/package=UpSetR>.
- Geigenberger, P., Thormahlen, I., Daloso, D.M., and Fernie, A.R. (2017). The unprecedented versatility of the plant thioredoxin system. *Trends Plant Sci* 22, 249-262.
- Genty, B., Briantais, J.-M., and Baker, N.R. (1989). The relationship between the quantum yield of photosynthetic electron transport and quenching of chlorophyll fluorescence. *Biochim Biophys Acta - Gen Subj* 990, 87-92.
- Gigli-Bisceglia, N., Van Zelm, E., Huo, W., Lamers, J., and Testerink, C. (2022). *Arabidopsis* root responses to salinity depend on pectin modification and cell wall sensing. *Development* 149, dev200363.
- Gimenez-Ibanez, S., Zamarreno, A.M., Garcia-Mina, J.M., and Solano, R. (2019). An evolutionarily ancient immune system governs the interactions between *Pseudomonas syringae* and an early-diverging land plant lineage. *Curr Biol* 29, 2270-2281 e2274.
- Golldack, D., Luking, I., and Yang, O. (2011). Plant tolerance to drought and salinity: stress regulating transcription factors and their functional significance in the cellular transcriptional network. *Plant Cell Rep* 30, 1383-1391.
- Gorelova, O., Baulina, O., Ismagulova, T., Kokabi, K., Lobakova, E., et al. (2019). Stress-induced changes in the ultrastructure of the photosynthetic apparatus of green microalgae. *Protoplasma* 256, 261-277.
- Gou, X., and Li, J. (2020). Paired receptor and coreceptor kinases perceive extracellular signals to control plant development. *Plant Physiol* 182, 1667-1681.
- Guleria, P., Mahajan, M., Bhardwaj, J., and Yadav, S.K. (2011). Plant small RNAs: biogenesis, mode of action and their roles in abiotic stresses. *Genomics Proteomics Bioinformatics* 9, 183-199.
- Gullner, G., Komives, T., Kiraly, L., and Schroeder, P. (2018). Glutathione S-transferase enzymes in plant-pathogen interactions. *Front Plant Sci* 9, 1836.
- Guo, X., Liu, D., and Chong, K. (2018). Cold signaling in plants: Insights into mechanisms and regulation. *J Integr Plant Biol* 60, 745-756.
- Habermann, K., Tiwari, B., Krantz, M., Adler, S.O., Klipp, E., et al. (2020). Identification of small non-coding RNAs responsive to GUN1 and GUN5 related retrograde signals in *Arabidopsis thaliana*. *Plant J* 104, 138-155.
- Haider, S., Iqbal, J., Naseer, S., Yaseen, T., Shaukat, M., et al. (2021). Molecular mechanisms of plant tolerance to heat stress: current landscape and future perspectives. *Plant Cell Rep* 40, 2247-2271.
- Han, Z., Xiong, D., Schneider, R., and Tian, C. (2023). The function of plant PR1 and other members of the CAP protein superfamily in plant-pathogen interactions. *Mol Plant Pathol* 24, 651-668.
- Haney, C.H., and Long, S.R. (2010). Plant flotillins are required for infection by nitrogen-fixing bacteria. *Proc Natl Acad Sci USA* 107, 478-483.
- Hao, H., Fan, L., Chen, T., Li, R., Li, X., et al. (2014). Clathrin and membrane microdomains cooperatively regulate RbohD dynamics and activity in *Arabidopsis*. *Plant Cell* 26, 1729-1745.
- Harris, B.J., Harrison, C.J., Hetherington, A.M., and Williams, T.A. (2020). Phylogenomic evidence for the monophyly of bryophytes and the reductive evolution of stomata. *Curr Biol* 30, 2001-2012 e2002.
- Hassani, A., Azapagic, A., and Shokri, N. (2021). Global predictions of primary soil salinization under changing climate in the 21st century. *Nat Commun* 12, 6663.
- Hauser, F., Waadt, R., and Schroeder, J.I. (2011). Evolution of abscisic acid synthesis and signaling mechanisms. *Curr Biol* 21, R346-355.

- He, M., and Ding, N.Z. (2020). Plant unsaturated fatty acids: Multiple roles in stress response. *Front Plant Sci* 11, 562785.
- He, M., Qin, C.X., Wang, X., and Ding, N.Z. (2020). Plant unsaturated fatty acids: Biosynthesis and regulation. *Front Plant Sci* 11, 390.
- Henderson, I.R., Zhang, X., Lu, C., Johnson, L., Meyers, B.C., et al. (2006). Dissecting *Arabidopsis thaliana* DICER function in small RNA processing, gene silencing and DNA methylation patterning. *Nat Genet* 38, 721-725.
- Hernandez-Garcia, J., Briones-Moreno, A., and Blazquez, M.A. (2021). Origin and evolution of gibberellin signaling and metabolism in plants. *Semin Cell Dev Biol* 109, 46-54.
- Hernández Estévez, I., and Rodríguez Hernández, M. (2020). "Plant Glutathione S-transferases: An overview". *Plant Gene* 23, 100233.
- Hernández, J.A., Gullner, G., Clemente-Moreno, M.J., Künstler, A., Juhász, C., et al. (2016). Oxidative stress and antioxidative responses in plant-virus interactions. *Physiol Mol Plant Pathol* 94, 134-148.
- Hisanaga, T., Okahashi, K., Yamaoka, S., Kajiwar, T., Nishihama, R., et al. (2019). A cis-acting bidirectional transcription switch controls sexual dimorphism in the liverwort. *EMBO J* 38, e100240.
- Hou, Z., Yang, Y., Hedtke, B., and Grimm, B. (2019). Fluorescence in blue light (FLU) is involved in inactivation and localization of glutamyl-tRNA reductase during light exposure. *Plant J* 97, 517-529.
- Huang, J., Li, Z., and Zhao, D. (2016). Deregulation of the OsmiR160 target gene *OsARF18* causes growth and developmental defects with an alteration of auxin signaling in rice. *Sci Rep* 6, 29938.
- Ichikawa, K., Shimizu, A., Okada, R., Satbhai, S.B., and Aoki, S. (2008). The plastid sigma factor SIG5 is involved in the diurnal regulation of the chloroplast gene *psbD* in the moss *Physcomitrella patens*. *FEBS Lett* 582, 405-409.
- Ichikawa, K., Sugita, M., Imaizumi, T., Wada, M., and Aoki, S. (2004). Differential expression on a daily basis of plastid sigma factor genes from the moss *Physcomitrella patens*. Regulatory interactions among *PpSig5*, the circadian clock, and blue light signaling mediated by cryptochromes. *Plant Physiol* 136, 4285-4298.
- Inglis, P.W., Pappas, M.C.R., Resende, L.V., and Grattapaglia, D. (2018). Fast and inexpensive protocols for consistent extraction of high quality DNA and RNA from challenging plant and fungal samples for high-throughput SNP genotyping and sequencing applications. *PLoS One* 13, e0206085.
- Ishizaki, K., Chiyoda, S., Yamato, K.T., and Kohchi, T. (2008). Agrobacterium-mediated transformation of the haploid liverwort *Marchantia polymorpha* L., an emerging model for plant biology. *Plant Cell Physiol* 49, 1084-1091.
- Ishizaki, K., Johzuka-Hisatomi, Y., Ishida, S., Iida, S., and Kohchi, T. (2013). Homologous recombination-mediated gene targeting in the liverwort *Marchantia polymorpha* L. *Sci Rep* 3, 1532.
- Ishizaki, K., Nonomura, M., Kato, H., Yamato, K.T., and Kohchi, T. (2012). Visualization of auxin-mediated transcriptional activation using a common auxin-responsive reporter system in the liverwort *Marchantia polymorpha*. *J Plant Res* 125, 643-651.
- Isner, J.C., Begum, A., Nuehse, T., Hetherington, A.M., and Maathuis, F.J.M. (2018). KIN7 kinase regulates the vacuolar TPK1 K(+) channel during stomatal closure. *Curr Biol* 28, 466-472 e464.
- Jahan, A., Komatsu, K., Wakida-Sekiya, M., Hiraide, M., Tanaka, K., et al. (2019). Archetypal roles of an abscisic acid receptor in drought and sugar responses in liverworts. *Plant Physiol* 179, 317-328.
- Jaiti, F., Verdeil, J.L., and El Hadrami, I. (2009). Effect of jasmonic acid on the induction of polyphenoloxidase and peroxidase activities in relation to date palm resistance against *Fusarium oxysporum* f. sp. *albedinis*. *Physiol Mol Plant Pathol* 74, 84-90.
- Jang, G., and Dolan, L. (2011). Auxin promotes the transition from chloronema to caulonema in moss protonema by positively regulating *PpRSL1* and *PpRSL2* in *Physcomitrella patens*. *New Phytol* 192, 319-327.
- Jarvi, S., Gollan, P.J., and Aro, E.M. (2013). Understanding the roles of the thylakoid lumen in photosynthesis regulation. *Front Plant Sci* 4, 434.
- Jeon, H.-W., Iwakawa, H., Naramoto, S., Herrfurth, C., Gutsche, N., et al. (2023). Contrasting and conserved roles of NPR pathways in diverged land plant lineages. *bioRxiv*, doi: <https://doi.org/10.1101/2022.07.19.500630>.
- Jodder, J. (2020). miRNA-mediated regulation of auxin signaling pathway during plant development and stress responses. *J Biosci* 45, 91.
- Johnson, M.P. (2016). Photosynthesis. *Essays Biochem* 60, 255-273.
- Jose, J., Ghantasala, S., and Choudhury, R.S. (2020). Arabidopsis transmembrane receptor-like kinases (RLKs): A bridge between extracellular signal and intracellular regulatory machinery. *Int J Mol Sci* 21, 4000.
- Junková, P., Daněš, M., Kocourková, D., Brouzdová, J., Kroumanová, K., et al. (2018). Mapping of plasma membrane proteins interacting with *Arabidopsis thaliana* Flotillin 2. *Front Plant Sci* 9, 991.
- Jurado-Flores, A., Delgado-Requerey, V., Galvez-Ramirez, A., Puerto-Galan, L., Perez-Ruiz, J.M., et al. (2020). Exploring the functional relationship between γ -Type thioredoxins and 2-Cys peroxiredoxins in *Arabidopsis* chloroplasts. *Antioxidants (Basel)* 9, 1072.
- Kassambara, A. (2023a). `ggpubr: 'ggplot2' Based publication ready plots`. R package version 0.6.0, URL <https://CRAN.R-project.org/package=ggpubr>.
- Kassambara, A. (2023b). `rstatix: Pipe-friendly framework for basic statistical tests`. R package version 0.7.2, URL <https://CRAN.R-project.org/package=rstatix>.
- Kato, H., Kouno, M., Takeda, M., Suzuki, H., Ishizaki, K., et al. (2017). The roles of the sole activator-type auxin response factor in pattern formation of *Marchantia polymorpha*. *Plant Cell Physiol* 58, 1642-1651.
- Kauss, D., Bischof, S., Steiner, S., Apel, K., and Meskauskiene, R. (2012). FLU, a negative feedback regulator of tetrapyrrole biosynthesis, is physically linked to the final steps of the Mg(++)-branch of this pathway. *FEBS Lett* 586, 211-216.

- Khraiweh, B., Arif, M.A., Seumel, G.I., Ossowski, S., Weigel, D., et al. (2010). Transcriptional control of gene expression by microRNAs. *Cell* 140, 111-122.
- Khraiweh, B., Zhu, J.K., and Zhu, J. (2012). Role of miRNAs and siRNAs in biotic and abiotic stress responses of plants. *Biochim Biophys Acta* 1819, 137-148.
- Kidwai, M., Ahmad, I.Z., and Chakrabarty, D. (2020). Class III peroxidase: an indispensable enzyme for biotic/abiotic stress tolerance and a potent candidate for crop improvement. *Plant Cell Rep* 39, 1381-1393.
- Kim, N., Jeong, J., Kim, J., Oh, J., and Choi, G. (2023). Shade represses photosynthetic genes by disrupting the DNA binding of GOLDEN2-LIKE1. *Plant Physiol* 191, 2334-2352.
- Kirchhoff, H., Hall, C., Wood, M., Herbstová, M., Tsabari, O., et al. (2011). Dynamic control of protein diffusion within the granal thylakoid lumen. *Proc Natl Acad Sci USA* 108, 20248-20253.
- Kitsios, G., and Doonan, J.H. (2011). Cyclin dependent protein kinases and stress responses in plants. *Plant Signal Behav* 6, 204-209.
- Klahn, S., Mikkat, S., Riediger, M., Georg, J., Hess, W.R., et al. (2021). Integrative analysis of the salt stress response in cyanobacteria. *Biol Direct* 16, 26.
- Kleist, T.J., Bortolazzo, A., Keyser, Z.P., Perera, A.M., Irving, T.B., et al. (2022). Stress-associated developmental reprogramming in moss protonemata by synthetic activation of the common symbiosis pathway. *iScience* 25, 103754.
- Klodmann, J., and Braun, H.P. (2011). Proteomic approach to characterize mitochondrial complex I from plants. *Phytochemistry* 72, 1071-1080.
- Kohchi, T., Yamato, K.T., Ishizaki, K., Yamaoka, S., and Nishihama, R. (2021). Development and molecular genetics of *Marchantia polymorpha*. *Annu Rev Plant Biol* 72, 677-702.
- Kolde, R. (2019). *pheatmap: Pretty heatmaps*. R package version 1.0.12, URL <https://CRAN.R-project.org/package=pheatmap>.
- Kramer, D.M., Johnson, G., Kiirats, O., and Edwards, G.E. (2004). New fluorescence parameters for the determination of QA redox state and excitation energy fluxes. *Photosynth Res* 79, 209.
- Kramer, M.F. (2011). Stem-loop RT-qPCR for miRNAs. *Curr Protoc Mol Biol* Chapter 15, Unit 15.10-15.10.
- Krasnikova, M.S., Goryunov, D.V., Troitsky, A.V., Solovyev, A.G., Ozerova, L.V., et al. (2013). Peculiar evolutionary history of miR390-guided TAS3-like genes in land plants. *Sci World J* 2013, 924153.
- Kroumanova, K., Kocourkova, D., Danek, M., Lamparova, L., Pospichalova, R., et al. (2019). Characterisation of *Arabidopsis* flotillins in response to stresses. *Biologia plantarum* 63, 144-152.
- Kubota, A., Ishizaki, K., Hosaka, M., and Kohchi, T. (2013). Efficient Agrobacterium-mediated transformation of the liverwort *Marchantia polymorpha* using regenerating thalli. *Biosci Biotechnol Biochem* 77, 167-172.
- Kumar, S., Stecher, G., Li, M., Knyaz, C., and Tamura, K. (2018). MEGA X: Molecular evolutionary genetics analysis across computing platforms. *Mol Biol Evol* 35, 1547-1549.
- Kuromori, T., and Shinozaki, K. (2010). ABA transport factors found in Arabidopsis ABC transporters. *Plant Signal Behav* 5, 1124-1126.
- Kyozuka, J., Nomura, T., and Shimamura, M. (2022). Origins and evolution of the dual functions of strigolactones as rhizosphere signaling molecules and plant hormones. *Curr Opin Plant Biol* 65, 102154.
- Kyte, J., and Doolittle, R.F. (1982). A simple method for displaying the hydropathic character of a protein. *J Mol Biol* 157, 105-132.
- Lang, D., Ullrich, K.K., Murat, F., Fuchs, J., Jenkins, J., et al. (2018). The *Physcomitrella patens* chromosome-scale assembly reveals moss genome structure and evolution. *Plant J* 93, 515-533.
- Laugier, E., Tarrago, L., Courteille, A., Innocenti, G., Eymery, F., et al. (2013). Involvement of thioredoxin y2 in the preservation of leaf methionine sulfoxide reductase capacity and growth under high light. *Plant Cell Environ* 36, 670-682.
- Lee, K.P., Li, M., Li, M., Liu, K., Medina-Puche, L., et al. (2023). Hierarchical regulatory module GENOMES UNCOUPLED1-GOLDEN2-LIKE1/2-WRKY18/40 modulates salicylic acid signaling. *Plant Physiol* 192, 3120-3133.
- Leng, L., Liang, Q., Jiang, J., Zhang, C., Hao, Y., et al. (2017). A subclass of HSP70s regulate development and abiotic stress responses in *Arabidopsis thaliana*. *J Plant Res* 130, 349-363.
- Lévy, J., Bres, C., Geurts, R., Chalhoub, B., Kulikova, O., et al. (2004). A putative Ca²⁺ and calmodulin-dependent protein kinase required for bacterial and fungal symbioses. *Science* 303, 1361-1364.
- Lewsey, M.G., and Carr, J.P. (2009). Effects of DICER-like proteins 2, 3 and 4 on cucumber mosaic virus and tobacco mosaic virus infections in salicylic acid-treated plants. *J Gen Virol* 90, 3010-3014.
- Leyser, O. (2018). Auxin Signaling. *Plant Physiol* 176, 465-479.
- Li, A., Sun, X., and Liu, L. (2022a). Action of salicylic acid on plant growth. *Front Plant Sci* 13, 878076.
- Li, C., Xu, M., Cai, X., Han, Z., Si, J., et al. (2022b). Jasmonate signaling pathway modulates plant defense, growth, and their trade-Offs. *Int J Mol Sci* 23.
- Li, J., Zhang, M., Sun, J., Mao, X., Wang, J., et al. (2020). Heavy metal stress-associated proteins in rice and *Arabidopsis*: Genome-wide identification, phylogenetics, duplication, and expression profiles analysis. *Front Genet* 11, 477.
- Li, M., and Kim, C. (2022). Chloroplast ROS and stress signaling. *Plant Commun* 3, 100264.
- Li, R., Liu, P., Wan, Y., Chen, T., Wang, Q., et al. (2012). A membrane microdomain-associated protein, *Arabidopsis* Flot1, is involved in a clathrin-independent endocytic pathway and is required for seedling development. *Plant Cell* 24, 2105-2122.
- Li, X., Wang, X., Yang, Y., Li, R., He, Q., et al. (2011). Single-molecule analysis of PIP2;1 dynamics and partitioning reveals multiple modes of *Arabidopsis* plasma membrane aquaporin regulation. *Plant Cell* 23, 3780-3797.

- Li, Y., Darley, C.P., Ongaro, V., Fleming, A., Schipper, O., et al. (2002). Plant expansins are a complex multigene family with an ancient evolutionary origin. *Plant Physiol* 128, 854-864.
- Li, Y., Yang, Z., Zhang, Y., Guo, J., Liu, L., et al. (2022c). The roles of HD-ZIP proteins in plant abiotic stress tolerance. *Front Plant Sci* 13, 1027071.
- Liao, Y., Smyth, G.K., and Shi, W. (2014). featureCounts: an efficient general purpose program for assigning sequence reads to genomic features. *Bioinformatics* 30, 923-930.
- Lin, P.C., Lu, C.W., Shen, B.N., Lee, G.Z., Bowman, J.L., et al. (2016). Identification of miRNAs and their targets in the liverwort *Marchantia polymorpha* by integrating RNA-Seq and degradome analyses. *Plant Cell Physiol* 57, 339-358.
- Lin, S.S., and Bowman, J.L. (2018). MicroRNAs in *Marchantia polymorpha*. *New Phytol* 220, 409-416.
- Liu, B., Li, P., Li, X., Liu, C., Cao, S., et al. (2005). Loss of function of *OsDCL1* affects microRNA accumulation and causes developmental defects in rice. *Plant Physiol* 139, 296-305.
- Liu, C., Axtell, M.J., and Fedoroff, N.V. (2012). The helicase and RNaseIII domains of *Arabidopsis* Dicer-Like1 modulate catalytic parameters during microRNA biogenesis. *Plant Physiol* 159, 748-758.
- Liu, Q., Feng, Y., and Zhu, Z. (2009). Dicer-like (DCL) proteins in plants. *Funct Integr Genomics* 9, 277-286.
- Liu, R., Xu, Y.H., Jiang, S.C., Lu, K., Lu, Y.F., et al. (2013). Light-harvesting chlorophyll a/b-binding proteins, positively involved in abscisic acid signalling, require a transcription repressor, WRKY40, to balance their function. *J Exp Bot* 64, 5443-5456.
- Liu, Y., Teng, C., Xia, R., and Meyers, B.C. (2020). PhasiRNAs in Plants: Their biogenesis, genic sources, and roles in stress responses, development, and reproduction. *Plant Cell* 32, 3059-3080.
- Livak, K.J., and Schmittgen, T.D. (2001). Analysis of relative gene expression data using real-time quantitative PCR and the $2^{-\Delta\Delta C_T}$ Method. *Methods* 25, 402-408.
- Locato, V., Cimini, S., and De Gara, L. (2018). ROS and redox balance as multifaceted players of cross-tolerance: epigenetic and retrograde control of gene expression. *J Exp Bot* 69, 3373-3391.
- Love, M.I., Huber, W., and Anders, S. (2014). Moderated estimation of fold change and dispersion for RNA-seq data with DESeq2. *Genome Biol* 15, 550.
- Lüttge, U. (2020). Terrestrialization: The Conquest of Dry Land by Plants. in Lüttge, U., Cánovas, F.M., Risueno, M., Leuschner C. and Pretzsch, H. (Hrsg.), *Progress in Botany* (Vol. 83, 65-89), Springer. <https://doi.org/10.1007/978-3-031-12782-3>.
- Ma, J., Wang, S., Zhu, X., Sun, G., Chang, G., et al. (2022). Major episodes of horizontal gene transfer drove the evolution of land plants. *Mol Plant* 15, 857-871.
- Madeo, G., Savojardo, C., Manfredi, M., Martelli, P.L., and Casadio, R. (2023). CoCoNat: a novel method based on deep learning for coiled-coil prediction. *Bioinformatics* 39.
- Manavella, P.A., Yang, S.W., and Palatnik, J. (2019). Keep calm and carry on: miRNA biogenesis under stress. *Plant J* 99, 832-843.
- Margis, R., Fusaro, A.F., Smith, N.A., Curtin, S.J., Watson, J.M., et al. (2006). The evolution and diversification of Dicers in plants. *FEBS Lett* 580, 2442-2450.
- Marino, G., Naranjo, B., Wang, J., Penzler, J.F., Kleine, T., et al. (2019). Relationship of GUN1 to FUG1 in chloroplast protein homeostasis. *Plant J* 99, 521-535.
- Maronova, M., and Kalyna, M. (2016). Generating targeted gene knockout lines in *Physcomitrella patens* to study evolution of stress-responsive mechanisms. *Methods Mol Biol* 1398, 221-234.
- Martí Ruiz, M.C., Jung, H.J., and Webb, A.a.R. (2020). Circadian gating of dark-induced increases in chloroplast- and cytosolic-free calcium in *Arabidopsis*. *New Phytol* 225, 1993-2005.
- Martin, W.F., and Allen, J.F. (2018). An algal greening of land. *Cell* 174, 256-258.
- Martinière, A., and Zelazny, E. (2021). Membrane nanodomains and transport functions in plant. *Plant Physiol* 187, 1839-1855.
- Masood, A., Shah, N.A., Zeeshan, M., and Abraham, G. (2006). Differential response of antioxidant enzymes to salinity stress in two varieties of *Azolla* (*Azolla pinnata* and *Azolla filiculoides*). *Environ Exp Bot* 58, 216-222.
- Matsui, H., Iwakawa, H., Hyon, G.S., Yotsui, I., Katou, S., et al. (2020). Isolation of natural fungal pathogens from *Marchantia polymorpha* reveals antagonism between salicylic acid and jasmonate during liverwort-fungus interactions. *Plant Cell Physiol* 61, 265-275.
- Mechela, A., Schwenkert, S., and Soll, J. (2019). A brief history of thylakoid biogenesis. *Open Biol* 9, 180237.
- Meng, Y., Chen, D., Ma, X., Mao, C., Cao, J., et al. (2010). Mechanisms of microRNA-mediated auxin signaling inferred from the rice mutant *osaxr*. *Plant Signal Behav* 5, 252-254.
- Meskauskiene, R., and Apel, K. (2002). Interaction of FLU, a negative regulator of tetrapyrrole biosynthesis, with the glutamyl-tRNA reductase requires the tetratricopeptide repeat domain of FLU. *FEBS Lett* 532, 27-30.
- Miller, J.B., Pratap, A., Miyahara, A., Zhou, L., Bornemann, S., et al. (2013). Calcium/Calmodulin-dependent protein kinase is negatively and positively regulated by calcium, providing a mechanism for decoding calcium responses during symbiosis signaling. *Plant Cell* 25, 5053-5066.
- Mizoi, J., Shinozaki, K., and Yamaguchi-Shinozaki, K. (2012). AP2/ERF family transcription factors in plant abiotic stress responses. *Biochim Biophys Acta* 1819, 86-96.
- Monte, I. (2023). Jasmonates and salicylic acid: Evolution of defense hormones in land plants. *Curr Opin Plant Biol* 76, 102470.
- Morris, J.L., Puttick, M.N., Clark, J.W., Edwards, D., Kenrick, P., et al. (2018). The timescale of early land plant evolution. *Proc Natl Acad Sci USA* 115, E2274-E2283.

- Moura, M.O., Fausto, A.K.S., Fanelli, A., Guedes, F.a.F., Silva, T.D.F., et al. (2019). Genome-wide identification of the Dicer-like family in cotton and analysis of the *DCL* expression modulation in response to biotic stress in two contrasting commercial cultivars. *BMC Plant Biol* 19, 503.
- Mullineaux, C.W. (2008). Factors controlling the mobility of photosynthetic proteins. *Photochem Photobiol* 84, 1310-1316.
- Mustroph, A., Stock, J., Hess, N., Aldous, S., Dreilich, A., et al. (2013). Characterization of the phosphofructokinase gene family in rice and its expression under oxygen deficiency stress. *Front Plant Sci* 4, 125.
- Mutak, A. (2018). *_cosinor2: Extended tools for cosinor analysis of rhythms_*. R package version 0.2.1, URL <https://CRAN.R-project.org/package=cosinor2>.
- Mutte, S.K., Kato, H., Rothfels, C., Melkonian, M., Wong, G.K., et al. (2018). Origin and evolution of the nuclear auxin response system. *Elife* 7, e33399.
- Naramoto, S., Hata, Y., Fujita, T., and Kyoizuka, J. (2022). The bryophytes *Physcomitrium patens* and *Marchantia polymorpha* as model systems for studying evolutionary cell and developmental biology in plants. *Plant Cell* 34, 228-246.
- Navarro, L., Dunoyer, P., Jay, F., Arnold, B., Dharmasiri, N., et al. (2006). A plant miRNA contributes to antibacterial resistance by repressing auxin signaling. *Science* 312, 436-439.
- Navazio, L., Formentin, E., Cendron, L., and Szabo, I. (2020). Chloroplast calcium signaling in the spotlight. *Front Plant Sci* 11, 186.
- Nieto-Sotelo, J., Ichida, A., and Quail, P.H. (1994). PF1: an A-T hook-containing DNA binding protein from rice that interacts with a functionally defined d(AT)-rich element in the oat phytochrome A3 gene promoter. *Plant Cell* 6, 287-301.
- Nishad, R., Ahmed, T., Rahman, V.J., and Kareem, A. (2020). Modulation of plant defense system in response to microbial interactions. *Front Microbiol* 11, 1298.
- Nishiyama, T., Sakayama, H., De Vries, J., Buschmann, H., Saint-Marcoux, D., et al. (2018). The Chara genome: Secondary complexity and implications for plant terrestrialization. *Cell* 174, 448-464 e424.
- Okada, R., Kondo, S., Satbhai, S.B., Yamaguchi, N., Tsukuda, M., et al. (2009). Functional characterization of CCA1/LHY homolog genes, *PpCCA1a* and *PpCCA1b*, in the moss *Physcomitrella patens*. *Plant J* 60, 551-563.
- Olmedo-Monfil, V., Durán-Figueroa, N., Arteaga-Vázquez, M., Demesa-Arévalo, E., Autran, D., et al. (2010). Control of female gamete formation by a small RNA pathway in *Arabidopsis*. *Nature* 464, 628-632.
- Ota, S.M., Kong, X., Hut, R., Suchecki, D., and Meerlo, P. (2021). The impact of stress and stress hormones on endogenous clocks and circadian rhythms. *Front Neuroendocrinol* 63, 100931.
- Pandey, S., Fartyal, D., Agarwal, A., Shukla, T., James, D., et al. (2017). Abiotic stress tolerance in plants: Myriad roles of ascorbate peroxidase. *Front Plant Sci* 8, 581.
- Paniagua, C., Bilkova, A., Jackson, P., Dabravolski, S., Riber, W., et al. (2017). Dirigent proteins in plants: modulating cell wall metabolism during abiotic and biotic stress exposure. *J Exp Bot* 68, 3287-3301.
- Patel, P., Mathioni, S.M., Hammond, R., Harkess, A.E., Kakrana, A., et al. (2021). Reproductive phasiRNA loci and DICER-LIKE5, but not microRNA loci, diversified in monocotyledonous plants. *Plant Physiol* 185, 1764-1782.
- Petersen, J., Rredhi, A., Szyttenholm, J., and Mittag, M. (2022). Evolution of circadian clocks along the green lineage. *Plant Physiol* 190, 924-937.
- Pfeifer, L., Mueller, K.K., and Classen, B. (2022). The cell wall of hornworts and liverworts: innovations in early land plant evolution? *J Exp Bot* 73, 4454-4472.
- Phukan, U.J., Jeena, G.S., and Shukla, R.K. (2016). WRKY transcription factors: Molecular regulation and stress responses in plants. *Front Plant Sci* 7, 760.
- Pietrykowska, H., Sierocka, I., Zielezinski, A., Alisha, A., Carrasco-Sanchez, J.C., et al. (2022). Biogenesis, conservation, and function of miRNA in liverworts. *J Exp Bot* 73, 4528-4545.
- Plavskin, Y., Nagashima, A., Perroud, P.F., Hasebe, M., Quatrano, R.S., et al. (2016). Ancient trans-acting siRNAs confer robustness and sensitivity onto the auxin response. *Dev Cell* 36, 276-289.
- Pokotylo, I., Kravets, V., and Ruelland, E. (2019). Salicylic acid binding proteins (SABPs): The hidden forefront of salicylic acid signalling. *Int J Mol Sci* 20, 4377.
- Powell, A.E., and Heyl, A. (2023). The origin and early evolution of cytokinin signaling. *Front Plant Sci* 14, 1142748.
- Pribil, M., Labs, M., and Leister, D. (2014). Structure and dynamics of thylakoids in land plants. *J Exp Bot* 65, 1955-1972.
- Printz, B., Lutts, S., Hausman, J.F., and Sergeant, K. (2016). Copper trafficking in plants and its implication on cell wall dynamics. *Front Plant Sci* 7, 601.
- Pucciariello, C., and Perata, P. (2021). The oxidative paradox in low oxygen stress in plants. *Antioxidants (Basel)* 10, 332.
- Qi, F., and Zhang, F. (2019). Cell cycle regulation in the plant response to stress. *Front Plant Sci* 10, 1765.
- Qu, F., Ye, X., and Morris, T.J. (2008). *Arabidopsis* DRB4, AGO1, AGO7, and RDR6 participate in a DCL4-initiated antiviral RNA silencing pathway negatively regulated by DCL1. *Proc Natl Acad Sci USA* 105, 14732-14737.
- R Core Team (2023). *_R: A language and environment for statistical computing_*. R foundation for statistical computing, Vienna, Austria. URL <https://www.R-project.org/>.
- Raja, P., Jackel, J.N., Li, S., Heard, I.M., and Bisaro, D.M. (2014). *Arabidopsis* double-stranded RNA binding protein DRB3 participates in methylation-mediated defense against geminiviruses. *J Virol* 88, 2611-2622.
- Rajagopalan, R., Vaucheret, H., Trejo, J., and Bartel, D.P. (2006). A diverse and evolutionarily fluid set of microRNAs in *Arabidopsis thaliana*. *Genes Dev* 20, 3407-3425.

- Rast, A., Heinz, S., and Nickelsen, J. (2015). Biogenesis of thylakoid membranes. *Biochim Biophys Acta* 1847, 821-830.
- Rea, G., De Pinto, M.C., Tavazza, R., Biondi, S., Gobbi, V., et al. (2004). Ectopic expression of maize polyamine oxidase and pea copper amine oxidase in the cell wall of tobacco plants. *Plant Physiol* 134, 1414-1426.
- Renault, H., Alber, A., Horst, N.A., Basilio Lopes, A., Fich, E.A., et al. (2017). A phenol-enriched cuticle is ancestral to lignin evolution in land plants. *Nat Commun* 8, 14713.
- Rensing, S.A. (2018a). Great moments in evolution: the conquest of land by plants. *Curr Opin Plant Biol* 42, 49-54.
- Rensing, S.A. (2018b). Plant evolution: Phylogenetic relationships between the earliest land plants. *Curr Biol* 28, R210-R213.
- Rensing, S.A. (2020). How plants conquered land. *Cell* 181, 964-966.
- Rensing, S.A., Goffinet, B., Meyberg, R., Wu, S.Z., and Bezanilla, M. (2020). The moss *Physcomitrium* (*Physcomitrella*) *patens*: A model organism for non-seed plants. *Plant Cell* 32, 1361-1376.
- Resemann, H.C., Lewandowska, M., Gi Mann, J., and Feussner, I. (2019). Membrane lipids, waxes and oxylipins in the moss model organism *Physcomitrella patens*. *Plant Cell Physiol* 60, 1166-1175.
- Reyes, J.C., Muro-Pastor, M.I., and Florencio, F.J. (2004). The GATA family of transcription factors in *Arabidopsis* and rice. *Plant Physiol* 134, 1718-1732.
- Rice, P., Longden, I., and Bleasby, A. (2000). EMBOS: The European molecular biology open software suite. *Trends Genet* 16, 276-277.
- Rivera-Milla, E., Stuermer, C.A., and Malaga-Trillo, E. (2006). Ancient origin of reggie (flotillin), reggie-like, and other lipid-raft proteins: convergent evolution of the SPFH domain. *Cell Mol Life Sci* 63, 343-357.
- Romani, F., Ribone, P.A., Capella, M., Miguel, V.N., and Chan, R.L. (2016). A matter of quantity: Common features in the drought response of transgenic plants overexpressing HD-Zip I transcription factors. *Plant Sci* 251, 139-154.
- Saavedra, L., Svensson, J., Carballo, V., Izmendi, D., Welin, B., et al. (2006). A dehydrin gene in *Physcomitrella patens* is required for salt and osmotic stress tolerance. *Plant J* 45, 237-249.
- Sah, S.K., Reddy, K.R., and Li, J. (2016). Abscisic acid and abiotic Stress tolerance in crop plants. *Front Plant Sci* 7, 571.
- Saleem, M., Fariduddin, Q., and Castroverde, C.D.M. (2021). Salicylic acid: A key regulator of redox signalling and plant immunity. *Plant Physiol Biochem* 168, 381-397.
- Saleh, O., Issman, N., Seumel, G.I., Stav, R., Samach, A., et al. (2011). *MicroRNA534a* control of *BLADE-ON-PETIOLE 1* and *2* mediates juvenile-to-adult gametophyte transition in *Physcomitrella patens*. *Plant J* 65, 661-674.
- Schaefer, D.G. (2001). Gene targeting in *Physcomitrella patens*. *Curr Opin Plant Biol* 4, 143-150.
- Schenk, P.M., Kazan, K., Rusu, A.G., Manners, J.M., and Maclean, D.J. (2005). The *SEN1* gene of *Arabidopsis* is regulated by signals that link plant defence responses and senescence. *Plant Physiol Biochem* 43, 997-1005.
- Schmidt, S.B., Eisenhut, M., and Schneider, A. (2020). Chloroplast transition metal regulation for efficient photosynthesis. *Trends Plant Sci* 25, 817-828.
- Schmittgen, T.D., and Livak, K.J. (2008). Analyzing real-time PCR data by the comparative C_T method. *Nat Protoc* 3, 1101-1108.
- Schneider, C.A., Rasband, W.S., and Eliceiri, K.W. (2012). NIH Image to ImageJ: 25 years of image analysis. *Nat Methods* 9, 671-675.
- Sello, S., Perotto, J., Carraretto, L., Szabo, I., Vothknecht, U.C., et al. (2016). Dissecting stimulus-specific Ca^{2+} signals in amyloplasts and chloroplasts of *Arabidopsis thaliana* cell suspension cultures. *J Exp Bot* 67, 3965-3974.
- Seung, D., Thalmann, M., Sparla, F., Abou Hachem, M., Lee, S.K., et al. (2013). *Arabidopsis thaliana* AMY3 is a unique redox-regulated chloroplastic alpha-amylase. *J Biol Chem* 288, 33620-33633.
- Shao, F., Qiu, D., and Lu, S. (2015). Comparative analysis of the Dicer-like gene family reveals loss of miR162 target site in *SmdCL1* from *Salvia miltiorrhiza*. *Sci Rep* 5, 9891.
- Shen, J., Xie, K., and Xiong, L. (2010). Global expression profiling of rice microRNAs by one-tube stem-loop reverse transcription quantitative PCR revealed important roles of microRNAs in abiotic stress responses. *Mol Genet Genomics* 284, 477-488.
- Shi, L.X., and Theg, S.M. (2010). A stromal heat shock protein 70 system functions in protein import into chloroplasts in the moss *Physcomitrella patens*. *Plant Cell* 22, 205-220.
- Shimamura, M. (2016). *Marchantia polymorpha*: Taxonomy, phylogeny and morphology of a model system. *Plant Cell Physiol* 57, 230-256.
- Shin, J.S., Kim, S.Y., So, W.M., Noh, M., Yoo, K.S., et al. (2020). Lon domain-containing protein 1 represses thioredoxin y2 and regulates ROS levels in *Arabidopsis* chloroplasts. *FEBS Lett* 594, 986-994.
- Shin, Y., Chane, A., Jung, M., and Lee, Y. (2021). Recent advances in understanding the roles of pectin as an active participant in plant signaling networks. *Plants (Basel)* 10, 1712.
- Solis, G.P., Hoegg, M., Munderloh, C., Schrock, Y., Malaga-Trillo, E., et al. (2007). Reggie/flotillin proteins are organized into stable tetramers in membrane microdomains. *Biochem J* 403, 313-322.
- Sugano, S.S., Nishihama, R., Shirakawa, M., Takagi, J., Matsuda, Y., et al. (2018). Efficient CRISPR/Cas9-based genome editing and its application to conditional genetic analysis in *Marchantia polymorpha*. *PLoS One* 13, e0205117.
- Sun, T., Zeng, S., Wang, X., Owens, L.A., Fe, Z., et al. (2022). GLKs directly regulate carotenoid biosynthesis via interacting with GBFs in nuclear condensates in plants. *bioRxiv* doi: <https://doi.org/10.1101/2022.09.09.507346>.

- Sunkar, R., and Zhu, J.K. (2004). Novel and stress-regulated microRNAs and other small RNAs from *Arabidopsis*. *Plant Cell* 16, 2001-2019.
- Taïbi, K., Taïbi, F., Ait Abderrahim, L., Ennajah, A., Belkhodja, M., et al. (2016). Effect of salt stress on growth, chlorophyll content, lipid peroxidation and antioxidant defence systems in *Phaseolus vulgaris* L. *S AFR J Bot* 105, 306-312.
- Tan, Q.W., Lim, P.K., Chen, Z., Pasha, A., Provart, N., et al. (2023). Cross-stress gene expression atlas of *Marchantia polymorpha* reveals the hierarchy and regulatory principles of abiotic stress responses. *Nat Commun* 14, 986.
- Tanaka, H., Suzuki, R., Okabe, N., Suzuki, T., and Kodama, Y. (2018). Salinity stress-responsive transcription factors in the liverwort *Marchantia polymorpha*. *Plant Biotechnol (Tokyo)* 35, 281-284.
- Teale, W.D., Paponov, I.A., and Palme, K. (2006). Auxin in action: signalling, transport and the control of plant growth and development. *Nat Rev Mol Cell Biol* 7, 847-859.
- Thelander, M., Landberg, K., and Sundberg, E. (2018). Auxin-mediated developmental control in the moss *Physcomitrella patens*. *J Exp Bot* 69, 277-290.
- Tian, G.W., Mohanty, A., Chary, S.N., Li, S., Paap, B., et al. (2004). High-throughput fluorescent tagging of full-length *Arabidopsis* gene products in planta. *Plant Physiol* 135, 25-38.
- Tian, T., Liu, Y., Yan, H., You, Q., Yi, X., et al. (2017). agriGO v2.0: a GO analysis toolkit for the agricultural community, 2017 update. *Nucleic Acids Res* 45, W122-W129.
- Tiwari, B., Habermann, K., Arif, M.A., Top, O., and Frank, W. (2021). Identification of small RNAs during high light acclimation in *Arabidopsis thaliana*. *Front Plant Sci* 12, 656657.
- Tiwari, B., Habermann, K., Arif, M.A., Weil, H.L., Garcia-Molina, A., et al. (2020). Identification of small RNAs during cold acclimation in *Arabidopsis thaliana*. *BMC Plant Biol* 20, 298.
- Top, O., Milferstaedt, S.W.L., Van Gessel, N., Hoernstein, S.N.W., Ozdemir, B., et al. (2021). Expression of a human cDNA in moss results in spliced mRNAs and fragmentary protein isoforms. *Commun Biol* 4, 964.
- Torii, K.U. (2004). Leucine-rich repeat receptor kinases in plants: structure, function, and signal transduction pathways. *Int Rev Cytol* 234, 1-46.
- Tsuzuki, M., Futagami, K., Shimamura, M., Inoue, C., Kunitomo, K., et al. (2019). An early arising role of the microRNA156/529-SPL module in reproductive development revealed by the liverwort *Marchantia polymorpha*. *Curr Biol* 29, 3307-3314 e3305.
- Tsuzuki, M., Nishihama, R., Ishizaki, K., Kurihara, Y., Matsui, M., et al. (2016). Profiling and characterization of small RNAs in the liverwort, *Marchantia polymorpha*, belonging to the first diverged land plants. *Plant Cell Physiol* 57, 359-372.
- Tucker, E.B., Lee, M., Alli, S., Sookhdeo, V., Wada, M., et al. (2005). UV-A induces two calcium waves in *Physcomitrella patens*. *Plant Cell Physiol* 46, 1226-1236.
- Tyanova, S., and Cox, J. (2018). Perseus: A bioinformatics platform for integrative analysis of proteomics data in cancer research. *Methods Mol Biol* 1711, 133-148.
- Tyanova, S., Temu, T., Sinitcyn, P., Carlson, A., Hein, M.Y., et al. (2016). The Perseus computational platform for comprehensive analysis of (prote)omics data. *Nat Methods* 13, 731-740.
- Valerio, C., Costa, A., Marri, L., Issakidis-Bourguet, E., Pupillo, P., et al. (2011). Thioredoxin-regulated beta-amylase (BAM1) triggers diurnal starch degradation in guard cells, and in mesophyll cells under osmotic stress. *J Exp Bot* 62, 545-555.
- Van De Poel, B., and De Vries, J. (2023). Evolution of ethylene as an abiotic stress hormone in streptophytes. *Environ Exp Bot* 214, 105456.
- Vanacker, H., Guichard, M., Bohrer, A.S., and Issakidis-Bourguet, E. (2018). Redox regulation of monodehydroascorbate reductase by thioredoxin y in plastids revealed in the context of water stress. *Antioxidants (Basel)* 7, 183.
- Vaucheret, H., and Voinnet, O. (2024). The plant siRNA landscape. *Plant Cell* 36, 246-275.
- Venzhik, Y.V., Shchyogolev, S.Y., and Dykman, L.A. (2019). Ultrastructural reorganization of chloroplasts during plant adaptation to abiotic stress factors. *Russ J Plant Physiol* 66, 850-863.
- Verma, S., and Mishra, S.N. (2005). Putrescine alleviation of growth in salt stressed Brassica juncea by inducing antioxidative defense system. *J Plant Physiol* 162, 669-677.
- Viaene, T., Landberg, K., Thelander, M., Medvecka, E., Pederson, E., et al. (2014). Directional auxin transport mechanisms in early diverging land plants. *Curr Biol* 24, 2786-2791.
- Vieira Dos Santos, C., Laugier, E., Tarrago, L., Massot, V., Issakidis-Bourguet, E., et al. (2007). Specificity of thioredoxins and glutaredoxins as electron donors to two distinct classes of Arabidopsis plastidial methionine sulfoxide reductases B. *FEBS Lett* 581, 4371-4376.
- Vlot, A.C., Sales, J.H., Lenk, M., Bauer, K., Brambilla, A., et al. (2021). Systemic propagation of immunity in plants. *New Phytol* 229, 1234-1250.
- Wang, C., Liu, Y., Li, S.S., and Han, G.Z. (2015). Insights into the origin and evolution of the plant hormone signaling machinery. *Plant Physiol* 167, 872-886.
- Wang, L., Zheng, K., Zeng, L., Xu, D., Zhu, T., et al. (2022). Reinforcement of CHH methylation through RNA-directed DNA methylation ensures sexual reproduction in rice. *Plant Physiol* 188, 1189-1209.
- Wang, S., Liang, H., Xu, Y., Li, L., Wang, H., et al. (2021a). Genome-wide analyses across Viridiplantae reveal the origin and diversification of small RNA pathway-related genes. *Commun Biol* 4, 412.
- Wang, Y., Mostafa, S., Zeng, W., and Jin, B. (2021b). Function and mechanism of jasmonic acid in plant responses to abiotic and biotic stresses. *Int J Mol Sci* 22, 8568.
- Wei, L., Gu, L., Song, X., Cui, X., Lu, Z., et al. (2014). Dicer-like 3 produces transposable element-associated 24-nt siRNAs that control agricultural traits in rice. *Proc Natl Acad Sci USA* 111, 3877-3882.

- Willmann, M.R., and Poethig, R.S. (2007). Conservation and evolution of miRNA regulatory programs in plant development. *Curr Opin Plant Biol* 10, 503-511.
- Winter, D., Vinegar, B., Nahal, H., Ammar, R., Wilson, G.V., et al. (2007). An "Electronic Fluorescent Pictograph" browser for exploring and analyzing large-scale biological data sets. *PLoS One* 2, e718.
- Wittmann, D., Sinha, N., and Grimm, B. (2021). Thioredoxin-dependent control balances the metabolic activities of tetrapyrrole biosynthesis. *Biol Chem* 402, 379-397.
- Xie, Z., Kasschau, K.D., and Carrington, J.C. (2003). Negative feedback regulation of Dicer-Like1 in *Arabidopsis* by microRNA-guided mRNA degradation. *Current Biology* 13, 784-789.
- Xu, Y.H., Liu, R., Yan, L., Liu, Z.Q., Jiang, S.C., et al. (2012). Light-harvesting chlorophyll a/b-binding proteins are required for stomatal response to abscisic acid in *Arabidopsis*. *J Exp Bot* 63, 1095-1106.
- Yamaoka, S., Inoue, K., and Araki, T. (2021). Regulation of gametangia and gametangiophore initiation in the liverwort *Marchantia polymorpha*. *Plant Reprod* 34, 297-306.
- Yasumura, Y., Moylan, E.C., and Langdale, J.A. (2005). A conserved transcription factor mediates nuclear control of organelle biogenesis in anciently diverged land plants. *Plant Cell* 17, 1894-1907.
- Ye, Y., Ding, Y., Jiang, Q., Wang, F., Sun, J., et al. (2017). The role of receptor-like protein kinases (RLKs) in abiotic stress response in plants. *Plant Cell Rep* 36, 235-242.
- You, C., Cui, J., Wang, H., Qi, X., Kuo, L.Y., et al. (2017). Conservation and divergence of small RNA pathways and microRNAs in land plants. *Genome Biol* 18, 158.
- You, C., Yu, Y., and Wang, Y. (2022). Small RNA in plant meiosis and gametogenesis. *Reprod Breed* 2, 65-70.
- Yu, M., Liu, H., Dong, Z., Xiao, J., Su, B., et al. (2017a). The dynamics and endocytosis of Flot1 protein in response to flg22 in *Arabidopsis*. *J Plant Physiol* 215, 73-84.
- Yu, Y., Jia, T., and Chen, X. (2017b). The 'how' and 'where' of plant microRNAs. *New Phytol* 216, 1002-1017.
- Zeng, X., Ye, L., Zhang, R., and Wang, P. (2023). Transcription factor GLK2 regulates key steps of anthocyanin biosynthesis to antagonize photo-oxidative stress during greening of *Arabidopsis* seedlings. *bioRxiv* doi: <https://doi.org/10.1101/2023.03.10.532066>.
- Zhan, J., and Meyers, B.C. (2023). Plant Small RNAs: Their biogenesis, regulatory roles, and functions. *Annu Rev Plant Biol* 74, 21-51.
- Zhang, B., You, C., Zhang, Y., Zeng, L., Hu, J., et al. (2020). Linking key steps of microRNA biogenesis by TREX-2 and the nuclear pore complex in *Arabidopsis*. *Nat Plants* 6, 957-969.
- Zhang, H., Zhu, J., Gong, Z., and Zhu, J.K. (2022). Abiotic stress responses in plants. *Nat Rev Genet* 23, 104-119.
- Zhao, Y. (2012). Auxin biosynthesis: a simple two-step pathway converts tryptophan to indole-3-acetic acid in plants. *Mol Plant* 5, 334-338.
- Zhou, F., Liu, S., Hu, Z., Kuang, T., Paulsen, H., et al. (2009). Effect of monogalactosyldiacylglycerol on the interaction between photosystem II core complex and its antenna complexes in liposomes of thylakoid lipids. *Photosynth Res* 99, 185-193.
- Zou, X., and Sun, H. (2023). DOF transcription factors: Specific regulators of plant biological processes. *Front Plant Sci* 14, 1044918.

List of abbreviations

2-ip	6-y-y-(dimethylallylamino)-purine
AA	Amino acid sequence
ABA	Absciscic acid
ABCB1	ATP-binding cassette B1
ABCG	ATP-binding cassette transporters
ABF	ABRE binding factors
ABI	ABA insensitive
ABRE	ABA-responsive cis-elements
ACT5	Actin 5
ACT5_P	Actin 5 promotor
ADA2	Adaptor 2 of SANT complex
AGO	Argonaute
ALA	5-aminolevulinic acid
AMF	Arbuscular mycorrhiza fungi
AP2	Apetala 2
AP2/ERF	Apetala 2/ethylene response factor
APIP1;2	Aquaporine PIP1;2
APX	Ascorbate peroxidases
ARE	Auxin-responsive elements
ARF	Auxin-responsive factors
asRNA	<i>Cis</i> -encoded antisense RNA
bHLH	Basic helix-loop-helix
bp	Base pairs
BR	Brassinosteroids
BOP	Blade-on-petiole
bZIP	Basic region/leucine zipper
C2HDZ	Class II homeodomain-leucine zipper
ACN	Acetonitrile
CCaMK -IPD3	Ca ²⁺ /calmodulin-dependent protein kinase-interacting protein of DMI3
CDC25	Cell division cycle 25
CDS	Coding sequence
chl	Chlorophyll
cip-1	Cyclopropylsterol isomerase 1
CKX1	Cytokinin oxidase 1
CL	Continuous light
CLSY	Classy
CMV	Cucumber mosaic virus
COI1	Corinatine insensitive 1
CRISPR/Cas9	Clustered regularly interspaced short palindromic repeats/CRISPR-associated protein 9
CRM1	Chromosomal maintenance 1
CRY1b	Cryptochrome 1b
CTR1	Constitutive triple response 1
Cu/ZnSOD	Cu/Zinc superoxide dismutase
CYCA	Cyclin A
D	Complete darkness
DAB	3,3-Diaminobenzidine
DAD	Diode array detector
DAG	Days after gemmae germination
DAMP	Damage-associated molecular pattern
DCL	Dicer-like
DE	Differentially expressed
DEG	Differentially expressed genes
DEP	Differentially expressed protein groups
DGDG	Digalactosyldiglyceride
DHNB	Dehydrin B
DIN1	Dark inducible 1
DIR	Dirigent
DND1_DSRM	Dead end protein 1 homologous to double-strand RNA binding
dnOPDA	Dinor-cis-OPDA
DOF	DNA binding with one finger
DRB4	Double-stranded RNA binding factor 4

DRM	Detergent-resistant membrane fractions
ds	Double-stranded
dsRBD	Double-stranded RNA binding
EF1 α	Elongation factor 1 α
EIN3	Ethylene insensitive 3
ER	Erlins
ERF	Ethylene-responsive transcription factor
ESI	Electrospray ionization
EXPA9	Expansin A9
FA	Fatty acid
FC	Fold change
FDR	False discovery rate
FGMYB	Female gametophyte-specific MYB
flg22	Flagellin 22
FLOT	Flotillin
FLU	Fluorescent in blue light
GA	Gibberellin
GARP2	Glutamic acid-rich-protein 2
GH3B	Gretchen hagen 3B
GLK2	Golden 2-like protein 2
GluTR	Glutamyl-tRNA-reductase
GO	Gene ontology
gRNA	Guide RNA
hc-RNAs	Heterochromatic small interfering RNAs
HEN1	Hua enhancer 1 methylase
HIR	Hypersensitive-induced reaction proteins
HPT	Histidine phosphotransfer proteins
HSP70-1	Heat shock cognate protein 70-1
HYL1	Hyponastic leaves 1
IAA	Indole-3-acetic acid
IAMT1	IAA carboxylmethyltransferase 1
JA	Jasmonate
JA-Ile	Jasmonoyl-isoleucine
JAZ	Jasmonate-ZIM domain
kb	Kilo base pairs
LC-MS	Liquid chromatography-tandem mass spectrometry
LD 16:8	Long-day 16 h light/8 h dark
LEA	Late embryogenesis abundant
LFQ	Label-free quantification
LHCA	Light-harvesting complex A
LHCB	Light-harvesting complex B
lncRNA	Long non-coding RNAs
LOB	Lateral organ bound
LOX	Lipoxygenase
LRR	Leucine-rich repeat
MADS	Mini chromosome maintenance1/Agamous/Deficiency/Serum response factor
MAMP	Microbe -associated molecular pattern
MAPK	Mitogen-activated protein kinase
MEE51	Maternal effect embryo arrest 51
MGDG	Monogalactosyldiacylglycerol
miRNA	MicroRNA
MYB	V-MYB Myeloblastosis viral oncogene homolog
MYC	Myelocytomatosis oncogene
m β CD	Methyl- β -cyclodextrin
NAA	Naphthaleneacetic acid
NAC	No apical meristem /Arabidopsis thaliana activation factor /Cup-shaped cotyledon
nat-siRNAs	Natural antisense transcript-derived small interfering RNAs
NCED	9'-cis epoxycarotenoid dioxygenase

N-CoR	Nuclear receptor corepressor
NDUFA2/B8	NADH-ubiquinone oxidoreductase B8 subunit
NDUFS8	NADH dehydrogenase ubiquinone iron-sulfur protein 8
NINJA	Novel interactor of JAZ
NOS_T	Nopaline synthase terminator
NPR	Nonexpressor of pathogenesis-related
npII	Neomycin phosphotransferase II
nt	Nucleotides
OPDA	12-oxo-phytodienoic acid
P5CDH	Δ^1 -pyroline-5-carboxylate dehydrogenase
PAGE	Polyacrylamide gel electrophoresis
PAM	Pulse-Amplitude-Modulation
PAMP	Pathogen-associated molecular pattern
PAR	Photosynthetically active radiation
PAZ	Piwi/Argonaute/Zwille
PC	Glycerophosphocholines
PCY	Plastocyanin
PE	Phosphatidylethanolamine
PFK	ATP-dependent phosphofructokinase
PFP	Pyrophosphate-fructose-6-phosphotransferase
PG	Glycerophosphoglycerol
phasiRNAs	Phased small interfering RNAs
PHB	Prohibitins
PIN	PIN-formed transporters
PME53	Pectin methylesterase 53
POD	Peroxygenase
PP2C	Type 2C protein phosphatase
PPO	Polyphenol oxidases
PR-1	Pathogenesis-related protein 1
pre-miRNA	Precursor miRNA
pri-miRNA	Primary miRNA
PRRs	Pattern recognition receptors
PsaD1	PSI subunit D1
PSI	Photosystem I
PSII	Photosystem II
PTGS	Posttranscriptional gene silencing
PYL	Pyrabactin resistance-like
PYR	Pyrabactin resistance
qRT-PCR	Quantitative real-time polymerase chain reaction
ra-siRNAs	Repeat-associated small interfering RNAs
Rboh	Respiratory burst oxidase homolog
RCAR	Regulatory component of abscisic acid receptor
RdDM	RNA-directed DNA methylation
RDR6	RNA-dependent RNA polymerase 6
RGF	Root meristem growth factors
RGI-like	RGF insensitive-like
RGI-SERK	RGF insensitive-somatic embryogenesis receptor-like kinase
RISC	RNA-induced silencing complex
RITS	RNA-induced transcriptional silencing
RLK/Pelle	Receptor-Like-Kinase/Pelle
RNase III	Ribonuclease 3
ROS	Reactive oxygen species
RRB	Type-B response regulators
SA	Salicylic acid
SANT	SWI3/ADA2/N-CoR/TF
SAR	Systemic acquired resistance
SAUR8	Small auxin upregulated 8
SCF	Skp1/Cul1/F-box complex
SEM	Standard error of means
SEN1	Senescence 1
SER1	Serrate 1
SGS3	Suppressor of gene silencing 3
SHH1	Sawadee homeodomain homolog 1

SHI	Short internodes
siRNA	Small interfering RNA
SKP2A	S-Phase kinase-associated <i>protein</i> 2A
SL	Strigolacton
SnRK2	Subclass III sucrose nonfermenting 1 – related protein kinase 2
SPFH	Stomatin/Prohibitin/Flotillin/HflK/C
SQDG	Sulfoquinosyl-diacylglycerol
sRNA	Small non-coding RNAs
ss	Single-stranded
STOM	Stomatins
SWI3	Switch_defective protein 2
TAA	Tryptophan aminotransferase
ta-siRNA	Trans-acting small interfering RNA
TBP	TATA-binding protein
TEM	Transmission electron microscopy
TF	Transcription factor III B
TGS	Transcriptional gene silencing
TIR	Transport inhibitor response 1
TP	Time point
TPL	Topless
TRS	Tröndle Restlichtverstärkersysteme
TRX-Y2	Thioredoxin Y2
TSPO1	Translocator protein 1
Tukey's HSD	Tukey's honesty significant difference
UFA	Unsaturated FA
UV	Ultraviolet
WGGC	West German Genome Center
WT	Wild type
YUC	YUCCA flavin monooxygenase

Appendix

1. Supplementary Figures

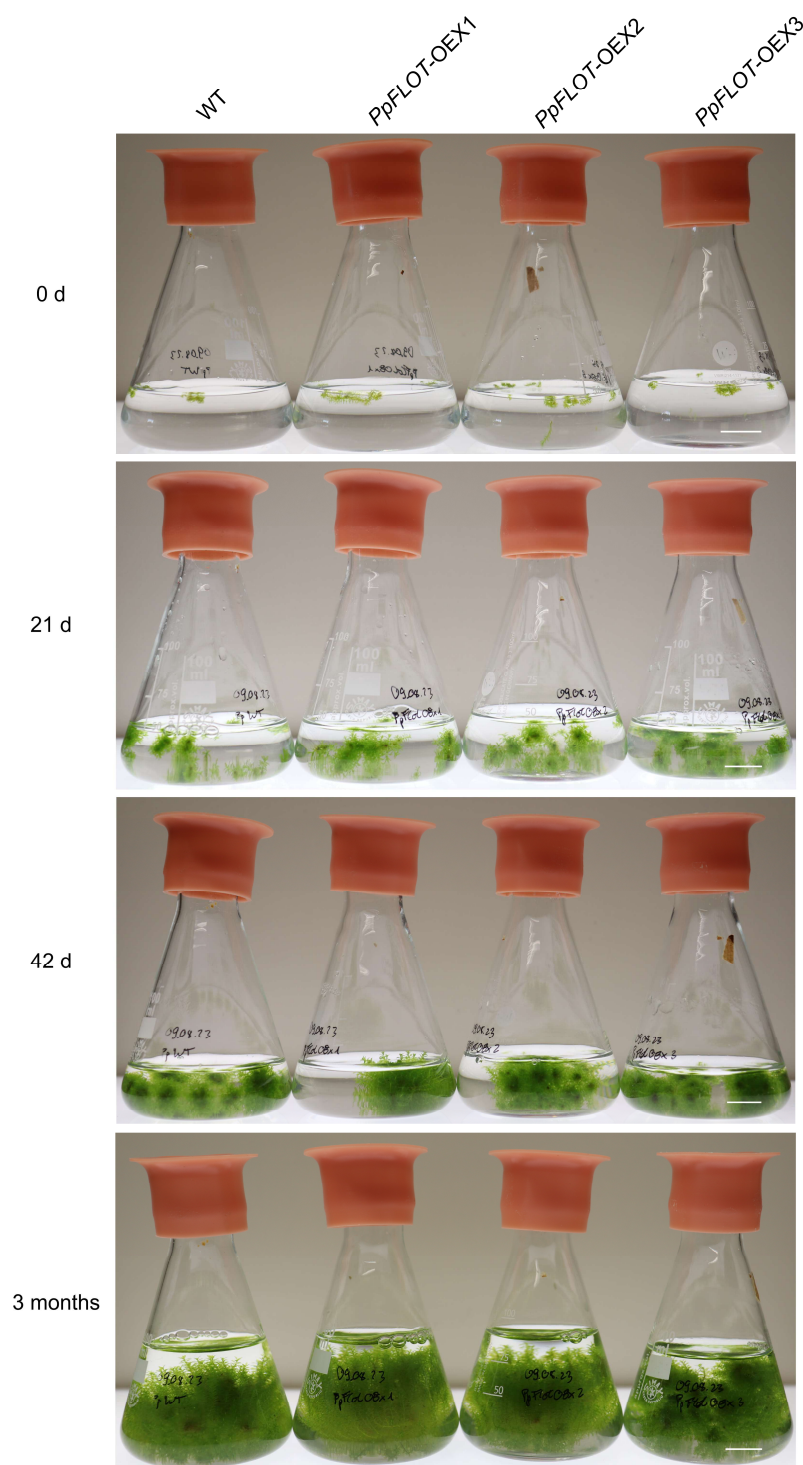
Question 1 - How does the loss of DCL genes influence the phytohormone response, salt tolerance, gene expression and the sRNA profile of *M. polymorpha*? Does the function of MpDCLs differ from those in *P. patens*?



Supplementary Figure 1: Overview of all generated *Mpdcl1a*^{ge} mutant lines

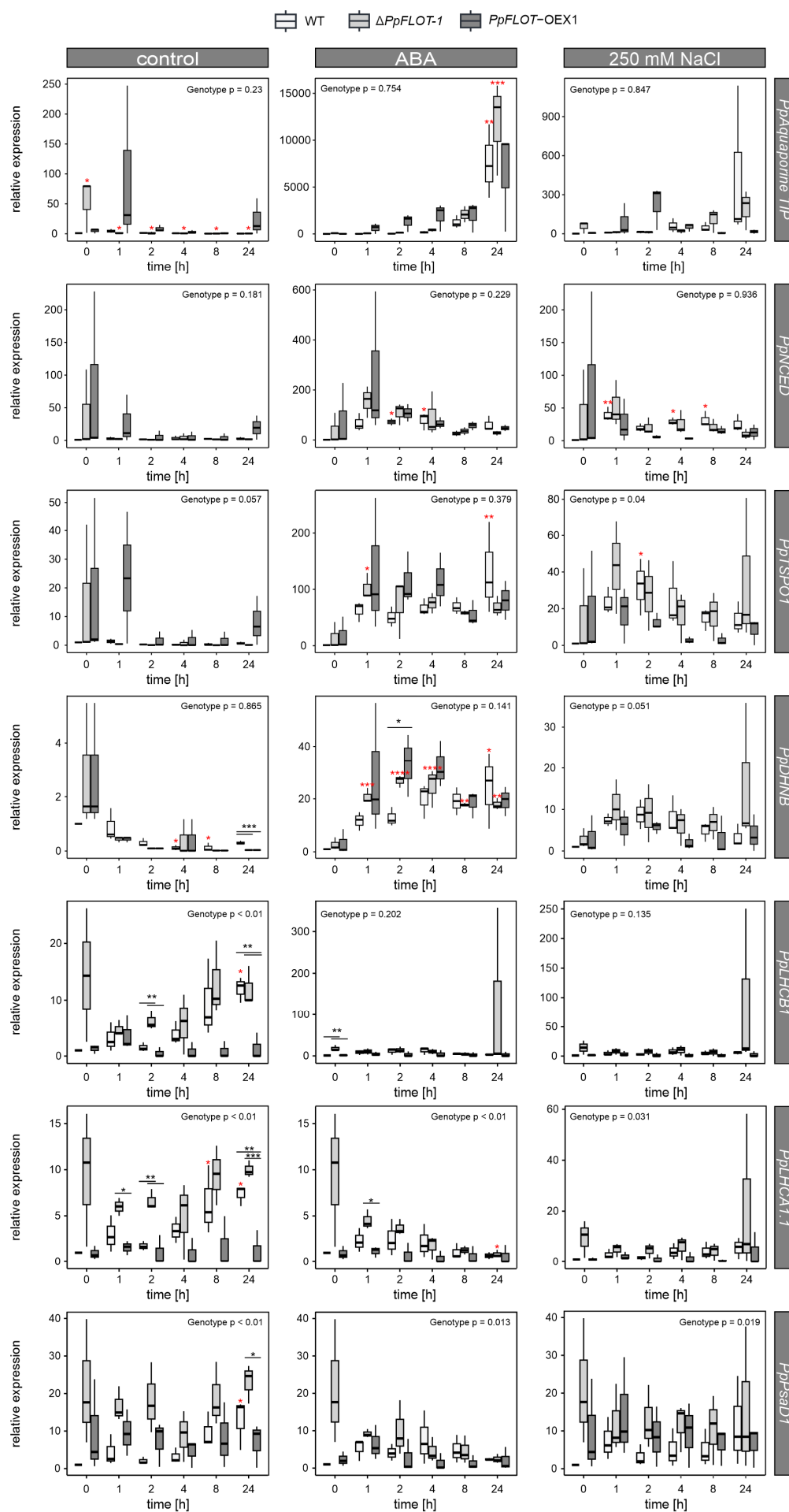
(A) All generated *Mpdcl1a*^{ge} lines grown for 4 weeks on standard medium under control conditions. Scale bar: 0.5 cm. **(B)** Alignment of WT MpDCL coding sequences and mutated coding sequences of all generated ♀ and ♂ *Mpdcl1a*^{ge} mutant lines. Only mutated regions are shown, with mutations highlighted in red. Deletions are indicated by dashes and on the protein level, these deletions are highlighted in lilac in the WT amino acid (AA) sequence. The WT AA sequence is positioned above, and the mutated AA sequence is positioned below the alignment.

Question 2 - Does the Band-7 protein FLOT modulate stress tolerance in *P. patens*? How is the expression of *PpFLOT* regulated? Are there differences in the function of bryophyte and seed plant FLOT?



Supplementary Figure 2: Growth of gametophores from *PpFLOT*-OEX lines submerged in liquid medium

P. patens WT and all three generated *PpFLOT*-OEX lines previously grown on solid medium were transferred to 50 ml liquid medium and observed for three months. Cultures were grown with continuous shaking at long-day conditions (Long-day: 16 h light/8 h dark; LD 16:8). Liquid media levels were maintained as needed to keep growing gametophore colonies submerged in the media. Images were captured at 0 d, 21 d, 42 d and three months after transfer. Scale bar represents 1 cm.



Supplementary Figure 3: Relative gene expression analyses of salt-induced genes and genes encoding components of photosystem I and II under control conditions and after ABA and salt treatment.

qRT-PCR results are shown as box blots illustrating the relative gene expression of *PpAquaporine TIP* (*Pp1s44_31*), *PpNCED* (*Pp1s412_7*), *PpTSPO1* (*Pp3c2_17540*), *PpDHNB* (*Pp3c5_11880*), *PpLHCB1* (*Pp3c2_35930*), *PpLHCA1.1* (*Pp3c13_14980*) and *PpPsaD1* (*Pp3c16_23780*) compared to WT expression at 0 h and normalized against *PpEF1α* as described by Schmittgen and Livak (2008). Measurements were conducted over 24 h under control conditions (left), treated with ABA (middle) and 250 mM NaCl treatment (right). The relative gene expression of the respective genes was measured for $\Delta PpFLOT-1$, WT and *PpFLOT-OEX1* protonema under control conditions in biological triplicates. Statistically significant changes in expression between the three genotypes were determined by ANOVA, with p-values provided in the respective graphs. Significant differential gene expression at a specific time point is indicated by black asterisks. Results of the Tukey's HSD of the time-dependent expression within the same genotype are marked by red asterisks when significant compared to 0 h of treatment. * $p < 0.05$, ** $p < 0.01$, *** $p < 0.001$, **** $p < 0.0001$.

2. Supplementary Tables

All supplementary Tables referred to in this study are deposited on an external data storage medium included in the printed version of this work. To give an overview of these tables in the electronic version, excerpts of Supplementary Tables 1, 2, 3, 9, 12, 13, 14, 15, 16, 19 and 20 are presented in this section and are referred to in the text as Tables. The raw mRNA and sRNA sequencing data files discussed in Question 1 are deposited on the NCBI SRA database under the BioProject ID PRJNA1073513 and will be public upon peer-reviewed publishing of the discussed data and of the manuscript connected to this dissertation.

2.1 List of Supplementary Tables on external data storage medium

Question 1 - How does the loss of DCL genes influence the phytohormone response, salt tolerance, gene expression and the sRNA profile of *M. polymorpha*? Does the function of MpDCLs differ from those in *P. patens*?

Supplementary Table 1. Sources of all protein sequences used to construct the phylogenetic tree in Figure 6 by neighbor joining and their annotated functional domains.

Supplementary Table 2. Guide RNAs used in CRISPR-Cas9 to mutate MpDCLs and confirmed mutations via Sanger sequencing in the respective mutant lines.

Supplementary Table 3. Oligonucleotides used for Question 1 in this study.

Supplementary Table 4. Lists of all significant differentially expressed sRNA classes.

Supplementary Table 5. Lists of all significant differentially expressed sRNA classes used in UpSet plot.

Supplementary Table 6. Lists of all significant differentially expressed mature miRNAs including TAS3.

Supplementary Table 7. Lists of all significant differentially expressed mature miRNAs used in UpSet plot.

Supplementary Table 8. Classes of all differentially expressed sRNAs: both summaries as well as distribution of differentially expressed sRNAs based on their size.

Supplementary Table 9. Overview of all significant differentially expressed mRNAs. DE mRNAs used in UpSet plots, venny analysis as well as heatmaps were also included.

Supplementary Table 10. Significant enriched GO terms for mRNA sequencing. Graphical results for respective categories obtained from AgriGO were also shown.

Supplementary Table 11. Validation of transcript levels by qRT-PCR. Fold changes and p-values from mRNA sequencing, and additional information about selected genes with their references were included.

Supplementary Table 12. Lists of miRNA target prediction of significant differentially expressed miRNAs and mRNA targets.

Supplementary Table 13. Lists of miRNA target prediction of anticorrelating miRNA:mRNA modules.

Supplementary Table 14. Lists of sRNA target prediction of significant differentially expressed sRNAs and mRNA targets.

Question 2 - Does the Band-7 protein FLOT modulate stress tolerance in *P. patens*? How is the expression of *PpFLOT* regulated? Are there differences in the function of bryophyte and seed plant FLOT?

Supplementary Table 15. Oligonucleotides used for Question 2 in this study.

Supplementary Table 16. Significantly differentially accumulated pigments in all *PpFLOT* mutant lines compared to the WT.

Supplementary Table 17. Results of ANOVA analysis comparing z-scores between WT and all *PpFLOT*-OEX lines.

Supplementary Table 18. Results of the GO term analysis of all differentially expressed protein groups between at least two tested genotypes.

Supplementary Table 19. Results of Student's *t*-test comparing protein expression of all *PpFLOT*-OEX lines with the WT.

Supplementary Table 20. Significant differentially accumulated lipids in all *PpFLOT* mutant lines compared to the WT.

2.2 Tables depicting excerpts out of the Supplementary Tables

Question 1 - How does the loss of DCL genes influence the phytohormone response, salt tolerance, gene expression and the sRNA profile of *M. polymorpha*? Does the function of MpDCLs differ from those in *P. patens*?

Table 1: Protein sequence IDs and sources used to construct DCL phylogenetic tree.

Excerpt out of Supplementary Table 1 listing Gene/Protein IDs of the DCL sequences used to generate the DCL phylogenetic tree. Information on the DCL domain structure can be found in Supplementary Table 1 on an external data storage medium.

Species	Gene/Protein ID	Gene/Protein name	Annotation source
<i>Marchantia polymorpha</i>	Mp7g12090	MpDCL1a	MarpolBase
	Mp6g09830	MpDCL1b	MarpolBase
	Mp1g02840	MpDCL3	MarpolBase
	Mp7g11720	MpDCL4	MarpolBase
	Mp7g16380	MpDCL-like	MarpolBase
<i>Physcomitrium patens</i>	Pp3c24_9630V3	PpDCL-like	Phytozome v13
	Pp3c1_24960V3	PpDCL-like	Phytozome v13
	Pp3c2_15900V3	PpDCL1a	Phytozome v13
	Pp3c1_24960V3	PpDCL1b	Phytozome v13
	Pp3c23_3450V3	PpDCL3	Phytozome v13
	Pp3c26_370V3	PpDCL4	Phytozome v13
<i>Arabidopsis thaliana</i>	AT1G01040	AtDCL1	Phytozome v13
	AT3G03300	AtDCL2	Phytozome v13
	AT3G43920	AtDCL3	Phytozome v13
	AT5G20320	AtDCL4	Phytozome v13
<i>Chara braunii</i>	G24199	-	MarpolBase
	G34091	-	MarpolBase
	G34093	-	MarpolBase
<i>Chlamydomonas reinhardtii</i>	Cre02.g141000.t1	CrDCL1	MarpolBase
	Cre16.g684715.t1	CrDCL2	MarpolBase
	Cre07.g345900.t1	CrDCL3	MarpolBase
<i>Azolla filiculoides</i>	Azfi_s0335.g065527	AzDCL-like	MarpolBase
	Azfi_s0154.g053526	AzDCL1	MarpolBase
	Azfi_s0014.g013625	AzDCL4	MarpolBase
	Azfi_s0002.g001222	AzDCL3	MarpolBase
<i>Anthoceros agrestis</i>	AagrOXF_evm.model.utg000041l.136	AgDCL3	MarpolBase
	AagrOXF_evm.model.utg000012l.16	AgDCL1	MarpolBase
	AagrOXF_evm.model.utg000049l.134	AgDCL-like	MarpolBase
	AagrOXF_evm.model.utg000035l.170	AgDCL4	MarpolBase
<i>Mesotaenium endlicherianum</i>	ME000009S10474	MeDCL1	MarpolBase
<i>Klebsormidium nitens</i>	kfl00384_0060	KnDCL1b	MarpolBase
	kfl00265_0060	KnDCL1a	MarpolBase

Species	Gene/Protein ID	Gene/Protein name	Annotation source
<i>Salvinia cucullata</i>	Sacu_v1.1_s0002.g000998	ScDCL1	MarpolBase
	Sacu_v1.1_s0139.g022615	ScDCL3b	MarpolBase
	Sacu_v1.1_s0089.g018689	ScDCL-like	MarpolBase
<i>Selaginella moellendorffii</i>	SmoeALL_86110	SmDCL1	MarpolBase
	SmoeALL_74321	SmDCL3c	MarpolBase
	SmoeALL_448444	SmDCL3a	MarpolBase
	SmoeALL_444049	SmDCL3b	MarpolBase
<i>Spirogloea muscicola</i>	SM000009S23464	-	MarpolBase
	SM000067S20362	-	MarpolBase
	SM000277S10343	-	MarpolBase
<i>Oryza sativa japonica</i>	Os09g0315100	OSDCL2b	UniProt
	Os03g0121800	OsDCL1	UniProt
	Os03t0583900	OsDCL2a	UniProt
	Os01t0909200	OsDCL3a	UniProt
	Os10g0485600	OsDCL3b	UniProt
	Os04g0509300	OsDCL4	UniProt
<i>Zea mays</i>	A0A0K1H3C4	ZmDCL1	UniProt
	A0A0K1H3E7	ZmDCL4	UniProt
	A0A1D6GM48	ZmDCL2	UniProt
	A0A1D6KSJ7	ZmDCL3b	UniProt
	A0A1B0NCT2	ZmDCL3a	UniProt
<i>Medicago truncatula</i>	Medtr7g118350	MtDCL1	Phytozome v13
	Medtr2g030490	MtDCL2a	Phytozome v13
	Medtr1g060740	MtDCL2b	Phytozome v13
	Medtr8g069975	MtDCL2c	Phytozome v13
	Medtr3g105390	MtDCL3	Phytozome v13
	Medtr4g116860	MtDCL4	Phytozome v13
<i>Anthoceros angustus</i>	AANG011249	AaDCL1	MarpolBase
	AANG006094	AaDCL4	MarpolBase
	AANG012083	AaDCL3	MarpolBase
	AANG009281	AaDCL-like	MarpolBase
<i>Anthoceros punctatus</i>	Apun_evm.model.utg000115l.177	AaDCL4	MarpolBase
	Apun_evm.model.utg000158l.40	AaDCL3	MarpolBase
	Apun_evm.model.utg000162l.37	AaDCL-like	MarpolBase
	Apun_evm.model.utg000340l.19	AaDCL1	MarpolBase
<i>Ceratodon purpureus</i>	CepurR40.2G076100	CpDCL1	Phytozome v13
	CepurR40.12G024900	CpDCL3	Phytozome v13
	CepurR40.7G000600	CpDCL4	Phytozome v13
	CepurR40.3G117100	CpDCL-like	Phytozome v13

Species	Gene/Protein ID	Gene/Protein name	Annotation source
<i>Sphagnum fallax</i>	Sphfalx06G063300	SpDCL3	Phytozome v13
	Sphfalx02G093400	SpDCL1	Phytozome v13
	Sphfalx14G057500	SpDCL-like	Phytozome v13
	Sphfalx17G041800	SpDCL-like	Phytozome v13
	Sphfalx19G085500	SpDCL4	Phytozome v13
<i>Diphasiastrum complanatum</i>	Dicom.18G083200	DcDCL1a	Phytozome v13
	Dicom.Y095700	DcDCL1b	Phytozome v13
	Dicom.06G085000	DcDCL-like	Phytozome v13
	Dicom.12G058600	DcDCL3	Phytozome v13
	Dicom.01G033700	Dc DCL4	Phytozome v13
<i>Ceratopteris richardii</i>	Ceric.22G041000	CrDCL1	Phytozome v13
	Ceric.14G005300	CrDCL3b	Phytozome v13
	Ceric.01G108700	CrDCL4	Phytozome v13
	Ceric.13G041700	CrDCL-like	Phytozome v13
	Ceric.22G046500	CrDCL3a	Phytozome v13
<i>Sphagnum magellanicum</i>	Sphmag17G038700	SmDCL-like	Phytozome v13
	Sphmag14G056800	SmDCL-like	Phytozome v13
	Sphmag02G101200	SmDCL1	Phytozome v13
	Sphmag06G064500	SmDCL3	Phytozome v13
	Sphmag19G088800	SmDCL4	Phytozome v13

Table 2: Description of the generated *Mpdcl^{ge}* lines used in this study.

Excerpt of Supplementary Table 2 listing generated *Mpdcl^{ge}* lines used in this study with a description of their respective mutation. Complete sequences can be found in Supplementary Table 2 on an external storage medium.

Gene	MarpolBase Tak v6.1	Transgenic lines	Sex	Mutation type in cDNA	Mutation type in amino acid sequence
<i>DCL1a</i>	Mp7g12090	<i>Mpdcl1a-6^{ge}</i>	♀	c.1012_1016del;1012_1016insA TTGT	p.G339del;D338E;E338_G340insLC
<i>DCL1b</i>	Mp6g09830	<i>Mpdcl1b-6^{ge}</i>	♀	c.600_876del	p.V200EfsX5
		<i>Mpdcl1b-7^{ge}</i>	♂	c.600_877del;600_877insCTTC TACTATGAAG	p.V200AfsX7
<i>DCL3</i>	Mp1g02840	<i>Mpdcl3-3^{ge}</i>	♂	c.425_542del	p.L142HfsX7
		<i>Mpdcl3-6^{ge}</i>	♀	c.426_541del;426_541insCTAT	p.E143LfsX1
<i>DCL4</i>	Mp7g11720	<i>Mpdcl4-1^{ge}</i>	♀	c.698_701del;698_706insTTAT TATCT	p.S233FfsX8
		<i>Mpdcl4-4^{ge}</i>	♂	c.690_711del	p.M230IfsX8

Table 3: Oligonucleotides used in Question 1 (Supplementary Table 3)

Name	Sequence (5' to 3')	Purpose
gRNA2.1	CTCGGTCCCATACGAAAGAGATGG	cloning into entry vector
gRNA2.2	AAACCCATCTCTTTCTGTATGGGAC	cloning into entry vector
gRNA12.1	CTCGGAAATCCTCGACTGTACTGG	cloning into entry vector
gRNA12.2	AAACCCAGTACAGTCGAGGATTTC	cloning into entry vector
gRNA13.1	CTCGGTTTACTTGGAAACTGGATG	cloning into entry vector
gRNA13.3	AAACCATCCAGTTTCCAAGTAAAC	cloning into entry vector
gRNA19.1	CTCGGGAAGTATGCTGGACTCTA	cloning into entry vector
gRNA19.2	AAACTAGAGTCCAGCATACTTTCC	cloning into entry vector
gRNA35.1	CTCGGATCAGGGCAGATTCTACAA	cloning into entry vector
gRNA35.2	AAACTTGTAAGTCTGCCCTGATC	cloning into entry vector
gRNA36.1	CTCGCGAAGCATAGTAGTCTGCAT	cloning into entry vector
gRNA36.2	AAACATGCAGACTACTATGCTTCG	cloning into entry vector
MpEF1a_fwd	CTGATTGCGCCGTTCTCATC	PCR
MpEF1a_rev	CGGAAGGCCTCTTAGGCTCA	PCR
RT-MpEF1a_fwd	TGAGCCTAAGAGGCCTTCCG	qRT-PCR
RT-MpEF1a_rev	CCAGTCTCCACTCGTCCCAC	qRT-PCR
MPDCL1a_Exon1-4_fwd_2	ACGATCGTGGCAGAGTTGAG	PCR/Sequencing
MPDCL1a_Exon1-4_rev_2	TGGGCACCTGACTCTTCAGT	PCR/Sequencing
MPDCL1a_Exon14-16_fwd	ACTTCTGGCCGATGAGGAAT	PCR/Sequencing
MPDCL1a_Exon14-16_rev	GGAAGCCTCTGAGCACCTCT	PCR/Sequencing
MPDCL1b_Exon1_fwd	CCGTCTGCTTCTTTGTTGCC	PCR/Sequencing
MPDCL1b_Exon1_rev	ATGATACCCGCACACGAAAG	PCR/Sequencing
MPDCL1b_Exon2_fwd	CGCTTCAATGCTTGGCTGTT	PCR/Sequencing
MPDCL1b_Exon2_rev	AAGGGGTAGCCGTCGATTTG	PCR/Sequencing
MPDCL3_Exon1-2_fwd	ACGACTGCAACATGGAGGAG	PCR/Sequencing
MPDCL3_Exon1-2_rev	GGCCCGGTCTCTAAACAAAGA	PCR
MPDCL4_Exon6-7_fwd	GACAGGCGGGTAGAATCACC	PCR/Sequencing
MPDCL4_Exon6-7_rev	GCTACCATGCAACGCAACTC	PCR/Sequencing
MPDCL1a_Ex1 2kb_fwd4	CCTGCCGAAGCATTGAGAGA	PCR/Sequencing
MPDCL1a_Ex1 2kb_rev4	ATGCTTGCCCCTGACACCTT	PCR/Sequencing
RT-DCL4(19+23)_compl fwd	AGAGCACATCGGCCCAAAT	PCR/Sequencing
RT-DCL4 19 fwd	CGATCGGCCTTCAAATGAACA	PCR/Sequencing
RT-DCL4 19 rev	TCGGGTTGACCCGTTTTTCT	PCR/Sequencing
Mapoly0100s0057_fwd	GCAAGGTATGCAGGTCGAGGT	qRT-PCR
Mapoly0100s0057_rev	GTTGGGAGCGATCTTTGAAGC	qRT-PCR
Mapoly0127s0054_fwd	AAGCAGCCAGGCGTGTGTA	qRT-PCR
Mapoly0127s0054_rev	CGCTTGATGAATCGCTCCTG	qRT-PCR
Mapoly0035s0054_fwd	GCTGTCCAATGGCGAAAATG	qRT-PCR
Mapoly0157s0009_fwd	CGTCATCGAGCGGAGACACT	qRT-PCR

Name	Sequence (5' to 3')	Purpose
Mapoly0157s0009_rev	GCCTGCCGATATTGTGCGTA	qRT-PCR
Mapoly0034s0029_fwd	ACAGCGAGCATAAGCGAGGA	qRT-PCR
Mapoly0034s0029_rev	TCTTCCCGGACTCTGGTGTG	qRT-PCR

Table 4: Overview of significant DE genes and their putative regulating DE miRNA and sRNA in *Mpdc1a-6^{9e}* and WT treated with 100 mM NaCl.

Excerpt of Supplementary Tables 9, 12, 13, 14 combining differentially expressed (DE) mRNAs from sequenced *Mpdc1a-6^{9e}* mutant and salt-treated WT that are discussed in the main text with their putative regulating miRNAs and sRNAs. Complete Supplementary Tables 9, 12, 13 and 14 are stored on an external data storage medium.

Gene name	Gene ID	mRNA			miRNA				sRNA					
		Mpdc1a ^{9e}	log ₂ (FC)	WT salt log ₂ (FC)	DE miRNA Mpdc1a ^{9e}	Mpdc1a ^{9e}	log ₂ (FC)	DE miRNA WT salt	WT salt log ₂ (FC)	DE sRNA Mpdc1a ^{9e}	Mpdc1a ^{9e}	log ₂ (FC)	DE sRNA WT salt	WT salt log ₂ (FC)
Mp1R-MYB17	Mp4g21300	-2.20	-	-	-	-	-	-	-	mpo-b3.0r1-12492	1.55	-	-	-
MpABC81	Mp2g02920	-1.39	-	-	-	-	-	-	-	mpo-b3.0r1-6036	-1.63	-	-	-
MpABC07	Mp4g15590	-1.04	-	-	mpo-b3.0r1-1971	-1.07	-	-	-	mpo-b3.0r1-2728	1.43	-	-	-
MpABCC9	Mp5g03360	1.00	-	-	-	-	-	-	-	mpo-b3.0r1-7304	-1.65	-	-	-
MpABCG13	Mp7g03860	-1.03	-	-	-	-	-	-	-	mpo-b3.0r1-11672	-6.98	-	-	-
MpABCG14	Mp2g17910	-2.39	-	-	-	-	-	-	-	mpo-b3.0r1-16280	-1.89	-	-	-
MpABCG2	Mp2g16700	-1.76	-	-	mpo-b3.0r1-2331	3.23	-	-	-	mpo-b3.0r1-19177	1.98	-	-	-
MpABCG20	Mp5g04860	1.87	-	-	mpo-b3.0r1-2510	-1.43	-	-	-	mpo-b3.0r1-21468	-6.18	-	-	-
MpABCG3	Mp2g14870	-1.39	-	-	-	-	-	-	-	mpo-b3.0r1-3015	-2.12	-	-	-
MpABCG30	Mp2g21800	1.04	1.58	-	mpo-b3.0r1-8349	-1.30	-	-	-	mpo-b3.0r1-5014	1.83	mpo-b3.0r1-10622	-1.56	-
MpABCG4	Mp8g12130	-1.56	-	-	-	-	-	-	-	mpo-b3.0r1-12896	-2.87	-	-	-
MpABCG5	Mp4g11430	1.29	-	-	mpo-b3.0r1-10192	3.11	-	-	-	mpo-b3.0r1-21213	-4.10	-	-	-
MpABCG7	Mp2g16720	-1.58	-	-	-	-	-	-	-	mpo-b3.0r1-14873	-2.16	-	-	-
MpABCG8	Mp4g22510	-2.09	-	-	-	-	-	-	-	mpo-b3.0r1-102	-2.12	-	-	-
MpASLBD11	Mp5g10960	-1.19	-	-	mpo-b3.0r1-14313	-2.28	-	-	-	mpo-b3.0r1-12492	1.55	-	-	-
MpASLBD12	Mp5g11460	-1.16	-	-	-	-	-	-	-	-	-	-	-	-
MpASLBD2	Mp8g11560	-1.10	-	-	-	-	-	-	-	mpo-b3.0r1-8596	-2.38	-	-	-
MpASLBD8	Mp6g08290	-	-1.27	-	-	-	-	-	-	-	-	-	-	-
MpBHLH30	Mp2g07130	-1.17	-	-	mpo-b3.0r1-16933	1.08	-	-	-	mpo-b3.0r1-19060	8.38	-	-	-
MpBHLH35	Mp2g04160	1.06	-	-	mpo-b3.0r1-16648	1.31	-	-	-	mpo-b3.0r1-14135	1.85	-	-	-
MpBHLH37	Mp2g04200	3.86	-	-	mpo-b3.0r1-3564	-1.55	-	-	-	mpo-b3.0r1-20893	-1.08	-	-	-
MpC2HDZ	Mp2g24200	-1.48	-	-	mpo-b3.0r1-4187	-2.31	-	-	-	mpo-b3.0r1-16084	-3.00	-	-	-
MpCAT4	Mp5g07320	-2.57	1.34	-	-	-	-	-	-	mpo-b3.0r1-656	-3.17	mpo-b3.0r1-7974	-2.05	-
MpCKX1	Mp5g03090	-1.18	-	-	-	-	-	-	-	mpo-b3.0r1-4620	-3.40	-	-	-
MpCTR1	Mp8g15840	-1.21	-	-	mpo-b3.0r1-1971	-1.07	-	-	-	mpo-b3.0r1-21338	1.44	-	-	-
MpERF14	Mp4g00380	-	1.14	-	-	-	-	-	-	-	-	-	-	-
MpERF15	Mp7g09350	-1.31	-	-	mpo-b3.0r1-12658	8.00	-	-	-	mpo-b3.0r1-9643	5.04	-	-	-
MpERF21	Mp5g22160	-1.57	-	-	-	-	-	-	-	mpo-b3.0r1-13658	-1.25	-	-	-
MpERF7	Mp6g04880	-1.18	-	-	mpo-b3.0r1-14660	-5.19	-	-	-	mpo-b3.0r1-1988	-2.78	-	-	-
MpFGMYB/ MpR2R3-MYB1	Mp1g17210	1.67	-	-	mpo-b3.0r1-10692	2.95	-	-	-	mpo-b3.0r1-9257	2.33	-	-	-
MpGARF2	Mp4g08700	-1.35	-	-	mpo-b3.0r1-2331	3.23	-	-	-	mpo-b3.0r1-13582	-1.89	-	-	-
MpGH3B	Mp2g14010	1.38	1.09	-	-	-	-	-	-	-	-	-	-	-
MpIAMT1	Mp7g11980	1.32	-	-	-	-	-	-	-	mpo-b3.0r1-4654	-1.84	-	-	-
MpLEA-like12	Mp3g04820	1.32	2.89	-	-	-	-	-	-	-	-	-	-	-
MpLEA-like15	Mp3g18220	1.60	1.32	-	-	-	-	-	-	mpo-b3.0r1-16157	3.59	-	-	-
MpLEA-like18	Mp4g05730	1.22	1.65	-	mpo-b3.0r1-10150	-3.73	-	-	-	mpo-b3.0r1-1182	-6.06	-	-	-
MpLEA-like22	Mp4g14800	1.71	1.77	-	-	-	-	-	-	mpo-b3.0r1-5987	-1.80	-	-	-
MpLEA-like24	Mp4g14830	1.34	1.29	-	-	-	-	-	-	mpo-b3.0r1-20709	-2.81	mpo-b3.0r1-21370	-2.10	-
MpLEA-like26	Mp4g14870	1.32	2.01	-	-	-	-	-	-	-	-	-	-	-
MpLEA-like36	Mp6g02990	2.59	3.10	-	-	-	-	-	-	mpo-b3.0r1-20585	-1.24	-	-	-
MpLEA-like38	Mp6g03010	1.40	2.16	-	-	-	-	-	-	-	-	mpo-b3.0r1-15844	-1.27	-
MpLEA-like46	Mp6g03130	-1.95	-1.62	-	-	-	-	-	-	mpo-b3.0r1-13109	-2.77	-	-	-
MpLEA-like62	Mp8g15940	1.17	-	-	-	-	-	-	-	mpo-b3.0r1-17815	-3.39	-	-	-
MpMAFKKK10	Mp4g08320	-1.36	-	-	-	-	-	-	-	mpo-b3.0r1-16036	-1.33	-	-	-
MpMHK3	Mp2g05880	1.06	-	-	mpo-b3.0r1-2947	-1.20	-	-	-	mpo-b3.0r1-2950	-2.14	-	-	-
MpNAC8	Mp6g02670	2.44	1.04	-	-	-	-	-	-	mpo-b3.0r1-6224	-3.02	mpo-b3.0r1-12443	-2.22	-
MpR2R3-MYB15	Mp3g09350	-1.02	-1.11	-	-	-	-	-	-	mpo-b3.0r1-20484	-5.67	-	-	-
MpR2R3-MYB8	Mp3g23170	-1.47	-	-	mpo-b3.0r1-2331	3.23	-	-	-	mpo-b3.0r1-21298	4.13	-	-	-
MpRGH-like	Mp1g04830	-1.02	-	-	mpo-b3.0r1-12192	1.16	-	-	-	mpo-b3.0r1-319	1.26	-	-	-
MpRLK-Pelle_L-LEC16	Mp5g05630	1.37	-	-	-	-	-	-	-	mpo-b3.0r1-20995	7.10	-	-	-
MpRLK-Pelle_L-LEC24	Mp5g15160	-2.30	1.27	-	mpo-b3.0r1-10522	2.71	-	-	-	mpo-b3.0r1-7613	-1.31	mpo-b3.0r1-18533	-1.81	-
MpRLK-Pelle_L-LEC4	Mp2g14530	-1.12	-1.35	-	mpo-b3.0r1-14313	-2.28	mpo-b3.0r1-14313	-3.05	-	mpo-b3.0r1-1239	-4.05	mpo-b3.0r1-5842	-1.74	-
MpRLK-Pelle_LysM2	Mp4g22390	-	-1.04	-	mpo-b3.0r1-18568	-	mpo-b3.0r1-18568	1.15	-	-	-	-	-	-
MpRLK-Pelle_LysM8	Mp6g15550	1.48	2.07	-	-	-	-	-	-	mpo-b3.0r1-12703	-1.39	mpo-b3.0r1-18858	-1.33	-
MpRLK-Pelle_RLCK-XVI	Mp1g22840	-	1.21	-	-	-	-	-	-	-	-	mpo-b3.0r1-17882	-3.11	-
MpRLK-Pelle_SD-2b1	Mp1g25080	-1.33	-	-	mpo-b3.0r1-10150	-3.73	-	-	-	mpo-b3.0r1-15801	-2.40	-	-	-
MpRLK-Pelle_WAK_LRK10L-12	Mp6g18060	-1.16	-	-	mpo-b3.0r1-14313	-2.28	-	-	-	mpo-b3.0r1-1707	-1.65	-	-	-
MpRLK-Pelle_WAK_LRK10L-4	Mp2g00490	-	-1.05	-	-	-	-	-	-	-	-	-	-	-
MpRLK-Pelle_WAK2	Mp3g01940	3.01	1.34	-	-	-	-	-	-	-	-	mpo-b3.0r1-1805	-2.06	-
MpRLK-Pelle_WAK3	Mp6g18030	-1.59	-	-	-	-	-	-	-	mpo-b3.0r1-11491	-2.73	-	-	-
MpRLK-Pelle_WAK4	Mp6g18070	-3.62	-	-	-	-	-	-	-	mpo-b3.0r1-15662	-3.78	-	-	-
MpRR-MYB6	Mp2g09320	-1.04	-	-	-	-	-	-	-	mpo-b3.0r1-8825	-1.14	-	-	-
MpSAUR8	Mp1g27980	1.54	1.39	-	-	-	-	-	-	-	-	-	-	-
MpSBG9/MpR2R3-MYB17	Mp1g09420	-1.91	-	-	mpo-b3.0r1-1971	-1.07	-	-	-	mpo-b3.0r1-16151	5.51	-	-	-
MpSHI	Mp3g19510	-1.01	-	-	-	-	-	-	-	mpo-b3.0r1-8670	-1.88	-	-	-
MpSKP2A	Mp8g10660	1.01	-	-	-	-	-	-	-	mpo-b3.0r1-21451	-5.17	-	-	-
MpTAA	Mp5g14320	1.50	-	-	-	-	-	-	-	mpo-b3.0r1-17581	-1.79	-	-	-
MpWRKY14	Mp6g16800	-1.04	-	-	-	-	-	-	-	mpo-b3.0r1-6317	-1.37	-	-	-
MpWRKY3	Mp5g05560	-	2.99	-	-	-	-	-	-	-	-	-	-	-
MpWRKY6	Mp1g08960	-1.56	1.16	-	-	-	-	-	-	mpo-b3.0r1-6317	-1.37	mpo-b3.0r1-2008	-2.00	-
MpWRKY7	Mp3g17660	-	1.78	-	mpo-b3.0r1-4942	-	mpo-b3.0r1-4942	-2.20	-	-	-	mpo-b3.0r1-2860	-1.51	-
MpWRKY8	Mp2g20960	1.02	-	-	mpo-b3.0r1-18568	1.73	-	-	-	mpo-b3.0r1-10695	-2.05	-	-	-
unknown n	Mp3g25440	1.86	-1.34	-	-	-	-	-	-	mpo-b3.0r1-6484	-1.38	mpo-b3.0r1-17884	-1.39	-
unknown n	Mp3g16740	-1.20	-	-	mpo-b3.0r1-12192	1.16	-	-	-	mpo-b3.0r1-10867	-6.75	-	-	-
unknown n	Mp6g16160	2.39	-	-	mpo-b3.0r1-10150	-3.73	-	-	-	mpo-b3.0r1-17007	-3.44	-	-	-
unknown n	Mp1g06050	1.34	-	-	mpo-b3.0r1-10150	-3.73	-	-	-	mpo-b3.0r1-14873	-2.16	-	-	-
unknown n	Mp4g16040	1.75	-	-	mpo-b3.0r1-10150	-3.73	-	-	-	mpo-b3.0r1-18988	-1.64	-	-	-

Table 5: Overview of significant DE genes and their putative regulating DE miRNA and sRNA in *Mpdc11b-6^{oe}* and WT treated with 100 mM NaCl. Excerpt of Supplementary Table 9, 12, 13 and 14 combining differentially expressed (DE) mRNAs from sequenced *Mpdc11b-6^{oe}* mutant and salt treated WT that are discussed in the main text with their putative regulating miRNAs and sRNAs. Complete Supplementary Tables 9, 12, 13 and 14 are stored on an external data storage medium.

Gene name	Gene ID	mRNA				miRNA				sRNA					
		<i>Mpdc11b^{oe}</i> log ₂ (FC)	WT salt log ₂ (FC)	<i>Mpdc11b^{oe}</i> salt/ WT salt log ₂ (FC)	<i>Mpdc11b^{oe}</i> salt/ <i>Mpdc11b^{oe}</i> cont log ₂ (FC)	DE miRNA <i>Mpdc11b^{oe}</i>	<i>Mpdc11b^{oe}</i> log ₂ (FC)	DE miRNA WT salt	WT salt log ₂ (FC)	DE sRNA <i>Mpdc11b^{oe}</i>	<i>Mpdc11b^{oe}</i> log ₂ (FC)	DE sRNA WT salt	WT salt log ₂ (FC)	DE sRNA <i>Mpdc11b^{oe}</i> salt/ WT salt	<i>Mpdc11b^{oe}</i> salt/ WT salt log ₂ (FC)
MpCKX1	Mp5g03090	-	-	-	-1.02	-	-	-	-	-	-	-	-	-	-
MpCYCB_1	Mp5g10030	1.05	-	-	-1.08	-	-	-	-	-	-	-	-	-	-
MpCDC25_1	Mp4g01900	1.09	-	-	-	-	-	-	-	mpo-b3.0r1-16537	-1.74	-	-	-	-
unknown	Mp5g10190	1.09	1.39	-	-	mpo-b3.0r1-16782	-2.20	mpo-b3.0r1-16782	-3.60	mpo-b3.0r1-21113	2.03	mpo-b3.0r1-15175	-3.09	-	-
MpCYCA	Mp2g25500	1.12	-	-	-	-	-	-	-	-	-	-	-	-	-
MpRLK-Pelle_UF	Mp3g15740	-	-	-	-1.08	-	-	-	-	-	-	-	-	-	-
MpRLK-Pelle_R*	Mp3g10530	-	-	-1.33	-	-	-	-	-	-	-	-	-	mpo-b3.0r1-19558	1.68
MpRLK-Pelle_W,	Mp3g18080	-	-	1.01	-	-	-	-	-	-	-	-	-	-	-
MpRLK-Pelle_L-1	Mp5g15160	-	1.27	-	-	-	-	-	-	-	-	-	-	-	-
MpRLK-Pelle_L-1	Mp2g14530	-	-1.35	-	-	-	-	mpo-b3.0r1-14313	-3.05	-	-	mpo-b3.0r1-18533	-1.81	-	-
MpRLK-Pelle_Ly	Mp4g22390	-	-1.04	-	-	-	-	mpo-b3.0r1-18568	1.15	-	-	-	-	-	-
MpRLK-Pelle_Ly	Mp6g15550	1.53	2.07	-	-	-	-	-	-	mpo-b3.0r1-21087	-3.98	mpo-b3.0r1-18858	-1.33	-	-
MpRLK-Pelle_RL	Mp1g22840	-	1.21	-	-	-	-	-	-	-	-	mpo-b3.0r1-17882	-3.11	-	-
MpRLK-Pelle_W,	Mp2g00490	-	-1.05	-	-	-	-	-	-	-	-	-	-	-	-
MpRLK-Pelle_W,	Mp3g01940	-	1.34	-	-	-	-	-	-	-	-	mpo-b3.0r1-1805	-2.06	-	-

Table 6: Overview of significant DE genes and their putative regulating DE miRNA and sRNA in *Mpdc13-6^{ge}* and *Mpdc14-1^{ge}*.

Excerpt of Supplementary Table 9, 12, 13, 14 combining differentially expressed (DE) mRNAs from sequenced *Mpdc13-6ge* and *Mpdc14-1ge* that are discussed in the main text with their putative regulating miRNAs and sRNAs. Complete Supplementary Tables 9, 12, 13 and 14 are stored on an external data storage medium.

Gene name	Gene ID	mRNA		miRNA				sRNA			
		Mpdc13 ⁹⁰	Mpdc14 ⁹⁰	DE miRNA	Mpdc13 ⁹⁰	DE miRNA	Mpdc14 ⁹⁰	DE sRNA	Mpdc13 ⁹⁰	DE sRNA	Mpdc14 ⁹⁰
		log ₂ (FC)	log ₂ (FC)	Mpdc13 ⁹⁰	log ₂ (FC)	Mpdc14 ⁹⁰	log ₂ (FC)	Mpdc13 ⁹⁰	log ₂ (FC)	Mpdc14 ⁹⁰	log ₂ (FC)
MpTAA	Mp5g14320	1.05	-	-	-	-	-	-	-	-	-
MpR2R3-MYB5	Mp8g11870	-1.54	-1.59	-	-	mpo-b3.0r1-19901	-1.57	mpo-b3.0r1-16693	-2.09	mpo-b3.0r1-3051	-1.63
MpPR1aa	Mpzg00770	4.98	-	-	-	-	-	mpo-b3.0r1-20756	1.00	-	-
MpPR1e	Mp2g11950	1.60	-	-	-	-	-	mpo-b3.0r1-18517	-6.38	-	-
MpPR1f	Mp2g15970	7.97	-	-	-	-	-	-	-	-	-
MpPR1p	Mp6g06330	4.14	-	-	-	-	-	mpo-b3.0r1-8854	1.78	-	-
MpPR1s	Mp6g06400	1.26	-	-	-	-	-	-	-	-	-
MpPR1z	Mpzg00760	1.87	-	-	-	-	-	-	-	-	-
unknow n	Mp1g08210	1.91	-	-	-	-	-	mpo-b3.0r1-13147	-2.48	-	-
MpDIR22	Mp7g04240	-1.13	-	-	-	-	-	mpo-b3.0r1-14084	-1.76	-	-
MpDIR35	Mp5g16900	-1.08	-	-	-	-	-	mpo-b3.0r1-21328	-3.17	-	-
MpDIR45	Mp3g24170	-1.13	-	-	-	-	-	-	-	-	-
MpDIR6	Mp8g06340	-1.00	-	-	-	-	-	-	-	-	-
MpDIR60	Mp6g14010	-1.11	-	-	-	-	-	mpo-b3.0r1-4664	-1.91	-	-
MpPOD129	Mp5g17590	-1.43	-	-	-	-	-	mpo-b3.0r1-15067	5.39	-	-
MpPOD130	Mp5g17600	-1.14	-	-	-	-	-	mpo-b3.0r1-15871	-1.69	-	-
MpPOD135	Mp6g13510	-1.18	-	-	-	-	-	mpo-b3.0r1-14084	-1.76	-	-
MpPOD136	Mp6g13520	-1.43	-	-	-	-	-	mpo-b3.0r1-14084	-1.76	-	-
MpPOD32	Mp3g16820	-1.04	-	-	-	-	-	mpo-b3.0r1-3542	2.09	-	-
MpPOD36	Mp3g22000	-1.04	-	-	-	-	-	mpo-b3.0r1-21405	-2.38	-	-
MpPOD51	Mp5g01630	-1.32	-	-	-	-	-	mpo-b3.0r1-15067	5.39	-	-
MpPOD64	Mp5g02850	-1.14	-	-	-	-	-	mpo-b3.0r1-7800	-1.92	-	-
MpPOD65	Mp5g03200	-1.23	-	-	-	-	-	-	-	-	-
MpPOD73	Mp5g04320	-1.77	-	-	-	-	-	mpo-b3.0r1-21468	-3.37	-	-
MpPOD80	Mp5g06870	-1.19	-	-	-	-	-	mpo-b3.0r1-16246	-6.73	-	-
MpPOD101	Mp5g13790	-1.24	-	-	-	-	-	mpo-b3.0r1-11973	2.72	-	-
MpPOD129	Mp5g17590	-1.43	-	-	-	-	-	mpo-b3.0r1-15067	5.39	-	-
MpPOD161	Mp7g19390	1.43	-	-	-	-	-	mpo-b3.0r1-21450	6.89	-	-
MpPOD31	Mp3g16800	1.15	-	-	-	-	-	mpo-b3.0r1-9261	-3.98	-	-
MpPOD41	Mp4g05810	1.37	-	-	-	-	-	-	-	-	-
MpLOX12	Mp8g01650	-1.03	-	-	-	-	-	mpo-b3.0r1-17251	6.78	-	-
MpLOX16	Mp2g16000	3.46	-	-	-	-	-	mpo-b3.0r1-12706	4.20	-	-
MpLOX7	Mp2g12250	-1.37	-	-	-	-	-	mpo-b3.0r1-19749	-2.16	-	-
MpCKX1	Mp5g03090	-	1.06	-	-	-	-	-	-	-	-
MpERF18	Mp5g12480	-	1.19	-	-	-	-	-	-	mpo-b3.0r1-6275	-

Question 2 - Does the Band-7 protein FLOT modulate stress tolerance in *P. patens*? How is the expression of *PpFLOT* regulated? Are there differences in the function of bryophyte and seed plant FLOT?

Table 7: Oligonucleotides used in Question 2 (Supplementary Table 15)

Name	Sequence (5' to 3')	Purpose
FLOT_5'site_Fwd_A/B	TTTTCAGCAAGATTCAATGTTTGGCAACCATAG	Gibson assembly
FLOT_5'site_Rev_B	CACCATGTTGACCTTGTCAAAAACCTCAGCC	Gibson assembly
nptII_Fwd_C	GGTTTTTGACAAGGTCAACATGGTGGAGCAC	Gibson assembly
nptII_Rev_C	ATCACCACAATTGCTCACTGGATTTTGGTTTTAG	Gibson assembly
FLOT_3'site_Fwd_D	AAATCCAGTGACGAATTGTGGTGATGGCAG	Gibson assembly
FLOT_3'site_Rev_D/A	TTCTAGAAAGATCAAATCCATTCCATACAATGAAC	Gibson assembly
FLOT_insert_Fwd	TTTTCAGCAAGATTCAATGTTTGGCAACCATAG	Gibson assembly
FLOT_insert_Rev	TTCTAGAAAGATCAAATCCATTCCATACAATGAAC	Gibson assembly
Pp_Flot_fwd	GTTTCGACATCAGTCCTGCCA	screening/qRT-PCR
Pp_Flot_rev	ACTGCTTTTCCATCTCCGCA	screening/qRT-PCR
FlotKO_5_screen_fwd	ACGCCCCAGTATCTCACACGA	screening
FlotKO_5_screen_rev	CTGCGCTGACAGCCGGAACA	screening
FlotKO_3_screen_fwd	TTCGCAGCGCATCGCCTTCTATC	screening
FlotKO_3_screen_rev	GCCATGCAAAAGCTTTCTAAAGACCAA	screening
PpFlot_compl_fwd	GAGTACTTGGTGGTCACGGG	screening
PpFlot_compl_rev	CTTGGAAGGAACGGCAATG	screening
ef1a_qrt2_f	GTACCTCCCAGGCTGACTGC	qRT-PCR
ef1a_qrt2_r	GTGCTCACGGGTCTGTCCAT	qRT-PCR
C45_fwd	GGCTGGTCATGGGTTGCG	screening/qRT-PCR
C45_rev	GAGGTCAACTGTCTCGCC	screening/qRT-PCR
PpFlot_Ex2_fwd	TACAAGGGTGACACTGGTG	qRT-PCR
PpFlot_Ex2_rev	TTCTGCAGTTCGGCCTTCAT	qRT-PCR
Hyg_fwd	CTCGGAGGGCGAAGAATCTC	screening
Hyg_rev	CAATGACCGCTGTTATGCGG	screening
Act5_OExpl_fwd	CTGCTGTAAGGTTCTGCGTC	screening
Act5_OExpl_rev	ATCATCGCAAGACCGGCAA	screening
Flot_qRT_fwd	CCGGTATGACGATGGAGGAC	qRT-PCR
Flot_qRT_rev	TGGCATTGTATATATGAAGACCGAAT	qRT-PCR
NptII probe fwd	TCCATCATGGCTGATGCAAT	Southern Blot
NptII probe rev	GGCGATACCGTAAAGCACGA	Southern Blot
Pp1s44_31V6.1F	GCTTCACTCTTGTGCCGTCC	qRT-PCR
Pp1s44_31V6.1R	CTACACGGACACGGCGATGA	qRT-PCR
Pp1s8_127V6.1F	GTA CTCTGTGACGCTCCCC	qRT-PCR
Pp1s8_127V6.1R	GATTCCGCAGGCCTTTGGTG	qRT-PCR
Pp1s412_7V6.1F	ATAGCAGAATCCGCCCCACC	qRT-PCR
Pp1s412_7V6.1R	TGGCATTAGCTTCTCCGCGA	qRT-PCR
Pp1s296_27V6.1F	AGATTGAAGCGGGCCGAAGA	qRT-PCR

Name	Sequence (5' to 3')	Purpose
Pp1s296_27V6.1R	TTGGACGTACTCCCTGCGAC	qRT-PCR
Dehydrin.B_qF	GAGCACCGAGAAGTACCAGG	qRT-PCR
Dehydrin.B_qR	ATCTCCTGTGCTAGCGTTCG	qRT-PCR
TSPO1_qF	CATGTTGCTTCACCTGACC	qRT-PCR
TSPO1_qR	CACGATGCTAAGCCCATGAC	qRT-PCR
ppt-miR167_SL	GTCGTATCCAGTGCAGGGTCCGAGGTATTCGCACT GGATACGACAGGATC	stem-loop PCR
5_ppt-miR167_F_3	CCCGGAAGCTGCCAGCAT	stem-loop PCR
Uni_rev	CCAGTGCAGGGTCCGAGGTAT	stem-loop PCR
Pp3c11_21140_F	AAATCCAGCCCGACGTCATT	qRT-PCR
Pp3c11_21140_R	GACGAGTTGTCCTGGTCGTT	qRT-PCR
Pp3c7_20480V3.1_F	TCACAGGGAGATGGTGCTGA	qRT-PCR
Pp3c7_20480V3.1_R	TCGGTTGCGTAGACCACAAA	qRT-PCR
Pp3c16_23780_F	AACCTCCGCCTCTCTGGTAT	qRT-PCR
Pp3c16_23780_R	GGGGTATCAGCGTTCAAGGT	qRT-PCR
Pp3c13_14980_F	CCGGAGTGTTGATCCCTGAG	qRT-PCR
Pp3c13_14980_R	GATCACAGGGAGATTGCCCC	qRT-PCR
Pp3c2_35930_F	TCTTCGTCCAAGCCATTGTT	qRT-PCR
Pp3c2_35930_R	GGGGGTGAAGTTGGTAGCAT	qRT-PCR

Table 8: Significant differentially accumulated pigments in all *PpFLOT* mutant lines compared to the WT

Excerpt out of Supplementary Table 16 listing all significant differentially expressed pigments of all *PpFLOT* mutant lines compared to the WT

Analysis	Metabolite	log ₂ (FC)
<i>ΔPpFLOT-1</i> vs WT	unknown 1	-0.66928
	unknown 4	-0.48704
	unknown 6	0.752728
	unknown 7	-0.65348
	unknown 12	0.470805
	Lutein	-0.26261
	unknown 16	-0.46845
	Lycopene	-1.13586
<i>PpFLOT</i> -OEX1 vs WT	unknown 10	-0.63879
	Lutein	-0.31101
	Zeaxanthin	-0.41228
	unknown 16	-0.48847
	Lycopene	-1.29802
<i>PpFLOT</i> -OEX2 vs WT	unknown 7	-0.60565
	unknown 10	-0.73859
	Lutein	-0.19595
	Zeaxanthin	-1.03002
	unknown 16	-0.36439
<i>PpFLOT</i> -OEX3 vs WT	unknown 4	-1.12596
	unknown 6	0.841273
	unknown 7	-0.56448
	unknown 10	-1.52588
	Lutein	-0.56574
	Zeaxanthin	-1.46649
	unknown 16	-0.36
	unknown 19	-2.36784
	unknown 25	0.362815
	Lycopene	-0.835760

Table 9: DE proteins in *PpFLOT*-OEX1, 2 and 3 compared to the WT

Excerpt of Supplementary Table 19 listing significant differentially expressed (DE) protein groups of *PpFLOT* mutant lines compared to WT that are discussed in the main text. The listed DE proteins are show either a $\log_2(\text{FC}) < -2$ and > 2 or accumulate correlating to *PpFLOT* expression. Complete Supplementary Table 19 is stored on an external data storage medium.

Main protein ID	Log ₂ (FC)			Main gene ID	Phytozome <i>A. thaliana</i> definition	Gene symbol
	<i>PpFLOT</i> - OEX1	<i>PpFLOT</i> - OEX2	<i>PpFLOT</i> - OEX3			
A0A2K1ICI4	-1.22	-1.36	-1.72	Pp3c26_10440	thioredoxin Y2	PpTRX-Y2
A9TRK2	-3.56	-2.65	-3	Pp3c4_21500	heat shock cognate protein 70-1	PpHSP70-1
A0A7I4CH40	-1.49	-1.46	-1.16	None	unknown	#NV
A0A2K1KJF2	3.03	3.44	5.93	Pp3c5_12660	Pectin lyase-like superfamily protein	PpPME53
Q84V44	2.16	2.55	2.42	Pp3c12_4560	expansin A9	PpEXPA9
A9SIS3	1.53	1.78	1.88	Pp3c15_4330	Alpha-helical ferredoxin	PpNDUFS8
A0A2K1IUJ9	1.69	1.66	2.02	Pp3c20_8510	NADH-ubiquinone oxidoreductase B8 subunit, putative	PpNDUFA2/B8
A0A2K1L177	1.26	1.38	1.88	Pp3c2_11980	Phosphofructokinase family protein	PpMEE51
A9RWY6	2.63	2.84	4.37	Pp3c18_20060	Translation elongation factor EF1B, gamma chain	PpGST
A0A2K1KKR9	2.2	3.04	3.1	Pp3c5_22920	photosystem II light harvesting complex gene 2.2	PpLHCB2
A0A2K1KVH5	8.12	8.88	9.79	Pp3c3_21910	SPFH/Band 7/PHB domain-containing membrane-associated protein family	PpFLOT
A9SIC2	3.96	4.01	3.88	Pp3c16_18500	Rhodanese/Cell cycle control phosphatase superfamily protein	PpSEN1

Table 10: List of all significant differentially accumulated lipids of all *PpFLOT* mutant lines compared to the WT (Supplementary Table 20)

Analysis	Lipid	ID	Chemical formula	log ₂ (FC)	p-value	q-value
<i>ΔPpFLOT-1</i> vs WT	DAG 34:3	11	C37H66O5	-3.10	0.02	0.01
	DAG 36:4	14	C39H68O5	-0.34	0.03	0.01
	MGDG 34:2	29	C43H78O10	-0.29	0.01	0.01
	PC 34:5	45	C42H74NO8P	-0.38	0.00	0.01
	PC 38:3	55	C46H86NO8P	1.86	0.00	0.00
	PC 38:5	56	C46H82NO8P	0.34	0.03	0.02
	PE 34:3	61	C39H72NO8P	0.48	0.01	0.01
	PE 36:2	62	C41H78NO8P	-0.70	0.01	0.00
	PE 36:2	64	C41H78NO8P	0.92	0.02	0.00
	PE 36:5	70	C41H72NO8P	0.28	0.03	0.02
	PE 38:2	71	C43H82NO8P	0.61	0.01	0.00
	PE 38:2	72	C43H82NO8P	2.28	0.04	0.03
	plastoquinone	79	C53H80O2	-0.71	0.01	0.00
	SQDG 34:3	80	C43H76O12S	-0.41	0.02	0.01
	FA 18:2	92	C18H32O2	2.49	0.00	0.00
	FA 18:2	94	C18H32O2	-0.45	0.00	0.01
	FA 18:2	95	C18H32O2	-2.42	0.01	0.00
	FA 18:2	96	C18H32O2	-0.64	0.01	0.01
	FA 20:2	105	C20H36O2	0.87	0.00	0.01
	FA 20:4	109	C19H31COOH	-0.82	0.00	0.01
	FA 20:4	110	C19H31COOH	3.46	0.00	0.00
	FA 21:0	114	C20H41COOH	0.95	0.00	0.00
	FA 22:0	115	C22H44O2	-2.00	0.00	0.00
	FA 22:1	116	C21H41COOH	0.64	0.00	0.01
	FA 24:1	118	C24H46O2	0.83	0.00	0.01
	FA 28:0	120	C27H55COOH	1.74	0.00	0.00
	FA 30:0	121	C29H59COOH	1.28	0.00	0.00
<i>PpFLOT-OEX1</i> vs WT	DAG 34:2	6	C37H68O5	-0.38	0.00	0.03
	DAG 36:4	14	C39H68O5	-0.60	0.01	0.02
	DGDG 34:6	25	C49H80O15	1.11	0.01	0.02
	DGDG 36:4	26	C51H88O15	-0.68	0.00	0.03
	MGDG 34:2	29	C43H78O10	-0.48	0.00	0.03
	MGDG 36:4	37	C45H78O10	-0.66	0.02	0.05
	PE 34:1	58	C39H76NO8P	-0.42	0.00	0.00
	FA 18:2	92	C18H32O2	3.61	0.01	0.02
	FA 18:3	101	C18H30O2	3.80	0.00	0.02
	FA 20:4	110	C19H31COOH	2.74	0.01	0.04
	FA 22:1	116	C21H41COOH	-0.65	0.01	0.03
	FA 26:0	119	C26H52O2	1.56	0.00	0.00
	FA 28:0	120	C27H55COOH	1.16	0.00	0.03
<i>PpFLOT-OEX2</i> vs WT	DAG 34:3	11	C37H66O5	-0.76	0.01	0.02
	DGDG 34:1	19	C49H90O15	0.39	0.02	0.02
	DGDG 34:6	25	C49H80O15	0.73	0.02	0.02

Analysis	Lipid	ID	Chemical formula	log ₂ (FC)	p-value	q-value
<i>PpFLOT-OEX2</i> vs WT	MGDG 34:6	35	C43H70O10	-0.39	0.01	0.02
	PC 34:5	45	C42H74NO8P	-0.53	0.00	0.02
	PC 34:6	46	C42H72NO8P	-0.94	0.00	0.10
	PC 36:5	51	C44H78NO8P	0.45	0.00	0.01
	PC 38:3	55	C46H86NO8P	2.61	0.00	0.05
	PE 34:2	59	C39H74NO8P	0.75	0.00	0.01
	PE 36:5	70	C41H72NO8P	-0.46	0.01	0.02
	PE 38:2	72	C43H82NO8P	2.53	0.02	0.04
	SQDG 34:3	80	C43H76O12S	1.01	0.00	0.02
	FA 18:2	95	C18H32O2	1.12	0.00	0.01
	FA 18:2	97	C18H32O2	1.30	0.00	0.03
	FA 20:2	105	C20H36O2	0.76	0.02	0.03
	FA 20:4	109	C19H31COOH	1.01	0.00	0.01
	FA 20:4	110	C19H31COOH	3.68	0.00	0.02
<i>PpFLOT-OEX3</i> vs WT	DGDG 34:2	20	C49H88O15	0.43	0.02	0.03
	DGDG 34:6	25	C49H80O15	1.18	0.01	0.00
	MGDG 34:2	29	C43H78O10	0.29	0.02	0.03
	MGDG 34:3	30	C43H76O10	4.93	0.02	0.03
	PC 36:4	49	C44H80NO8P	0.50	0.01	0.00
	PC 36:5	52	C44H78NO8P	0.56	0.00	0.00
	PC 38:3	55	C46H86NO8P	1.86	0.02	0.03
	PC 38:5	56	C46H82NO8P	-2.14	0.00	0.00
	PE 34:1	58	C39H76NO8P	0.68	0.00	0.00
	PE 34:2	59	C39H74NO8P	1.32	0.00	0.00
	PE 34:3	61	C39H72NO8P	0.38	0.02	0.03
	PE 36:2	63	C41H78NO8P	-2.55	0.00	0.00
	PE 38:2	71	C43H82NO8P	1.04	0.01	0.00
	PG 34:2	75	C40H75O10P	0.36	0.03	0.05
	FA 17:0	90	C16H33COOH	0.38	0.00	0.00
	FA 18:2	92	C18H32O2	3.88	0.00	0.00
	FA 18:2	93	C18H32O2	0.60	0.01	0.02
	FA 18:2	95	C18H32O2	1.95	0.00	0.00
	FA 18:3	101	C18H30O2	3.49	0.00	0.00
	FA 20:1	104	C20H38O2	0.60	0.03	0.03
	FA 20:2	105	C20H36O2	1.83	0.00	0.00
	FA 20:4	110	C19H31COOH	4.06	0.00	0.00
	FA 22:0	115	C22H44O2	-2.99	0.02	0.03
	FA 24:1	118	C24H46O2	2.81	0.00	0.00
	FA 30:0	121	C29H59COOH	0.42	0.02	0.03
	FA 34:0	123	C33H67COOH	0.63	0.00	0.00

3. Publications connected to this dissertation

Peer-reviewed

Arif, M.A., Top, O., **Csicsely, E.**, Lichtenstern, M., Beheshti, H., Adjabi, K., and Frank, W. et al. (2022). DICER-LIKE1a autoregulation based on intronic microRNA processing is required for stress adaptation in *Physcomitrium patens*. *The Plant Journal* 109 (1), 227-240. <https://doi.org/10.1111/tpj.15570>

Non peer reviewed

Csicsely, E., Oberender, A., Georgiadou, A., Gutsche, N., Zachgo, S., Top, O., Frank, W. (2023). Identification and characterization of *DICER-LIKE* genes and their roles in *Marchantia polymorpha* development and stress adaptation. *bioRxiv* 2023.02.03.526932; doi: <https://doi.org/10.1101/2023.02.03.526932>

Unpublished manuscripts

Csicsely, E., Oberender, A., Georgiadou, Alz, J., Kiel, S., Gutsche, N., Zachgo, S., Grünert, J., Klingl, A., Top, O., Frank, W. (2024). Identification and characterization of *DICER-LIKE* genes and their roles in *Marchantia polymorpha* development and stress adaptation. - currently in preparation

Csicsely, E., Raulea, I. M., Mühlbauer, S., Schwenkert, S., Lehmann, M., Klingl, A., Top, O., Frank, W. (2024). Expression levels of the Band-7 protein FLOTILLIN modulate salt tolerance and pathogen defense pathways of *Physcomitrium patens*.

Acknowledgments

I would like to express my gratitude to everyone who assisted and supported me during the completion of this thesis. Firstly, I would like to thank Prof. Dr. Wolfgang Frank for providing me with an opportunity to work on the miRNA biosynthesis and the function of Flotillin in bryophytes. I am also thankful for all of your support, input and suggestions throughout my research and writing this thesis. Furthermore, I would also like to extend my many thanks to Dr. Oguz Top for all his support, input and guidance during the design and execution of all experiments. I am also grateful for all your patience in editing my writing and for listening to me discuss my theories and hypotheses. Many thanks to both of you, this would not have been possible without your support.

I would like to thank Stefan Kirchner, Yi An, Dr. Kristine Habermann, Dr. Bhavika Tiwari and all past and present members of the AG Frank for their aid and support during the laboratory work. Next, I would like to express my gratitude to Anja Oberender, Victoria Holzer, Anastasia-Styliani Georgiadou, Johanna Alz, Sebastian Kiel and all former students in our Lab who worked with me on this research topic during their practical research courses, Bachelor, or Master theses for assisting me with the experimental work.

I am also grateful to Dr. Nora Gutsche and Dr. Peter Schröder for teaching me how to work with *M. polymorpha* and supporting me in establishing this model organism in the Lab. Additionally, I want to thank the AG Geigenberger, especially David González-Gampo, for teaching me how to do electrolyte leakage measurements in plants.

I am also thankful to Susanne Mühlbauer, Jennifer Grünert and Prof. Dr. Andreas Klingl for generating microscopy images and their support in these experiments. Additionally, I would like to thank Dr. Serena Schwenkert and Dr. Martin Lehmann for generating the proteomics and metabolomics data and providing their input during the bioinformatical analysis.

I would also like to express my gratitude towards my thesis advisory committee members, Prof. Dr. Sabine Zachgo and Prof. Dr. Thomas Nägele, for their valuable advice and suggestions during the course of this study.

I would like to express my gratitude to the DFG for funding this research and to the MAdLand community for their active participation in exchanging information during the annual meetings.

Lastly, I would like to thank my friends Nadine Zellmann, Luana Schirling and Susi Schank, as well as my family, for their unwavering support, belief in me, and for listening to my concerns and boosting my confidence and motivation throughout this journey.

I want to thank all of you, then without your contributions, interest and efforts, this dissertation would not have been possible.

Curriculum vitae

Name Erika Csicsely

Education

Since 07.2020 PhD student at Ludwig-Maximilians-Universität München, Dissertation: *“Molecular innovations in bryophyte lineages assisting adaptations for survival in terrestrial environments “* at the Faculty of Biology, Department Plant Molecular Cell Biology

04.2017 - 10.2019 Master of Science Biology at Johannes-Gutenberg Universität Mainz, Master Thesis: *“Transcriptional knockdown of RNA-binding proteins in a cellular model of aging”* at the Institute of Organismic and Molecular Evolution

04.2014 - 04.2017 Bachelor of Science Biology at Johannes-Gutenberg Universität Mainz. Bachelor Thesis: *“Diurnal Regulation of Arr1 in the Retina of mice”* at the Institute of Functional and Clinical Anatomy

2010 - 2013 Willi-Graf Gymnasium, Saarbrücken

Work experience

01.2015 - 06.2020 Student assistant and assistant by Ganzimmun Diagnostics AG, Mainz

Volunteer work

Since 09.2020 PhD student representative on the MAdLand DFG Priority Programme 2237 committee

Conferences

09.2020 MAdLand Black Forest Workshop and Kickoff Meeting 2020

09.2021 MAdLand 2nd Annual Meeting and Workshop 2021, participated with an oral presentation about *“Comparative analysis of an autoregulatory loop in microRNA biogenesis that is crucial for stress adaptation in early land plants”*

09.2022 MAdLand 3rd Annual Meeting 2022, participated with an oral presentation about *“Functions of DICER-LIKE proteins in Marchantia polymorpha”*; winner of 3rd TPJ-ECR prize for an excellent oral presentation

09.2023 MAdLand 4th Annual Meeting 2023, participated with the poster *“Evolutionary impact of small RNA-dependent gene expression in bryophytes during the molecular adaptation for life on land”*